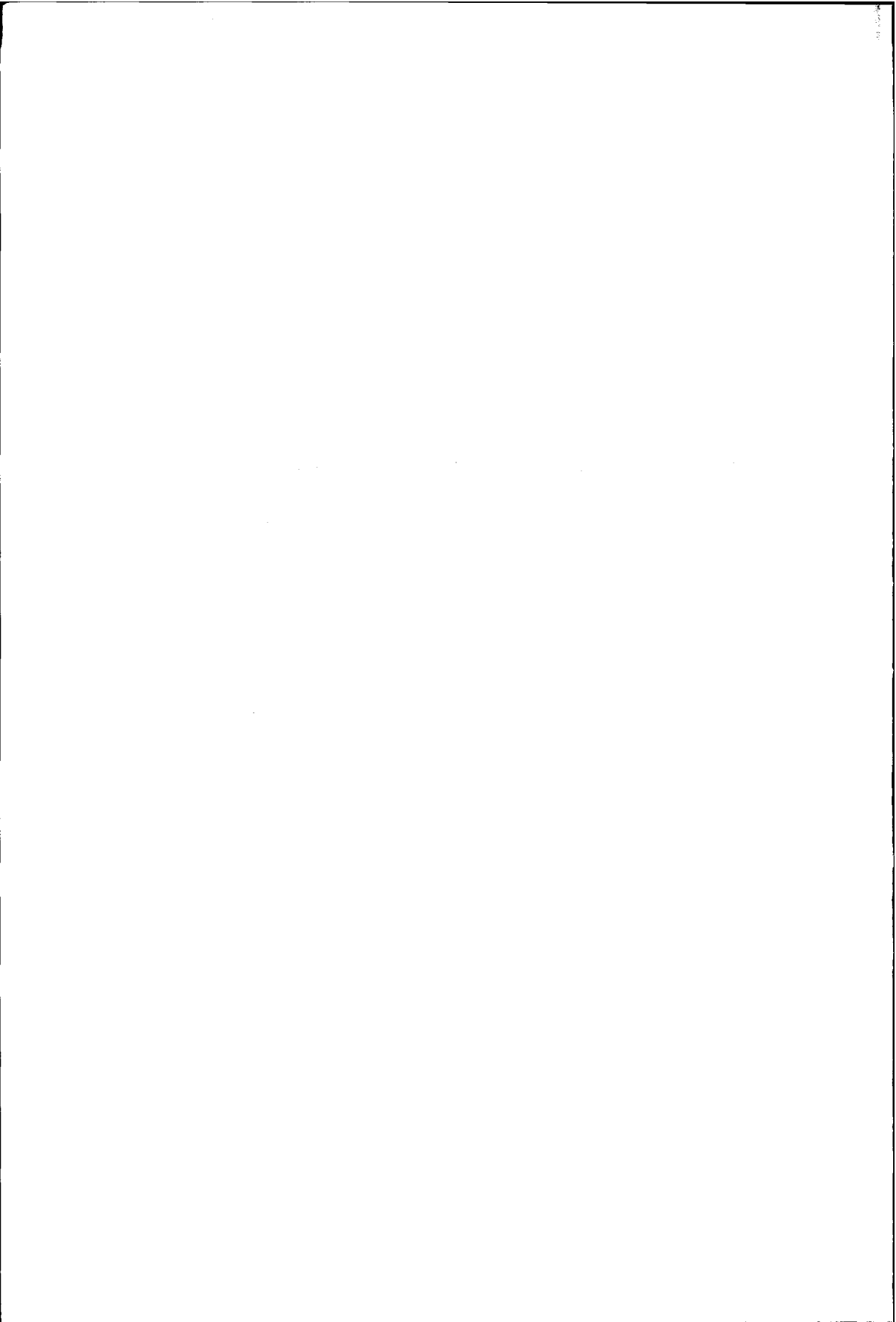


720410 722074  
3-12-74 3351

TR 3351

## **Aliasing in one-point turbulence measurements**

Theory, DNS and hotwire experiments



**Aliasing in one-point turbulence measurements**  
**Theory, DNS and hotwire experiments**

**Vertekening in eenpuntsmetingen aan turbulentie**  
**Theorie, DNS en hittedraadproeven**

**Proefschrift**

ter verkrijging van de graad van doctor  
aan de Technische Universiteit Delft,  
op gezag van de Rector Magnificus prof.ir. K.F. Wakker,  
in het openbaar te verdedigen ten overstaan van een commissie,  
door het College voor Promoties aangewezen,  
op vrijdag 25 juni 1999 te 10.30 uur

door

**Arjan VAN DIJK**  
doctorandus in de natuurkunde,  
geboren te Amsterdam

Dit proefschrift is goedgekeurd door de promotor:  
Prof.dr.ir. F.T.M. Nieuwstadt

Samenstelling promotiecommissie:

Rector Magnificus,	voorzitter
Prof.dr.ir. F.T.M. Nieuwstadt,	Technische Universiteit Delft, promotor
Prof.dr.ir. P.G. Bakker,	Technische Universiteit Delft
Dr.ir. P.M.T. Broersen,	Technische Universiteit Delft
Prof.dr.ir. H. Hoeijmakers,	Universiteit Twente
Prof.dr. J.C.R. Hunt, FRS,	University of Cambridge, Engeland
Dr.ir. A.F.G. Jacobs,	Landbouwniversiteit Wageningen
Prof.dr. D. Lohse,	Universiteit Twente

Copyright ©1999 by  
A. van Dijk  
Frederik Hendrikstraat 125  
NL - 3583 VJ Utrecht  
All rights reserved

ISBN 90-9012799-2  
NUGI 812, 811 en 815



# Summary

## Aliasing in one-point turbulence measurements

Theory, DNS and hotwire experiments

Arjan van Dijk

The subject of this thesis is the interpretation of one-point velocity measurements in a turbulent flow field in terms of three-dimensional spatial energy spectra. Our motivation to start this study is that there is no clear relation between the wavelength in conventional spectra of one-point measurements and three-dimensional structure size. Conventional spectra of one-point measurements are constructed from time-series of observations. With help of Taylor's hypothesis these observations are converted into spatial observations along a line, from which the so called *one-point spectrum* can be estimated. One studies the one-point spectrum to get information on the spatial structure of turbulence. Unfortunately this one-point spectrum is blurred by aliasing, which means that signal components from small structures are observed as associated with larger structures. Therefore a procedure is needed to un-alias the one-point spectrum such that one can interpret its results in terms of the three-dimensional structure of turbulence. Until now there is not much more to unalias one-point measurements than an old isotropic relation. However, in real situations one observes anisotropic distributions of fluctuations. Exchange processes are for example studied in the context of climate research and one-point measurements are a commonly used source of information. Without a proper un-aliasing tool, one cannot estimate the preferential directions of velocity fluctuations induced by structures of a certain size. Consequently, without an anisotropic model, one cannot expect to gain much insight into the dynamics of exchange processes from one-point measurements.

In this study we have constructed a theoretical model which relates one-point spectra to three-dimensional spectra. The resulting relations are assessed by means of a direct numerical simulation (DNS), and are then applied to windtunnel measurements on the upstream stagnation line of grid generated turbulence in stagnant plate flow and the achievements are discussed.

The model which we have developed is based on a statistical description of the probability density of the directions in which turbulent structures of a certain wavelength induce a velocity fluctuation as a function of the orientation of the wavevector. For isotropic turbulence this probability density function can be regarded as spherical in  $k$ -space. Here we make use of ellipsoids, with which we extend the existing theory to incompressible, homogeneous, but anisotropic flow. The three-dimensional spectrum is solved from the model with use of a linear

expansion of the anisotropy around isotropy. We found a set of six relations in closed form, which give the symmetric part of the three-dimensional spectrum as a function of the symmetric part of the one-point spectrum. This work can be considered as the first theory to exploit all independent information in the symmetric part of one-point turbulence spectra to estimate the three-dimensional spectrum.

Our unaliasing relations depend on the third derivative of the one-point spectrum. Therefore we require an estimator for the one-point spectrum, which allows for differentiation. We have constructed two different methods to estimate these spectral derivatives. The first method is based on logarithmic smoothing of the one-point spectrum, estimated via Fast Fourier Transform (FFT), followed by curve fitting of the double logarithmic spectrum. The resulting fit-curve is then differentiated analytically. The second method uses autoregressive modelling (AR) to find an analytic expression for the spectrum, which then is differentiated to find the spectral derivatives. To eliminate insignificant wiggles due to noise from the estimated functions, the function is smoothed via logarithmic convolution. We have a preference for the FFT-based method to the AR-based method, because the latter method is simply incapable of estimating spectra for large structures and for the small scales we have not managed to eliminate the influence of noise amplification by differentiation.

In the DNS we have simulated grid generated turbulence. We have made a comparison between direct estimates for the three-dimensional spectrum via the Fourier transform of three-dimensional velocity fields and indirect estimates via application of our new unaliasing relations to simulated one-point measurements. The comparison has not been successful. There was no correspondence between the two estimates but the scatter in the estimates was also very large. We have many suggestions to improve this test. Most of them are related to the spatial resolution of the simulation and consequently to computer power. In this direction further study is advisable.

Our next step to verify our theory has been to collect time-series of turbulent velocity fields. For this we have constructed a four-hotwire probe and a setup for three dimensional calibration. We have examined which hot-wire calibration model gives the best estimates for both the velocity vector and for the anisotropy of a flow. In an investigation of many calibration methods we found that the best method is to model the responses of the wires as functions of the velocity field and not vice versa. To estimate the velocity vector from a set of four wire readings one has to solve the four response equations simultaneously. A fast method has been developed to make a temperature calibration of the probe.

With our hot-wire probe we have measured the velocity vector in grid generated turbulent flow on the stagnation line upstream of a vertical flat plate. The plate was implemented to break the initial axisymmetry of the grid turbulence, to create a situation in which our unaliasing theory could show its power to extend the reconstruction of the three-dimensional spectrum from one-point observations to anisotropic turbulence. Moreover the flow geometry presented the possibility to verify the Rapid Distortion theories of Batchelor and Proudman (1954) and of Hunt (1973).

In the one-point spectra we observed that when the plate is approached, all velocity components of the large scales are amplified and all velocity components of the small scales are attenuated. This observation is at variance with the asymptotic Rapid Distortion theories by Hunt and by Batchelor and Proudman. The relative contribution the three velocity components to the kinetic energy is found to react to the approach of the plate as follows. For all wavelengths

the reaction to the plate is the same. In longitudinal (streamwise) direction nothing happened and the relative gain of the vertical fluctuations was made at the cost of the relative contribution to the energy by the lateral fluctuations. For the lateral and vertical fluctuations this re-ordering of fluctuations is supported by small scale RDT-asymptotics. The indifference of the longitudinal fluctuations could not be explained. Nor could we explain why the redistribution of the fluctuations over the three dimensions did not depend on the structure size.

Our unaliasing relations were used to estimate the three-dimensional spectrum from the one-point spectrum. The AR-based implementation resulted in more or less constant functions as estimates for the three-dimensional spectrum. We ascribe this non-realistic behaviour to the earlier mentioned problems with AR. The FFT-based method resulted in a spectrum which satisfied two of our expectations: from the one-point spectrum to the three-dimensional spectrum the longitudinal fluctuations are amplified and the lateral fluctuations are attenuated. Moreover we observed that characteristics were shifted from the large scales to the smaller scales.

We conclude that we have succeeded in developing a set of practically applicable relations, with which for the first time one can interpret anisotropic one-point spectra in terms of three-dimensional spectra.



# Samenvatting

## Vertekening in eenpuntsmetingen aan turbulentie

Theorie, DNS en hittedraadproeven

Arjan van Dijk

Dit proefschrift behandelt de uitleg van eenpunts snelheidsmetingen aan een turbulente stroming in termen van driedimensionale energiespectra. We hebben dit onderzoek uitgevoerd omdat er geen goede relatie bestaat tussen de golflengte in spectra van eenpuntsmetingen en ruimtelijke structuurgrootten. Conventionele spectra worden gemaakt van tijdreeksen van waarnemingen. Met behulp van Taylor's hypothese worden deze waarnemingen vertaald naar ruimtelijke waarnemingen langs een lijn, waaruit het zogenaamde eenpuntsspectrum wordt geschat. Het eenpuntsspectrum wordt bestudeerd om informatie te verkrijgen over de ruimtelijke structuur van turbulentie. Helaas hebben spectra van eenpuntsmetingen last van vertekening, waardoor een te grote golflengte wordt toegekend aan structuren. Hierom is er een procedure nodig om eenpuntsspectra te corrigeren voor deze vertekening, zodanig dat de resultaten ervan te interpreteren zijn in termen van de ruimtelijke structuur van turbulentie. Tot op heden is er niet veel meer beschikbaar om deze vertekening te corrigeren dan een oude isotrope relatie, terwijl menig onderzoeker in de praktijk anisotrope snelheidsverdelingen ziet. Uitwisselingsprocessen worden onder meer bestudeerd in het kader van klimaatonderzoek en hierbij wordt vaak gebruik gemaakt van eenpuntsmetingen. Zonder een geschikt instrument is het niet mogelijk om een schatting te geven van de voorkeursrichtingen van de fluctuaties die worden opgewekt door structuren van een bepaalde maat. Het laat zich raden dat het zonder anisotroop correctiemodel voor vertekening lastig is om via eenpuntsmetingen inzicht te verkrijgen in de dynamica van uitwisselingsprocessen.

In deze studie hebben we een model gemaakt dat eenpuntsspectra koppelt aan ruimtelijke spectra. De afgeleide verbanden zijn getest in een direct numerieke simulatie (DNS). Vervolgens zijn ze toegepast op windtunnelmetingen verricht op de stroomopwaartse stagnatielijns in de stroming van roosterturbulentie rond een vlakke plaat.

Het model dat we hebben ontwikkeld is gebaseerd op een statistische beschrijving van de kansdichtheidsfunctie van de richting waarin structuren van een bepaalde golflengte snelheidsfluctuaties induceren als functie van de richting van de golfvector. Voor isotrope turbulentie kan deze kansfunctie als een bol in de  $k$ -ruimte worden voorgesteld. Wij hebben gebruik gemaakt van ellipsoïden om de isotrope theorie uit te breiden tot een onsamendrukbare, homogene, maar

anisotrope stroming. Het ruimtelijke spectrum is opgelost uit het model met behulp van een eerste-orde ontwikkeling van het anisotropie karakter rond isotropie. We hebben een set van zes gesloten vergelijkingen gevonden, die het symmetrische deel van het golfgetalspectrum geven als functie van het symmetrische deel van het eenpuntsspectrum. Dit werk kan worden beschouwd als de eerste theorie die gebruik maakt van alle onafhankelijke informatie in het symmetrische deel van het eenpuntsspectrum bij het schatten van het ruimtelijke spectrum.

Onze verbanden voor vertekeningscorrectie hangen af van de derde afgeleide van het eenpuntsspectrum. Daarom hebben we een differentieerbare schatter voor het spectrum nodig. We hebben twee methoden ontwikkeld om spectrale afgeleiden te schatten. De eerste methode is op basis van logaritmisch glad poetsen van het eenpuntsspectrum, dat geschat wordt via Fast Fourier Transformatie (FFT), waarna een functie wordt aangepast aan het dubbellogaritmisch spectrum. De resulterende fitkromme wordt analytisch gedifferentieerd. De tweede methode maakt gebruik van een Autoregressief model (AR) om een analytische uitdrukking te vinden voor het spectrum, die vervolgens analytisch wordt gedifferentieerd om spectrale afgeleiden te schatten. Om rimpels in de met AR geschatte functies te verwijderen worden ze glad gepoetst met een logaritmische convolutie. We hebben een voorkeur voor de methode die gebruik maakt van FFT boven de methode op basis van AR omdat laatstgenoemde methode niet in staat is een schatting te geven van spectra voor lange golven. Verder is het ons voor kleine golflengten niet gelukt om de invloed van ruis in het AR-spectrum, die versterkt wordt bij differentiatie, te onderdrukken.

In de DNS hebben we roosterturbulentie nagebootst. We hebben een vergelijking gemaakt tussen een directe schatting van het golfgetalspectrum, verkregen door ruimtelijke snelheidsvelden te Fourier-transformeren, en een indirecte schatting, die we verkregen door ons correctiemodel voor vertekening los te laten op de spectra van nagebootste eenpuntsmetingen. De vergelijking heeft geen vrucht afgeworpen. Er was geen overeenkomst tussen beide schattingen, maar de onzekerheid in de schattingen was ook zeer groot. We hebben een groot aantal suggesties om deze test te verbeteren. De meeste hiervan houden verband met het ruimtelijk oplossend vermogen van de simulatie, en dus met rekenkracht. Verdere studie in deze richting wordt aanbevolen.

De volgende stap die we hebben gezet om onze theorie te testen is geweest het het vergaren van tijdreeksen van turbulente snelheidsvelden. Hiertoe hebben we een vier-hittedraadssonde gemaakt en een opstelling om deze ruimtelijk te ijken. We hebben onderzocht welk ijkmodel van een vierdraadssonde de beste schatting oplevert voor zowel de snelheidsvector als voor de anisotropie. In een vergelijking van een groot aantal ijkmethoden vonden we dat het verkieslijk is de respons van de draden te modelleren als functie van de aangeboden snelheidsvector en niet omgekeerd. Om uit vier gemeten hittedraadspanningen een schatting te geven voor de snelheidsvector moeten de vier responsvergelijkingen simultaan worden opgelost. Voor het uitvoeren van een temperatuur-ijking van de sonde hebben we een snelle methode ontwikkeld.

Met onze sonde hebben we de snelheidsvector gemeten in roosterturbulentie op de stagnatielijn voor een verticale vlakke plaat. De plaat was aangebracht om de aanvankelijke axisymmetrie van de roosterturbulentie te breken, om zo een situatie te genereren waarin ons model voor de correctie voor vertekening zijn kracht kon laten zien om de reconstructie van het ruimtelijke spectrum uit het eenpuntsspectrum te generaliseren tot anisotrope turbulentie. Bovendien bood deze geometrie de mogelijkheid om de Rapid Distortion theorieën van Batchelor and Proudman (1954) en van Hunt (1973) te toetsen.

In de eenpuntsspectra namen we waar dat, bij het naderen van de plaat, alle snelheidscomponenten van de grote structuren versterkt werden, terwijl alle snelheidscomponenten van kleine structuren werden verzwakt. Deze waarneming strookt niet met de Snelle Vervormingstheorieën (RDT) van Hunt en van Batchelor en Proudman. We zagen dat de relatieve bijdrage aan de kinetische energie van fluctuaties in de drie richtingen als volgt op het naderen van de plaat reageerden: Voor alle golflengten was de reactie gelijk. In de hoofdstroomrichting gebeurde er niets en de relatieve winst van de verticale fluctuaties ging ten koste van de relatieve bijdrage tot de energie van de laterale fluctuaties. Deze herschikking van laterale en verticale fluctuaties wordt voor de kleine structuren ondersteund door asymptotische RDT. Voor de onverschilligheid van fluctuaties in de langsrichting hebben we geen verklaring kunnen vinden. Tevens hebben we niet kunnen verklaren waarom de herschikking van fluctuaties, in reactie op het naderen van de plank, niet van de structuurgrootte af hangt.

Onze verbanden voor de correctie voor vertekening zijn gebruikt om het golfgetalspectrum te schatten uit het eenpuntsspectrum. De AR-methode leverde een min of meer constante functie op als schatting voor het golfgetalspectrum. We schrijven dit niet-realistisch gedrag toe aan de eerdergenoemde problemen met AR. De FFT-methode leverde een spectrum op dat op twee manieren aan onze verwachtingen voldeed: van het eenpuntsspectrum naar het golfgetalspectrum werden fluctuaties in de langsrichting versterkt en in de dwarsrichtingen verzwakt. Verder zagen we dat karakteristieken verschoven van de grote schalen naar de kleine schalen.

We concluderen dat we erin zijn geslaagd om een set praktisch toepasbare verbanden te ontwikkelen, waarmee men voor het eerst anisotrope eenpuntsspectra kan interpreteren in termen van ruimtelijke spectra.





# Contents

<b>Summary</b>	<b>I</b>
<b>Samenvatting</b>	<b>V</b>
<b>General introduction</b>	<b>5</b>
<b>1 Turbulence basics</b>	<b>11</b>
Introduction . . . . .	11
1.1 General turbulence characteristics . . . . .	12
1.2 One-point measurements and Taylor's hypothesis . . . . .	14
1.3 Characteristics of grid generated turbulence . . . . .	15
1.3.1 Decay of kinetic energy . . . . .	15
1.3.2 Homogeneity and isotropy . . . . .	16
1.3.3 Development of characteristic lengthscales . . . . .	16
1.4 Dynamical equations and rapid distortion . . . . .	17
1.5 The evolution tensor for commuting strain . . . . .	21
1.6 Turbulence impinging on a flat plate . . . . .	22
<b>2 The aliasing problem in one-point measurements</b>	<b>27</b>
Introduction . . . . .	27
2.1 Basic tensor notation . . . . .	28
2.2 Velocity spectrum . . . . .	29
2.3 The second-order velocity correlation tensor . . . . .	32
2.4 Correlation spectrum . . . . .	33
2.5 Restrictions and assumptions . . . . .	35
2.6 Linearly polarised waves . . . . .	37

2.7	Integrated spectra . . . . .	39
2.8	The aliasing problem . . . . .	40
2.8.1	Tools for building a model ss-pdf . . . . .	42
2.8.2	An ellipsoid related to the wavenumber spectral tensor . . . . .	44
2.8.3	Realization of a model ss-pdf . . . . .	45
2.8.4	Aliasing relations . . . . .	47
2.8.5	Unaliasing relations . . . . .	49
2.9	Axisymmetric turbulence . . . . .	52
	Conclusion . . . . .	53
<b>3</b>	<b>Estimation of spectra and spectral derivatives</b>	<b>55</b>
	Introduction . . . . .	55
3.1	Time-spectra and basic notation . . . . .	55
3.2	Selection of analogue filter- and sampling frequency . . . . .	57
3.3	Consequences of finite sets of samples . . . . .	58
3.3.1	The effect of correlation function windowing . . . . .	59
3.3.2	Different windows . . . . .	59
3.4	Allowed spectral leakage for turbulence measurements . . . . .	60
3.4.1	Correlation function window width for turbulence . . . . .	61
3.4.2	Postponing correlation function windowing . . . . .	62
3.5	Cospectral tensor estimation via Fast Fourier Transform . . . . .	64
3.5.1	High-pass filtering . . . . .	64
3.5.2	Data windowing . . . . .	66
3.5.3	Error estimation of spectral density . . . . .	66
3.6	Spectral density estimation via autoregressive modelling . . . . .	69
3.6.1	Stability criterion for AR-models . . . . .	69
3.6.2	Order estimation for AR-processes . . . . .	70
3.6.3	Determination of AR coefficients via the Yule-Walker method . . . . .	71
3.6.4	Determination of AR-coefficients via Burg's method . . . . .	72
3.6.5	Relation between AR-coefficients and spectra . . . . .	74
3.7	Spectral density estimation via moving average modelling . . . . .	75
3.7.1	Estimation of MA-parameters . . . . .	76
3.7.2	Relation between MA-coefficients and spectra . . . . .	77

3.8	Comparison of FFT-, AR- and MA-models . . . . .	78
3.9	The estimation of derivatives of spectra . . . . .	80
3.9.1	Differentiating FFT-based spectra . . . . .	81
3.9.2	Differentiating AR-based spectra . . . . .	85
3.9.3	Conclusion . . . . .	86
<b>4</b>	<b>Comparison of theory with DNS</b>	<b>87</b>
	Introduction . . . . .	87
4.1	Description of the model . . . . .	87
4.1.1	Specification of the DNS method . . . . .	88
4.1.2	Specification of the calculation . . . . .	89
4.2	Characteristics of the DNS simulations . . . . .	90
4.2.1	Lateral homogeneity of the velocity variance . . . . .	93
4.2.2	Lateral homogeneity of the anisotropy . . . . .	94
4.2.3	Magnitude of the anisotropy . . . . .	96
4.3	Direct estimation of tensor $\Psi$ . . . . .	97
4.4	Indirect estimation of tensor $\Psi$ with unaliasing theory . . . . .	99
4.4.1	Estimation of one-point spectrum $\Theta$ . . . . .	99
4.4.2	From $\Theta$ to $\Psi$ . . . . .	105
4.4.3	Asymptotic theory . . . . .	110
4.5	Discussion and conclusion . . . . .	111
<b>5</b>	<b>Metrology and experimental setup</b>	<b>115</b>
	Introduction . . . . .	115
5.1	Analogue filtering and electronic signal conditioning . . . . .	116
5.2	Peripheral apparatus . . . . .	116
5.2.1	Measurement of pressure . . . . .	117
5.2.2	Measurement of temperature . . . . .	119
5.3	The hotwire calibration unit . . . . .	121
5.3.1	Construction of the miniature windtunnel . . . . .	121
5.3.2	Calibration of contraction pressure . . . . .	123
5.3.3	Mean flow homogeneity check . . . . .	123
5.3.4	Turbulence level check . . . . .	127

5.3.5	Pitch and yaw facility . . . . .	127
5.4	The four hotwire probe: design . . . . .	128
5.5	The grid . . . . .	130
5.5.1	Expected flow characteristics . . . . .	130
5.5.2	Homogeneity check . . . . .	131
5.6	The windtunnel . . . . .	133
5.7	The testsection . . . . .	135
5.7.1	Specification of testsection and traversing mechanism . . . . .	135
5.7.2	Laminar velocity profile in the testsection . . . . .	136
5.7.3	Velocity profiles of gridflow . . . . .	141
5.7.4	The velocity terminator . . . . .	147
<b>6</b>	<b>Hot-wire anemometry</b>	<b>151</b>
	Introduction . . . . .	151
6.1	Historical background . . . . .	152
6.2	CTA-circuit . . . . .	153
6.3	Cooling of a wire . . . . .	154
6.3.1	Normal cooling of an element . . . . .	154
6.3.2	Directional sensitivity of an element . . . . .	156
6.3.3	Non-ideal effects . . . . .	158
6.4	Temperature drift of the fluid . . . . .	159
6.4.1	Temperature dependence of the signal . . . . .	160
6.4.2	Correction for temperature drift . . . . .	161
6.5	Velocity calibration methods . . . . .	161
6.5.1	Effective velocity methods . . . . .	162
6.5.2	Look-up table method . . . . .	165
6.5.3	Lemonis' indirect subprobe method . . . . .	166
6.5.4	Full 4-wire indirect model . . . . .	167
6.5.5	Direct method: subprobe model . . . . .	167
6.5.6	Direct method: 4-wire model . . . . .	169
6.6	Test of calibration methods . . . . .	170
6.6.1	Test of laws of King and Jørgensen . . . . .	170
6.6.2	Test of other indirect- and direct calibration methods . . . . .	177

Conclusion . . . . .	184
<b>7 Experiments on turbulent stagnation-point flow</b>	<b>187</b>
Introduction . . . . .	187
7.1 Mean flow upstream of the terminator . . . . .	187
7.2 Hotwire measurements on the stagnation line . . . . .	193
7.3 Estimation of the one-point spectral tensor . . . . .	194
7.4 Estimation of the wavenumber spectral tensor . . . . .	200
7.5 Discussion and conclusion . . . . .	209
<b>Main conclusions and discussion</b>	<b>211</b>
<b>A Curve-fitting through data with measurement errors</b>	<b>217</b>
Introduction . . . . .	217
A.1 No errors known . . . . .	218
A.2 Only $y$ -errors . . . . .	219
A.3 Uncorrelated $x$ - and $y$ -errors . . . . .	220
A.4 Data with correlated errors in $x$ and $y$ . . . . .	222
A.5 Tuning and quality of a class of fitcurves . . . . .	225
A.5.1 Quality of a single model . . . . .	226
A.5.2 Detection of outliers: the Chauvenet criterion . . . . .	226
A.5.3 Tuning the number of model parameters . . . . .	227
A.5.4 The importance of residual plots . . . . .	227
A.6 Process of fitting . . . . .	228
<b>B Time-ordered exponential for non-commuting tensor fields</b>	<b>231</b>
Introduction . . . . .	231
B.1 Commutation problems . . . . .	232
B.1.1 The determinant of the time-ordered exponential . . . . .	234
B.2 Analysis of the exponential function . . . . .	234
B.2.1 Mathematical lemmas . . . . .	234
B.2.2 Differentiating the commuting solution . . . . .	235
B.3 Solving the time-ordered exponential . . . . .	236
B.4 An application of the commutator method: circular cylinder flow . . . . .	237

B.5	Definitions of commutator integrals . . . . .	240
<b>C</b>	<b>Characterisation of anisotropy</b>	<b>241</b>
	Introduction . . . . .	241
C.1	Invariants . . . . .	241
C.2	Invariants of the Reynoldsstress-tensor . . . . .	242
C.3	The original Lumley-triangle . . . . .	243
C.4	Modified Lumley-triangle and character plot . . . . .	243
<b>D</b>	<b>Betz-manometer and air-density</b>	<b>247</b>
D.1	Calibration of a Betz-manometer . . . . .	247
D.2	Density of wet air . . . . .	247
<b>E</b>	<b>Correction of hot-wire data for ambient temperature drift</b>	<b>251</b>
	Introduction . . . . .	251
E.1	Application of the temperature method . . . . .	251
	E.1.1 Determination of hot-wire temperature . . . . .	252
	E.1.2 Temperature coefficient of resistance . . . . .	253
	E.1.3 Direct determination of $T_{\text{hot}}$ . . . . .	255
E.2	Practical test of the temperature method . . . . .	256
	E.2.1 The set-up . . . . .	256
	E.2.2 The experiment . . . . .	258
	E.2.3 Discussion . . . . .	259
E.3	Application of the resistance method . . . . .	260
E.4	Practical test of resistance method . . . . .	262
	E.4.1 Set-up . . . . .	262
	E.4.2 The experiment . . . . .	263
	E.4.3 Discussion . . . . .	264
E.5	Discussion on temperature correction . . . . .	265
	E.5.1 Additional ideas . . . . .	265
	E.5.2 Conclusion . . . . .	265
<b>F</b>	<b>The effects of hot-wire separation</b>	<b>267</b>
<b>G</b>	<b>Fitting laws of King and Jørgensen</b>	<b>271</b>

Introduction . . . . . 271

G.1 Conversion to reference temperature . . . . . 271

G.2 Determination of  $A$  and  $n$  . . . . . 271

G.3 Estimation of  $\phi$  . . . . . 272

G.4 Estimation of  $\theta$ ,  $k$ ,  $h$  and  $B$  . . . . . 274

**Literature** . . . . . **275**





# Observation

The crucial trigger for science is astonishment. To make ourselves susceptible to our surprise we have to allow our senses to pass all impressions to the brain, where they can be combined. In turbulence research a remarkable achievement in this respect was made in the year 1508 by Leonardo da Vinci, who made detailed drawings and descriptions of water falling into a container (see figure 1).

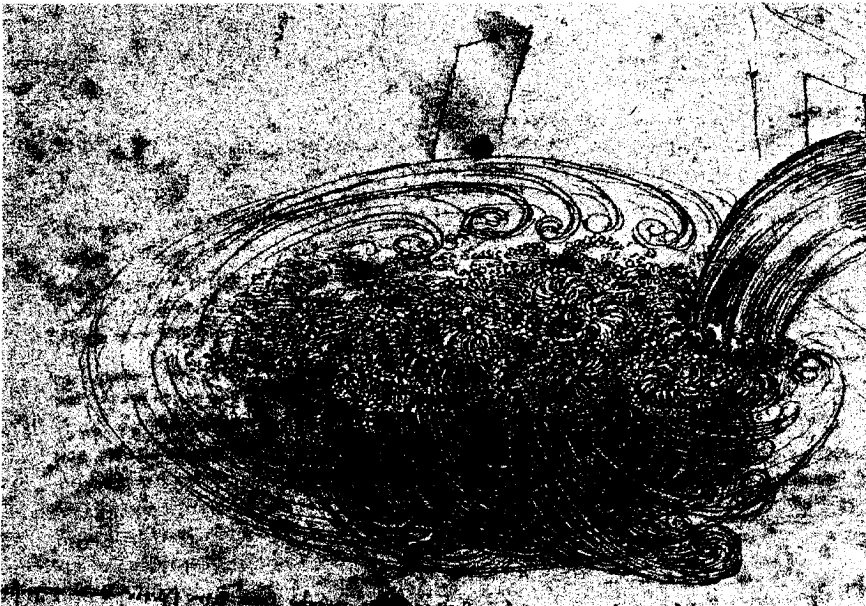


Figure 1: Observations by Leonardo da Vinci, 1508-1509

Despite the educational effort today's state of the art in turbulence research is not much more than a mathematical formulation of Da Vinci's observations. I wanted to know whether this lack of progress is to be attributed to either "nature" (our brains are too small to develop knowledge on a higher level) or to "nurture" (some aspects of life restrict our possibilities to develop intellectual capacities, which under better circumstances could have bloomed). Therefore in 1994 I presented Da Vinci's experiment to the pupils in a primary school without suggesting the answer (which I would not have known). The observations of two girls (age 11) are shown

in figure 2. A translation of their findings is:

The experiment of toppling a bucket of water into a larger container:

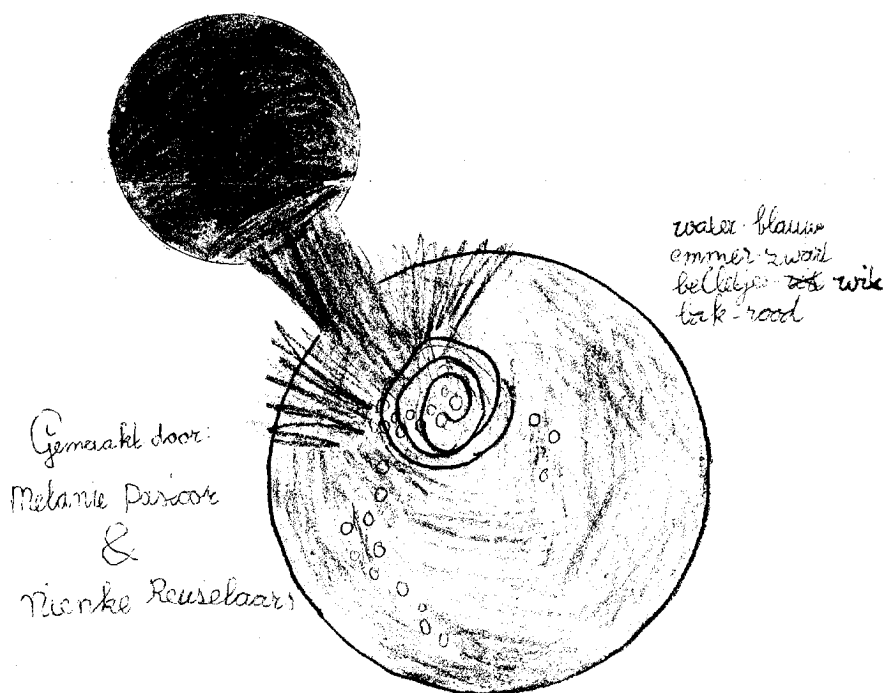
When you let the water flow into a container, all you see is little bubbles, then the water starts to spin, then wavelets appear. When the wavelets have stopped and the bubbles have snapped then the water comes to rest. At first the water is a real shambles, later there is still some structure in it.

By: Melanie Pastoor and Nienke Reuselaars

In these three sentences the girls nominate: two-phase flow, vorticity, surface effects, dissipation (both 2D and 3D), buoyancy, the chaotic nature of turbulence, it's coherency and the tendency of the correlation length to grow in decaying turbulence. This is a very complete observation. The difference between the report by Da Vinci and the account of the experiment by Pastoor and Reuselaars is found in the details of the drawings corresponding with the observations, not in the observations themselves.

This brings me to the conclusion that "nature" is not the restricting factor in today's research. Without pointing out the cause of the stagnation I suggest a method to circumvent the problem: science will make a better chance in the future if research groups start to collaborate with local primary schools.

Het proefje met ~~een~~ een emmer met water teg. lopen in een grote lak.



als je het water in een lak laat lopen zie je allemaal witte belletjes dan gaat het water draaien daarna komen er kleine golfjes.  
Als de golfjes zijn gestopt en de belletjes zijn geknapt dan komt het water tot stilstand.

Eerst is het ~~een~~ water een grote jumboel daarna zit er nog een laagje structuur in.

Figure 2: Observations by Melanie Pastoor and Nienke Reuselaars, 1994



# General introduction

For a general characterisation of the phenomenon *turbulence* we recall Bradshaw's definition (Bradshaw, 1971):

"Turbulence is a three-dimensional time-dependent motion in which vortex stretching causes velocity fluctuations to spread to all wavelengths between a minimum determined by viscous forces and a maximum determined by the boundary conditions of the flow. It is the usual state of fluid motion except at low Reynolds numbers."

From this description we read that turbulence is all about dynamics in flows. Laminar flows, no matter how swiftly they go, are not half as interesting as turbulent flows, because a laminar flow does not interact with itself. Interaction is a key to exchange processes in flows and therefore people who want to monitor exchange processes (whether it is in nature or in industry) are principally interested in better understanding of the turbulent part of a flow, and less in the laminar part. An example of such an exchange process is the interaction between the atmosphere and the oceans, which to a great extent influences our weather and climate (see e.g. (Katsaros et al., 1987)). A different example is the mixing of fuel and air in combustion engines. Without turbulent mixing the fuel would not burn and consequently our car would remain without momentum.

Three important parameters in turbulent fluctuations are the lengthscales and the timescales of the fluctuations and the distribution of the associated motions over the three directions. The timescale is often coupled to the lengthscale. Different lengthscales can have different dynamics. Size discrimination may help to understand the resulting dynamics of a group of structures of different sizes. One studying the interaction mechanism of each size of structure individually and sums the results. From the distribution over the directions of the motions we can see where the contents of this structure is going to. We illustrate this with two coherent structure types in atmospheric flow with different dynamics: large scale high- and low pressure systems rotate around a vertical axis and not around a horizontal axis. The exchange process associated with this preference is to redistribute and mix the weather over the Earth's atmosphere instead of transporting it vertically from the atmosphere to the ground. On the other hand, small scale vortical atmospheric structures with a horizontal rotation axis can be induced by friction with the Earth's surface (which absorbs horizontal momentum).

The researcher whose task it is to measure all exchange processes in a turbulent flow is confronted with the following problem: there are so many of them! In most atmospheric flows the

smallest structure size is about a millimetre. In an atmosphere with a height of several kilometres the number of such quasi-independently moving blobs of air is beyond imagination. To make life easier many scientists use a sensor, which can locally probe passing air parcels. Such a sensor is placed at a position of interest and connected with a data-recording device. When the data-recording starts to work, a time of waiting begins for the researcher. The position of the sensor is assumed to be representative for the whole area of interest and from the one-point signal (a one-dimensional series of samples) one hopes to be able to reconstruct the character of the original three-dimensional flow. To collect a sufficient amount of statistical information many magnetic tapes or other storage units are filled with bytes.

Much information of the three-dimensional coherence of turbulence is lost in one-point measurements since only a thin filament of the structures is probed. Consider a dustdevil which on its path finds an anemometer. The encounter of a whirlwind is a beautiful sight and will make a lasting memory (see the plot on the top in figure 3). When back in the laboratory, the awe-inspired researcher plays back the passage of the whirl as recorded by his anemometer. The resulting plot of for example the lateral velocity is not very likely to excite him (or her). On the bottom in figure 3 we have plotted the one-point signal as measured by the anemometer: Beep!

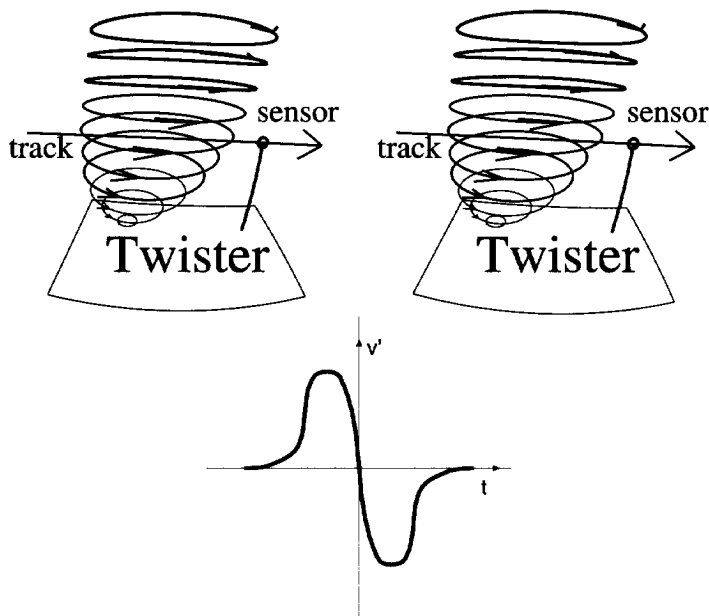


Figure 3: Example of the passage of a coherent structure; Top: the structure in three dimensions; Bottom: what a one-point measurement makes of it: "beep". For an explanation about stereoscopic viewing see the last page of this introduction.

The problem, of revealing the nature of a turbulent flow via the scrutiny of one-point measurements, is inherent to the one-point method. Turbulent structures are represented by three-dimensional plane waves, which are related to the structures via a three-dimensional Fourier

transform. With use of Taylor's hypothesis one translates the frequency-spectrum of one-point measurements to a one-dimensional spatial spectrum. The spectrum of one-point measurements is blurred by aliasing of a kind which is the three dimensional analogue of the situation in figure 4. Two ducks swim in a pond with a plane wave. Quacker B follows the the path indicated by the squares and will assign a wavelength to the plane wave twice as large as the wavelength seen by quacker A, who follows the path marked with the circles. They both swim through the same wave.

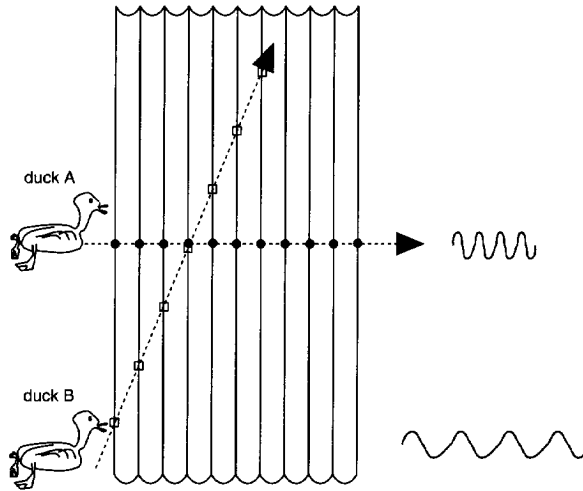


Figure 4: Two ducks in a pond. For all ducks swimming a different line than duck A the distance between two waves will seem longer than what both we and duck A would call "the wavelength" of this wave in the pond.

A lack of versatile tools to analyse one-point measurements in terms of a three-dimensional structure has restricted turbulence research for several decades to the application of the rusty mathematical machinery, which was developed under the assumption of homogeneous, isotropic, stochastically stationary, incompressible turbulence (see e.g. (Tennekes and Lumley, 1972, page 263) and (Batchelor, 1953, page 143)). In this classic theory, the amount of energy could vary with structure size, but the distribution over the three directions of the fluctuations was prescribed to be equal. This rigid constraint of the character of the flow has as a consequence that this classic theory is capable of handling the spectrum of only one independent quantity: the kinetic energy. Measurement of the longitudinal velocity spectrum suffices to estimate the kinetic energy spectrum. The lateral velocity spectra are merely used as redundant information to check if they would give the same estimate for the kinetic energy. The remaining six components of the velocity correlation spectrum are simply assumed to be zero.

Since long one has been able to measure more than one velocity component, and with the simultaneous measurement of all three velocity components one can construct a correlation spectrum with nine (!) different components. Such a measurement is still made at one point in the flow and from its results one still obtains one-point spectra. Sreenivasan and Narasimha (1978) have made an attempt to extend the relation for isotropic turbulence to axisymmetric turbulence with the axis of symmetry in the direction of the mean flow. Strong assumptions

in their analysis lead to uncertainty about his solutions. Their choice for axisymmetry around a fixed axis restricts the extension of the isotropic unaliasing relations to the inclusion of just one more parameter from a collection of in total eight non-interpreted parameters. Lindborg (1995) has started to analyse triple-correlations, while he does not yet have a model for the interpretation of measured double-correlations.

The goal of the present study is to devise a model for the interpretation of one-point turbulent velocity measurements in terms of three-dimensional structures for anisotropic flow conditions. This theory exploits as much independent information from one-point turbulent velocity measurements as possible. The difference in interpretation of fluctuations between such a new theory and the classic interpretation is illustrated in figure 5. With our anisotropic model one will finally be able to verify theories about the anisotropic parts of the spectrum with help of one-point measurements.

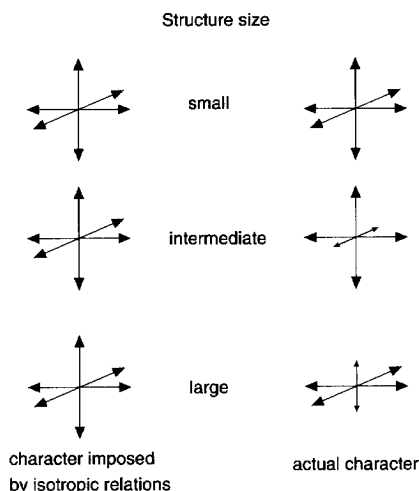


Figure 5: With the classic unaliasing theory (on the left) the distribution of fluctuations over the three dimensions is supposed to be isotropic for all lengthscales. In reality (on the right) the flow may well be anisotropic, and the anisotropy character may differ from lengthscale to lengthscale. This is not a stereographic picture.

## Outline

In chapter 1 we briefly review some general turbulence characteristics. Grid generated turbulence is introduced as our reference flow and the qualities of this type of flow are discussed. The relation between a straining mean flow and its impact on turbulence is reviewed and subsequently elaborated for a flow around a flat plate. Stagnant plateflow is chosen because it is the simplest type of flow to create in practice and from this type of flow we expect the mean strain to break the expected initial axisymmetry of the approaching (grid) turbulence. Turbulence with controlled symmetry breaking will give a good opportunity to demonstrate the power



of the fully anisotropic unaliasing relations that will be developed in chapter 2. Furthermore, a diagram is developed for the characterisation of anisotropy.

In chapter 2 we introduce a group of spectra, which are often used to represent turbulence statistics. The problem of aliasing in one-point spectra is exposed. In this part of the thesis we develop our principal theory, relating the aliased one-point spectral tensor to the wavenumber spectral tensor. The model will then be solved to generate a set of equations in closed form, which can be used to unalias spectra from one-point measurements.

The unaliasing relations that are developed in chapter 2 depend on the third derivative of the one-point spectrum. To calculate these we require an analytical model of the spectrum. In chapter 3 three methods to estimate spectra are reviewed: Fast Fourier Transform (FFT), Autoregressive models (AR) and Moving Average models (MA). Two of these models, FFT and AR, are extended to the estimation of spectral derivatives to create a method to practically implement our unaliasing relations.

With help of the results of a Direct Numerical Simulation (chapter 4) we will make an effort to assess our unaliasing relations. We will simulate our reference flow, i.e. grid generated turbulence and compare two estimates for the wavenumber spectrum: an indirect estimate obtained via our unaliasing model (using the tools from chapter 3) applied to a simulated one-point measurement and a direct estimate found via the Fourier transform of three dimensional flow fields.

To find out if our unaliasing relations are a meaningful tool in practice, we will perform hot-wire measurements on grid generated turbulence in a windtunnel. The setup and the calibration of peripheral apparatus is discussed in chapter 5.

The principles of hot-wire anemometry and an investigation into the best calibration method for a four-wire probe are presented in chapter 6. In this chapter we will also make sure that our calibration method correctly estimates the anisotropy character of the flow.

In chapter 7 we will give the results of our hot-wire measurements on the stagnation line in flow in front of a flat plate placed normal to the mean flow in grid generated turbulence. The correspondence with our measurements of large- and small scale asymptotic theories for the distortion of turbulence will be discussed. Our unaliasing theory will be applied to these measurements and differences in performance between the two estimation methods will be studied. We will also show to which extent our theory estimates a different anisotropy for the flow than the classic one-point spectrum.

At the end of this thesis we will review the general conclusions of this study and give recommendations for further research.

In this thesis some of the figures dealing with three dimensions have been drawn for stereoscopic viewing (for example figure 3). To achieve the three-dimensional effect one has to focus at infinity, allowing the left eye to look at the left picture and the right eye to simultaneously look at the right picture. One should try to overlay both pictures. As a result of this one will see three pictures, of which the middle one will show the stereoscopic effect. The ones who do not manage to accomplish this may regard the stereoscopic pictures in this text as double-printed ordinary perspective drawings.



# Chapter 1

## Turbulence basics

### Introduction

In the general introduction to this thesis we have explained that it is our aim to develop a method to interpret one-point measurements in a turbulent flow field. Before we can start to construct such a method, we first have to have a basic notion of what turbulence is. This chapter is intended to provide the necessary background information for our theory and for the numerical and experimental tests by briefly reviewing some standard material on turbulent flow.

In the first section of this chapter we will introduce definitions of turbulence characteristics.

In this thesis we will discuss spatial correlations of fluctuations and how we can extract information about spatial correlations from one-point measurements. We will use Taylor's hypothesis to translate time series from one-point measurements into spatial series. This hypothesis, which we can use to test our theory, is discussed in section 1.2.

In section 1.3 we will introduce grid-generated turbulence as the basic turbulent flow to test our theory both in the direct numerical simulation (chapter 4) and in our windtunnel experiments (chapter 7). The characteristics of grid generated turbulence, as found in earlier studies, will be outlined.

The equations of motion will be presented in section 1.4. In the rest of this study we will be considering only the turbulent component of flows. We will show under which conditions turbulence signals can be decomposed into their mean and fluctuating contributions and what the consequences are for the equations of motion. Rapid Distortion theory will be introduced to simplify these equations.

In our windtunnel experiments we will create a turbulent flow with an essentially anisotropic character by positioning a long plate normal to the flow. The reaction of a turbulent flow to this type of distortion has been studied by Batchelor and Proudman (1954), Hunt (1973) and Bearman (1972) using Rapid Distortion theory. General expressions resulting from their analysis for evolution tensors of fluctuating vorticity and velocity fields are outlined in section 1.5. The specific solutions of the velocity evolution tensors for stagnant plate flow are given in section 1.6 for the limiting cases when the impinging eddies are either much larger than the diameter of the plate, or when they are much smaller. These expressions will be used to compare with the stagnation line experiments in chapter 7.

## 1.1 General turbulence characteristics

In this section we will outline some basic turbulence characteristics, which will be used frequently throughout this study. For detailed derivations and broad accounts of turbulence one is referred to textbooks by e.g. Batchelor (1953), Hinze (1975), Tennekes and Lumley (1972) or Nieuwstadt (1992).

An important parameter is the Reynolds number  $Re$ :

$$Re \equiv \frac{UL}{\nu} \quad (1.1)$$

where  $U$  is a characteristic velocity and  $L$  is a characteristic length scale. The Reynolds number can be interpreted as the ratio of inertial and viscous forces. It is also related to the possible richness of structure of a flow, defined as the ratio of the largest and the smallest lengthscales that can occur in the flow:

$$\frac{L}{\eta} \sim Re^{3/4} \quad (1.2)$$

In this relation lengthscale  $L$  is called the macroscale or correlation length of the flow. The macroscale, which gives the largest lengthscale in a flow, is mostly determined by a characteristic size of the boundary. Kolmogorov's lengthscale  $\eta$  is the smallest lengthscale that can be found in a turbulent flow. It is defined by:

$$\eta = \left( \frac{\nu^3}{\epsilon} \right)^{1/4}, \quad (1.3)$$

where  $\epsilon$  is the energy dissipation rate per unit mass. Dissipative forces based on viscosity inhibit the formation of structures with lengthscale smaller than Kolmogorov's lengthscale. The dissipation in relation 1.3 can be estimated in practice with an empirical relation:

$$\epsilon = \frac{u^3}{L} \quad (1.4)$$

A third lengthscale, which is often used, is Taylor's microscale  $\lambda$ . It is defined as the point on the horizontal axis in the autocorrelation function of the longitudinal velocity fluctuations, where the osculation parabola at the origin of the function hits the horizontal axis (see figure 1.1). In formula:

$$\left. \frac{\partial^2 \rho(x)}{\partial x^2} \right|_{x=0} \equiv \frac{-2}{\lambda^2} \quad (1.5)$$

$$\rho(dx) \equiv \frac{u'(x_1, x_2, x_3) u'(x_1 + dx, x_2, x_3)}{(u')^2} \quad (1.6)$$

Taylor's microscale is larger than Kolmogorov's dissipation length  $\eta$  and smaller than macroscale  $L$ . Another (compatible) definition of lengthscale  $\lambda$  is:

$$\lambda = \frac{RMS(u)}{RMS \left( \frac{\partial u}{\partial x} \right)} \quad (1.7)$$

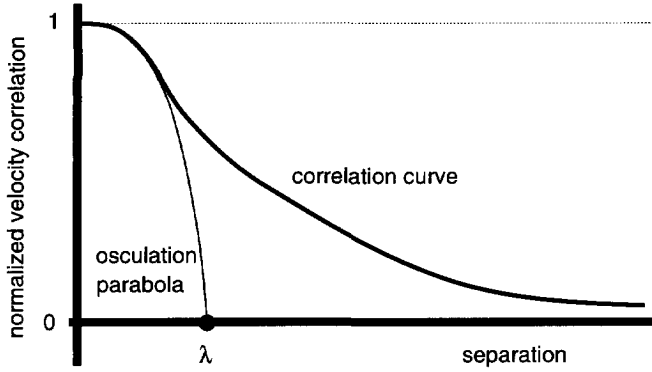


Figure 1.1: Definition of Taylor's microscale  $\lambda$ . The parabola is a fit to the origin of the spatial correlation function of the velocity component along the separation vector.

where  $u$  is the fluctuating velocity component defined as the deviation from the mean. From this formulation we see that  $\lambda$  is the separation over which velocity differences are of the same order as the deviations of the local velocity from the mean value. Hinze (1975, page 42) interprets Taylor's microscale as "a measure of the average dimension of the smallest eddies" and as "a measure of the average dimension of the eddies that are mainly responsible for dissipation". Turbulence is often described by a cascade process, in which kinetic energy is passed on from large eddies to the smaller eddies in a continuous process until the energy is dissipated into heat by viscous effects when it has arrived at a certain small scale. Following Hinze's interpretation we know that this lengthscale is Taylor's microscale. When the kinetic energy is dissipated at Taylor's microscale, this lengthscale forms a distinction between which turbulent eddies represent significant kinetic energy, and which eddies don't. This relative small energy content of structures smaller than  $\lambda$  (and their forthcoming impotence to contribute significantly to dynamical processes) entitles experimenters to restrict their measurements to a spatial resolution of the order of Taylor's microscale. In our windtunnel experiments we will have  $\eta \sim 0.3\text{mm}$  and  $\lambda \sim 1\text{mm}$ , while the sensing zone of our probe is 1 mm wide.

If via relation 1.2 one regards the Reynolds number as the extent to which viscous forces in a flow can be neglected, then a large Reynolds number would suggest that the associated flow would not show any viscosity-related characteristics. The non-linear nature of the equations of motion (which will be presented in the following section) inhibit such simplification. The Reynolds number does not express *if* viscosity plays a role, but according to relation 1.2 *at which lengthscale* it manifests itself. Viscous effects at the small scales can lead to separation of a flow from solid boundaries. Thus relatively small viscous forces can play a dominating role in the formation of large scale structures. Without viscous effects a laminar flow would for example not be able to become turbulent.

In this section we have introduced many characteristic lengthscales of a turbulent flow. A turbulent flow comprises structures of many different lengthscales between the Kolmogorov scale and the macroscale. We present two empirical relations for the participation to well developed turbulence by relatively large and relatively small scale structures. Later in this study we will introduce a mathematical model to decompose turbulence into structures of different lengths-

cales  $l$ : the Fourier transform. A Fourier transform sorts structures by wavenumber  $k \equiv 2\pi/l$  (see sections 2.4 and 2.7 for the definition of spectra). The kinetic energy spectrum  $E(k)$  of well-developed three dimensional turbulence with a large Reynolds number is characterised by two regimes:

$$E(k) \sim k^4 \quad \text{for very large scales: } k \downarrow 0 \quad (1.8)$$

$$E(k) \sim k^{-5/3} \quad \text{in the inertial subrange} \quad (1.9)$$

The former of these relations is a theoretical result of Batchelor and Proudman (1956). Hinze (1975, page 227) remarks that this theory is probably applicable to grid generated turbulence, which is the kind of turbulence that will be used in the experiments in this study. Further discussion about this  $k^4$ -dependence of the energy spectrum can be found in (Tennekes and Lumley, 1972, page 254). For the definition of the inertial subrange one is referred to textbooks on turbulence, e.g. Tennekes and Lumley (1972, page 264). The following interpolation formula for the two regimes in the spectrum was proposed by Kármán (1948):

$$E(k, t) = c_1 \frac{k^4}{\left(1 + c_2 k^2\right)^{17/6}} \quad (1.10)$$

where constants  $c_1$  and  $c_2$  depend on time.

This relation gives an indication of how the kinetic energy in a turbulent flow may be distributed over the various lengthscales. At least as important as this energy spectrum, and the essential point in this study, is the partitioning of this kinetic energy over the three dimensions: the (an)isotropy of the flow. To allow for coordinate free characterisation of a flow's anisotropy we introduce three invariants in appendix C. The construction of Lumley's anisotropy triangle is demonstrated and a proposition is made to rescale this diagram such that linear deviations from isotropy correspond with linear departures from the isotropy point in the rescaled diagram.

## 1.2 One-point measurements and Taylor's hypothesis

Many experimental techniques are based on single point probing: the sensor gives the value of a quantity for the air locally passing through its sensing volume. An example is a thermometer. Examples of non-local techniques are photography and radar. To gain knowledge about the spatial structure of turbulence using single point probing methods, one should place a great many probes and record the quantity of interest at the positions of all probes *simultaneously*. This approach is not very practical. Experimenters are confronted with limitations in availability of probes and processing units. Moreover to insert all these probes in the flow would certainly lead to distortion and consequently give a distorted impression of the character of the flow. To circumvent part of this problem one probes whole filaments in the flow with a single probe by shooting the probe through the flow in an interval of time  $\Delta t$  which is short when compared with the life-times  $\delta t$  of the turbulent structures:

$$\Delta t \ll \delta t \quad (1.11)$$

This relation requires the turbulent velocity  $u'$  to be small compared with mean velocity  $U_{\text{mean}}$ :

$$\frac{u'}{U} \ll 1 \quad (1.12)$$

With this assumption distances  $l$  are derived from time-delays  $t$  via:

$$l = t U_{\text{mean}} \\ u'(x_1, x_2, x_3) = u'(-t U_{\text{mean}}, x_2, x_3) \quad (1.13)$$

where velocity  $U$  of the probes is along the  $x_1$ -direction. Assumption 1.13 is called "Taylor's hypothesis", or the "frozen turbulence concept". Generally one applies relation 1.13 to measurements obtained with fixed probes in a flow passing with relatively high mean velocity. In such cases the mean flow is required to be homogeneous in the mean flow direction.

The inevitability to invoke Taylor's hypothesis in the interpretation of one-point measurements restricts the applicability of one-point methods to situations in which the requirements for Taylor's hypothesis are met. Favre et al. (1953) have studied the use of Taylor's hypothesis for grid-generated turbulence at  $x/M = 40$  ( $M$  is the mesh size of the grid). They found a good correspondence between directly measured spatial correlations and estimates found via Taylor's hypothesis up to a separation of  $18M$ .

## 1.3 Characteristics of grid generated turbulence

To test the theories, which will be developed in the next chapter, we require a reference flow which is well described in literature and which can be easily generated in both numerical simulations and in experiments. The flow will have to be weakly turbulent (both for the application of Taylor's hypothesis and for comparability with certain flow distortion theories which will be presented later in this chapter). Preferably the flow will have to be approximately homogeneous and isotropic. A flow with these characteristics is grid-generated turbulence. Many researchers have studied this type of flow, see e.g. (Batchelor, 1953) and (Comte-Bellot and Corrsin, 1966). In this section we will outline the characteristics of grid-generated turbulence found in literature.

Grid-turbulence is made by leading laminar flow through a grid (see section 5.5 for a description of the grid in our experimental setup) to generate a set of jets. These jets will interact with the air at rest behind the bars, become instable and make the transition to turbulence. At some distance behind the grid the mixing of the turbulent jets will result in homogeneous turbulence with a weak axisymmetric preference for the mean flow direction.

### 1.3.1 Decay of kinetic energy

Turbulent kinetic energy is produced as a result of the interaction with the grid. In the absence of other production mechanisms the kinetic energy will decay with the distance from the

grid. Batchelor (1953) found that the fluctuation level  $u/U$  of the longitudinal velocity in grid generated turbulence decays according to the following empirical law:

$$\frac{u^2}{U^2} = a \frac{M}{x - x_0} \quad (1.14)$$

where  $a$  is a proportionality constant, and where  $x_0$  is a constant, usually called a virtual origin.

### 1.3.2 Homogeneity and isotropy

Batchelor (1953, page 133) has found that gridflow becomes homogeneous and isotropic at  $x = 10M$ . In a later study Comte-Bellot and Corrsin (1966, page 657) have found that homogeneity and isotropy are not reached until  $x = 40M$ . Comte-Bellot and Corrsin have not given an explanation why their estimate is so substantially larger than that of Batchelor.

### 1.3.3 Development of characteristic lengthscales

Corrsin (1963) found that after passing through the grid correlation length  $L$  grows with distance according to:

$$L \sim (x - x_1)^{\frac{2}{3}} \quad (1.15)$$

where  $x_1$  is a virtual origin, which is typically found to be  $x_1 = 3M$ . From relation 1.15 we can calculate that, for large distances from the grid ( $x \gg 3M$ ), doubling the distance from the grid gives a 20 percent growth in correlation length.

Batchelor (1953, page 136) gives an empirical law for the development of Kolmogorov's and Taylor's lengthscales in grid generated turbulence:

$$\eta = 3.1M \left( \frac{x}{M} \right)^{0.5} \left( \frac{UM}{\nu} \right)^{-0.75} \quad (1.16)$$

$$\lambda^2 = \frac{10\nu}{U}(x - x_1) \quad (1.17)$$

where  $x_1 \sim 10M$  and viscosity  $\nu$  of air is  $15 \times 10^{-6} \text{m}^2 \text{s}^{-1}$ . Like Kolmogorov's lengthscale, Taylor's microscale gains 40 percent when the distance to the grid is doubled.

From relations 1.15, 1.16 and 1.17 we see that all characteristic lengthscales grow with the distance from the grid. At first sight this behaviour seems to contradict the idea that all eddies break up into increasingly smaller eddies. There is however no contradiction: the small scales are dissipated faster than the large scales, which leads to a *relative* growth of the larger scales. The *absolute* energy per lengthscale however decreases. The different dynamics of large and small scales is reflected in a smaller decay exponent for the large scales than for the small scales. A consequence of the faster growth of the micro lengthscale than the macroscale is that their ratio decreases (as expected) with distance from the grid: with time the flow will contain less different lengthscales.



## 1.4 Dynamical equations and rapid distortion

In this section we will give the equations of motion of a Newtonian fluid. In subsequent sections we will use these equations to find relations for the reaction of the flow in our windtunnel experiments in chapter 7.

The dynamics in a fluid (with density  $\rho$ , local velocity  $\mathbf{U}(\mathbf{x}, t)$ , pressure  $p$  and kinematic viscosity  $\nu$ ) is governed by the Navier-Stokes equations:

$$\frac{D\mathbf{U}}{Dt} \equiv \frac{\partial \mathbf{U}}{\partial t} + \mathbf{U} \cdot \nabla \mathbf{U} = -\frac{1}{\rho} \nabla p + \nu \nabla^2 \mathbf{U} \quad (1.18)$$

and for our case also by the condition of incompressibility:

$$\nabla \cdot \mathbf{U} = 0. \quad (1.19)$$

In irrotational flow one can show that pressure and (absolute) velocity are related via Bernoulli's law:

$$p + \frac{1}{2} \rho u^2 = \text{constant} \quad (1.20)$$

With this relation we will be able to estimate the mean velocity of our windtunnel with a pressure transducer.

In both observations and in simulations one has discovered that an important contribution to the dynamics of turbulent flows is associated with coherent motions with an eddying nature. To combine this observation with a mathematical concept, we introduce vorticity  $\boldsymbol{\Omega}$  as the curl of the velocity field:

$$\boldsymbol{\Omega}(\mathbf{x}, t) \equiv \nabla \times \mathbf{U}(\mathbf{x}, t) \quad (1.21)$$

An equation for the development of vorticity is found when one takes the curl of Navier-Stokes equation 1.18:

$$\frac{D\boldsymbol{\Omega}}{Dt} \equiv \frac{\partial \boldsymbol{\Omega}}{\partial t} + \mathbf{U} \cdot \nabla \boldsymbol{\Omega} = \left( \nabla \mathbf{U} \right)^T \cdot \boldsymbol{\Omega} + \nu \nabla^2 \boldsymbol{\Omega} \quad (1.22)$$

The velocity gradient can be decomposed into its symmetric and antisymmetric parts  $\bar{\bar{S}}$  and  $\bar{\bar{A}}$  as follows:

$$\nabla \mathbf{U} = \bar{\bar{S}} + \bar{\bar{A}} \quad (1.23)$$

$$\bar{\bar{S}} \equiv \frac{1}{2} \left( \nabla \mathbf{U} + \left( \nabla \mathbf{U} \right)^T \right) \quad (1.24)$$

$$\bar{\bar{A}} \equiv \frac{1}{2} \left( \nabla \mathbf{U} - \left( \nabla \mathbf{U} \right)^T \right) \quad (1.25)$$

Tensor  $\bar{\bar{S}}$  is called the strain and its action is to stretch along its three perpendicular axes. Tensor  $\bar{\bar{A}}$  represents a flow's tendency to rotate things.

To distinguish between mean flow quantities and turbulence induced fluctuations about these mean values we make the following decomposition (mean values are indicated with an overline);

fluctuations with a prime):

$$\mathbf{U}(\mathbf{x}, t) = \overline{\mathbf{U}}(\mathbf{x}) + \mathbf{u}'(\mathbf{x}, t) \quad (1.26)$$

$$\mathbf{\Omega}(\mathbf{x}, t) = \overline{\mathbf{\Omega}}(\mathbf{x}) + \mathbf{\omega}'(\mathbf{x}, t)$$

$$\bar{\bar{\mathbf{S}}}(\mathbf{x}, t) = \bar{\bar{\mathbf{S}}}(\mathbf{x}) + \bar{\bar{\mathbf{S}}}(\mathbf{x}, t) \quad (1.27)$$

$$\bar{\bar{\mathbf{A}}}(\mathbf{x}, t) = \bar{\bar{\mathbf{A}}}(\mathbf{x}) + \bar{\bar{\mathbf{A}}}(\mathbf{x}, t) \quad (1.28)$$

$$p(\mathbf{x}, t) = \bar{p}(\mathbf{x}) + p'(\mathbf{x}, t) \quad (1.29)$$

This splitting is called the "Reynolds' decomposition". This decomposition is mostly used when the mean flow is relatively stationary. Both in our DNS (chapter 4) and in our windtunnel experiments we can fix the mean velocity and therefore meet this requirement.

The equations for fluctuating velocity and vorticity can be written as:

$$\begin{aligned} \underbrace{\frac{\partial \mathbf{u}'}{\partial t}}_I + \underbrace{\mathbf{U} \cdot \nabla \mathbf{u}'}_{II} + \underbrace{\mathbf{u}' \cdot \nabla \mathbf{U}}_{III} + \underbrace{\mathbf{u}' \cdot \nabla \mathbf{u}' - \overline{\mathbf{u}' \cdot \nabla \mathbf{u}'}}_{IV} &= \underbrace{-\frac{1}{\rho} \nabla p'}_V + \underbrace{\nu \nabla^2 \mathbf{u}'}_{VI} \quad (1.30) \\ \underbrace{\frac{\partial \mathbf{\omega}'}{\partial t}}_{VII} + \underbrace{\mathbf{U} \cdot \nabla \mathbf{\omega}'}_{VIII} + \underbrace{\mathbf{u}' \cdot \nabla \mathbf{\Omega}}_{IX} + \underbrace{\mathbf{u}' \cdot \nabla \mathbf{\omega}' - \overline{\mathbf{u}' \cdot \nabla \mathbf{\omega}'}}_{X} &= \underbrace{\bar{\bar{\mathbf{G}}} \cdot \mathbf{\omega}'}_{XI} + \underbrace{\bar{\bar{\mathbf{g}}} \cdot \mathbf{\Omega}}_{XII} + \underbrace{\bar{\bar{\mathbf{g}}} \cdot \mathbf{\omega}' - \overline{\bar{\bar{\mathbf{g}}} \cdot \mathbf{\omega}'}}_{XIII} + \underbrace{\nu \nabla^2 \mathbf{\omega}'}_{XIV} \quad (1.31) \end{aligned}$$

where symbols  $\bar{\bar{\mathbf{G}}} = \bar{\bar{\mathbf{G}}} + \bar{\bar{\mathbf{g}}} \equiv \nabla \mathbf{U}$  are used for the velocity gradient tensor.

The terms in relations 1.30 and 1.31 represent:

- *I and VII*: Local time change.
- *II and VIII*: Advection by the mean flow of inhomogeneities in the fluctuations of velocity and vorticity.
- *III and IX*: Advection by the fluctuating velocity of inhomogeneities in mean velocity and vorticity.
- *IV and X*: Nonlinear interactions between fluctuations.
- *V*: Fluctuating pressure forces.
- *VI and XIV*: Viscous dissipation and diffusion.
- *XI*: Straining and rotation of fluctuating vorticity by mean flow inhomogeneity.
- *XII*: Straining and rotation of mean vorticity by fluctuating inhomogeneity.
- *XIII*: Nonlinear straining and rotational interactions between fluctuations.

We will now reduce the number of relevant terms in relations 1.30 by making assumptions about the flow.

In our study we will create situations in which a weakly turbulent flow field (with characteristic velocity  $u'$  and characteristic eddy-size  $l$ ) is distorted 'rapidly' during the passage (with mean velocity  $U_\infty$ ) of an obstacle (with characteristic size  $a$ ). 'Rapidly' here means that the turbulent eddy turnover time  $\tau$  is slow compared to mean flow distortion time  $T$ :

$$T \ll \tau \quad \Rightarrow \quad \frac{u'}{U_\infty} \ll \frac{l}{a} \quad (1.32)$$

With the assumption of rapid distortion we will be able to simplify the equation of motion so that we can calculate analytically certain aspects of its solution. We adopt Hunt's conditions (Hunt, 1973, last line on page 630) for rapid distortion of turbulence with characteristic scales  $l$  much smaller than lengthscale  $a$  associated with the cause of the distortion (see Hunt's article for a derivation of these conditions). These are:

$$\begin{aligned} \frac{a}{l} &\gg 1 \\ \text{Re}^{-1} = \frac{\nu}{U_\infty a} &\ll \frac{\text{RMS}(u'_\infty)}{U_\infty} \ll \frac{l}{a} \\ \text{Re}^{0.5} &\gg \frac{a}{l} \end{aligned} \quad (1.33)$$

where symbol  $\infty$  refers to undistorted quantities. In a recent study Kevlahan and Hunt (1997) (page 360) found that the above condition for validity of RDT underestimates the time period during which one can use RDT. Their relation 6.2b would therefore confirm that we correctly restricted our analysis to RDT in the cases where we have checked the validity of relation 1.33.

Any path along the mean flow can be parametrised using time  $t$  as coordinate. There is a free choice of labelling one point on any mean flow trajectory to have  $t = 0$ . With the above assumptions we can reduce the relations for fluctuating velocity and vorticity in an irrotational mean flow ( $\bar{\Omega} = 0$  and consequently  $\bar{A} = 0$ ) to:

$$\frac{\overline{D}\mathbf{u}'}{Dt} = -\bar{S} \cdot \mathbf{u}' - \frac{1}{\rho} \nabla p' \quad (1.34)$$

$$\frac{\overline{D}\boldsymbol{\omega}'}{Dt} = \bar{S} \cdot \boldsymbol{\omega}' \quad (1.35)$$

In these relations symbol  $\frac{\overline{D}}{Dt}$  is used for material derivatives along mean velocity field  $\bar{\mathbf{U}}$ .

The latter is called the linearised inviscid vorticity equation. The dynamic equation for vorticity has simpler form than the dynamic equation for velocity, because it does not have a pressure dependence. Therefore, when one is solving turbulence problems, one often puts much emphasis on vortex dynamics and takes recourse to this equation (e.g. Lighthill (1956)). Under RDT-conditions the mean flow is not influenced by the fluctuating flow.

A popular method to find a solution for the velocity field is to split the velocity field into two contributions  $\mathbf{u}_d$  and  $\mathbf{u}_b$ . For detailed discussions of this decomposition of the velocity field into a distortion solution and a blocking solution one is referred to the articles by Serrin (1959),

Goldstein (1978) and Hunt and Hussain (1991). In this section we will restrict the presentation to outlining the characteristics of the method. The first component  $\mathbf{u}_d$  is called the 'distortion solution' and is determined by the effect of vortex stretching along mean flow trajectories. The second component  $\mathbf{u}_b$  is called the 'blocking solution', and it makes the distortion solution satisfy the boundary conditions:

$$\begin{aligned}\mathbf{u}' &= \mathbf{u}_d + \mathbf{u}_b \\ \nabla \times \mathbf{u}_d &= \boldsymbol{\omega}' \\ \mathbf{u}_b \cdot \mathbf{n} &= -\mathbf{u}_d \cdot \mathbf{n} \quad \text{on the boundary}\end{aligned}\tag{1.36}$$

The vorticity of the distortion solution equals the vorticity of the total distorted flow solution. This implies that the blocking solution is irrotational, and can be written as the gradient of a scalar potential  $\phi$ :

$$\mathbf{u}_b = \nabla \phi \quad \text{with} \quad \frac{\partial \phi}{\partial n} = -\mathbf{u}_d \cdot \mathbf{n} \quad \text{on the boundary}\tag{1.37}$$

$$\nabla \cdot \mathbf{u}_b = -\nabla \cdot \mathbf{u}_d\tag{1.38}$$

More than a century ago Weber (1868) has shown that the following evolution equation leads to a distortion velocity, which satisfies relation 1.36:

$$\frac{D\mathbf{u}_d}{Dt} = -(\nabla \bar{\mathbf{U}}) \cdot \mathbf{u}_d\tag{1.39}$$

$$\frac{D\boldsymbol{\omega}'}{Dt} = (\nabla \bar{\mathbf{U}}) \cdot \boldsymbol{\omega}'\tag{1.40}$$

The vorticity evolution equation is copied to show its symmetry with the equation for the distortion solution. Although pressure is left out of the equation for  $\mathbf{u}_d$ , its vorticity correctly represents vorticity of the total velocity field. Early references to Weber's work are made by Lamb (1879) and Milne-Thomson (1938). The transformation in relation 1.36 has become popular just in the last decade.

From relations 1.39 and 1.40 we see that the influences of the mean velocity gradient on respectively the fluctuating velocity and the fluctuating vorticity of the distortion solution are of opposing sort: a positive velocity gradient gives a local decrease of the velocity field and an increase of the vorticity field. We now follow fluctuating velocity  $\mathbf{u}_d$  and vorticity  $\boldsymbol{\omega}'$  along trajectories of mean flow  $\mathbf{U}(\mathbf{x})$  and express quantities at time  $t$  in their initial values  $\mathbf{u}_d(0)$  and  $\boldsymbol{\omega}'(0)$  and an evolution tensor  $\bar{\bar{\mathbf{A}}}(t)$ . The opposing effect of mean flow gradients on the distortion solution for the velocity and vorticity implies that the respective evolution tensors for  $\mathbf{u}_d$  and  $\boldsymbol{\omega}'$  are each others inverses (this can be shown by differentiation of the relation  $\bar{\bar{\mathbf{A}}} \cdot \bar{\bar{\mathbf{A}}}^{-1} = \bar{\delta}$ ):

$$\mathbf{u}_d(t) = \bar{\bar{\mathbf{A}}}^{-1}(t) \cdot \mathbf{u}_d(0)\tag{1.41}$$

$$\boldsymbol{\omega}'(t) = \bar{\bar{\mathbf{A}}}(t) \cdot \boldsymbol{\omega}'(0),\tag{1.42}$$

where  $\bar{\bar{\mathbf{A}}}(t)$  is a second order tensor, which is yet to be constructed. Substitution of relation 1.42 into inviscid vorticity equation (1.40) gives the following relation:

$$\left( \frac{D\bar{\bar{\mathbf{A}}}(t)}{Dt} \right) \cdot \boldsymbol{\omega}'(0) = (\nabla \bar{\mathbf{U}})(t) \cdot \bar{\bar{\mathbf{A}}}(t) \cdot \boldsymbol{\omega}'(0).\tag{1.43}$$

which must hold for arbitrary vorticity fields. The evolution tensor must therefore be constructed such that:

$$\frac{D\bar{\bar{A}}(t)}{Dt} = \left( \nabla \bar{U} \right) (t) \cdot \bar{\bar{A}}(t). \quad (1.44)$$

If we have an expression for the evolution tensor, then we still have not solved the equation for the total velocity field. To find the velocity field we have to either:

- use the distortion solution for the vorticity field, integrate the vorticity field over the domain using laws of Biot and Savart and solve a Laplace-type of equation to incorporate the boundary conditions for the velocity.
- or use the distortion solution for the fluctuating velocity field and solve a Poisson-type of equation for potential  $\phi$  of the blocking solution to make the total solution satisfy incompressibility.

It is a major problem in the application of Weber's transformation to find expressions for potential  $\phi$ . An effort to construct this potential was made by Atassi and Grzedzinski (1989). They show that potential  $\phi$  diverges near stagnation points.

## 1.5 The evolution tensor for commuting strain

Evolution tensor  $\bar{\bar{A}}$  is easy to find when the eigenvectors of the strain field have constant directions over the flow domain. In this case, we solve the evolution matrix in the reference frame of these eigenvectors. Every eigenvalue of the evolution matrix is just the exponential of the integral of the eigenvalues of the strain field along the corresponding trajectory. Thus, the evolution matrix for a flow with eigenvectors of the velocity gradient along constant axes is given by the following expression:

$$\bar{\bar{A}}(t) = \exp \left\{ \int_0^t \left( \nabla \bar{U} \right) (\tau) d\tau \right\} \quad (1.45)$$

where the exponential for tensors is defined to be a Taylor-expansion into a series of powers of the tensor as follows: <sup>1</sup>

$$\begin{aligned} e^{\bar{\bar{x}}} &\equiv \sum_{n=0}^{\infty} \frac{1}{n!} (\bar{\bar{x}})^n \\ &\equiv \bar{\bar{0}} + \bar{\bar{x}} + \frac{1}{2} \bar{\bar{x}} \cdot \bar{\bar{x}} + \frac{1}{6} \bar{\bar{x}} \cdot \bar{\bar{x}} \cdot \bar{\bar{x}} + \dots \end{aligned} \quad (1.46)$$

The condition on the eigenvectors of the mean velocity gradient to have constant orientation implies that, in a product of local velocity gradient tensors, these tensors may be commuted: their order does not make a difference. When the orientation of the eigenvectors of the velocity

<sup>1</sup>Note that for a diagonal matrix the exponential mapping gives just the scalar exponential of the matrix-elements. This is why in practice the exponential of a matrix is determined via its system of eigenvectors.

gradient are not constant throughout the domain, which is generally the case, then the vorticity evolution tensor is relatively difficult to calculate. The point in this commutation problem is quite subtle and it is easily overseen (e.g. Kida and Hunt (1989, equation 2.18a)). In appendix B we show that in general relation 1.45 is invalid and we derive a relation (called the Time-ordered Exponential), which extends relation 1.45 to non-commuting velocity gradients.

## 1.6 Turbulence impinging on a flat plate

The practical test of the unaliasing theory that will be developed in this study is an application to grid-generated turbulence around a flat plate with its longest dimension in vertical direction (chapter 7). The plate is used to create non-axisymmetric anisotropic turbulence, such that our theory can show its full power (see figure 1.2). In this section we will outline the results of asymptotic RDT-studies to the velocity distortion tensor by Hunt (1973) for relatively large scale structures and by Batchelor and Proudman (1954) for relatively small scale structures. The generation and distortion by a plate of grid-generated turbulence is schematically drawn in figure 1.2.

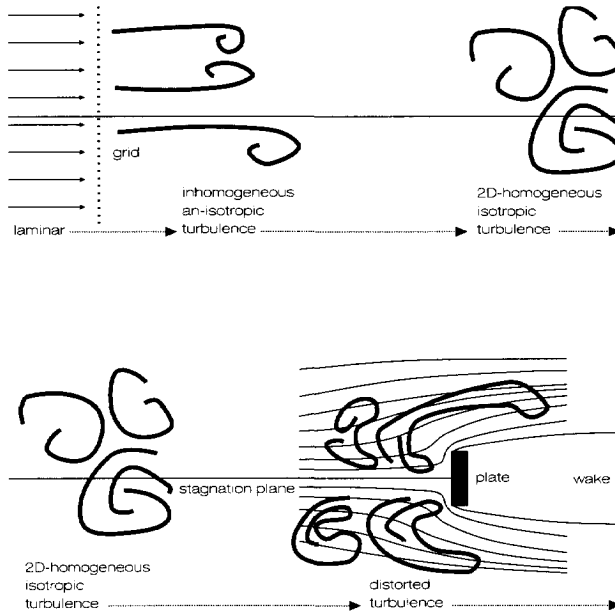


Figure 1.2: A laminar flow passes through a grid and becomes turbulent. Non-linear self-interactions of the turbulence change the character to approximately isotropic in three directions and homogeneous in the lateral directions. This homogeneous turbulence approaches a flat plate placed normal to the mean flow and interacts with the mean flow's velocity gradient and with the impenetrable boundary set by the plate.

Strictly speaking RDT-assumptions 1.33 are invalid close to the stagnation point, because the length of stay of the flow in the stagnation region is too long. Nevertheless we will use an

RDT-based method to model the distortion of turbulence by the presence of a plate. In practice the stagnation point on the plate will not have a stationary position. Coherently moving parcels of fluid will force the stagnation point to drift about the plate's surface. This mechanism will wash eddies down the plate in a time shorter than expected from mean flow calculations with a fixed stagnation point. There is also a measurement problem close to the stagnation point: the calibration of our hot-wire probe is restricted to a cone around the mean velocity vector, while near the plate the direction of the local velocity can fall outside this cone. Therefore we will not be able to give estimates for the velocity very close to the plate. These are two reasons why we do not expect to encounter problems with RDT-assumptions in our study.

In the situation given in figure 1.2 both the mean flow and the boundary conditions are invariant under:

- Reflection in any horizontal plane (in mean flow direction and normal to the length of the plate)
- Translation in vertical direction (along the length of the plate)
- Reflection in the stagnation plane (i.e. the plane connecting all stagnation lines, see figure 1.2)

From these symmetries we know that on the stagnation line the eigenvectors of the mean velocity gradient tensor are along the coordinate axes if the mean flow is homogeneous upstream of the plate. Moreover we can conclude that there is no gradient in the length direction of the plate. Incompressibility of the fluid the velocity gradient tensor to have to trace. Therefore we can estimate the velocity gradient on the stagnation line from the (measured) velocity  $U(x/M)$  on the stagnation line as function of the distance to the plate:

$$\nabla U(x/M) = \text{diag} \left\{ \frac{\partial U_x(x/M)}{\partial x}, -\frac{\partial U_x(x/M)}{\partial x}, 0 \right\} \quad (1.47)$$

With relation 1.45 the evolution tensor for vorticity associated with relation 1.47 is:

$$\bar{\bar{A}}(x/M) = \text{diag} \left\{ \exp \left( \frac{U_x(x/M)}{U_\infty} - 1 \right), \exp \left( -\frac{U_x(x/M)}{U_\infty} + 1 \right), 1 \right\} \quad (1.48)$$

$$\simeq \text{diag} \left\{ \frac{U_x(x/M)}{U_\infty}, 2 - \frac{U_x(x/M)}{U_\infty}, 1 \right\} \quad \text{in the far field} \quad (1.49)$$

In these two relations we have used Taylor's hypothesis 1.13 to make the relations  $t \rightarrow x$  and  $t = 0 \rightarrow x = -\infty$ .  $U_\infty$  is the mean velocity along the  $x_1$ -axis far upstream of the plate.

From this expression we get the following formula for the evolution tensor for distortion velocity  $u_d$ :

$$\bar{\bar{A}}^{-1}(x/M) = \text{diag} \left\{ \exp \left( \frac{U_x(x/M)}{U_\infty} - 1 \right), \exp \left( -\frac{U_x(x/M)}{U_\infty} + 1 \right), 1 \right\} \quad (1.50)$$

$$\simeq \text{diag} \left\{ 2 - \frac{U_x(x/M)}{U_\infty}, \frac{U_x(x/M)}{U_\infty}, 1 \right\} \quad \text{in the far field} \quad (1.51)$$

Bearman (1972) has made an experimental study on the stagnation line of turbulent flow around a flat plate placed normal to the mean flow (see figure 1.2). He found confirmation of the RDT theories developed by Hunt (1973) for the distortion of large structures and by Batchelor and Proudman (1954) for the smaller eddies:

- The velocity field associated with eddies with size much larger than the width of the plate follows the quasi-steady distortion of the mean flow (blockage):

$$\begin{aligned} \mathbf{u}'/\mathbf{u}'_\infty &\equiv \left( \frac{\text{RMS} \left( u'(x/M) \right)}{\text{RMS} \left( u'(\infty) \right)}, \frac{\text{RMS} \left( v'(x/M) \right)}{\text{RMS} \left( v'(\infty) \right)}, \frac{\text{RMS} \left( w'(x/M) \right)}{\text{RMS} \left( w'(\infty) \right)} \right) \\ &= \left( \frac{U(x/M)}{U(\infty)}, 2 - \frac{U(x/M)}{U(\infty)}, 1 \right) \end{aligned} \quad (1.52)$$

This relation is derived as follows: fluctuations in the mean flow scale with the mean flow, vertical fluctuations are indifferent to the plate and the lateral component is taken such that continuity is satisfied.

It is interesting to see that these relations for the fluctuating *velocity* equal far field approximation 1.49 of the corresponding elements for the *vorticity* evolution tensor, and not of the velocity evolution tensor in relation 1.51. This surprising result shows that, for large eddies, blockage overshadows vortex stretching such that the resulting total velocity distortion gives the opposite effect of straining distortion alone.

- When the scale of the eddies was much smaller than the diameter of the plate (which will be the case in our study) the distortion of the velocity field was dominated by the action of mean flow strain on vorticity:

$$\begin{aligned} \mathbf{u}'/\mathbf{u}'_\infty &= \left( \frac{3}{4(c^2-1)} \left( 1 + \frac{c(c^4-c^2-1)}{(c^4-1)^{0.5}} y \right), \right. \\ &\quad \frac{3}{4c^2} \left( 1 + \frac{c(c^4+c^2-1)}{(c^2-1)(c^4-1)^{0.5}} (x-y) \right), \\ &\quad \left. \frac{3}{4c^2(c^2-1)} \left( -1 + \frac{c(c^4-c^2+1)}{(c^4-1)^{0.5}} ((c^2+1)y-x) \right) \right) \end{aligned}$$

where

$$\begin{aligned} c &\equiv \frac{U(\infty)}{U(x/M)} \\ x &\equiv \int_0^{(1-c^{-4})^{0.5}} \left\{ 1 - c^2 t^2 / (1 + c^2) \right\}^{-0.5} (1 - t^2)^{-0.5} dt \\ y &\equiv \int_0^{(1-c^{-4})^{0.5}} \left\{ 1 - c^2 t^2 / (1 + c^2) \right\}^{0.5} (1 - t^2)^{-0.5} dt \end{aligned} \quad (1.53)$$



When the mean streamwise velocity is less than half of its undistorted value ( $c > 2$ , near field approximation), then these relations can be simplified to give:

$$\begin{aligned} u'/u'_\infty = & \left( \left[ \frac{3U(\infty)}{4U(x/M)} + \frac{3U(x/M)}{8U(\infty)} \left[ \log \left( \frac{4U(\infty)}{U(x/M)} \right) - \frac{1}{2} \right] \right]^{0.5} \right. \\ & \left. \frac{3U(x/M)}{4U(\infty)} \left[ \log \left( \frac{4U(\infty)}{U(x/M)} \right) - 1 \right] \right. \\ & \left. \left[ \frac{3U(\infty)}{4U(x/M)} - \frac{3U(x/M)}{8U(\infty)} \left[ \log \left( \frac{4U(\infty)}{U(x/M)} \right) - \frac{3}{2} \right] \right]^{0.5} \right) \end{aligned} \quad (1.54)$$

The far field approximation is:

$$u'/u'_\infty = \left( \frac{7}{4} - \frac{3U(x/M)}{4U(\infty)}, \frac{1}{4} + \frac{3U(x/M)}{4U(\infty)}, 1 \right) \quad (1.55)$$

When we compare relation 1.55 with relation 1.51 for the far field approximation of distortion velocity  $u_d$ , we see that there is qualitative agreement. Vertical fluctuations are not affected by the plate, fluctuations along the stagnation line are amplified and fluctuations in the  $y$ -direction are attenuated. There is a small difference between the two estimates for the proportionality with which the fluctuations respond to changes in the mean velocity along the stagnation line. This difference is to be attributed to the neglect of blockage velocity component  $u_b$ , which not only accounts for the blockage by the plate, but which also makes the velocity field incompressible.

- Close to the plate the behaviour of small scale structures is not only influenced by mean flow straining, but also by blockage.

The effects of mean plate flow on turbulence of intermediate size (comparable with the diameter of the plate) is a combination of blockage and distortion: attenuation of energy at low wavenumbers and amplification at high wavenumbers. The first known reference to report an amplification of small scale structures ahead of an obstacle is a study by Piercy and Richardson (1930).

In chapter 7 we will use asymptotic relations 1.52 and 1.53 for the distorted turbulent intensities along the stagnation line of a bluff body placed in homogeneous turbulence to estimate bounds between which we can expect to find our measurements. We will also calculate a distortion tensor following relation 1.50 and see if its behaviour as a function of the distance to the stagnation point shows any resemblance with the measured values.

An in-depth study to the distortion of turbulence around bluff bodies has been recently carried out by Saxena et al. (1998). They use a second-order Taylor's expansion of the velocity field in the vicinity of the stagnation point as a function of the distance to the stagnation point. This expansion is combined with the decomposition of the velocity field in a distortion solution and a blocking solution, which was presented in section 1.4). The theory shows quantitative correspondence with experiments on the distortion of turbulent structures of sizes comparable with or larger than the characteristic width of the obstacle. It is beyond the scope of the present study to implement this model.



## Chapter 2

# The aliasing problem in one-point measurements

### Introduction

In the former chapter we have presented a review of basic turbulence characteristics. In the sections about Rapid Distortion and plate flow we found that the dynamics in a flow depends on the size of the structures involved. In this chapter we will introduce spectra as the classic tool to decompose three-dimensional fields into a set of "basic structures" each with a different characteristic lengthscale. This concept will be used to analyse turbulent velocity fields. The principle of one-point measurements is introduced and a relation is constructed between one-point spectra and spectra which use the three-dimensional wavelength.

This chapter is rather mathematically oriented. To facilitate reading we will first present the definitions and notations of tensors.

A turbulent flow is characterised by coherent structures of finite size. The coherent structures lead to a correlation of the velocity field on a distance proportional to their size. As turbulence consists of a large number of these structures, a correlation analysis, or alternatively a spectral decomposition, is made of the velocity field. The velocity spectrum, polarisation and the Fourier transform, will be defined in the second section. The velocity correlation tensor and its characteristics is presented in section 2.3 and the associated spectrum in section 2.4. The correlation spectrum will be related to the velocity spectrum via what will be called the *spectral structure probability density function (ss-pdf)*.

The restriction of the analysis to incompressible flows without net swirl and the consequences for the mathematical machinery is discussed in sections 2.5 and 2.6.

In practice one often uses integrated spectra. These integrated spectra are defined in section 2.7. The most important of these spectra in the light of this thesis are the one-point spectrum and the wavenumber spectrum.

The aliasing problem of one-point measurements will be studied next. In one-point flow measurements the fluid which is probed in course of the measurement forms a thin filament through

the measuring point and is oriented roughly parallel to the mean velocity vector. Information about the flow outside this (virtual) measuring line is in principle not available. Velocity in those points has to be modelled with help of the samples obtained at the measuring point. In section 2.8 we will make a statistical model of anisotropic turbulence which relates three-dimensional velocity statistics to one-point observations. For 3D-anisotropic turbulence aliasing relations will be constructed between one-dimensional spectra and three-dimensional spectra. Results of this analysis will enable us to interpret experimental data from one-point measurements in terms of 3D spectral quantities which are used in turbulence theory.

In section 2.9 we will compare our fully anisotropic model with Sreenivasan's model for axisymmetric turbulence.

Conclusions will be given in the last section of this chapter.

## 2.1 Basic tensor notation

In this section some basic tensor notation is presented.

Our motivation to use general tensor notation is best expressed by a statement made by Lindborg (1995), who in the first appendix of his study of axisymmetric turbulence remarks:

"The advantage of the dyadic representation is that it is more geometrical in character than the Cartesian tensor representation, and that the coordinate-system independence is totally displayed."

We will exploit this general representation and refrain from presenting tensors in index notation until separate components of tensors will be needed. Tensors of second order will be marked with a double bar, e.g.  $\bar{\bar{R}}$ , and vectors with boldface notation, e.g.  $\mathbf{v}$ .

The following definitions will be used: Superscript  $t$  will denote the **transpose** (interchanged rows and columns) of a tensor or vector, e.g.  $\hat{\mathbf{u}}^t$ . The tilde will denote the **complex conjugate**, e.g.  $\tilde{x}$ . Superscript  $*$  will denote the **hermitian conjugate** defined as:

$$\mathbf{q}^* \equiv \tilde{\mathbf{q}}^t \quad (2.1)$$

The **scalar product** of two vectors  $\mathbf{p}, \mathbf{q}$  which are elements of three dimensional complex vector-space  $\mathbb{C}^3$  is defined by:

$$(\mathbf{p} \cdot \mathbf{q}) \equiv \sum_{i=1}^3 p_i q_i^* \quad (2.2)$$

We will use the symbol  $\otimes$  to denote the dyadic product, e.g.  $(\mathbf{a} \otimes \mathbf{b}^t)$  denotes the dyadic product of a column vector (a vector written as a stack of three components) and a row vector (written as a row of three components). The transpose of a dyadic product is given by:

$$(\mathbf{a} \otimes \mathbf{b}^t)^t = \mathbf{b} \otimes \mathbf{a}^t \quad (2.3)$$

Tensor  $\bar{T}$  is called self-adjoint (or hermitian) when it equals its hermitian conjugate:

$$\bar{T} = \bar{T}^* \quad (2.4)$$

It is known from functional analysis (Griffel, 1981) that self-adjoint operators have orthogonal (not necessarily real!) eigenvectors with real eigenvalues.

## 2.2 Velocity spectrum

From physics we know that phenomena often depend on the wavelengths or frequencies of the processes involved in the interactions. Interactions of waves with comparable sizes (or frequencies) tend to be non-linear. For waves with non-comparable sizes (or frequencies) the interactions can sometimes be linearised. When physicists combine the mathematical concept of Hilbert-spaces with size or frequency discriminating physics, then Fourier analysis is the most popular tool adopted for analysis. The best known ancient reference to expansions of signals into spherical harmonics is the *Almagest* (Ptolemaeus, 170). Ptolemaeus, who uses epicycles to model orbits of planets, has not invented the expansion method of signals into spherical harmonics. The *epi-cycle* model was probably independently developed by Apollonius of Perga (5 BC) and by Hipparchos of Rhodos (7 BC). Reviews of their work can be found in books on astronomy, e.g. the books by Thurston (1994) and Hoskin (1997).

The main reason for the choice of spherical harmonics to analyse signals is the Wiener-theorem which states that a homogeneous stochastic signal can be described in terms of an integral of Fourier components. Other reasons are that a Fast Fourier Transform exists and that everybody else uses sinusoidals. A problem in interpreting the velocity spectrum of a turbulent velocity field in terms of waves is that waves by definition have an infinite spatial extent. Therefore, it is not directly obvious how to interpret the finite spatial structure of turbulence in terms of waves.<sup>1</sup>

From functional analysis we know that sinusoidal functions form a complete and orthogonal set for building absolutely integrable functions on an infinite domain (see Griffel (1981)). Absolute integrability means that the integral of the absolute value of the function over the full domain exists. This implies that functions cannot be very singular, and that they will have to fall off to zero towards either infinite boundary fast enough for the function to be absolutely integrable. The simple behaviour of these sinusoidal functions (waves) under differentiation and integration facilitates the understanding of the effects on waves which involve these operations.

It must be kept in mind that spectral analysis of a flow field is static, like analysis of a snapshot of the flow. Only if one fully understands the consequences of the Navier-Stokes equation in a certain flow, then one might look for a coupling of spectra to dynamics of that flow.

The spatial Fourier-transform of instantaneous velocity field  $\mathbf{u}(\mathbf{x})$  (notations conform Batchelor

<sup>1</sup>One proposal put forward by Tennekes (1976) is based on an interpretation in terms of wavepackets. Recently, methods like wavelet analysis (see Meneveau (1991); Farge (1992)) have been developed, which use functions with a finite correlation length. Moreover, these functions couple spatial and time evolution. These methods can possibly be of help in the future.

(1953)) reads:

$$\mathbf{u}(\mathbf{x}) = \int \hat{\mathbf{u}}(\mathbf{k}) e^{i\mathbf{k} \cdot \mathbf{x}} d\mathbf{k} \quad \hat{\mathbf{u}}(\mathbf{k}) = \frac{1}{8\pi^3} \int \mathbf{u}(\mathbf{x}) e^{-i\mathbf{k} \cdot \mathbf{x}} d\mathbf{x} \quad (2.5)$$

These integrals can in principle be only defined when the function  $\mathbf{u}(\mathbf{x})$  satisfies some regularity conditions at  $|\mathbf{x}| \rightarrow \infty$ . The random function  $\mathbf{u}(\mathbf{x})$  (which will be assumed to be homogeneous later in this study) does not in general obey such conditions and as a result the integrals do not exist. One may find some way around this problem by employing the notation of Riemann-Stieltjes integrals and for details we refer to Batchelor (1953). In order to keep our notation simple we shall nevertheless assume that the integrals exist.

We should also keep in mind that Fourier coefficients  $\hat{\mathbf{u}}(\mathbf{k})$  have complex components. Velocity is a measurable quantity and consequently coefficients  $\hat{\mathbf{u}}(\mathbf{k})$  must be chosen such that velocity  $\mathbf{u}(\mathbf{x})$  is real valued. This means that we have to impose:

$$\hat{\mathbf{u}}(-\mathbf{k}) = \tilde{\hat{\mathbf{u}}}(\mathbf{k}) \quad (2.6)$$

**Definition 2.1** Vector  $\hat{\mathbf{u}}(\mathbf{k})$  will be called the **polarisation** of the wave with wavevector  $\mathbf{k}$ .

Real and imaginary parts of  $\hat{\mathbf{u}}(\mathbf{k})$  are associated with cosine- and sine-waves respectively, and consequently are a quarter of a cycle out of phase.

**Definition 2.2** A wave with wave-vector  $\mathbf{k}$  is called **linearly polarised** when the real and imaginary parts of the corresponding  $\hat{\mathbf{u}}(\mathbf{k})$  are linearly dependent vectors (i.e. one is a multiple of the other).

An example of a linearly polarised wave is shown in figure 2.1.

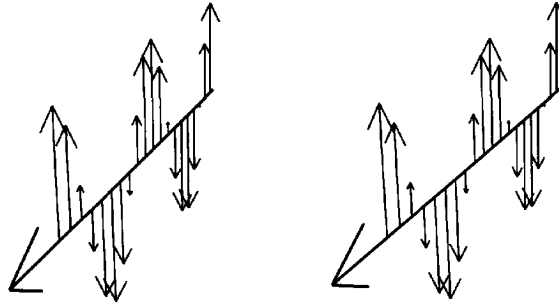


Figure 2.1: Linearly (transversely) polarised wave; The thick central arrow is the wavevector

**Theorem 2.1** Every wave with (complex) polarisation  $\mathbf{b}$  can be expressed as the sum of two linearly polarised waves, with a quarter of a period phase-difference and perpendicular polarisations:

$$\hat{\mathbf{u}} e^{i\mathbf{k} \cdot \mathbf{x}} = \left( \hat{\mathbf{u}}_a + i\hat{\mathbf{u}}_b \right) e^{i(\mathbf{k} \cdot \mathbf{x} - \phi)} \quad \text{with} \quad \hat{\mathbf{u}}_a \perp \hat{\mathbf{u}}_b \quad (2.7)$$

where  $\hat{\mathbf{u}}_a$  and  $\hat{\mathbf{u}}_b$  are real vectors, and where  $\phi$  is a phase-angle.

*Proof:* Introduce  $\hat{\mathbf{u}}_1$  and  $\hat{\mathbf{u}}_2$  as the real and imaginary components of polarisation  $\hat{\mathbf{u}}$ . One single wave with certain wave-vector can thus be split into two linear waves:

$$\hat{\mathbf{u}}e^{i\mathbf{k}\cdot\mathbf{x}} = \hat{\mathbf{u}}_1e^{i\mathbf{k}\cdot\mathbf{x}} + \hat{\mathbf{u}}_2e^{i(\mathbf{k}\cdot\mathbf{x}+\pi/2)} \quad (2.8)$$

These two linearly polarised waves can be related to two other linearly polarised waves which are obtained from the former waves by a phase-shift  $\phi$ :

$$\hat{\mathbf{u}}e^{i\mathbf{k}\cdot\mathbf{x}} = (\hat{\mathbf{u}}_1 \cos \phi + \hat{\mathbf{u}}_2 \sin \phi)e^{i(\mathbf{k}\cdot\mathbf{x}-\phi)} + i(-\hat{\mathbf{u}}_1 \sin \phi + \hat{\mathbf{u}}_2 \cos \phi)e^{i(\mathbf{k}\cdot\mathbf{x}-\phi)} \quad (2.9)$$

Define vectors  $\hat{\mathbf{u}}_a$  and  $\hat{\mathbf{u}}_b$  as:

$$\hat{\mathbf{u}}_a \equiv \hat{\mathbf{u}}_1 \cos \phi + \hat{\mathbf{u}}_2 \sin \phi \quad (2.10)$$

$$\hat{\mathbf{u}}_b \equiv -\hat{\mathbf{u}}_1 \sin \phi + \hat{\mathbf{u}}_2 \cos \phi \quad (2.11)$$

and we can write the wave as:

$$\hat{\mathbf{u}}e^{i\mathbf{k}\cdot\mathbf{x}} = (\hat{\mathbf{u}}_a + i\hat{\mathbf{u}}_b) e^{i(\mathbf{k}\cdot\mathbf{x}-\phi)} \quad (2.12)$$

The scalar product of linear polarisation vectors  $\hat{\mathbf{u}}_a$  and  $\hat{\mathbf{u}}_b$  of these two waves is:

$$\hat{\mathbf{u}}_a \cdot \hat{\mathbf{u}}_b = (\hat{\mathbf{u}}_1 \cos \phi + \hat{\mathbf{u}}_2 \sin \phi) \cdot (-\hat{\mathbf{u}}_1 \sin \phi + \hat{\mathbf{u}}_2 \cos \phi) \quad (2.13)$$

$$= \frac{1}{2} \left( (\hat{\mathbf{u}}_1 \cdot \hat{\mathbf{u}}_2) \cos 2\phi - (||\hat{\mathbf{u}}_1||^2 - ||\hat{\mathbf{u}}_2||^2) \sin 2\phi \right) \quad (2.14)$$

The scalar product gives information concerning the orthogonality of the linear polarisations. It is zero if we take  $\phi$  according to:

$$\phi = \frac{1}{2} \arctan \frac{\hat{\mathbf{u}}_1 \cdot \hat{\mathbf{u}}_2}{||\hat{\mathbf{u}}_1||^2 - ||\hat{\mathbf{u}}_2||^2} \quad (2.15)$$

With this choice for  $\phi$ , the polarisations of the two waves (which differ one quarter of a cycle in phase) are perpendicular, which proves the theorem.

**Definition 2.3** *The two linearly polarised waves in relation 2.7 are called a wave's **basic waves**.*

From the foregoing analysis of basic waves we can conclude that:

**Corollary 2.1** *A linearly polarised wave has one basic wave with zero amplitude.*

**Definition 2.4** *A wave with wave-vector  $\mathbf{k}$  is called **circularly polarised** when the two basic waves have equal amplitude. In general waves are called **elliptically polarised**.*

An example of a circularly polarised wave is shown in figure 2.2.

Now construct the vector triplet  $(\hat{\mathbf{u}}_a, \hat{\mathbf{u}}_b, \mathbf{k})$ .

**Definition 2.5** *There are two **classes of elliptic polarisations**: the polarisations where the vector triplet forms a right-handed frame (the vector product of the first two vectors points in the direction of the third) and the ones where the vector triplet forms a left-handed frame (the vector product of the first two vectors points in the direction opposite to the third). These two classes of elliptic polarisations are called **opposite elliptic polarisations**.*

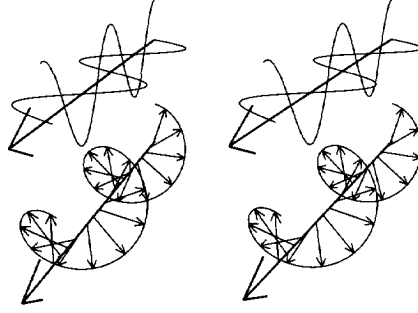


Figure 2.2: Circularly polarised wave (lefthanded); At the top the two basic waves are drawn, at the bottom the compound wave.

**Definition 2.6** Waves with equal wavevector and with polarisations  $\mathbf{b} = \hat{\mathbf{u}}_a + i\hat{\mathbf{u}}_b$  and  $\tilde{\mathbf{b}} = \hat{\mathbf{u}}_a - i\hat{\mathbf{u}}_b$  (related via complex conjugation) are called **conjugate waves**.

Without proof we present the following theorem:

**Theorem 2.2** Conjugate polarisations  $\mathbf{b}$  and  $\tilde{\mathbf{b}}$  belong to waves of opposite elliptic polarisation classes.

In figure 2.3 a pair of conjugate waves is shown.

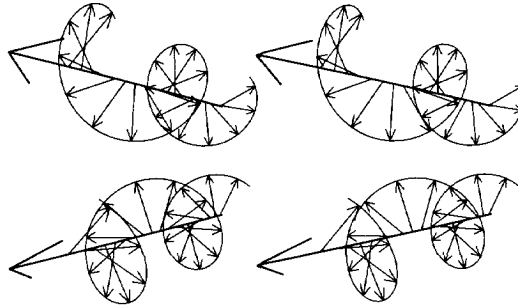


Figure 2.3: Conjugate waves

## 2.3 The second-order velocity correlation tensor

We define velocity correlation tensor  $R_{ij}$  at position  $\mathbf{x}$  as function of separation  $\mathbf{r}$  as the expectation value of the product of the velocity at position  $\mathbf{x}$  and the velocity at the point which is  $\mathbf{r}$  separated from  $\mathbf{x}$ . In index notation the correlation tensor is defined as:

$$R_{ij}(\mathbf{x}, \mathbf{r}) \equiv \mathcal{E} \left( u_i(\mathbf{x}) u_j(\mathbf{x} + \mathbf{r}) \right) \quad (2.16)$$



where  $\mathcal{E}$  denotes the expectation value of its argument. The expectation value of a quantity is obtained by proportional averaging over all possible stochastic realizations, i.e. realizations are weighted with the probability of the realization.

In dyadic notation the definition of the second-order velocity correlation tensor is written as:

$$\bar{\bar{R}}(\mathbf{x}, \mathbf{r}) \equiv \mathcal{E} \left( \mathbf{u}(\mathbf{x}) \otimes \mathbf{u}'(\mathbf{x} + \mathbf{r}) \right) \quad (2.17)$$

The second order velocity correlation tensor provides us with the spatial and directional distribution of turbulent kinetic energy. Furthermore, the correlation tensor expresses the directional transport of turbulent momentum.

## 2.4 Correlation spectrum

We want to link the spectrum of the velocity field to the spectrum of the correlation tensor. To accomplish this we substitute the velocity spectrum in the definition of the correlation function. For reasons which will become clear later, we will start to examine the transpose of the correlation tensor:

$$\bar{\bar{R}}^t(\mathbf{x}, \mathbf{r}) = \mathcal{E} \left( \int \hat{\mathbf{u}}(\mathbf{k}) e^{i\mathbf{k} \cdot (\mathbf{x} + \mathbf{r})} d\mathbf{k} \otimes \int \hat{\mathbf{u}}^t(\mathbf{k}') e^{i\mathbf{k}' \cdot \mathbf{x}} d\mathbf{k}' \right) \quad (2.18)$$

The velocity is real valued and consequently equals its complex conjugate. This allows us to write:

$$\bar{\bar{R}}^t(\mathbf{x}, \mathbf{r}) = \mathcal{E} \left( \int \hat{\mathbf{u}}(\mathbf{k}) e^{i\mathbf{k} \cdot (\mathbf{x} + \mathbf{r})} d\mathbf{k} \otimes \int \hat{\mathbf{u}}^*(\mathbf{k}') e^{-i\mathbf{k}' \cdot \mathbf{x}} d\mathbf{k}' \right) \quad (2.19)$$

$$= \mathcal{E} \left( \int \int \hat{\mathbf{u}}(\mathbf{k}) \otimes \hat{\mathbf{u}}^*(\mathbf{k}') e^{i(\mathbf{k} - \mathbf{k}') \cdot \mathbf{x}} d\mathbf{k}' e^{i\mathbf{k} \cdot \mathbf{r}} d\mathbf{k} \right) \quad (2.20)$$

We adopt the following assumption:

**Assumption 2.1** *The flow is homogeneous.*

For homogeneous flow the correlation tensor equals its average over  $\mathbf{x}$ -space. Expression 2.20 contains a factor which oscillates with  $\mathbf{x}$ . This makes all contributions to the correlation function vanish except for the wave with zero wavevector (i.e.  $\mathbf{k} = \mathbf{k}'$ ). This leads us to the following relation for the correlation tensor for homogeneous flow:

$$\bar{\bar{R}}^t(\mathbf{r}) = \mathcal{E} \left( \int \int \hat{\mathbf{u}}(\mathbf{k}) \otimes \hat{\mathbf{u}}^*(\mathbf{k}') \delta(\mathbf{k} - \mathbf{k}') d\mathbf{k}' e^{i\mathbf{k} \cdot \mathbf{r}} d\mathbf{k} \right) \quad (2.21)$$

$$= \mathcal{E} \left( \int \hat{\mathbf{u}}(\mathbf{k}) \otimes \hat{\mathbf{u}}^*(\mathbf{k}) e^{i\mathbf{k} \cdot \mathbf{r}} d\mathbf{k} \right) \quad (2.22)$$

$$= \int \mathcal{E} \left( \hat{\mathbf{u}}(\mathbf{k}) \otimes \hat{\mathbf{u}}^*(\mathbf{k}) \right) e^{i\mathbf{k} \cdot \mathbf{r}} d\mathbf{k} \quad (2.23)$$

where  $\delta$  is Dirac's delta-function. Expression 2.23 for the correlation tensor can be combined with the definition of the Fourier transform:

$$\bar{\bar{R}}(\mathbf{r}) = \int \bar{\bar{\Phi}}(\mathbf{k}) e^{i\mathbf{k} \cdot \mathbf{r}} d\mathbf{k} \quad \bar{\bar{\Phi}}(\mathbf{k}) \equiv \frac{1}{8\pi^3} \int \bar{\bar{R}}(\mathbf{r}) e^{-i\mathbf{k} \cdot \mathbf{r}} d\mathbf{r} \quad (2.24)$$

to give an explicit form for the transpose of spectral tensor  $\bar{\bar{\Phi}}$ :

$$\bar{\bar{\Phi}}^t(\mathbf{k}) = \mathcal{E} \left( \hat{\mathbf{u}}(\mathbf{k}) \otimes \hat{\mathbf{u}}^*(\mathbf{k}) \right) \quad (2.25)$$

We see that the transpose of the spectral tensor can be regarded as the expectation value of polarisation-dyads. The spectral tensor  $\bar{\bar{\Phi}}(\mathbf{k})$  itself gives a distorted view of which polarisations one can expect to find in flow realizations. This is illustrated by the following relation:

$$\bar{\bar{\Phi}}(\mathbf{k}) = \mathcal{E} \left( \tilde{\hat{\mathbf{u}}}(\mathbf{k}) \otimes \tilde{\hat{\mathbf{u}}}^*(\mathbf{k}) \right) \quad (2.26)$$

$\bar{\bar{\Phi}}$  can be regarded as the expectation value of the *conjugate* of the polarisation-dyads of waves present in the flow. This is why we started the spectral examination of the correlation tensor with its transpose.

We will describe the averaging process over all turbulent flow realizations (needed when we want to determine expectation values) with a function called the spectral structure probability density function.

**Definition 2.7** *The definition of the spectral structure probability density function or ss-pdf is:*

$$C(\mathbf{k}, \mathbf{b}) \equiv \mathcal{E} \left( ||\hat{\mathbf{u}}||^2 \right)_{\mathbf{k}, \mathbf{b}} \quad (2.27)$$

Spectral structure pdf  $C(\mathbf{k}, \mathbf{b})$  describes the proportionality with which energy can be found in a wave with wavevector  $\mathbf{k}$  and with polarisation  $\hat{\mathbf{u}}$  in (unit-)direction  $\mathbf{b}$ . Mutatis mutandum, the squareroot of the ss-pdf gives the proportionality of the polarisation of waves with wavevector  $\mathbf{k}$  and with polarisation in (unit-)direction  $\mathbf{b}$ .

Using the description of stochastic averaging of realizations we can reformulate expression 2.25 to:

$$\bar{\bar{\Phi}}^t(\mathbf{k}) = \int C(\mathbf{k}, \mathbf{b}) \left( \mathbf{b} \otimes \mathbf{b}^* \right) d\mathbf{b} \quad (2.28)$$

From relation 2.6 for real valued velocity fields combined with relation 2.28 and with relation 2.3 we see that:

$$\bar{\bar{\Phi}}(-\mathbf{k}) = \tilde{\bar{\bar{\Phi}}}(\mathbf{k}) = \bar{\bar{\Phi}}^t(\mathbf{k}) \quad (2.29)$$

Tensor  $\bar{\bar{\Phi}}$  is self-adjoint. This implies (see text around relation 2.4) that  $\bar{\bar{\Phi}}$  can be written as (see Kampé de Fériet (1948); Batchelor (1953)):

$$\bar{\bar{\Phi}}(\mathbf{k}) = s_1 \mathbf{a}(\mathbf{k}) \otimes \mathbf{a}^*(\mathbf{k}) + s_2 \mathbf{b}(\mathbf{k}) \otimes \mathbf{b}^*(\mathbf{k}) + s_3 \mathbf{c}(\mathbf{k}) \otimes \mathbf{c}^*(\mathbf{k}) \quad (2.30)$$

where eigenvectors  $\mathbf{a}$ ,  $\mathbf{b}$  and  $\mathbf{c}$  are orthogonal complex unit vectors in the direction of  $\bar{\bar{\Phi}}$ 's eigenvectors, and where  $s_1, s_2$  and  $s_3$  are (by definition real non-negative) eigenvalues. The spectral tensor gives the proportional average (i.e. a sum in which individual contributions are lost) of all possible realisations. Consequently, the terms in expression 2.30 specify the directions of preference of the ensemble of all possible waves with wavevector  $\mathbf{k}$ .

The eigenvectors of the spectral tensor tempt one to think of the function as an ellipsoidal distribution of kinetic energy. This is a misleading point of view: In contrast with the spectral tensor, the ss-pdf gives the proportionality of *individual* realisations. There is no need for  $C$  to be ellipsoidal. In figure 2.4 an example is given of an ss-pdf having a minimum for waves polarised in the direction of the largest eigenvector of the spectral tensor. In this example no waves can be found having their polarisation in the direction of  $ev2$ . Nevertheless this axis gives the major eigenvector of the correlation spectrum.

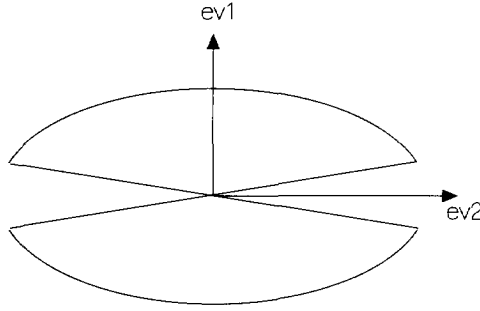


Figure 2.4: Radial plot of an ss-pdf with a minimum value for waves polarised along major principal axis  $ev2$  of the correlation spectrum. The wavevector is normal to the plotted function and consequently points out of the paper.

## 2.5 Restrictions and assumptions

We see from the definition that the correlation tensor for zero separation ( $\mathbf{r} = \mathbf{0}$ ) is symmetric. For non-zero separation the correlation tensor can have an anti-symmetric part. An antisymmetric part in the correlation tensor leads to a complex valued spectral tensor with complex eigenvectors. A symmetric correlation tensor would lead to a spectral tensor with real valued eigenvectors. This would simplify analysis considerably. We therefore want to know which wave distributions can give imaginary contributions to the correlation spectrum.

The analysis goes as follows: Both the collection of all waves and the collection of all conjugate waves span the same space (for every wave it is possible to construct a conjugate wave). Therefore we can build the correlation spectrum via relation 2.28 both from all possible waves and from all possible conjugate waves. Combination of these two constructions gives:

$$\bar{\Phi}^t(\mathbf{k}) = \frac{1}{2} \int \{ C(\mathbf{k}, \mathbf{b}) (\mathbf{b} \otimes \mathbf{b}^*) + C(\mathbf{k}, \tilde{\mathbf{b}}) (\tilde{\mathbf{b}} \otimes \tilde{\mathbf{b}}^*) \} d\mathbf{b} \quad (2.31)$$

Using relation 2.7 for basic waves (with real vectors  $\mathbf{b}_a$  and  $\mathbf{b}_b$  as polarisations of the basic waves of a wave with polarisation  $\mathbf{b}$ ) we can express this as:

$$\bar{\Phi}^t(\mathbf{k}) = \bar{\Phi}_c(\mathbf{k}) + i\bar{\Phi}_q(\mathbf{k}) \quad (2.32)$$

where cospectrum  $\bar{\Phi}_c$  and quadrature spectrum  $\bar{\Phi}_q$  are defined as:

$$\bar{\Phi}_c(\mathbf{k}) \equiv \int C_c(\mathbf{k}, \mathbf{b}) \left( \mathbf{b}_a \otimes \mathbf{b}'_a + \mathbf{b}_b \otimes \mathbf{b}'_b \right) \quad (2.33)$$

$$C_c(\mathbf{k}, \mathbf{b}) \equiv \frac{1}{2} \{ C(\mathbf{k}, \mathbf{b}) + C(\mathbf{k}, \tilde{\mathbf{b}}) \} \quad (2.34)$$

$$\bar{\Phi}_q(\mathbf{k}) \equiv \int C_q(\mathbf{k}, \mathbf{b}) \left( \mathbf{b}_a \otimes \mathbf{b}'_b - \mathbf{b}_b \otimes \mathbf{b}'_a \right) d\mathbf{b} \quad (2.35)$$

$$C_q(\mathbf{k}, \mathbf{b}) \equiv -\frac{1}{2} \{ C(\mathbf{k}, \mathbf{b}) - C(\mathbf{k}, \tilde{\mathbf{b}}) \} \quad (2.36)$$

Quantities  $C_c$  and  $C_q$  are called respectively co-spectral structure pdf and quadrature spectral structure pdf.

The quadrature spectrum is antisymmetric. Therefore it can be written as the vector product with a vector  $\omega$ , which we call the *swirl-vector* (tensor  $\bar{\bar{\epsilon}}$  is the antisymmetric permutation tensor):

$$\bar{\Phi}_q(\mathbf{k}) = \bar{\bar{\epsilon}} \cdot \int C_q(\mathbf{k}, \mathbf{b}) \omega d\mathbf{b} \quad (2.37)$$

$$\omega \equiv \mathbf{b}_a \times \mathbf{b}_b \quad (2.38)$$

We define a quantity called the *swirl fraction* (symbol  $S(k)$ ) for a complex spectral contribution  $T(k)$  (to either  $\Theta(k)$  or to  $\Psi(k)$ ) as the ratio of the length of the associated swirl vector and the tensor's trace:

$$S(k) \equiv \frac{\omega(k)}{\text{Trace}(T(k))} \quad (2.39)$$

where  $\omega(k)$  is the length of  $\omega(k)$ , with the sign of  $\omega_1$ . The sign is included to discriminate between the two classes of swirl. The swirl fraction expresses the degree of circular polarisation of the flow.

Definition 2.31 shows that the correlation spectrum is real valued and consequently has real valued eigenvectors if the ss-pdf has the same value for conjugate waves. A complex valued correlation spectrum therefore shows a net preference of the turbulent flow for motions with a certain swirl. This means that one class of elliptic polarisations is favoured to the class with opposite elliptic polarisations. Such a preference can be realized in experiments e.g. by letting a fluid pass through a grid of small swirl-elements. Another situation in which net swirl can be expected is a turbulent boundary layer: interaction of the flow with the boundary will favour the production of one class of elliptically polarised waves.

**Assumption 2.2** From here we will consider turbulent flow in which the basic waves are independent.

**Corollary 2.2** A consequence of the above assumption is that the flow has no preference for either class of elliptic polarisations (see figure 2.3), i.e.: there is no net swirl. Therefore, via relation 2.35, the spectral tensor is real valued and symmetric:

$$\bar{\Phi} \in \left( \mathbb{R}^3 \otimes \mathbb{R}^{3'} \right) \Rightarrow \bar{\bar{R}} = \bar{\bar{R}}^t \quad (2.40)$$

There is another consequence of assumption 2.2 worth mentioning:

**Corollary 2.3** *In relation 2.33 for the cospectrum we see that both the term for the contribution by all first basic waves and the term for the contribution by all second basic waves must be identical. As a consequence we can regard the ss-pdf as the expectation value of only linearly polarised waves. This allows us to restrict relation 2.28 to real valued vectors  $\mathbf{b}$ .*

**Assumption 2.3** *From here we will restrict the present study to incompressible fluids.*

In an incompressible fluid there are no longitudinal waves. The effect on the character of  $\bar{\Phi}$  is that for an incompressible flow we have (take the divergence of the velocity in relation 2.5):

$$\hat{\mathbf{u}}(\mathbf{k}) \perp \mathbf{k} \quad (2.41)$$

which means that all waves must be transversal waves and consequently all wave vectors are perpendicular to the velocity which they induce.

For solenoidal flow the co-sspdf will have to admit only those waves satisfying relation 2.41. This limitation can be expressed by the introduction of a solenoidal ss-pdf  $C_s(\mathbf{k}, \mathbf{b})$ , defined by:

$$C_c(\mathbf{k}, \mathbf{b}) = C_s(\mathbf{k}, \mathbf{b}) \delta \left( \frac{(\mathbf{b} \cdot \mathbf{k})}{|\mathbf{k}|} \right) \quad (2.42)$$

Kampé de Fériet (Kampé de Fériet, 1948, relation I5) has found that relation 2.41 for incompressible flow shows that wave-vector  $\mathbf{k}$  is one of the eigenvectors in expression 2.30, having zero eigenvalue. Thus for incompressible flow  $\bar{\Phi}$  can be expressed in the form:

$$\bar{\Phi}(\mathbf{k}) = \frac{E'(\mathbf{k})}{4\pi k^2} \left( \mathbf{b}'(\mathbf{k}) \otimes \mathbf{b}'^t(\mathbf{k}) \right) + \frac{E''(\mathbf{k})}{4\pi k^2} \left( \mathbf{b}''(\mathbf{k}) \otimes \mathbf{b}''^t(\mathbf{k}) \right) \quad (2.43)$$

$$0 = \mathbf{b}'(\mathbf{k}) \cdot \mathbf{b}''(\mathbf{k}) = \mathbf{b}'(\mathbf{k}) \cdot \mathbf{k} = \mathbf{b}''(\mathbf{k}) \cdot \mathbf{k} \quad (2.44)$$

where  $\mathbf{b}'$  and  $\mathbf{b}''$  are unit vectors along the eigenvectors of  $\bar{\Phi}$ .  $E'(\mathbf{k})$  and  $E''(\mathbf{k})$  are scalar energy functions.

## 2.6 Linearly polarised waves

From relation 2.28 and from corollary 2.3 we know that the spectral tensor associated with a particular wave-vector can be written as the weighted integration of all possible linear polarisations of waves with that wave-vector. We will therefore proceed by analysing which linearly polarised waves can contribute to a wave with wavevector  $\mathbf{k}$ .

Let us introduce spherical coordinates  $(k, \theta, \phi)$  for wavevector  $\mathbf{k}$  (as shown in figure 2.5).

$$\mathbf{k} = k \begin{pmatrix} \cos \theta \\ \sin \theta \cos \phi \\ \sin \theta \sin \phi \end{pmatrix} \quad (2.45)$$

Define  $\mathbf{b}$  to be the (unit) direction (normal to  $\mathbf{k}$ ) along which an arbitrary linearly polarised wave with wavevector  $\mathbf{k}$  induces its velocity (see figure 2.6). Once  $\mathbf{k}$  is fixed there is one degree

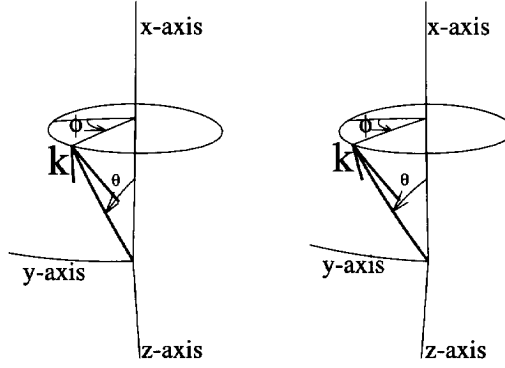


Figure 2.5: Orientation of the wavevector

of freedom to choose vector  $\mathbf{b}$ . Two mutually perpendicular choices for  $\mathbf{b}$  are  $\mathbf{b}_1$  and  $\mathbf{b}_2$  (see figure 2.6). Vector  $\mathbf{b}_1$  is chosen to be the vector in the  $x = 0$ -plane, perpendicular to the plane

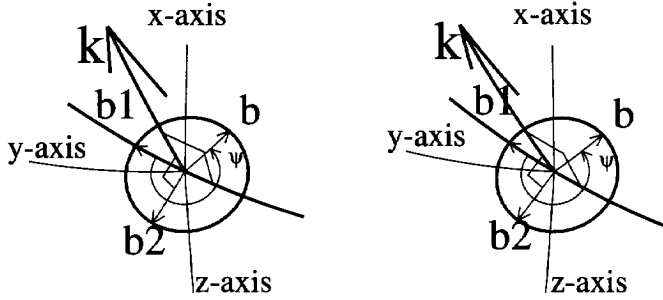


Figure 2.6: Orientation of polarisations

spanned by the  $\mathbf{k}$ -vector and the  $z$ -axis, and vector  $\mathbf{b}_2$  is normal both to  $\mathbf{b}_1$  and to  $\mathbf{k}$ :

$$\mathbf{b}_1 = \begin{pmatrix} 0 \\ -\sin \phi \\ \cos \phi \end{pmatrix} \quad \mathbf{b}_2 = \begin{pmatrix} -\sin \theta \\ \cos \theta \cos \phi \\ \cos \theta \sin \phi \end{pmatrix} \quad (2.46)$$

Define  $\psi$  as the rotation angle of  $\mathbf{b}$  around  $\mathbf{k}$  pointing from  $\mathbf{b}_1$  to  $\mathbf{b}_2$ . Let  $\chi$  be the angle between a vector  $\mathbf{b}$  and the wavevector (for incompressible flow  $\chi$  equals  $\pi/2$ ):

$$\cos(\chi) \equiv \frac{\mathbf{b} \cdot \mathbf{k}}{k} \quad (2.47)$$

We can combine relation 2.42 for the solenoidal ss-pdf (the argument of the delta-function is just the cosine of angle  $\theta$ ) with the currently developed coordinate notation to express relation 2.28

for the spectral tensor for incompressible flow by an integration over angle  $\psi$ :

$$\bar{\Phi}(\mathbf{k}) = \int C_s(\mathbf{k}, \mathbf{b}) \delta\left(\frac{\mathbf{b} \cdot \mathbf{k}}{k}\right) (\mathbf{b} \otimes \mathbf{b}') d\mathbf{b} \quad (2.48)$$

$$= \int_0^{2\pi} \int_0^\pi C_s(\mathbf{k}, \mathbf{b}(\chi, \psi)) \delta(\cos(\chi)) (\mathbf{b}(\chi, \psi) \otimes \mathbf{b}'(\chi, \psi)) \sin(\chi) d\chi d\psi \quad (2.49)$$

$$= \int_0^{2\pi} \int_{-1}^1 C_s(\mathbf{k}, \mathbf{b}(\chi, \psi)) \delta(\cos(\chi)) (\mathbf{b}(\chi, \psi) \otimes \mathbf{b}'(\chi, \psi)) d\cos(\chi) d\psi \quad (2.50)$$

$$= \int_0^{2\pi} C_s(\mathbf{k}, \mathbf{b}(\psi)) (\mathbf{b}(\psi) \otimes \mathbf{b}'(\psi)) d\psi \quad \text{and} \quad \chi = \frac{\pi}{2} \quad (2.51)$$

For all possible choices for  $\mathbf{b}$ , the direction of induced velocity of a transversal polarised wave with wavevector  $\mathbf{k}$ , are given by the circle of polarisation directions:

$$\mathbf{b}(\psi) = \cos(\psi)\mathbf{b}_1 + \sin(\psi)\mathbf{b}_2 \quad (2.52)$$

With relation 2.51 for the co-spectrum and parametrisation 2.52 for incompressible polarisation directions we have tools to perform model calculations on spectra. These tools will be used later in this chapter to build a model for the unaliasing of one-dimensional spectra.

## 2.7 Integrated spectra

We define wavenumber spectral tensor  $\bar{\Psi}$  as the sum of all spectral tensors  $\bar{\Phi}$  associated with waves having the same wavenumber  $k$ :

$$\bar{\Psi}(k) \equiv \int \bar{\Phi}(\mathbf{k}) dA(k) \quad (2.53)$$

$$= \int \bar{\Phi}(\mathbf{k}) k^2 \sin(\theta) d\theta d\phi \quad (2.54)$$

$$= \int C(\mathbf{k}, \mathbf{b}) (\mathbf{b} \otimes \mathbf{b}') k^2 \sin(\theta) d\theta d\phi d\psi \quad (2.55)$$

where  $A(k)$  is the surface of a sphere with radius  $k$ .

The trace of tensor  $\bar{\Psi}$  is related to what is called the scalar energy spectrum  $E(k)$ , giving the energy per unit volume represented by all waves with wavenumber  $k$ :

$$E(k) \equiv \frac{1}{2} \text{Trace}(\bar{\Psi}(k)) \quad (2.56)$$

$$= \int \frac{1}{2} C \sin(\theta) k^2 d\theta d\phi d\psi \quad (2.57)$$

Tensor  $\bar{\Psi}$  can be related to the sum  $\bar{\bar{S}}$  of all contributions to velocity correlation tensor  $\bar{\bar{R}}$  having constant separation  $r$ :

$$\bar{\bar{S}}(r) \equiv \frac{1}{4\pi r^2} \int \bar{\bar{R}}(\mathbf{r}) dA(r) \quad (2.58)$$

We call  $\bar{\bar{S}}$  the wavenumber correlation tensor. The relation between the wavenumber correlation tensor and the wavenumber spectral tensor is established via the following analysis:

$$\bar{\bar{S}}(r) = \frac{1}{4\pi} \int_0^{2\pi} \int_0^\pi \int_{\mathbb{R}^3} \bar{\bar{\Phi}}(\mathbf{k}) e^{i\mathbf{k} \cdot \mathbf{r}} d\mathbf{k} \sin(\theta_r) d\theta_r d\phi_r \quad (2.59)$$

$$= \frac{1}{4\pi} \int_{\mathbb{R}^3} \int_0^{2\pi} \bar{\bar{\Phi}}(\mathbf{k}) \int_{-1}^1 e^{ikr \cos(\theta_r)} d\cos(\theta_r) d\phi_r d\mathbf{k} \quad (2.60)$$

$$= \frac{1}{2} \int_{\mathbb{R}^3} \bar{\bar{\Phi}}(\mathbf{k}) \frac{1}{ikr} \{e^{ikr} - e^{-ikr}\} d\mathbf{k} \quad (2.61)$$

$$= \int_{\mathbb{R}^3} \bar{\bar{\Phi}}(\mathbf{k}) \text{sinc}(kr) d\mathbf{k} \quad (2.62)$$

$$= \int_0^\infty \bar{\bar{\Psi}}(k) \text{sinc}(kr) dk \quad (2.63)$$

where the sinc-function is defined as:

$$\text{sinc}(x) \equiv \frac{\sin x}{x} \quad (2.64)$$

The inverse relation between  $\bar{\bar{\Psi}}$  and  $\bar{\bar{S}}$  yields:

$$\bar{\bar{\Psi}}(k) = \frac{2}{\pi} \int_0^\infty \bar{\bar{S}}(r) kr \sin(kr) dr \quad (2.65)$$

We see from relation 2.58 that  $\bar{\bar{S}}(0)$  provides us with the Reynolds stress tensor:

$$\bar{\bar{S}}(0) = \bar{\bar{R}}(\mathbf{0}) \quad (2.66)$$

Relation 2.63 shows the linear decomposition of the Reynolds stress into stress tensor contributions by spectral components with constant wavelength:

$$\bar{\bar{R}}(\mathbf{0}) = \int_0^\infty \bar{\bar{\Psi}}(k) dk \quad (2.67)$$

## 2.8 The aliasing problem

In case we are able to measure the instantaneous velocity of a flow *in all points* then the definitions and relations given in the former sections are magnificent tools to observe the complete spectral tensor. However, in practice only one-point observations are available. The problem with one-point measurements is that most of the turbulent flow will not pass through the sensing zone of the instrument and consequently is not probed. Still we seek information on 3D-coherence. Application of Taylor's hypothesis provides (under certain circumstances, as shown in section 1.2) information on the velocity field *along a straight line*. This also means that waves with a wavevector not aligned with the sampled line enter the probe signal as an aliased larger wave (see figure 2.7). This complicates the interpretation of measured signals in terms of single wave components. Citriniti and George (1996) conclude about this complication:

The one-dimensional spectrum can be a very misleading investigative device for the turbulence researcher due to the inability to assess where energy contained at various frequencies or wave numbers comes from.



The question is now: how and with which assumptions can we obtain estimates for spectral quantities, as defined in the former sections, out of the measured velocity field along a line? This means that we have to estimate the effect of aliasing.

Aliasing depends on the direction of the wave-vector relative to the mean flow. On the other hand, the complete spectral tensor (which is what we seek) is built by the polarisations of the contributing waves. As found earlier, the polarisation of solenoidal waves is perpendicular to the wave-vector. This orthogonality between wavevector (the quantity by which waves are sorted) and polarisation (the physical effect of the waves) makes it difficult to analyse the aliasing problem. The use of an ss-pdf to describe stochastic averaging of all possible turbulent flow realizations, adopted in the former section, enables us to estimate the effect of aliasing.

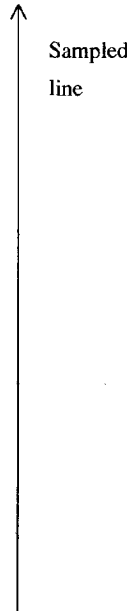


Figure 2.7: Aliasing in one point measurements

Suppose we have taken samples of the velocity vector along a line and let us take the  $x$ -coordinate along the direction of the sampled line. In our experiment we measure three velocity components simultaneously. This enables us to construct correlation tensor  $\bar{\bar{\Theta}}$  as function of a wavenumber  $k_1$ . The one dimensional spectral tensor of the samples is called  $\bar{\bar{\Theta}}$  and is related to tensors  $\bar{\bar{R}}$  and  $\bar{\bar{\Phi}}$  via:

$$\bar{\bar{\Theta}}(k_1) \equiv \frac{1}{2\pi} \int_{-\infty}^{\infty} \bar{\bar{R}}(r_1, 0, 0) e^{-ik_1 r_1} dr_1 = \int_{-\infty}^{\infty} \int_{-\infty}^{\infty} \bar{\bar{\Phi}}(k_1, k_2, k_3) dk_2 dk_3 \quad (2.68)$$

We see from its definition that tensor  $\bar{\bar{\Theta}}$  is self-adjoint.

The analysis we have made in the previous sections of this chapter is based on the assumption that the correlation spectrum is real valued. Relation 2.68 shows that we have to make the same

assumption for  $\bar{\bar{\Theta}}$  before we can apply results of the former analysis of  $\bar{\bar{\Phi}}$  (see section 2.5 on the reasons why)<sup>2</sup>.

A full reconstruction of  $\bar{\bar{\Phi}}$  (a tensor function of a vector variable) is not possible when one has only one-dimensional spectrum  $\bar{\bar{\Theta}}$ . The structures of spectra  $\bar{\bar{\Psi}}$  and  $\bar{\bar{\Theta}}$  show close resemblance: both spectra are real valued symmetric tensors as function of a single wavenumber. We therefore try to couple them and realize the following:

**Aim** We will try to reconstruct  $\bar{\bar{\Psi}}(k)$  from measured one dimensional spectra  $\bar{\bar{\Theta}}$  by means of a model solenoidal ss-pdf  $Cs_m(\mathbf{k}, \psi)$  (index  $m$  indicates "model").

Once the ss-pdf will be modelled, we will be able to see how the collection of waves composing the spectrum aliases onto a single line and consequently we will be able to derive relations to unalias measured one-dimensional spectra.

## 2.8.1 Tools for building a model ss-pdf

The extrapolation of samples on a line to samples in the whole 3D-domain can only be made when we adopt *assumptions* about the ss-pdf. Based on different assumptions many fundamentally different choices for the solenoidal ss-pdf can be constructed, which through relation 2.28 all will give the same one-dimensional spectral tensor  $\bar{\bar{\Theta}}$ . In the first subsection we will construct an isotropic model, which in the second subsection will be extended to anisotropic flow.

### 2.8.1.1 The isotropic model

Let us start with an isotropic approximation for the ss-pdf. In an isotropic situation the ss-pdf does not have any directional dependence. This means that it neither depends on the direction of the polarisation (angle  $\psi$ ) nor on the direction of the wavevector. Consequently the ss-pdf only depends on the length of the wavevector:

$$Cs_{m,\text{isotropic}}(\mathbf{k}, \psi) = Cs_0(k) \quad (2.69)$$

The consequence of this relation for the ss-pdf is that the energy functions in relation 2.43 are identical. Using this identity, we can write the spectral tensor for isotropic incompressible turbulence as an isotropic tensor from which the projection on the wave-vector is subtracted. Knowing that  $\mathbf{b}_1$ ,  $\mathbf{b}_2$  and  $\mathbf{k}$  form an orthogonal set, we can use the following identity relation ( $\bar{\bar{\delta}}$  is Kronecker's delta-tensor):

$$\bar{\bar{\delta}} = \mathbf{b}_1 \otimes \mathbf{b}_1^t + \mathbf{b}_2 \otimes \mathbf{b}_2^t + \frac{\mathbf{k} \otimes \mathbf{k}^t}{k^2} \quad (2.70)$$

---

<sup>2</sup>By discarding the imaginary part of one-dimensional spectra we throw away an amount of information which has the same structure as the imaginary part of spectral tensor  $\bar{\bar{\Psi}}$ . We therefore expect that a future analysis focused on this imaginary part, conducted in a way similar to the present method, will generalise the results of this study to turbulence with net swirl.

to simplify expression 2.43 for the spectral tensor for isotropic turbulence to:

$$\bar{\Phi}_{\text{isotropic}}(\mathbf{k}) = \frac{E'(k)}{4\pi k^2} \left( \bar{\delta} - \frac{1}{k^2} \mathbf{k} \otimes \mathbf{k}^t \right) \quad (2.71)$$

which matches Batchelor's relation (3.4.12).

From scalar normalisation relation 2.57 we get the following expression for the isotropic solenoidal ss-pdf:

$$Cs_0(k) = \frac{E(k)}{4\pi^2 k^2} \quad (2.72)$$

The collection of all polarisations  $\mathbf{x}$  with magnitude equal to the squareroot of the corresponding ss-pdf, defines a sphere:

$$\frac{\mathbf{x} \cdot \mathbf{x}^t}{Cs_0(k)} = 1 \quad (2.73)$$

This is a second-order surface.

### 2.8.1.2 An anisotropic model

The isotropic model which we constructed in the former subsection is solely based on the trace of the wavenumber spectral tensor. Therefore it does not satisfy the following consistency requirement:

**Requirement** *The method to construct model ss-pdf  $Cs_m$  from wavenumber spectrum  $\bar{\Psi}$  must be such that integration of the model ss-pdf via relation 2.55 correctly integrates back to  $\bar{\Psi}$  independent of the choice of  $\bar{\Psi}$ .*

At each wavenumber  $k$  tensor  $\bar{\Psi}$  merely gives the principal axes plus eigenvalues of all contributions to the correlation tensor by waves with this wavenumber. The exact structure of the ss-pdf is lost in  $\bar{\Psi}$ . Consider a certain  $\bar{\Psi}(k)$  (with its eigenvectors). Without having data from measurements taken along multiple lines in the flow we cannot tell which waves have contributed to  $\bar{\Psi}$  and which have not.

To get accurate estimates for the expectation value of a spectral component one averages spectra over several independent realizations of the flow. When the flow which is studied has a chaotic nature, then the ss-pdf involved in averaging of turbulent flow realizations to obtain  $\bar{\Psi}$  will be smooth. In practice the ss-pdf does not have to be smooth. As an example of a non-smooth ss-pdf, consider a random flow involving five different linearly polarised waves with the same wavenumber, which dominate every realization of the flow. In this case ss-pdf  $Cs$  would be sharply peaked (out of an infinite number of waves, only five discrete modes have non-zero probability). Such choice for  $Cs_m$  favours the five polarisation directions to all other polarisations, whereas we are seeking a smooth ss-pdf. When we are processing data from one-point measurements, we expect to have no reason to give an unproportionally large priority to certain directions.

We are looking for the most plausible, smooth choice for  $Cs_m$ . We have already seen that the zeroth order approximation in anisotropy of the ss-pdf is a surface of second order in the

polarisation vector. We therefore postulate:

**Postulate** *The simplest generalisation of a spherical ss-pdf for isotropic flow to anisotropic flow is given by the combination of a spherical plus an ellipsoidal ss-pdf since the latter is of second order in the polarisation vector either:*

$$C_{sm}(\text{anisotropy}) = \alpha C_{s0}(k) + C_{s\text{ellipsoidal}}(\Psi(\mathbf{k})) \quad (2.74)$$

where  $\alpha$  is a proportionality constant. Isotropic ss-pdf  $C_{s0}(k)$  is given in relation 2.72. In the following section we will construct a flow-linked ellipsoid which can be used to model the ellipsoidal part in this relation.

## 2.8.2 An ellipsoid related to the wavenumber spectral tensor

For each wavenumber  $k$  we seek to build an ellipsoidal contribution for the ss-pdf conform relation 2.74. To build an ellipsoidal function which has a close relation with the velocity field we define an ellipsoid, called  $\Pi(k)$ , as follows: The direction of the semi-axes of the ellipsoid are aligned with the eigenvectors of  $\bar{\Psi}(k)$ . The lengths of the semi-axes are proportional to  $n$ -th powers of the eigenvalues of  $\bar{\Psi}(k)$ . The length of the vectors pointing to the surface of this ellipsoid defines a smooth ellipsoidal function. A polarised wave distribution, of which the ss-pdf for waves polarised in the direction of these vectors is proportional to this function, has the same eigenvectors as  $n$ -th powers of  $\bar{\Psi}(k)$  has (but not necessarily the same eigenvalues!).

We will now study ellipsoid  $\Pi(k)$  spanned by  $n$ -th powers of the eigenvectors of  $\bar{\Psi}(k)$ . Unit vectors in eigenvector directions are called  $\mathbf{ev}_1, \mathbf{ev}_2, \mathbf{ev}_3$  and  $\bar{\Psi}(k)$ 's eigen-values are called  $E_1, E_2, E_3$ . Via relation 2.28 the ss-pdf weights dimensionless unit-vector diadics (comparable to a second power) resulting in spectral tensor contributions. Tensor  $\bar{\Psi}(k)$  is quadratic in velocity. To weight individual polarisation directions with something having the dimension of a velocity, will have to use the *squareroot* of  $\bar{\Psi}(k)$ 's eigenvalues. The power  $n$  of the eigenvalues mentioned in the former paragraph is thus  $n = 0.5$ . Ellipsoid  $\Pi(k)$  is given by all points  $\mathbf{x}$  with:

$$\Pi(k) : \quad 1 = \left( \frac{(\mathbf{x} \cdot \mathbf{ev}_1)}{\sqrt{E_1}} \right)^2 + \left( \frac{(\mathbf{x} \cdot \mathbf{ev}_2)}{\sqrt{E_2}} \right)^2 + \left( \frac{(\mathbf{x} \cdot \mathbf{ev}_3)}{\sqrt{E_3}} \right)^2 \quad (2.75)$$

$$= \mathbf{x}^t \cdot \left( \frac{(\mathbf{ev}_1 \otimes \mathbf{ev}_1)}{E_1} + \frac{(\mathbf{ev}_2 \otimes \mathbf{ev}_2)}{E_2} + \frac{(\mathbf{ev}_3 \otimes \mathbf{ev}_3)}{E_3} \right) \cdot \mathbf{x} \quad (2.76)$$

Compare relation 2.76 to the form which we can give for  $m$ -th powers of tensor  $\bar{\Psi}(k)$ :

$$\bar{\Psi}^m(k) = \left( E_1^m (\mathbf{ev}_1 \otimes \mathbf{ev}_1) + E_2^m (\mathbf{ev}_2 \otimes \mathbf{ev}_2) + E_3^m (\mathbf{ev}_3 \otimes \mathbf{ev}_3) \right) \quad (2.77)$$

and we see that  $\Pi(k)$  is given by points  $\mathbf{x}$  with:

$$\Pi(k) : \quad \mathbf{x} \cdot \bar{\Psi}^{-1}(k) \cdot \mathbf{x} = 1 \quad (2.78)$$

From an arbitrary unit-vector  $\mathbf{b}$  we can construct a vector on  $\Pi$  by the following linear rescaling:

$$\mathbf{b} \rightarrow c \mathbf{b} \quad (2.79)$$

$$c \equiv (\mathbf{b} \cdot \bar{\Psi}^{-1}(k) \cdot \mathbf{b})^{-0.5} \quad (2.80)$$

### 2.8.3 Realization of a model ss-pdf

In this section we will use ellipsoid  $\Pi(k)$  to generalise the isotropic model ss-pdf to anisotropy. The following sections in this chapter will exploit this model. Most of the analysis from this point is an inevitable consequence of the ss-pdf generalisation via ellipsoid  $\Pi(k)$ ! Suggestion 2.74 is a linear combination of a spherical and an ellipsoidal contribution. With the relations found in the former section we can express the model solenoidal ss-pdf as:

$$Cs_m(\text{anisotropy})(\mathbf{k}, \mathbf{b}) = \alpha Cs_0(k) + Cs_{\Pi(k)}(\mathbf{k}, \mathbf{b}) \quad (2.81)$$

$$= \alpha Cs_0(k) + Cs_1(k)(\mathbf{b} \cdot \bar{\Psi}^{-1} \cdot \mathbf{b})^{-0.5} \quad (2.82)$$

where  $Cs_0$  is the isotropic ss-pdf given in relation 2.72, and  $Cs_1$  is the coefficient for the ellipsoidal term. Note that there is no need for the anisotropic correction term in relation 2.82 for the model solenoidal ss-pdf to vanish in the isotropic limit since it will take an isotropic form and consequently it may sustain.

Some direct consequences of the model are:

**Corollary 2.4** *The integral of vector diadics over the cross-section of  $\Pi(k)$  with the plane through the origin perpendicular to  $\mathbf{k}$  defines a smooth function. This integral describes the generalisation of an isotropic model  $\bar{\Phi}$  to anisotropy. Note that in general the probability density of waves contributing to  $\bar{\Phi}(\mathbf{k})$  is not elliptic, though the resulting tensor has two nonzero eigenvectors.*

**Corollary 2.5** *Ellipsoid  $\Pi(k)$ , on which the model solenoidal ss-pdf is based, does not depend on the direction of the wavevector, but solely on its length. Consequently, for waves with the same wavenumber, solenoidal ss-pdf  $Cs_m(\mathbf{k}, \mathbf{b})$  is constant for all waves having the same polarisation vector  $\mathbf{b}$ , irrespective of the orientation of wavevector  $\mathbf{k}$ . (Naturally the full ss-pdf includes a delta-function via definition 2.42, which rules out all incompressible waves. Therefore the full ss-pdf does depend on the direction of the wavevector):*

$$Cs_m(\mathbf{k}, \mathbf{b}) = Cs_m(k, \mathbf{b}) \quad (2.83)$$

In general relations 2.82 and 2.57 lead to intricate unsolvable relations between  $\bar{\Theta}(k)$  and  $\bar{\Psi}(k)$ . Therefore we will now restrict ourselves to the following assumption:

**Assumption 2.4** *We will examine turbulent flows with small anisotropy.*

Split spectral tensor  $\bar{\Psi}$  into isotropic and anisotropic parts:

$$\frac{1}{2}\bar{\Psi}(k) = E(k)\left(\frac{1}{3}\bar{\delta} + \bar{X}(k)\right) \quad (2.84)$$

where  $\bar{X}(k)$  is  $\bar{\Psi}(k)$ 's normalised anisotropy tensor:

$$\bar{X}(k) \equiv \frac{1}{2E(k)}\bar{\Psi}(k) - \frac{1}{3}\bar{\delta} \quad (2.85)$$

The anisotropic term in expression 2.82 can be expanded around isotropy:

$$(\mathbf{b} \cdot \bar{\Psi}^{-1} \cdot \mathbf{b})^{-0.5} = \left\{ \frac{1}{2E(k)} \mathbf{b} \cdot \left( \frac{1}{3} \bar{\delta} + \bar{X}(k) \right)^{-1} \cdot \mathbf{b} \right\}^{-0.5} \quad (2.86)$$

$$= \left\{ \frac{3}{2E(k)} \mathbf{b} \cdot \left( \bar{\delta} + 3\bar{X}(k) \right)^{-1} \cdot \mathbf{b} \right\}^{-0.5} \quad (2.87)$$

$$= \left\{ \frac{3}{2E} \left[ 1 - 3(\mathbf{b} \cdot \bar{X} \cdot \mathbf{b}) + O(\bar{X}^2(k)) \right] \right\}^{-0.5} \quad (2.88)$$

$$= \sqrt{\frac{2E}{3}} \left[ 1 + \frac{3}{2}(\mathbf{b} \cdot \bar{X} \cdot \mathbf{b}) + O(\bar{X}^2(k)) \right] \quad (2.89)$$

$$= \sqrt{\frac{2E}{3}} \left[ 1 + \frac{3}{2}(\mathbf{b} \cdot \left\{ \frac{1}{2E(k)} \bar{\Psi}(k) - \frac{1}{3} \bar{\delta} \right\} \cdot \mathbf{b}) + O(\bar{X}^2(k)) \right] \quad (2.90)$$

$$= \frac{1}{\sqrt{E}} \frac{1}{2} \sqrt{\frac{3}{2}} \left[ \left( \frac{1}{3} \text{Trace}(\bar{\Psi}) + \mathbf{b} \cdot \bar{\Psi} \cdot \mathbf{b} \right) + O(\bar{X}^2(k)) \right] \quad (2.91)$$

$$= \beta(k) \text{Trace}(\bar{\Psi}) + \gamma(k) (\mathbf{b} \cdot \bar{\Psi} \cdot \mathbf{b}) + O(\bar{X}^2(k)) \quad (2.92)$$

where  $\beta$  and  $\gamma$  represent the scalar functions involved.

We now substitute relation 2.92 for the ellipsoidal term in relation 2.82 for the model solenoidal ss-pdf. As an onset to normalisation we introduce two new scalar functions  $Cs'_0(k)$  and  $Cs'_1(k)$ , related to scalar functions  $Cs_0(k)$  and  $Cs_1(k)$  by separation of functional dependences which we expect to be present. We divide out both the surface of the sphere with radius  $k$ , and the circumference of the  $\psi$ -circle. Moreover, from  $Cs_0(k)$  we strip the trace of  $\bar{\Psi}$ :

$$Cs_m(\text{anisotropy}) = Cs'_0(k) \frac{\text{Trace}(\bar{\Psi}(k))}{8\pi^2 k^2} + Cs'_1(k) \frac{(\mathbf{b} \cdot \bar{\Psi} \cdot \mathbf{b})}{8\pi^2 k^2} \quad (2.93)$$

At this stage there are two important problems to be solved:

- How do we construct scalar functions  $Cs'_0(k)$  and  $Cs'_1(k)$  in relation 2.93 for the model ss-pdf such that  $Cs_m$  satisfies normalisation?
- How do we introduce the eigenvalues of  $\bar{\Psi}$  into scalar functions  $Cs'_0(k)$  and  $Cs'_1(k)$  such that the ss-pdf satisfies consistency?

It looks difficult to find scalar functions  $Cs'_0(k)$  and  $Cs'_1(k)$ . Though there is no reason why it should work, an attempt has been made to answer both questions by: "*with two constant scalar functions*".

One of the worries we have is the following: the *eigenvectors* of  $\bar{\Psi}$  will be correctly represented by this method, but we have to see whether the *eigenvalues* will follow. For every wavenumber there are three eigenvalues to be matched by the model  $\bar{\Psi}$  obtained from the model ss-pdf. The suggested linear combination of a spherical and an ellipsoidal term gives only TWO parameters to simultaneously match the THREE eigenvalues. We can only hope that this lack of freedom will not spoil the calculation of the consequences of the assumption.

Two scalar functions have been substituted for  $Cs'_0(k)$  and  $Cs'_1(k)$ . To check the consistency of this guess, relation 2.93 has been substituted into relations 2.28 and 2.54. Analytic integration of these relations by the MAPLE program for analytic mathematics has shown that for symmetric  $\bar{\Psi}$  the choice:

$$Cs'_0(k) = -\frac{3}{2} \quad (2.94)$$

$$Cs'_1(k) = \frac{15}{2} \quad (2.95)$$

$$\Rightarrow Cs_m(\mathbf{k}, \mathbf{b}) = \frac{15}{2} \left( -\frac{1}{5} \text{Trace}(\bar{\Psi}(k)) + \mathbf{b} \cdot \bar{\Psi}(k) \cdot \mathbf{b} \right) \cdot \frac{1}{8\pi^2 k^2} \quad (2.96)$$

for the terms in relation 2.93 is the *unique* choice for parameter functions  $Cs'_0(k)$  and  $Cs'_1(k)$  satisfying consistency relation 2.55.

The restriction of the calculation to symmetric  $\bar{\Psi}$  (which was a necessary restriction for MAPLE to be able to meet relation 2.55) is consistent with the restrictions made in the present analysis via relations 2.29 and 2.40.

Relation 2.55 proves that the decomposition proposed in relation 2.96 satisfies the consistency requirement on the model ss-pdf. Both the eigenvectors and *all three* eigenvalues of  $\bar{\Psi}$  are correctly represented by this choice for an ss-pdf of polarised waves.

We can reformulate relation 2.96 to:

$$\frac{1}{2} Cs(\mathbf{k}, \mathbf{b}) = \frac{E(k)}{8\pi^2 k^2} \left( 1 + \frac{15}{2} \mathbf{b} \cdot \bar{\bar{X}}(k) \cdot \mathbf{b} \right) \quad (2.97)$$

This expression for the solenoidal ss-pdf can be used to give amplitudes to waves in kinematic simulations. Such simulations can be of use to simulate anisotropic turbulence generated by a grid in laminar flow, or turbulence in homogeneous shear flow.

We see that for isotropic turbulence relation 2.97 for the ss-pdf reduces to the form given by relation 2.72.

## 2.8.4 Aliasing relations

Relation 2.97 gives us the tool to compute the aliasing of flow measurements with an anisotropic ss-pdf. The aliased wavelength at which the spectral contributions to  $\bar{\Psi}(k)$  will be found in the signal measured along the line depends only on  $\theta$  (see figure 2.7). Let  $\xi$  be the wavenumber in the measured signal. Then wavevector  $\mathbf{k}$  aliases onto wavenumber:

$$\xi = k_1 = k \cos(\theta) \quad (2.98)$$

We can substitute the following relations for coordinates  $\theta$ ,  $\xi$  and  $k$ :

$$\cos(\theta) = \frac{\xi}{k}; \quad \sin^2(\theta) = 1 - \left( \frac{\xi}{k} \right)^2 \quad (2.99)$$

into relation 2.54 for the wavenumber spectral tensor to find:

$$\bar{\Psi}(k) = k^2 \int_0^\pi \sin(\theta) \int_0^{2\pi} \bar{\Phi}(\mathbf{k}) d\phi d\theta \quad (2.100)$$

$$= \int_0^k k \int_0^{2\pi} \bar{\Phi}(\mathbf{k}) d\phi d\xi \quad (2.101)$$

$$= \int_0^k \bar{F}(\xi, k) d\xi \quad (2.102)$$

where  $\bar{F}(\xi, k)$  is defined by:

$$\bar{F}(\xi, k) \equiv k \int_0^{2\pi} \bar{\Phi}(\mathbf{k}) d\phi \quad (2.103)$$

From this definition we see that  $\bar{F}(\xi, k)$  gives the contribution to  $\bar{\Psi}(k)$  from all waves with identical physical and identical aliased wavelengths.

One-dimensional spectrum  $\bar{\Theta}(\xi)$  is obtained from  $\bar{F}$  by integration over the physical wavelengths that can contribute:

$$\bar{\Theta}(\xi) = \int_\xi^\infty \bar{F}(\xi, k) dk \quad (2.104)$$

Combination of relation 2.97 for the ss-pdf, relation 2.28 for the coupling of the ss-pdf with the spectral tensor and relations 2.103 and 2.104 for the coupling between the spectral tensor and the measured one-dimensional spectra yields the anisotropic aliasing relation for one dimensional spectra. The expression found with MAPLE is:

$$\Theta_{ij}(\xi) = \int_\xi^\infty \frac{3}{256k^5} \begin{pmatrix} f_{11} & f_{12} & f_{13} \\ f_{12} & f_{22} & f_{23} \\ f_{13} & f_{23} & f_{33} \end{pmatrix} dk \quad (2.105)$$

$$f_{11} \equiv 4(k^2 - \xi^2)((22\Psi_{11} - 3\Psi_{22} - 3\Psi_{33})k^2 + (-30\Psi_{11} + 15\Psi_{22} + 15\Psi_{33})\xi^2)$$

$$f_{12} \equiv 40(k^2 - \xi^2)(k^2 + 3\xi^2)\Psi_{12}$$

$$f_{13} \equiv 40(k^2 - \xi^2)(k^2 + 3\xi^2)\Psi_{13}$$

$$f_{22} \equiv (4\Psi_{11} + 29\Psi_{22} - \Psi_{33})k^4 + (24\Psi_{11} + 14\Psi_{22} - 6\Psi_{33})k^2\xi^2 \\ + (-60\Psi_{11} + 45\Psi_{22} + 15\Psi_{33})\xi^4$$

$$f_{23} \equiv 10(3k^4 + 2k^2\xi^2 + 3\xi^4)\Psi_{23}$$

$$f_{33} \equiv (4\Psi_{11} - \Psi_{22} + 29\Psi_{33})k^4 + (24\Psi_{11} - 6\Psi_{22} + 14\Psi_{33})k^2\xi^2 \\ + (-60\Psi_{11} + 15\Psi_{22} + 45\Psi_{33})\xi^4$$

For isotropic turbulence this relation reduces to:

$$\Theta_{ij}(\xi)[\text{isotropy}] = \int_\xi^\infty \begin{pmatrix} \frac{1}{2} \frac{E(k)(k^2 - \xi^2)}{k^3} & 0 & 0 \\ 0 & \frac{1}{4} \frac{E(k)(k^2 + \xi^2)}{k^3} & 0 \\ 0 & 0 & \frac{1}{4} \frac{E(k)(k^2 + \xi^2)}{k^3} \end{pmatrix} dk \quad (2.106)$$

which corresponds to Batchelor (1953)'s expressions (3.4.17) and (3.4.19).

The inverse of this relation will allow for the correction of measured spectra for aliasing.



## 2.8.5 Unaliasing relations

In the former section we found the aliasing relations for anisotropic turbulence. In this section we will invert them to give relations which can be used to interpret spectra of measured data.

With use of the following relation for arbitrary (tensor-) functions  $\bar{G}(\xi, k)$ :

$$\frac{d}{d\xi} \int_{\xi}^{\infty} \bar{G}(\xi, k) dk = \int_{\xi}^{\infty} \frac{d}{d\xi} \bar{G}(\xi, k) dk - \bar{G}(\xi, \xi) \quad (2.107)$$

and definition of specific differential operator  $\mathcal{D}$  by

$$\mathcal{D} \equiv \frac{4}{3} k^5 \frac{d}{dk} \frac{1}{k} \frac{d}{dk} \frac{1}{k} \frac{d}{dk} \quad (2.108)$$

we find the inverse of relation 2.105 to be:

$$2\mathcal{D}\Theta_{11} = -22\Psi_{11} + 3\Psi_{22} + 3\Psi_{33} - 2k\Psi'_{11} + 3k\Psi'_{22} + 3k\Psi'_{33} \quad (2.109)$$

$$\frac{1}{5}\mathcal{D}\Theta_{12} = -\Psi_{12} + k\Psi'_{12} \quad (2.110)$$

$$\frac{1}{5}\mathcal{D}\Theta_{13} = -\Psi_{13} + k\Psi'_{13} \quad (2.111)$$

$$8\mathcal{D}\Theta_{22} = -4\Psi_{11} - 29\Psi_{22} + \Psi_{33} + 4k\Psi'_{11} + 29k\Psi'_{22} - k\Psi'_{33} \\ + 4k^2\Psi''_{11} - 11k^2\Psi''_{22} - k^2\Psi''_{33} \quad (2.112)$$

$$\frac{4}{5}\mathcal{D}\Theta_{23} = -3\Psi_{23} + 3k\Psi'_{23} - k^2\Psi''_{23} \quad (2.113)$$

$$8\mathcal{D}\Theta_{33} = -4\Psi_{11} + \Psi_{22} - 29\Psi_{33} + 4k\Psi'_{11} - k\Psi'_{22} + 29k\Psi'_{33} \\ + 4k^2\Psi''_{11} - k^2\Psi''_{22} - 11k^2\Psi''_{33} \quad (2.114)$$

where a prime denotes differentiation with respect to  $k$ .

This defines three separate differential equations for  $\Psi_{12}$ ,  $\Psi_{13}$  and  $\Psi_{23}$  respectively, plus a set of three coupled differential equations for  $\Psi_{11}$ ,  $\Psi_{22}$  and  $\Psi_{33}$ .

The following differential relations for arbitrary functions  $f$  of  $k$  can help solve these equations:

$$k^n \frac{d}{dk} \frac{f(k)}{k^{n-1}} = -(n-1)f(k) + k \frac{d}{dk} f(k) \quad (2.115)$$

$$k^m \frac{d}{dk} \frac{1}{k^{m-n-1}} \frac{d}{dk} \frac{f(k)}{k^{n-1}} = (m-1)(n-1)f(k) - (m+n-3)k \frac{d}{dk} f(k) + k^2 \frac{d^2}{dk^2} f(k) \quad (2.116)$$

For isotropic turbulence the unaliasing relations give:

$$-4E + E' = k^5 \frac{d}{dk} \frac{E}{k^4} = k^5 \frac{d}{dk} \frac{1}{k} \frac{d}{dk} \frac{1}{k} \frac{d}{dk} \Theta_{11} \\ \Rightarrow E = k^3 \frac{d}{dk} \frac{1}{k} \frac{d}{dk} \Theta_{11} \quad (2.117)$$

$$-4E + 4kE' - k^2E'' = -k^5 \frac{d}{dk} \frac{1}{k^2} \frac{d}{dk} \frac{1}{k} \frac{d}{dk} E = 2k^5 \frac{d}{dk} \frac{1}{k} \frac{d}{dk} \frac{1}{k} \frac{d}{dk} \Theta_{22,33} \\ \Rightarrow E = 2k \int_k^{\infty} \kappa \frac{d}{d\kappa} \frac{1}{\kappa} \frac{d}{d\kappa} \Theta_{22,33} d\kappa \quad (2.118)$$

which is equivalent to relations 3.4.18 and 3.4.19 of Batchelor.

Now assume that both  $\bar{\Psi}$  and  $\frac{d}{dk}\bar{\Psi}$  go to zero when  $k$  goes to infinity. Replace relations 2.112 and 2.114 by their difference and their sum. With help of relations 2.115 and 2.116 we can solve four out of six unaliasing equations analytically (repeated partial integration from  $k$  to infinity is used):

$$\Psi_{12} = \frac{4}{15} \left( k^2 \Theta_{12}'' - 4k \Theta_{12}' + 3\Theta_{12} - 3k \int_k^\infty x^{-2} \Theta_{12} dx \right) \quad (2.119)$$

$$\Psi_{13} = \frac{4}{15} \left( k^2 \Theta_{13}'' - 4k \Theta_{13}' + 3\Theta_{13} - 3k \int_k^\infty x^{-2} \Theta_{13} dx \right) \quad (2.120)$$

$$\Psi_{23} = \frac{8}{15} \left( -2k \Theta_{23}' + 4\Theta_{23} - 3k \int_k^\infty x^{-4} (x^2 + k^2) \Theta_{23} dx \right) \quad (2.121)$$

$$\begin{aligned} (\Psi_{22} - \Psi_{33}) = \frac{8}{15} \left( -2k(\Theta_{22} - \Theta_{33})' + 4(\Theta_{22} - \Theta_{33}) \right. \\ \left. - 3k \int_k^\infty x^{-4} (x^2 + k^2) (\Theta_{22} - \Theta_{33}) dx \right) \end{aligned} \quad (2.122)$$

Two differential equations remain to be solved:

$$-11\Psi_{11} + 3\Psi_{22} - k\Psi_{11}' + 3k\Psi_{22}' = \frac{3}{2}(\Psi_{22} - \Psi_{33}) + \frac{3}{2}k(\Psi_{22} - \Psi_{33})' + \mathcal{D}\Theta_{11} \quad (2.123)$$

$$\begin{aligned} -\Psi_{11} - 7\Psi_{22} + k\Psi_{11}' + 7k\Psi_{22}' + k^2\Psi_{11}'' - 3k^2\Psi_{22}'' = \\ -\frac{7}{2}(\Psi_{22} - \Psi_{33}) + \frac{7}{2}k(\Psi_{22} - \Psi_{33})' - \frac{3}{2}k^2(\Psi_{22} - \Psi_{33})'' + \mathcal{D}(\Theta_{22} + \Theta_{33}) \end{aligned} \quad (2.124)$$

The right hand sides in these two equations are known in principle.

The solution of differential equations 2.123 and 2.124 will now be obtained by careful substitutions. Let us first give a more compact notation for relations 2.123 and 2.124 by introduction of names for both right hand and left hand sides:

$$l_1(k) \equiv -11\Psi_{11} + 3\Psi_{22} - k\Psi_{11}' + 3k\Psi_{22}' \quad (2.125)$$

$$r_1(k) \equiv \frac{3}{2}(\Psi_{22} - \Psi_{33}) + \frac{3}{2}k(\Psi_{22} - \Psi_{33})' + \mathcal{D}\Theta_{11} \quad (2.126)$$

$$l_2(k) \equiv -\Psi_{11} - 7\Psi_{22} + k\Psi_{11}' + 7k\Psi_{22}' + k^2\Psi_{11}'' - 3k^2\Psi_{22}'' \quad (2.127)$$

$$r_2(k) \equiv -\frac{7}{2}(\Psi_{22} - \Psi_{33}) + \frac{7}{2}k(\Psi_{22} - \Psi_{33})' - \frac{3}{2}k^2(\Psi_{22} - \Psi_{33})'' + \mathcal{D}(\Theta_{22} + \Theta_{33}) \quad (2.128)$$

A smart combination of relations 2.123 and 2.124 is given by:

$$kl_1' - l_1 + l_2 = 10 \{ (\Psi_{11} - \Psi_{22}) - k(\Psi_{11} - \Psi_{22})' \} \quad (2.129)$$

$$= -10k^2 \partial_k \left[ \frac{1}{k} (\Psi_{11} - \Psi_{22}) \right] \quad (2.130)$$

Substitution of this relation into relations 2.123 and 2.124 yields:

$$(\Psi_{11} - \Psi_{22}) = k \int_k^\infty \frac{10}{x} \{xr'_1(x) - r_1(x) + r_2(x)\} dx \quad (2.131)$$

$$\begin{aligned} \Psi_{11} = & -\frac{3}{2}k^4 \int_k^\infty \frac{1}{x^5} \left\{ (\Psi_{11} - \Psi_{22}) + x(\Psi_{11} - \Psi_{22})' \right. \\ & \left. + \frac{1}{2}(\Psi_{22} - \Psi_{33}) + \frac{1}{2}x(\Psi_{22} - \Psi_{33})' + \frac{1}{3}\mathcal{D}\Theta_{11} \right\} dx \end{aligned} \quad (2.132)$$

After several hours of unremitting labour we find the following solutions for wavenumber spectral tensor components  $(\Psi_{11} - \Psi_{22})$  and  $\Psi_{11}$ :

$$\begin{aligned} (\Psi_{11} - \Psi_{22}) = & \frac{2}{15} \left( -k^2\Theta''_{22} + 8k\Theta'_{22} - 11\Theta_{22} + 3k \int_k^\infty x^{-4}(3x^2 + 2k^2)\Theta_{22}dx \right. \\ & \left. - k^2\Theta''_{33} + 5\Theta_{33} - 3k \int_k^\infty x^{-4}(x^2 + 2k^2)\Theta_{33}dx - k^3\Theta'''_{11} + 3k^2\Theta''_{11} - 3k\Theta'_{11} \right) \end{aligned} \quad (2.133)$$

$$\begin{aligned} \Psi_{11} = & \frac{-1}{15} \left( 3k^2(\Theta_{22} + \Theta_{33})'' + 3k(\Theta_{22} + \Theta_{33})' - 6(\Theta_{22} + \Theta_{33}) \right. \\ & \left. + 6k \int_k^\infty x^{-2}(\Theta_{22} + \Theta_{33})dx + 3k^3\Theta'''_{11} - 4k^2\Theta''_{11} + 4k\Theta'_{11} \right) \end{aligned} \quad (2.134)$$

Relations 2.119, 2.120, 2.121, 2.122, 2.133 and 2.134 provide us with the desired tools to get the wavenumber spectral tensor from cospectra of one-point measurements of the velocity vector. This set of relations solves part of the fundamental problem, which was formulated by Citriniti and George (1996) in their conclusion quoted in the introduction to section 2.8.

We can perform a symmetry check on our solution for  $\bar{\Psi}$ . When observe the *same* experiment in a frame of reference, rotated a quarter round the first coordinate axis, then the outcome of the experiment in the rotated frame must be closely related to the outcome in the original frame. This symmetry (which is one check for the correctness of the solution) is seen as follows:

Combination of relation 2.133 for  $(\Psi_{11} - \Psi_{22})$  and relation 2.122 for  $(\Psi_{22} - \Psi_{33})$  gives the following relation for  $(\Psi_{11} - \Psi_{33})$ :

$$\begin{aligned} (\Psi_{11} - \Psi_{33}) = & \frac{2}{15} \left( -k^2\Theta''_{33} + 8k\Theta'_{33} - 11\Theta_{33} + 3k \int_k^\infty x^{-4}(3x^2 + 2k^2)\Theta_{33}dx \right. \\ & \left. - k^2\Theta''_{33} + 5\Theta_{22} - 3k \int_k^\infty x^{-4}(x^2 + 2k^2)\Theta_{22}dx - k^3\Theta'''_{11} + 3k^2\Theta''_{11} - 3k\Theta'_{11} \right) \end{aligned} \quad (2.135)$$

We see that this expression could have been obtained directly from relation 2.133 by interchanging indices 2 and 3. Moreover, relations 2.119 for  $\Psi_{12}$  and 2.120 for  $\Psi_{13}$  transform into one another when we interchange indices 2 and 3. Relations 2.121, 2.122 and 2.134 are unchanged under this action. This concludes the check of the solution for the wavenumber spectral tensor for symmetry of the lateral coordinates.

We can now give an expression for the scalar energy per wavenumber:

$$E(k) = \frac{1}{2} \text{Trace}(\Psi(k)) \quad (2.136)$$

$$= -\frac{1}{6}k^3\Theta_{11}''' - \frac{1}{6}k^2(\Theta_{22} + \Theta_{33})'' - \frac{5}{6}k(\Theta_{22} + \Theta_{33})' + \Theta_{22} + \Theta_{33} - k \int_k^\infty x^{-2}(\Theta_{22} + \Theta_{33}) dx \quad (2.137)$$

The solution for  $\bar{\Psi}(\bar{\Theta})$  has terms which depend on third order derivatives of measured spectra. We have seen in section 3.9 that the estimation of these derivatives is a very non-trivial matter!

## 2.9 Axisymmetric turbulence

In the past studies have been conducted to axisymmetric turbulence. In this subsection we will compare the results of these studies with the relations we found in the former subsection.

Sreenivasan and Narasimha (1978) (to be referred to below as SN) have examined flow with the  $x_1$ -axis as axis of symmetry. In this case relations 2.119 to 2.122 are all four trivial. Relations 2.123 and 2.124 reduce to:

$$-11\Psi_{11} + 3\Psi_{22} - k\Psi'_{11} + 3k\Psi'_{22} = \mathcal{D}\Theta_{11} \quad (2.138)$$

$$-\Psi_{11} - 7\Psi_{22} + k\Psi'_{11} + 7k\Psi'_{22} + k^2\Psi''_{11} - 3k^2\Psi''_{22} = 2\mathcal{D}\Theta_{22,33} \quad (2.139)$$

In their article SN refer to Batchelor (1953), who has pointed out that  $\bar{\Phi}$  in this case should be of the form:

$$\Phi_{ij}(k) = A_1 k_i k_j + A_2 a_i a_j + A_3 \delta_{ij} + A_4 a_i k_j + A_5 a_j k_i \quad (2.140)$$

where  $\mathbf{a} = (1, 0, 0)$  is the axis of symmetry and where  $A_i$  are functions of  $k$  and of  $\xi$ . Symmetry in  $i$  and  $j$  and continuity can be used to show that set  $[A_i]$  contains only two independent functions. In their section 4 SN suggest that, due to this feature, it can be expected that e.g. two elements of  $[A_i]$  do not depend on  $\xi$ .

With our relations 2.28 and 2.96 we find that:

$$A_1 = \frac{3}{64\pi k^6} \left( 15\varepsilon\xi^2 - (\Psi_{11} + 7\Psi_{22})k^2 \right) \quad (2.141)$$

$$A_2 = \frac{15}{32\pi k^2} \varepsilon \quad (2.142)$$

$$A_3 = -\frac{3}{64\pi k^4} \left( 5\varepsilon\xi^2 - (\Psi_{11} + 7\Psi_{22})k^2 \right) \quad (2.143)$$

$$A_4 = A_5 = -\frac{15}{32\pi k^4} \varepsilon \xi \quad (2.144)$$

$$\varepsilon \equiv \Psi_{11} - \Psi_{22}$$

It is clear that only  $A_2$  is independent of  $\xi$ . Therefore SN's ansatz I, that both  $A_1$  and  $A_2$  do not depend on  $\xi$ , is in disagreement with relation 2.141. We also observe that  $A_1$  and  $A_2$  both

contain contributions zeroth order in  $\epsilon$ , a measure for the deviation from isotropy. This is why SN's ansatz I A, an expansion of ansatz I around isotropy, gives results which agree with Reynolds and Tucker (1975)'s "hypothetical strain model". It also explains why the discrepancy between results of ansatz I A and of Reynolds and Tucker's model increases with anisotropy. Ansatz II, in which SN put that  $A_2$  and  $A_3$  do not depend on  $\xi$ , violates our relation 2.143. It is not surprising that results obtained with ansatz II deviate strongly from those found using Reynolds and Tucker's method. Similarly we find Ansatz III ( $A_1$  and  $A_3$  independent of  $\xi$ ) to be in disagreement with both relations 2.141 and 2.143. It seems appropriate that, in their conclusion, SN suggest to make use of Ansatz I A if possible.

Lindborg (1995) was right when he made his quotation which is given in the introduction to this analysis. Only he did not take the possibilities to full extent: In his study, third order correlation tensors are examined while no closed forms are given for spectral contributions to the second-order correlations. Fortunately this left us the chance to present the unaliasing relations derived in the former subsection.

## Conclusion

In this chapter we have used a statistical approach to construct a set of six equations for the unaliasing of one-point spectra. With this set one can interpret six out of nine components of the velocity correlation spectrum. The model is restricted to weakly anisotropic, incompressible turbulence without net swirl. It is well possible that the same method can also be used to model the unaliasing of the three remaining components of the velocity correlation spectrum, which are associated with net swirl. The dependence of our relations on the third derivative of the one-point spectrum requires an estimation method for spectral derivatives. The practical applicability of our relations depends on the success of the development of such a method. This will be the subject of the following chapter. We have shown that with our unaliasing method we are able to interpret the performance of an axisymmetric turbulence model in a broader context.



# Chapter 3

## Estimation of spectra and spectral derivatives

### Introduction

The main topic of this chapter is to develop a method to estimate spectra and spectral derivatives from measured time-series. These functions are the keys to the practical application of the unaliasing relations for one-point spectra, which we constructed in chapter 2.

In physics a great many theories exist that use expansions of signals in periodic base-functions and in chapter 2 we have done our utmost to construct our own contribution. The scientist who thinks that the introduction of spectra in his or her analysis provides a simple way to benefit from the merits of periodic functions without further ado, is mistaken. When trying to compare theory with measurement he or she is confronted with an often neglected field of research: sampling theory.

We will determine criteria for experiments such that spectral estimates can be reliably calculated from measured data. Emphasis is put on the estimation of the power spectrum. We will review the influence on the spectral estimates resulting from taking finite, discrete sets of samples from a continuous signal. In sections 3.5, 3.6 and 3.7 three different methods from literature to estimate the cospectrum will be presented: Smoothing of a periodogram (obtained via Fast Fourier Transform), autoregressive modelling and moving average modelling. In section 3.8 a comparison of these methods will be made, based on data from representative turbulence measurements. Application of these methods to the estimation of derivatives up to third order of the spectrum will be discussed in section 3.9.

### 3.1 Time-spectra and basic notation

With Taylor's hypothesis 1.13 we will be able to estimate spatial spectra (for which we have developed our unaliasing relations in the former chapter) via time-spectra of one-point measurements. Therefore in this chapter we will be concentrated on the analysis of time-series.

The relations between a signal  $f(t)$  ( $-\infty < t < \infty$ ), which is continuous in time, and its **Fourier transform**  $F(\omega)$  are known in principle (see section 2.2 about spectral analysis):

$$f(t) = \int_{-\infty}^{\infty} F(\omega) e^{i\omega t} d\omega \quad \Leftrightarrow \quad F(\omega) = \frac{1}{2\pi} \int_{-\infty}^{\infty} f(t) e^{-i\omega t} dt \quad (3.1)$$

We will use symbol  $\mathcal{F}$  to indicate the Fourier transform of its argument. Capital letters are used to represent the Fourier transforms of the respective lower case letters.

The squared amplitude of the Fourier transform of a signal is usually called a **periodogram**.

In this chapter symbol  $*$  will denote the **convolution** of two functions:

$$(f * g)(t) \equiv \int_{-\infty}^{\infty} f(\tau) g(t - \tau) d\tau \quad (3.2)$$

We will use the so called "convolution theorem" from Fourier analysis, which states that the convolution of two functions and the product of their Fourier transforms are related to one another via Fourier transform:

$$\mathcal{F}(f * g) = FG \quad f * g = \mathcal{F}^{-1}(FG) \quad (3.3)$$

The **correlation** of two functions is defined to be:

$$\text{Corr}(f, g)(t) \equiv \int_{-\infty}^{\infty} f(\tau) g(\tau - t) d\tau \quad (3.4)$$

Application of the convolution theorem to correlation function 3.4 gives:

$$\mathcal{F}(\text{Corr}(f, g)) = FG^* \quad \text{Corr}(f, g) = \mathcal{F}^{-1}(FG^*) \quad (3.5)$$

Here superscript  $*$  is used to denote the Hermitian conjugate (= complex conjugate plus transpose). Superscript  $t$  will be used to denote the transpose.

The correlation tensor  $\bar{R}$  of vector function  $\mathbf{u}(t)$  is defined to be:

$$\bar{R}(\tau) \equiv \mathcal{E} \left( \mathbf{u}(t) \otimes \mathbf{u}^t(t - \tau) \right) \quad (3.6)$$

where the **expectation value** (symbol  $\mathcal{E}$ ) is obtained by proportional averaging over all possible stochastic realizations, i.e. all realizations are weighted with their probability.

The **Cospectral tensor**  $\bar{\Phi}$  is defined to be the Fourier transform of the correlation tensor:

$$\bar{\Phi} \equiv \mathcal{F}(\bar{R}) \quad (3.7)$$

The taking of the expectation value and Fourier transformation are both linear operations. Consequently, under conditions that the Fourier transform exists, we can interchange the Fourier transform in the definition of the cospectral tensor and the expectation value in the definition of the correlation function. Formally this reasoning is incorrect for infinite ranges, because the expectation value does not exist, but in practice we will encounter "just very large sets", for which the reasoning holds. As a result we can rewrite relation 3.7 for the cospectral tensor to:

$$\bar{\Phi} = \mathcal{E} \left( \mathcal{F} \left( \mathbf{u}(t) \otimes \mathbf{u}^t(t - \tau) \right) \right) \quad (3.8)$$



which via a homogeneity assumption can be shown to be equivalent to:

$$\bar{\Phi} = \mathcal{E} \left( \mathbf{F}(\omega) \otimes \mathbf{F}^t(\omega) \right) \quad (3.9)$$

For scalar functions the cospectral tensor is called the **spectral density function** (symbol  $h(\omega)$ ). In the following sections much effort is spent on the estimation of the cospectral tensor.

A **stationary stochastic process** is a process with a certain randomness of which the statistical properties do not change over time.

In the rest of this chapter we will assume that the generation of turbulence signals is a stationary stochastic process.

## 3.2 Selection of analogue filter- and sampling frequency

In the introduction to this chapter we mentioned that practical application of spectral analysis is non-trivial. This originates from the following: *To calculate the spectrum of a signal via relation 3.1, one has to integrate the signal with infinite accuracy over an infinite domain.*

Most processes in physics are continuous in nature. Modern measuring techniques however sample such continuous processes at regular intervals. As a consequence the infinite amount of information between two sampling points of a continuous process  $f(t)$  is replaced by only one data point, giving the value of the quantity at one instant (or averaged over some suitable time period depending on the experimental set-up).

When instantaneous values are sampled, aliasing occurs. This is the leaking of high frequency components into low frequency components. To eliminate the aliasing problem, one has to apply a low-pass filter and carefully select the sampling frequency. We will give suggestions for analogue filter cut-off- and sampling frequencies.

The highest frequency component in a signal which can be estimated from a set of discrete samples taken of the signal is half the sampling frequency  $\omega_{\text{sampling}}$ :

$$\omega_{\text{estimate}} \leq 0.5 \omega_{\text{sampling}} \quad (3.10)$$

This is called the Nyquist criterion. Due to this criterion the energy of components in the signal of frequencies higher than half the sampling frequency is folded into low-frequency components (see Priestley (1981, p. 224)). If the energy in the signal at these high frequencies is large, then the folded energy spoils the estimates of the low-frequency components of the spectrum. This aliasing effect is demonstrated in figures 3.1 and 3.2. To make sure that no relevant information is lost in the digitisation process of a continuous signal, one has to take the following steps:

1. Estimate the highest relevant frequency  $\omega_{\text{highest}}$  present in the continuous signal.
2. To prevent aliasing of high frequency components use analogue low-pass filtering with cut-off frequency  $\omega_{\text{cut-off}}$  (to be determined). Due to Nyquist criterion 3.10, the sampling frequency has to be higher than twice the cut-off frequency of the analogue filter, which in its turn has to be higher than  $\omega_{\text{highest}}$ . We adopt relations between highest relevant frequency, analogue filter cut-off frequency and sampling frequency. Our choice for the

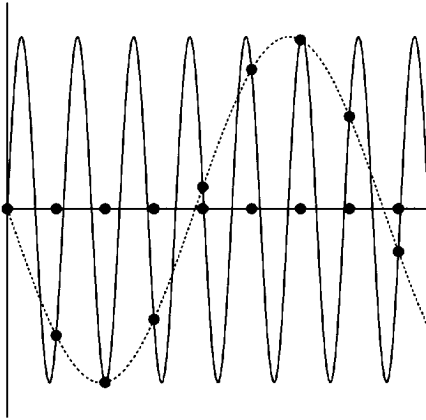


Figure 3.1: Undersampling of a sine-wave yields a wave with lower frequency.

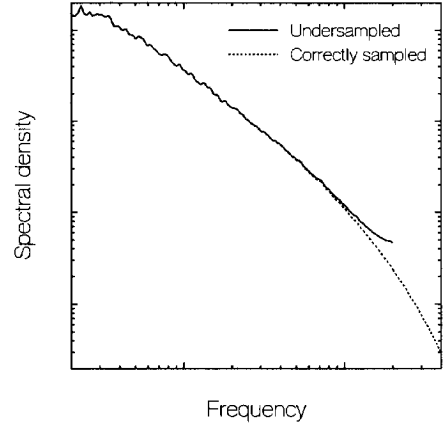


Figure 3.2: Double logarithmic plot of two spectra of the same signal; the dashed line shows the true spectrum, the thick line shows the spectrum after undersampling the signal with a factor five. The energy contained in the overshoot of the spectrum of undersampled data equals the energy which is present in the high frequency spectral segment of the correctly sampled data and which is missed by the undersampled dataset.

relation between highest and cut-off frequencies is obvious: they must obey the Nyquist criterion. At the cut-off frequency the signal is not yet fully set to zero by the filter. Therefore the sampling frequency is taken to be larger than twice the cut-off frequency. A larger factor than say three would lead to enormous amounts of data to be stored in an experiment, due to oversampling. A factor smaller than two would not be sufficient for the filter to have dropped off to a low value. The factor 2.5, which we adopt, is a compromise between data storage and noise suppression, which has shown to be good in practical situations.

$$\text{cut-off} = 2 \omega_{\text{highest}} \quad \text{Nyquist criterion} \quad (3.11)$$

$$\omega_{\text{sampling}} = 2.5 \omega_{\text{cut-off}} \quad \text{cutting range for filter} \quad (3.12)$$

$$\Rightarrow \omega_{\text{sampling}} = 5 \omega_{\text{highest}} \quad (3.13)$$

From this point we will assume that the signal has been sampled such that the effect of aliasing has been eliminated.

### 3.3 Consequences of finite sets of samples

To find the cospectral tensor with infinite accuracy, we need the correlation function on an infinite support. To find *all possible* correlations on an *infinite* domain, we need to have an

infinitely long and infinitely dense set of samples. In reality one will only have countable sets of finite lengths. This will allow for the calculation of correlations up to a limited delay. Consequently we can estimate only the central part of the correlation function. In this section we will derive the relation between the Fourier transform of the full correlation function and the Fourier transform of only the central (or *windowed*) part of the correlation function.

### 3.3.1 The effect of correlation function windowing

We cut off the correlation function (defined on  $t \in (-\infty, \infty)$ ) at the ends such as to include only correlations up to a certain delay. This is done by multiplication of the full correlation function with a window function  $w_\alpha(t)$ . The window is centred around  $t = 0$  and has half width  $\alpha$ . The Fourier transform of window  $w(t)$  is called  $W(\omega)$ .

With use of relation 3.3 for the Fourier transform of a product we find:

$$\mathcal{F}(\bar{R}w_\alpha) = \bar{\Phi} * W_\alpha \quad (3.14)$$

The full cospectrum is convolved against the Fourier transform of the window. This effect is also known as *spectral leakage*: the information which should be found at frequency  $\omega$  is smeared out over a neighbourhood of  $\omega$ , where the size of this neighbourhood is determined by the width of the Fourier transform of the window. We now understand that the finiteness of a set of samples intrinsically leads to spectral leakage in the spectral estimates. This is important to keep in mind when we will be selecting a record length for an experiment with prescribed spectral resolution.

### 3.3.2 Different windows

In this subsection we give some examples of often used pairs of window functions, related via Fourier transform (non-normalised functions are given. The width of spectral window  $W(\omega)$  is seen to vary with the reciprocal of the width  $\alpha$  of correlation window  $w(t)$ . Plots are drawn in figures 3.3 and 3.4).

$$\begin{array}{lll} w_\alpha(t) = e^{-3\frac{t^2}{\alpha^2}} & & \Longleftrightarrow W_\alpha(\omega) = e^{-\frac{1}{12}\omega^2\alpha^2} \\ w_\alpha(t) = \begin{array}{l} 1 \\ 0 \end{array} & \begin{array}{l} \text{for } t \in (-\alpha, \alpha) \\ \text{otherwise} \end{array} & \Longleftrightarrow W_\alpha(\omega) = \frac{\sin(\omega\alpha)}{\omega\alpha} \equiv \text{sinc}(\omega\alpha) \\ w_\alpha(t) = \begin{array}{l} (1 + \cos(\pi t/\alpha))/2 \\ 0 \end{array} & \begin{array}{l} \text{for } t \in (-\alpha, \alpha) \\ \text{otherwise} \end{array} & \Longleftrightarrow W_\alpha(\omega) = \frac{\text{sinc}(\omega\alpha)}{\left(1 - \left(\frac{\omega\alpha}{\pi}\right)^2\right)} \end{array} \quad (3.15)$$

From figures 3.3 and 3.4 we see that a square window gives strongly oscillating contributions from correlations at larger delays. Among the smooth windows there is no best choice. Their effects are pretty much the same. We see that those windows in time space which give rise to a narrower central peak in the spectral space simultaneously induce stronger side-lobes (in the spectral space). Since goniometric functions are difficult to compute, we use the following

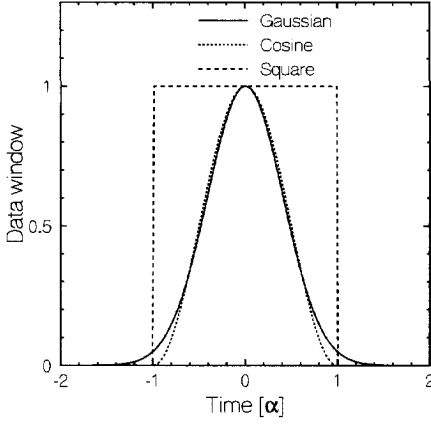


Figure 3.3: Window functions; the functional space on which these windows and their Fourier transforms live respectively can be interchanged by Fourier transform.

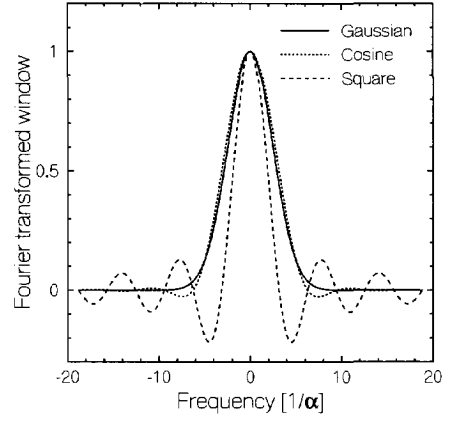


Figure 3.4: Fourier transforms of window functions.

window:

$$W_{\alpha, \omega_0}(\omega) = \begin{cases} (1 - ((\omega - \omega_0)\alpha)^2)^2 & \text{for } |\omega - \omega_0| \leq \alpha^{-1} \\ 0 & \text{otherwise} \end{cases} \quad (3.16)$$

This fourth power window resembles closely the cosine window and the transform of this fourth power window resembles closely the transform of the cosine window (which is why we do not show this function in a graph). The Fourier transform of the window in definition 3.16 (which lives on the same space as correlation functions) has few side-lobes. We therefore adopt this window.

Once we will know which spectral leakage will be allowed, then we will know which minimal window width must be taken.

### 3.4 Allowed spectral leakage for turbulence measurements

This section we will study the effect of spectral leakage in more detail for the analysis of turbulence signals. Let us call  $M$  the maximum delay up to which we want to have the correlation function, and  $\omega$  the angular frequency of the wave for which we are estimating the cospectral tensor. We will show that, in the processing of turbulence signals,  $M$  depends on  $\omega$ . Restricting the correlation function to delays smaller than  $M$  is called windowing. We will show that we can postpone this windowing from direct application to the correlation function until after we have taken its Fourier transform. This step will be useful in the application of windows with different widths.

### 3.4.1 Correlation function window width for turbulence

In turbulent flow waves of a certain wavelength are assumed to be associated with coherent structures of sizes comparable with that wavelength (Tennekes and Lumley, 1972). In non-periodic flow coherent structures have finite correlation lengths. Finiteness of the correlation lengths of the coherent structures means that in a turbulent time signal  $f(t)$  independent realizations of structures with period  $T$  can be found in segments of the signal which contain a number  $N_\alpha$  of wave periods:

$$N_\alpha T = \frac{2\pi N_\alpha}{\omega} \quad (3.17)$$

This means that the delay, up to which one has to estimate the correlation function, depends on the frequency (range) of the spectrum, which one wants to estimate.

The estimate for the cospectral tensor is now made as follows:

- Use the second relation in correlation theorem 3.5 to calculate the correlation tensor  $\bar{\bar{R}}(t)$  of a very long dataset. This means that we Fourier transform the complete vector signal's components, make all nine products of these Fourier transforms with their complex conjugates, and transform back.
- Now for each frequency  $\omega$  at which we want to estimate the cospectrum we cut off the edges of the correlation function (by application of a window) such that only correlations are considered up to a delay which is *a fixed number times the period of the respective wave*.

$$\bar{\bar{R}}(t) \rightarrow w_{\alpha,\omega}(t)\bar{\bar{R}}(t) \quad (3.18)$$

$$\text{width}(w_{\alpha,\omega}(t)) \equiv \alpha(\omega) = N_\alpha T(\omega) = \frac{2\pi N_\alpha}{\omega} \quad (3.19)$$

- Fourier transform these windowed correlation functions using the following relation:

$$\bar{\bar{\Phi}}(\omega) = \mathcal{F}(w_{\alpha,\omega}(t)\bar{\bar{R}}(t))(\omega) \quad (3.20)$$

This is just one way to estimate the cospectral tensor. A different method, which is often used, is the following:

- Cut the original dataset into subsets to form 'independent realizations'.
- Fourier transforms of these realizations are averaged to get an estimate for the cospectral tensor.

This latter method to estimate the spectrum is less accurate than the former method outlined in this subsection. The reason for this difference is that in the former method many more products of delayed signals contribute to the estimate than in the latter. In the latter method sample products are only used when a delayed couple of samples belongs to one subset; in the former method all possible delayed couples are used.

We see from relation 3.19 that the width of the correlation window depends on the reciprocal of the frequency of the respective estimate. Methods like Fast Fourier Transform are not capable of handling variable window width. This is the reason why in the following subsection we will show how windowing of the correlation function can be postponed until after its Fourier transform has been calculated.

### 3.4.2 Postponing correlation function windowing

We will now show a way to circumvent the problem mentioned at the end of the previous subsection that FFT cannot handle variable window widths.

Assume that there are no periodic effects in the flow or other non-turbulent, spectrally sharply peaked, contributions to the signal. Via the interpretation of spectral leakage given at the end of subsection 3.3.1, we can postpone the cutting off of the correlation function until we have calculated the Fourier transform of the non-windowed correlation function. To get the desired periodogram from the Fourier transformed full correlation function we convolve the periodogram of the full correlation function against a Fourier transformed window (relations 3.15):

$$\bar{\Phi}(\omega) = \mathcal{F}(\bar{\mathcal{R}}) * W(\alpha, \omega) \quad (3.21)$$

In the previous subsection we used correlation theorem 3.5 to calculate correlation tensor  $\bar{\mathcal{R}}(t)$ . This meant that we calculated the Fourier transform of the very long vector signal, made products and transformed back. In this subsection we have found that windowing can be postponed until after the correlation function has been Fourier transformed without any windowing. Therefore two actions of Fourier transforming cancel in the cospectrum estimation process given in this subsection, and consequently can be left out: The smoothing operation can be applied directly on the products that are formed after the first Fourier transform has been taken of the complete dataset.

In the previous subsection we saw that for turbulence signals window width  $\alpha$  varies with the reciprocal of  $\omega$ . The width of the band over which the large spectrum is to be smoothed using relation 3.21 (to mimic the effect of wavelength dependent correlation cut-off) is the inverse of the width of the window given by relation 3.19. As a consequence the spectral window width is a constant fraction of the angular frequency at which the estimate is calculated:

$$\text{width}(W_\alpha(\omega)) = \frac{\omega}{2\pi N_\alpha} \quad (3.22)$$

This means that in a plot with logarithmic frequency axis, the window, against which the raw spectrum is convolved for smoothing (we will use the window of definition 3.16), has constant width. Smoothing will only be justified if the underlying actual spectrum has no structure in the interval over which the smoothing is carried out. This is the reason why at the start of this subsection we have made the assumption that the signal contains no periodic contributions (which would give narrow peaks in the spectrum).

The relation between the methods to construct estimates for the cospectral tensor given in this and in the previous subsection is schematically drawn in figure 3.5. An intuitive way to see why waves correlate up to a delay which is a number of times their wavelength and thus why

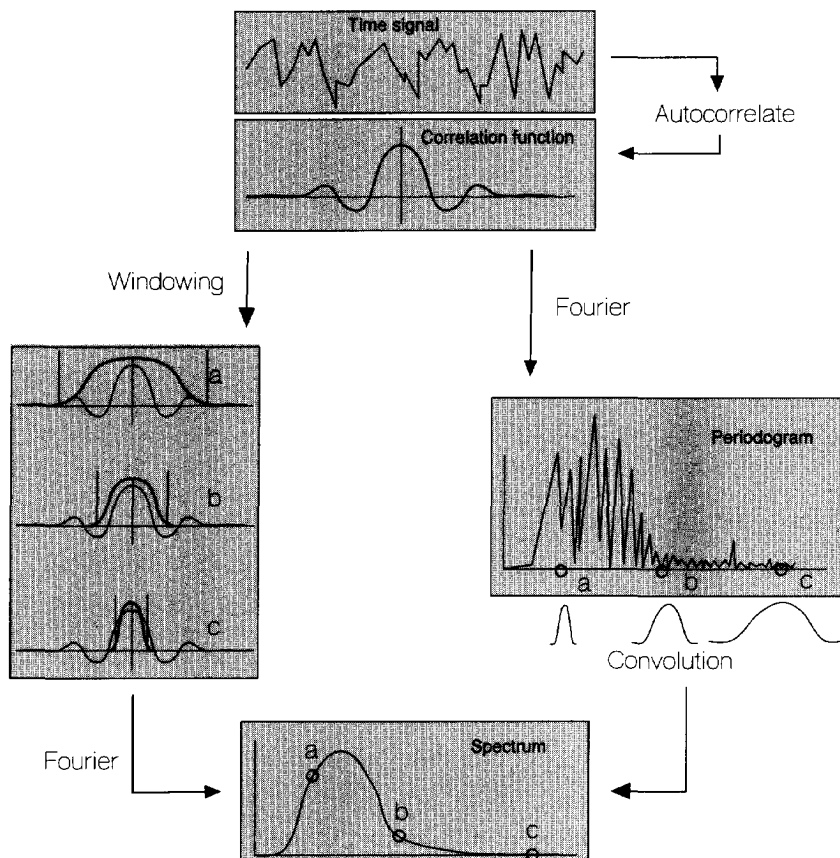


Figure 3.5: Two equivalent ways to estimate a spectrum

turbulence researchers use logarithmic frequencies is the following: Interactions in a turbulent flow between structures with comparable sizes tend to be more non-linear than interactions between structures with dimensions of different orders of magnitude. A logarithmic frequency sorts the spectral information by order of magnitude. Consequently smoothing windows for cospectra with width proportional to the frequency are used (Uittenbogaard, 1995).

Turbulence spectra can contain independent information in frequency ranges down to a certain bandwidth. An estimate for this bandwidth is given in relation 3.22. We conclude that:

In turbulent spectra (free from spectrally peaked, resonant contributions) the amount of possible independent local bandwidths is constant for frequency ranges where the bounding frequencies differ by a constant factor. In other words: the best way to look at turbulence spectra uses a logarithmic frequency axis.

### 3.5 Cospectral tensor estimation via Fast Fourier Transform

In section 3.4 we have presented two different ways to come from a large dataset  $\mathcal{D}$  to an estimate for the cospectrum via a Fourier transform. Efficient Fourier transform procedures calculate spectral values at a whole range of frequencies in one call. The width of the window is then restricted to a fixed value. Therefore we prefer the method to make cospectral estimates outlined in section 3.4.2 (smoothing of a large periodogram) to the method of section 3.4.1 (windowing of the correlation function with a specific window for each frequency separately, and calculation of the Fourier integral for each windowed correlation function). In this section we will outline some important steps in a popular method to calculate Fourier integrals: via Fast Fourier transform (FFT).

FFT is an efficient method to calculate Fourier transforms. (see Priestley (1981, p.575) for a detailed description). An important step in the FFT is that the dataset is considered to be periodic on the finite interval. This wrapping of the head to the tail induces an artificial jump in the signal, which in its turn calls for the need of many high wavenumber contributions to the Fourier transform. This unwanted effect will be addressed in this section.

#### 3.5.1 High-pass filtering

There is one effect which particularly leads to unwanted high frequency contributions in an FFT-based spectrum: the presence of contributions to a signal which fluctuate on a timescale longer than the total length of the data record. These slow variations give the dataset of a stationary signal a non-stationary appearance and induce a strong jump when FFT glues the signal's head to it's tail. To make sure that a signal is stationary on the timescale of the available dataset we have to detrend or high-pass filter it.

To achieve high-pass filtering we fit a polynomial through the dataset, and subtract this polynomial from the dataset. Application of a zeroth order polynomial subtracts the mean value from a dataset. If we use a first order polynomial, then we get linear trend correction. In general, subtraction from a signal of an  $n$ -th order polynomial can remove  $n - 1$  macroscopic bendings from the signal. A sinusoidal function has two bendings per period. In this study degree  $n$  is



given value 6, a choice which is motivated as follows: in this way we can remove 5 bendings from a dataset, which corresponds with two and a half period of a sinusoidal wave. Most of the contributions to the signal coming from waves with a wavelength, which is larger than  $2/5$  of the length of the record can thus be eliminated from the signal. To our opinion waves with a shorter wavelength than  $2/5$  of the record length will not be interpreted erroneously as a non-stationary contribution to the signal. The effect of high-pass filtering is shown in figures 3.6, 3.7 and 3.8, where a signal is shown both before and after detrending.

During the rest of this section we will assume that the dataset has been detrended. Naturally no spectral estimates can be given below the cut-off frequency of the high-pass filter.

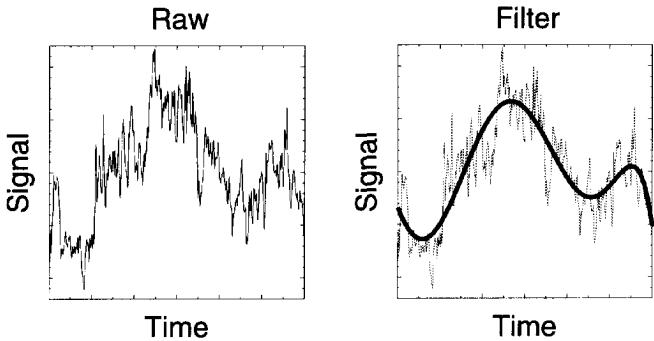


Figure 3.6: Preprocessing of data: the raw signal.

Figure 3.7: A highpass filter of sixth order.

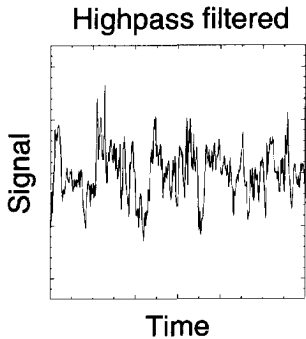


Figure 3.8: Dataset after highpass filtering.

### 3.5.2 Data windowing

After the signal has been detrended, the values of the signal at the head and at the tail are nearly equal. The exact matching of head and tail is accomplished by multiplication of the signal with a so called *tapering window*  $w(x)$ , which goes to zero at the first and last part of the signal. We already have discussed the need to apply a window to the correlation function (see subsection 3.4) (but had decided to replace this operation by convolution in the spectral space). Here we see that there are two stages of windowing in the process of spectral estimation of turbulence signals.

When a taper is used, which pushes the function to zero over a large portion of the dataset, then a substantial part of the data is lost due to this action. Nevertheless we have to window the dataset, to make it possible for the FFT to consider the data to be periodic, without causing large jumps to occur from one end of the data to the other end. To reduce data-loss to a minimum we here look for a tapering window which leaves intact (i.e. un-tapered) the broadest possible central part of the dataset that still will allow us to wrap the dataset without introducing a macroscopic step.

After the signal has been detrended, the longest wavelength that can be found in the signal is  $2/5$  of the record-length. We consider a quarter of one period of a sine wave to be the shortest segment of a sine, which still displays the "jumping power" of a periodic function: in a quarter of a period a sine wave (with unit amplitude) can have a maximum difference in value of 1.4; for smaller segments the maximum difference in value decreases linearly to zero.

The largest delay over which we can thus expect to find steps in the high-pass filtered signal is one quarter of the high-pass filter's cut-off period. In our case (sixth order polynomial) this corresponds with a delay equal to  $1/10$  of the length of the record. We therefore take a square window (most of the time equal to 1) which is rounded off towards zero at the ends by half a period of a cosine function. The portion of the data which is smoothly forced to zero is taken to be ten percent of the record length. The effect of data windowing is shown in figures 3.9, 3.10 and 3.11.

An example of the method presented in this section to estimate the cospectrum of a turbulent velocity signal is shown in figures 3.12 and 3.13.

### 3.5.3 Error estimation of spectral density

In this subsection we will calculate how many data samples  $N$  must be taken in an experiment to estimate with a certain accuracy the spectral density via smoothing of the single periodogram of the complete dataset. Suppose we want to find an estimate for the spectral density with accuracy  $\beta$  and with upper bound for the relative spectral leakage  $\Gamma$  (bandwidth as a fraction of the frequency). The value for  $\Gamma$  must still be specified. We adopt  $\Gamma = 0.2$ , which is a practical compromise between narrow bandwidth (more information about the spectrum) and available data storage capacity (narrower bandwidth would require more data than our system can handle). We call the lowest interesting frequency in the signal  $f_{\text{lowest}}$ . Let the sampling frequency be  $f_{\text{sampling}}$ .

The standard deviation in the unsmoothed periodogram of one realization equals its expectation

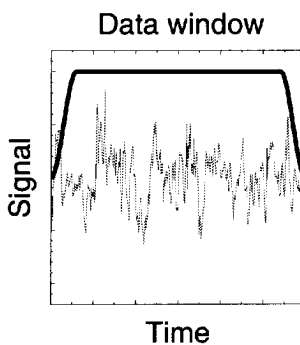
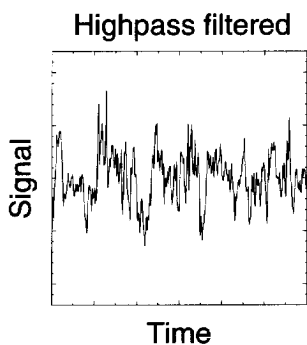


Figure 3.9: Preprocessing of data:  
filtered signal.

Figure 3.10: Data window.

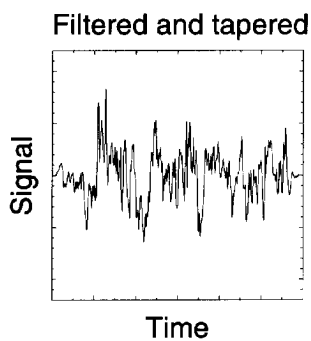


Figure 3.11: Signal after window-  
ing.

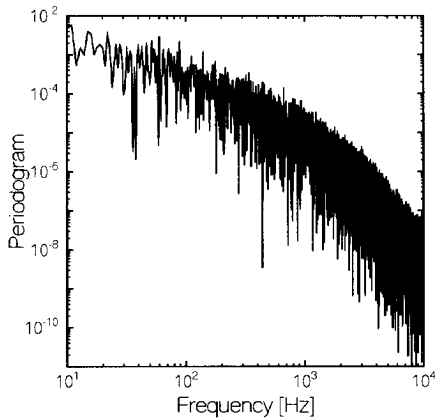


Figure 3.12: Estimation of spectral density via periodogram: periodogram of a dataset.

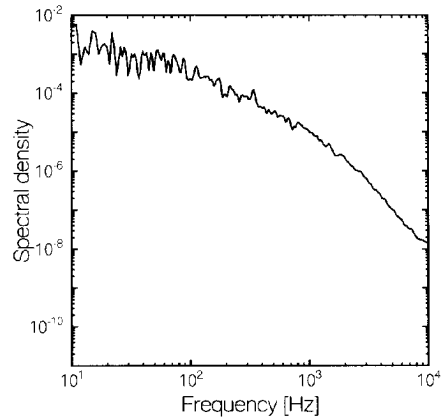


Figure 3.13: The same periodogram after smoothing.

value (Priestley, 1981, p.454), i.e. the error in one realization of the spectrum is 100%.

The lower the frequency, the less a spectral estimate is affected/improved by the smoothing operation which is performed on the periodogram to get the spectral density. Therefore, to get the desired accuracy over the whole desired spectral range, we must take number of samples  $N$  such that (after smoothing) the estimate for the spectral density at  $f_{\text{lowest}}$  has accuracy  $\beta$ . Then this accuracy will also be met by spectral estimates at higher frequencies.

In the action of smoothing, the periodogram is convolved against a bell-shaped window (e.g. the taper defined in relation 3.16), which at  $f_{\text{lowest}}$  contains say  $m$  other spectral values. To get accuracy  $\beta$  in the spectral density, there must be  $m = \beta^{-2}$  spectral estimates within the smoothing window in the spectral space at  $f_{\text{lowest}}$ . This number of spectral estimates  $m$  that can be found in the periodogram within the convolution-bell around  $f_{\text{lowest}}$  is related to the width of the bell (given by the imposed absolute spectral leakage (at the lowest interesting frequency)  $\Gamma f_{\text{lowest}}$ ) and frequency increment  $\Delta f$  between neighbouring spectral estimates in the FFT-based periodogram:

$$m = \frac{\Gamma f_{\text{lowest}}}{\Delta f} = \beta^{-2} \quad (3.23)$$

$\Delta f$  is of course given by the ratio of sampling frequency  $f_{\text{sampling}}$  and the number of samples  $N$  in the dataset:

$$\Delta f = \frac{f_{\text{sampling}}}{N} \quad (3.24)$$

(e.g. The FFT of 20000 samples taken at 500 Hz yields spectral values at every  $500/20000 = 0.025$  Hz)

Substitution of relation 3.24 for the frequency increment into relation 3.23 for the number of spectral estimates in the smoothing bell gives the following relation for the necessary number

of samples to be collected in an experiment to get the desired accuracy in the spectrum:

$$N = \frac{f_{\text{sampling}}}{f_{\text{lowest}}} \frac{1}{\Gamma\beta^2} = 5 \frac{f_{\text{highest}}}{f_{\text{lowest}}} \frac{1}{\Gamma\beta^2} \quad (3.25)$$

The latter equation follows by virtue of relation 3.13.

An accuracy of 10% in a situation where the relevant frequency range is (5Hz, 4kHz) and where 20% spectral leakage is allowed thus requires the taking of  $2 \cdot 10^6$  samples at 20 kHz.

### 3.6 Spectral density estimation via autoregressive modelling

A disadvantage of the method described in the former section to estimate the spectral density is that the estimate is not given in functional form. This can make it difficult to estimate derivatives of the spectral density. To circumvent this problem we will study an alternative method to estimate the spectral density of a stationary stochastic process: via a so-called autoregressive model (AR). The essence of autoregressive modelling is to model the difference between the spectrum of the signal and the spectrum of white noise by assuming that the signal has a memory. This memory will be represented by letting samples be related to previous samples via a set of linear dependences using memory coefficients  $A_i$  (related to the correlation function). The part of the signal which is not accounted for by these memory functions, i.e. the random part, is modelled using white noise  $\epsilon_t$ . Using this concept we can write for a three-dimensional signal  $\mathbf{u}_t$  (the signal is assumed to have zero mean):

$$\mathbf{u}_t = \epsilon_t - \bar{A}_1 \cdot \mathbf{u}_{t-1} - \bar{A}_2 \cdot \mathbf{u}_{t-2} - \dots - \bar{A}_n \cdot \mathbf{u}_{t-n} \quad (3.26)$$

Covariance function  $\bar{\Sigma}$  of white noise part  $\epsilon$  is defined via the following observation:

$$\mathcal{E} \left( \epsilon_t \otimes \epsilon_{t-\tau}' \right) (\tau) = \mathcal{E} \left( \epsilon_t \otimes \epsilon_t' \right) \delta(\tau) \equiv \bar{\Sigma} \delta(\tau) \quad (3.27)$$

Notice that tensor  $\bar{\Sigma}$  does not depend on delay  $\tau$ .

In the following subsection we will give a criterion for the stability of autoregressive models. Then we will give a criterion to estimate up to which order an autoregressive model is significant, i.e. discernable from white noise. In the two following subsections we will present methods to extract coefficients  $\bar{A}_i$  from a given time series. These coefficients are related to the auto- and cross-spectra of the signal. In contrast with the results of FFT-estimates, the spectral estimates found via AR give a functional representation and thus provide information concerning the *shape* of the spectrum.

#### 3.6.1 Stability criterion for AR-models

Not every combination of autoregressive memory coefficients  $\bar{A}_i$  give a stationary stochastic process. For certain combinations of coefficients, it may happen that the corresponding autoregressive model diverges (i.e. the process goes to plus or minus infinity). An example: a one dimensional model with  $n = 1$ ,  $A_1 = -10$  and  $\Sigma = 10^{-10}$  will let a signal increase from timestep

to timestep by an order of magnitude.

Before we formulate the stability criterion, we introduce the (complex valued) **characteristic polynomial**  $p(z)$  associated with an ( $n$ -th order) AR-model (parameter  $z$  is a complex number):

$$p(z) \equiv z^n + \sum_{j=1}^n A_j z^{n-j} = \sum_{j=0}^n A_j z^{n-j} \quad (3.28)$$

$$A_0 \equiv 1 \quad (3.29)$$

A necessary and sufficient condition for an autoregressive model to be stable (see Priestley (1981) for a derivation of this criterion) is that all  $n$  roots of it's characteristic polynomial  $p(z) = 0$  are found inside the unit circle  $|z| \leq 1$ . This criterion will be used in the following sections to assess stability of AR-models that are reconstructed from datasets.

### 3.6.2 Order estimation for AR-processes

Suppose one has calculated all AR-memory tensors  $\bar{A}_{j=1..\tilde{n}}$  up to order  $\tilde{n}$ -th for a signal  $\bar{u}_i$ . (One has to take  $\tilde{n}$  larger than the order  $n$  which one expects the final model will have). In this subsection we will give a criterion for the highest order  $n \leq \tilde{n}$  in the AR-process, which is significantly discernable from white noise (i.e. the probability, that the differences between estimates made with this  $n$ -th order model and the true dataset is to be attributed to effects of autoregressive coefficients of order higher than  $n$ , is smaller than the probability, that they find their origin in pure white noise).

First we calculate the (squared) residuals  $\text{Res}_j$  for all AR-models of order  $0 \leq j \leq \tilde{n}$ :

$$\text{Res}(j) \equiv \mathcal{E} |\mathbf{u}(t) - \mathbf{u}_{j\text{th}}(t)|^2 \quad (3.30)$$

In this relation symbol  $\mathcal{E}$  is used to denote the average over the dataset and  $\mathbf{u}_{j\text{th}}(t)$  is the  $j$ -th order estimate for signal  $\mathbf{u}(t)$  calculated via relation 3.26, using the first  $j$  memory tensors from the  $\tilde{n}$ -th order estimate:

$$\mathbf{u}_{j\text{th}}(t) \equiv -\bar{A}_1 \cdot \mathbf{u}_{t-1} - \bar{A}_2 \cdot \mathbf{u}_{t-2} - \dots - \bar{A}_j \cdot \mathbf{u}_{t-j} \quad (3.31)$$

Broersen (1998) has shown that if one wants to use AR-coefficients for the estimation of the spectral density then one should use as maximum significant order the order  $i$  at which the following function (named Cic) has its minimum value:

$$\text{Cic}(i) \equiv \ln \left( \frac{\text{Res}(i)}{\text{Res}(0)} \right) + \text{Max} \left( p \sum_{j=1}^i V(j), -1 + \prod_{j=1}^i \frac{1+V(j)}{1-V(j)} \right) \quad (3.32)$$

where

$$p = 3 \quad (\text{penalty factor})$$

$$V(j) \equiv \frac{1}{\tilde{n} - j + 1} \quad (3.33)$$

Under the assumption that the order  $i$  of the model is much smaller than the number of samples  $n$ , this criterion can be simplified to the so called Gic-criterion:

$$\text{Gic}(i) \equiv \ln \left( \frac{\text{Res}(i)}{\text{Res}(0)} \right) + \frac{3i}{\tilde{n}} \quad (3.34)$$

In this study we adopt the Cic-criterion for AR-processes.

### 3.6.3 Determination of AR coefficients via the Yule-Walker method

There is a simple mathematical solution for the problem of finding AR-coefficients from a given time series. This method is called the Yule-Walker method (YW). In this subsection we will present this method because of it's simplicity and to elucidate certain details in the problem of reconstructing AR-coefficients. The YW-method is based on the following idea:

Take the expectation value of the tensor product of relation 3.26 for the sample with number  $t$  with the transpose of signal having sample number  $t - m$  (for any non-negative integer  $m$ ). We thus get the so called Yule-Walker equations:

$$\sum_{i=0}^n \bar{A}_i \cdot \bar{R}(m-i) = 0 \quad \text{for } 0 < m < \infty \quad (3.35)$$

$$\sum_{i=0}^n \bar{A}_i \cdot \bar{R}(-i) = \bar{\Sigma} \quad \text{for } m = 0 \quad (3.36)$$

Correlation function  $\bar{R}(\tau)$  was defined in relation 3.6.

Yule-Walker equations 3.35 and 3.36 are linear in autoregressive coefficients  $\bar{A}_i$ . To find the coefficients of an  $n$ -th order autoregressive model, one must generate at least  $n$  Yule-Walker equations. These equations are found by letting  $m$  in relation 3.35 take values  $m = 1, 2, \dots, n$ . The white noise's covariance is found with use of equation 3.36 found with  $m = 0$ . More than  $n$  equations will make an overdetermined system, which will have to be solved using least squares methods. The maximum delay of correlations  $\tilde{n}$  which we will use in the Yule-Walker method to solve the autoregressive parameters is determined visually from a graph of the correlation function. For each component of the correlation tensor the delay is taken beyond which the correlation function starts to look noisy. Incorporation of correlations for delays longer than this point would force the Yule-Walker system to spend all its force to model the wiggles in the far zone of the correlation function, where the original signal has only weak correlation. This would render the Yule-Walker method an inadequate method to find the lower order AR-coefficients accurately. To solve this problem, beyond the delay which was determined from the graph the correlation function is set to zero, i.e. correlations with longer delays are not used. This characterises the maximum delay used in Yule-Walker models.

We have tested the Yule-Walker method as follows: We used relation 3.26 and some randomly chosen coefficients  $A_i$  to make third-order (i.e. true model order  $n = 3$ ), one-dimensional autoregressive models. Coefficients  $A_i$  were taken in decreasing absolute value such that the stability criterion of section 3.6.1 was met. We assumed that the signal had been zero for negative time. A Gaussian random number generator was used in combination with relation 3.26 to let the AR

model make timesteps for  $t \geq 0$ . From the test signals we tried to reconstruct the corresponding AR-coefficients using the Yule-Walker method. If we chose suggested model order  $\tilde{n} = 3$  then the true autoregressive memory coefficients that had been used to construct the test signals were correctly reproduced by the YW-model.

We did a second test on the third order test signals from the former paragraph. This time we used a maximum suggested autoregressive order  $\tilde{n} = 10$  and compared the first three memory coefficients (the true AR-order of the signal  $n$  is 3) with those obtained via the first test. In this case we could not see any agreement between the estimated coefficients found in the attempt to model the signal and the true coefficients used to generate the dataset. In the model which was used to generate these data all autoregressive parameters for order higher than three were zero. Therefore we expected that the Yule-Walker model would give a solution for the AR-coefficients with small values for the coefficients of order higher than three. This appeared not to be the case. This test has shown that one has to know in advance the order of the autoregressive model if the Yule-Walker model is to be used to find the coefficients. Before one can interpret the AR-model parameters of models found with Yule-Walker, one has to make sure that one uses the model, which is best according to the Cic-criterion. Parameters from other models should not be considered for further use.

A third test was carried out on a one-component signal from a turbulence measurement. The estimates for all AR-coefficients substantially depended on the suggested maximum order  $\tilde{n}$  of the model. To estimate the order of the best model (using Cic-criterion 3.32), the residuals for all models of order equal to or smaller than  $\tilde{n}$  were calculated. It happened that for certain orders smaller than  $\tilde{n}$  the residuals became larger than the mean square of the original signal! If this were correct, then this would imply that not modelling at all would give better predictions than lower order modelling. Only when most or all  $\tilde{n}$  memory coefficients were taken into account, then the residual would improve (i.e. become smaller than the mean square of the signal).

The tests which were carried out in this section show that the Yule-Walker method is not a good method to estimate autoregressive parameters to model turbulence signals. The reason is that, in the Yule-Walker method, the values of individual coefficients appear to depend on the value of (arbitrary) maximum model order  $\tilde{n}$ .

### 3.6.4 Determination of AR-coefficients via Burg's method

In the previous subsection we found that the Yule-Walker method is inadequate to reconstruct AR-coefficients from turbulence signals. In this subsection we will use a different method, called Burg's method (see Priestley (1981, p.606), for a derivation of this method), to determine autoregressive coefficients  $\bar{A}_{0 \leq i \leq n}$  from a time signal  $u_t$ . Without giving a proof of specific steps in Burg's method, we will give all steps necessary to estimate coefficients  $A_i$ .

Burg's method makes use of the so called **reflection coefficients** or **partial correlations**. They are defined as follows: A normal correlation function does not directly show independent correlation information: all  $j$ -th point correlations  $R(j)$  intrinsically lead to 'inherited' correlations  $(R(j))^k$  for delays  $kj$  (e.g. ten percent correlation between nearest neighbours leads to one percent, i.e. ten percent of ten percent, correlation between next nearest neighbours). Reflection coefficients  $R_c(j)$  express the difference between the  $j$ -th correlation and the sum of the



correlations 'inherited' from shorter delays:

$$Rc(j) = R(j) - \sum_{i=1}^{j-1} Rc(i)^{j/i} \quad (3.37)$$

where  $i$  may only take those values where  $j/i$  is an integer number. Naturally the first partial correlation equals the first correlation:  $Rc(1) = R(1)$ .

In Burg's method partial correlation function  $Rc(j)$  is reconstructed for delays  $j = 1$  to  $j = \tilde{n}$ . This is done via  $\tilde{n}$  iterations of the following procedure from  $j = 1$  to  $j = \tilde{n}$ . Take two (identical) copies of the original dataset ( $N$  datapoints) to start with and call them  $x_{1 \leq i \leq N}$  and  $y_{1 \leq i \leq N}$ .

**begin of procedure** ( $j$  is the loop parameter)

- Give  $x_i$  a shift of one sample. Now the delay between sets  $x$  and  $y$  corresponds with the delay  $j$  (in the first iteration of this procedure  $j = 1$ ) for which the partial correlation function is currently being evaluated:

$$\text{replace } \begin{pmatrix} x_i \\ y_i \end{pmatrix} \text{ by } \begin{pmatrix} x_{i+1} \\ y_i \end{pmatrix} \quad (3.38)$$

- Partial correlation  $Rc(j)$  is calculated from:

$$Rc(j) = \frac{2 \sum_{i=1}^{N-j} x_i y_i}{\sum_{i=1}^{N-j} x_i x_i + \sum_{i=1}^{N-j} y_i y_i} \quad (3.39)$$

The specific form of the denominator in relation 3.39 stabilises end-effects near  $i = 1$  and  $i = N$ , where data-loss is caused by the shifting of the arrays. The function in relation 3.39 does not look like a correlation function, but one has to observe that, via  $j$  times the first step in this procedure, the samples in array  $x$  have been shifted by  $j$  samples.

- $Rc(j)$ 's influence is removed from either copy of the dataset ( $x$  and  $y$ ) that is used in the procedure:

$$\text{replace } \begin{pmatrix} x_i \\ y_i \end{pmatrix} \text{ by } \begin{pmatrix} x_i - Rc(j)y_i \\ y_i - Rc(j)x_i \end{pmatrix} \quad (3.40)$$

**end of procedure**

To apply Burg's method we used a FORTRAN translation of MATLAB routine 'TimBurg'<sup>1</sup>. We converted reflection coefficients  $Rc(i)$  into AR-memory coefficients  $A_i$  by use of a FORTRAN-translation of the MATLAB-routine 'rc2poly'.

Burg's method implicitly assumes that the multiplication of memory coefficients is commutative. For scalar processes this is a proper assumption. For multi-component time series the associated memory coefficients  $\bar{A}_i$  are second order tensors, which in general do not commute

<sup>1</sup>This MATLAB routine, which enabled us to use large datasets, was kindly supplied by P.M.T. Broersen from the Signal Processing research group, Faculty of Technical Physics.

with one another. With a tensor AR-model, the order in which the influences of reflection coefficients of different orders are removed from the signal in Burg's method matters. The non-commutative nature of the memory tensors renders Burg's method an improper tool to calculate these tensors. Therefore we will restrict calculations to signals consisting of one component. This means that all vectors and tensors in relations 3.26 and 3.27 become scalars. Consequently we will only be able to estimate *diagonal* spectral tensors.

Burg's method was tested on the same test signals that had been used to test the Yule-Walker method (e.g.  $n = 3$  with  $A_1 = -0.6$ ,  $A_2 = -0.15$  and  $A_3 = 0.1$ ). The autoregressive parameters were in all cases found within a few percent of the values that had been used to construct the test signals. Moreover the order of the model was in all cases correctly found by Broersen's Cic-criterion. A test on the output of a turbulence velocity measurement (1.800.000 samples) showed that an AR-model of order 286 can represent these data: a reduction of the amount of data with more than three orders of magnitude!

### 3.6.5 Relation between AR-coefficients and spectra

To find the relation between AR-coefficients  $\bar{A}_i$  and the auto- and cross-spectra of signal  $u_t$  we write the signal in its spectral decomposition as follows:

$$u_t = \int \hat{u}_\omega e^{i\omega t} d\omega \quad (3.41)$$

Angular frequency  $\omega$  is scaled such that the wave with  $\omega = \pi$  has phase difference of half a wave from sample to sample. This wave's frequency is the Nyquist frequency.

At a different time  $(t - j)$  relation 3.41 gives:

$$u_{t-j} = \int e^{-i\omega j} \hat{u}_\omega e^{i\omega t} d\omega \quad (3.42)$$

Now substitute relation 3.42 for the signal at a shifted time and relation 3.41 for the spectral decomposition of the signal into autoregressive model 3.26:

$$\begin{aligned} \epsilon_t &= u_t + \bar{A}_1 \cdot u_{t-1} + \bar{A}_2 \cdot u_{t-2} + \dots + \bar{A}_n \cdot u_{t-n} \\ &= \int \left( \hat{u}_\omega + \bar{A}_1 \cdot e^{-i\omega} \hat{u}_\omega + \bar{A}_2 \cdot e^{-2i\omega} \hat{u}_\omega + \dots + \bar{A}_n \cdot e^{-ni\omega} \hat{u}_\omega \right) e^{i\omega t} d\omega \\ &= \int \left( \bar{\delta} + e^{-i\omega} \bar{A}_1 + e^{-2i\omega} \bar{A}_2 + \dots + e^{-ni\omega} \bar{A}_n \right) \cdot \hat{u}_\omega e^{i\omega t} d\omega \\ &= \int \bar{G}_\omega \cdot \hat{u}_\omega e^{i\omega t} d\omega \end{aligned} \quad (3.43)$$

where

$$\bar{G}_\omega \equiv \bar{\delta} + e^{-i\omega} \bar{A}_1 + e^{-2i\omega} \bar{A}_2 + \dots + e^{-ni\omega} \bar{A}_n \quad (3.44)$$

Fourier transforming relation 3.9 for the cospectrum yields the following relation for second order correlation tensor  $\bar{R}$ :

$$\bar{R}(\tau) = \int \mathcal{E} \left( \hat{u}_\omega \otimes \hat{u}_\omega^* \right) e^{i\omega \tau} d\omega \quad (3.45)$$

The relation between relation 3.45 and the autoregressive parameters is found as follows:

$$\bar{\Sigma}\delta(\tau) = \int \bar{\Sigma} e^{i\omega\tau} d\omega \quad (3.46)$$

$$= \mathcal{E} \left( \mathbf{e}_t \otimes \mathbf{e}_{t-\tau}^t \right) \quad (3.47)$$

$$= \mathcal{E} \left( \int \bar{G}_\omega \cdot \hat{\mathbf{u}}_\omega e^{i\omega\tau} d\omega \otimes \int \hat{\mathbf{u}}_{\omega'}^* \cdot \bar{G}_{\omega'}^* e^{-i\omega't} e^{i\omega'\tau} d\omega' \right) \quad (3.48)$$

$$= \mathcal{E} \left( \int \int \left( \bar{G}_\omega \cdot \hat{\mathbf{u}}_\omega \otimes \hat{\mathbf{u}}_{\omega'}^* \cdot \bar{G}_{\omega'}^* \right) e^{i(\omega-\omega')t} d\omega e^{i\omega'\tau} d\omega' \right) \quad (3.49)$$

For stationary stochastic processes the expectation value does not depend on time. Consequently, for each realization we can replace expression 3.49 by its time average:

$$\int \bar{\Sigma} e^{i\omega\tau} d\omega = \int \left( \bar{G}_\omega \cdot \mathcal{E} \left( \hat{\mathbf{u}}_\omega \otimes \hat{\mathbf{u}}_\omega^* \right) \cdot \bar{G}_\omega^* \right) e^{i\omega\tau} d\omega \quad (3.50)$$

The Fourier transform of this relation gives:

$$\bar{G}_\omega \cdot \mathcal{E} \left( \hat{\mathbf{u}}_\omega \otimes \hat{\mathbf{u}}_\omega^* \right) \cdot \bar{G}_\omega^* = \bar{\Sigma} \quad (3.51)$$

from which we can find the following relation for the Fourier components of the second order correlation tensor  $\bar{R}_\tau$  as given by relation 3.45:

$$\mathcal{E} \left( \hat{\mathbf{u}}_\omega \otimes \hat{\mathbf{u}}_\omega^* \right) = \bar{G}_\omega^{-1} \cdot \bar{\Sigma} \cdot \left( \bar{G}_\omega^{-1} \right)^* \quad (3.52)$$

This result matches relation 9.4.23 of Priestley (1981). For scalar signals relation 3.52 can be written as:

$$\mathcal{E} \left( \hat{u}_\omega \hat{u}_\omega^* \right) = \frac{\Sigma}{|1 + e^{-i\omega} A_1 + e^{-2i\omega} A_2 + \dots + e^{-ni\omega} A_n|^2} \quad (3.53)$$

In section 3.6.4 we found a way to determine tensor  $\bar{G}_\omega$ . Together with this method relation 3.52 gives the autoregressive estimate for the cross-spectral amplitudes of a vector process.

An example of a spectrum determined via AR using Burg's method and the Cic-criterion is presented in figure 3.14. The same turbulence velocity data has been used as was shown in figure 3.12 for the cospectral estimates using FFT.

### 3.7 Spectral density estimation via moving average modeling

Autoregressive models can be powerful tools in practical applications. There is however a second important class of models called Moving Average models. The reason why yet another model will be introduced is the following: In the next section MA-models will be shown to be better than FFT-based models (and not better than AR-models, but complementary). In this section we will introduce the model, give a method to find the model parameters from a dataset and show the relation between the model parameters and the corresponding power spectrum.

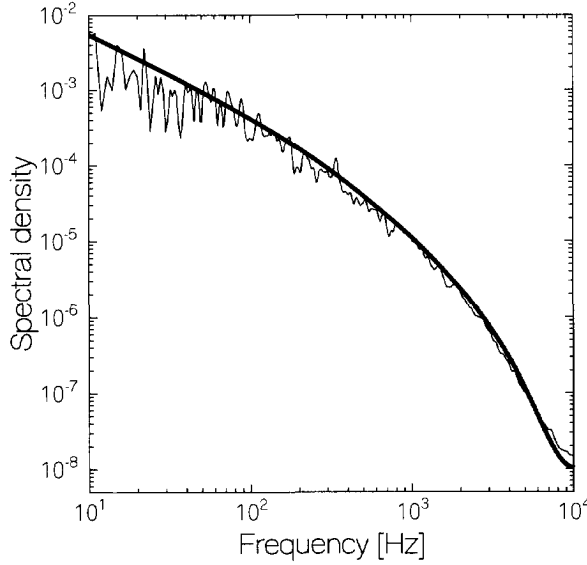


Figure 3.14: Spectrum of turbulence data determined via AR; the FFT based estimate is shown as a thin line

A moving average model of order  $n$  (called  $MA(n)$ ) is defined by the following relation for a sample at time  $t$ :

$$\mathbf{u}_t = \bar{\bar{B}}_0 \cdot \boldsymbol{\epsilon}_t + \bar{\bar{B}}_1 \cdot \boldsymbol{\epsilon}_{t-1} + \cdots + \bar{\bar{B}}_n \cdot \boldsymbol{\epsilon}_{t-n} \quad (3.54)$$

Like in the autoregressive case, tensors  $\bar{\bar{B}}_i$  are called memory coefficients. Vector process  $\boldsymbol{\epsilon}_t$  is a three component white noise process, and consequently has no memory: its value at any instant  $t$  is uncorrelated with its value at  $t - j$  (for non-zero  $j$ ). Though components of  $\boldsymbol{\epsilon}_t$  are uncorrelated with components at a different time, different vector components of  $\boldsymbol{\epsilon}_t$  *can be* correlated when they have zero delay. This is e.g. the case when the vector process has all of its components identical (and therefore in fact is a scalar process).

### 3.7.1 Estimation of MA-parameters

To estimate MA-parameters for a  $q$ -th order moving average model  $MA(q)$  from a dataset we use Durbin's trick (see Durbin (1959) for an account of this method, with proofs). This means that we calculate the MA-coefficients via the following steps:

- First construct an AR-model for the data of sufficiently high order (using Burg's method, see subsection 3.6.4). Determine the optimal order  $K$  of this model using the Cic-criterion (see subsection 3.6.2).
- Take the first  $p$  model parameters of the model determined in the former step. The order  $p$

is taken to be (see Broersen (1996)):

$$p = 2K + q \quad (3.55)$$

where  $K$  was determined via the Cic-criterion in the first step and where  $q$  is the order of the MA-model which we are constructing.

- Consider the  $p$  AR-parameters in their turn as if they were a timeseries on their own (this step may seem a bit odd at first sight). Use them as *input data sequence* for a second AR-model, of order  $q$ . Higher order coefficients tend to be smaller than lower order coefficients. Therefore the AR-coefficients (of the first AR-model) themselves are not a stationary dataset. This means that the Burg-method cannot be invoked to solve the second AR-system for it's coefficients. Instead of using Burg's method we have to use the Yule-Walker method (see subsection 3.6.3).

The  $q$  AR-parameters of this second model are the MA( $q$ )-parameters, which we were calculating.

To find the optimal MA-model we use the above procedure to calculate MA-coefficients for a number of model orders  $q$ . Back-substitution of these MA-models into the original dataset gives the respective residuals. This is done via relation 3.54, where noise component  $\epsilon_{t-j}$  is the residual of the  $t - j$ -th sample. The procedure of calculating the residuals is initialised by setting all  $\epsilon_{t-j}$ 's to zero.

The Gic-criterion is used on these residuals to estimate the best MA-order.

### 3.7.2 Relation between MA-coefficients and spectra

The derivation of the relation between moving average model parameters and the spectrum of the signal is an analogue of the derivation of spectra for AR-models. We use the same scaling for angular frequency  $\omega$  in MA-models as we used for AR-models (the wave with  $\omega = \pi$  has phase difference of half a wave from sample to sample).

First we give the analogue of relation 3.42 for white noise at time  $t - j$ . This analogue is constructed using Fourier transform  $\hat{\epsilon}$  of white noise, which of course is a constant:

$$\epsilon_t = \int \hat{\epsilon}_\omega e^{i\omega t} d\omega \quad (3.56)$$

$$\Rightarrow \epsilon_{t-j} = \int e^{-i\omega j} \hat{\epsilon}_\omega e^{i\omega t} d\omega \quad (3.57)$$

This expression for shifted noise (noise on a previous time) is substituted into definition 3.54 of the moving average model to give:

$$u_t = \int \bar{H}_\omega \cdot \hat{\epsilon}_\omega e^{i\omega t} d\omega \quad (3.58)$$

$$\text{where} \quad \bar{H}_\omega \equiv \bar{B}_0 + e^{-i\omega} \bar{B}_1 + e^{-2i\omega} \bar{B}_2 + \dots + e^{-ni\omega} \bar{B}_n \quad (3.59)$$

The Fourier transform of relation 3.58 for moving average signals readily gives us the desired power spectrum of MA-processes:

$$\mathcal{E} \left( \hat{\mathbf{u}}_{\omega} \otimes \hat{\mathbf{u}}_{\omega}^* \right) = \mathcal{E} \left( \bar{\bar{\mathbf{H}}}_{\omega} \cdot \hat{\mathbf{e}}_{\omega} \otimes \left( \bar{\bar{\mathbf{H}}}_{\omega} \cdot \hat{\mathbf{e}}_{\omega} \right)^* \right) \quad (3.60)$$

$$= \bar{\bar{\mathbf{H}}}_{\omega} \cdot \mathcal{E} \left( \hat{\mathbf{e}}_{\omega} \otimes \hat{\mathbf{e}}_{\omega}^* \right) \cdot \bar{\bar{\mathbf{H}}}_{\omega}^* \quad (3.61)$$

Knowing that the expectation value of the squared amplitude of white noise does not depend on frequency, and remembering that the tensor product of white noise with itself was called  $\bar{\bar{\Sigma}}$ , we can write relation 3.61 for the spectrum of MA-signals as:

$$\mathcal{E} \left( \hat{\mathbf{u}}_{\omega} \otimes \hat{\mathbf{u}}_{\omega}^* \right) = \bar{\bar{\mathbf{H}}}_{\omega} \cdot \bar{\bar{\Sigma}} \cdot \bar{\bar{\mathbf{H}}}_{\omega}^* \quad (3.62)$$

which matches relation 9.4.24 of Priestley (1981). For scalar processes relation 3.62 reduces to:

$$\mathcal{E} \left( \hat{u}_{\omega} \hat{u}_{\omega}^* \right) = \Sigma |\bar{\bar{B}}_0 + e^{-i\omega} \bar{\bar{B}}_1 + e^{-2i\omega} \bar{\bar{B}}_2 + \dots + e^{-ni\omega} \bar{\bar{B}}_n|^2 \quad (3.63)$$

An example of a spectrum determined via MA-modelling is shown in figure 3.15. The same turbulence velocity data has been used as was shown in figures 3.12, 3.13 and 3.14 for the cospectral estimates using Fourier transform and autoregressive modelling respectively.

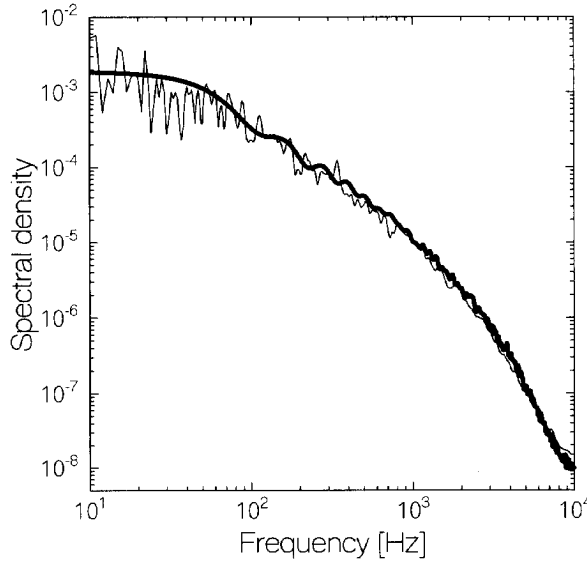


Figure 3.15: Spectrum of turbulence data estimated via MA; the FFT-based estimate is shown as a thin line

### 3.8 Comparison of FFT-, AR- and MA-models

We now have three different methods to estimate the spectral density of a given dataset: via FFT, via AR and via MA. In this section we will compare these three models and make a choice

for the analysis of turbulence measurements. Criteria will be: the absence of artificial effects like tapering windows, and the behaviour of the models in the tests, which were made earlier in this chapter.

First we compare FFT-based estimates for the spectral density with MA-based estimates. Kay and Marple (1981, p.22) have shown that MA( $q$ )-based spectral estimates are identical to estimates in which the Fourier transform is made of a correlation function which is exact up to delay  $q$ . This differs from FFT-based estimates: FFT also Fourier transforms the correlation function. FFT, however, considers data to be periodic (see subsection 3.5). To eliminate wrap-around effects, FFT applies tapering windows to push the dataset to zero near the ends. This tapering (plus the wrap-around) leads to a distorted estimate of the correlation function and consequently gives a distorted view of the power spectral density. MA-routines have no need for tapering, and still manage to calculate the Fourier transform of the correlation function. Therefore MA-routines are better estimators for spectra than FFT-based routines.

MA- and AR-models can be compared through their residuals, i.e. the part of the signal which is not predicted by the models. Residuals are found via backsubstitution of the original dataset into the model using either relation 3.31 or relation 3.54. With either (MA- or AR-) model we cannot give hindcasts for *all* samples from the original dataset: Let  $l$  be the order of the model. Then we cannot give meaningful predictions of the first  $l$  samples of the data. Therefore we have to correct the residual based on the last  $n-l$  estimates by division by a factor  $(1-l/n)$  (for large datasets and moderate model orders this factor will be negligible). Thus we obtain an estimate for the residual which we would have found from  $n$  predictions. Furthermore we have compared an  $l$ -th order model with  $n$  samples, but model and samples are not independent! Out of  $n$  degrees of freedom, the model has taken  $l$  degrees. This calls for another correction of the residual to estimate the residual which we would have found in case the model had been established independently from the data used to test its merits. The correction is done by multiplication of the residual with a factor  $(1+l/n)$  (again, if  $n \gg l$  this factor can be disregarded). When we take into account these two corrections, then we can compare different models. A residual, to which these two corrections have been applied, gives what is defined as the **prediction error** of the model: the RMS expectation value of the difference between the actual value of a signal and its prediction based on the signal taken at previous times by use of an independent model:

$$(\text{Prediction error})^2 = \frac{n+l}{n-l} \frac{1}{n-l} \sum_{i=l+1}^n |u_i - u_{i,\text{model}}|^2 \quad (3.64)$$

where  $u_{i,\text{model}}$  is the value which is found for  $u_i$  via substitution of old values of  $u$  into the model.

We use both FFT- and AR- and MA-modelling to analyse a dataset of 100.000 samples of a turbulent velocity measurement (turbulence at 40 mesh sizes behind a square grid, see chapter 7 for details of the measurement). The ratio of the corrected residuals (via relation 3.64) to the mean square of the samples is plotted in figure 3.16. In figure 3.17 the Cic-values corresponding with these residuals (see relation 3.32) are presented. For MA- and AR-models, the minimum of this latter function provides the best model of its kind. For FFT-models the Cic-function has no application: a limited number of FFT-components would imply a cut-off in the spectrum, an unwanted characteristic. To find the best model, we look for the model with the lowest value of criterion Cic (see relation 3.32). We see from figure 3.17 that for AR-models the value of Cic

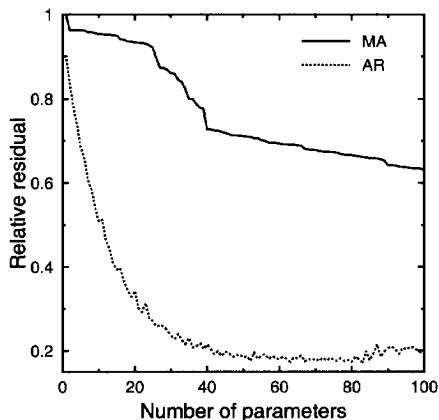


Figure 3.16: Residual (normalised using the mean square of the signal) as function of the number of model parameters, i.e. the order of the model

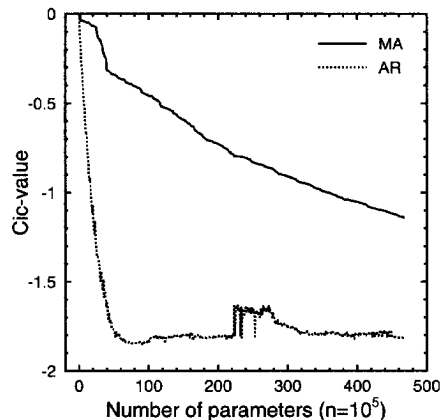


Figure 3.17: Cic-values corresponding with the residuals

drops to a much lower value with the number of parameters than for MA-models. This brings us to the conclusion that AR-models are better tools to analyse grid-generated turbulence signals than MA-models.

### 3.9 The estimation of derivatives of spectra

In the preceding section we have concluded that AR-models are the best instrument to estimate the cospectrum of a turbulence signal. Later in this study (in chapter 2) we will need estimates for derivatives of the cospectrum up to third order. These derivatives of spectra will be used in relations for other spectra. They will always appear in terms of the following shape ( $S$  denotes a spectrum and  $f$  represents frequency):

$$f^j \frac{d^j S(f)}{df^j} \quad (3.65)$$

Therefore  $j$ -th order derivatives are multiplied with  $f^j$ . The dimensions of expressions of the type given in formula 3.65 are equal to the dimensions of the original spectrum  $S$ , independent of order  $j$  of the derivative. Spectral derivatives of the type 3.65 are directly related to their future application and can be compared.

Spectral estimates are not necessarily differentiable. Small details in the spectrum can give significant information about the spectrum, but not about the derivative (a sharp peak in the spectrum can correctly represent a significant amount of energy, but the *exact shape* of the peak can be still unreliable). Smoothing of the estimates for the derivatives is necessary to eliminate the artificial blowing up of non-significant details in spectral estimates. Earlier in this chapter we have shown that it is reasonable to expect that turbulence spectra are logarithmically smooth. We



will use this characteristic of turbulence spectra as justification to convolve derivatives of spectra against a frequency-window with constant relative width. We set this width to 5 percent, which is a compromise between detail and smoothness. The range of 50 Hz to 4000 Hz (the range where we expect to find turbulence in our measurements) contains 90 independent frequency bands with 5 percent width.

In this section we will show how to estimate these derivatives from the AR-model. To allow for comparison, we will also include the FFT-based estimates for the derivatives of the spectrum. We will start with the latter.

### 3.9.1 Differentiating FFT-based spectra

Before differentiation both estimated and true spectra are smoothed by convolution against a 5-percent window. To differentiate the cospectral estimates produced via Fourier transform we take difference quotients of nearest neighbours.

To prevent uncontrolled amplification of small wiggles in the spectrum from one differentiation to the next, the estimates for differentiated spectra have to be smoothed. To assess the quality of a smoothing method, we constructed a test-signal of which the spectrum was known. This signal was generated using the AR-model which was found for turbulence velocity data in section 3.8. Below 50 Hz the spectrum is considered not to describe turbulence phenomena, and above 4 kHz the low-pass filter is active. Therefore we will look at the behaviour of the derivatives in the range between 50 Hz and 4 kHz. The quality of a model for the estimation of the derivative of order  $j$  of spectrum  $S(f)$  is expressed by quality factor  $q_j$ , which is defined by the following relation:

$$q_j^2 \equiv \frac{\int_{50\text{Hz}}^{4\text{kHz}} \left( f^j \frac{d^j S(f)}{df^j} - f^j \frac{d^j S(f)}{df^j}_{\text{model}} \right)^2 df}{\int_{50\text{Hz}}^{4\text{kHz}} \left( f^j \frac{d^j S(f)}{df^j} \right)^2 df} \quad j = 0, 1, 2, 3 \quad (3.66)$$

We have tested two methods to smooth FFT-based spectral differentiation:

1. From figures 3.13 and 3.14 we conclude that 'typical' double logarithmic plots of turbulence spectra show relatively simple curves. We fit a polynomial through the logarithm of the cospectrum as function of the logarithm of the frequency. The resulting relation between cospectral values and frequency can be differentiated analytically with respect to the frequency. This method can only be used for the diagonal components of the co-spectrum since other components can become negative. Spectral estimates obtained via this method will have a functional shape similar to the results from the original FFT-based method, except for the oscillations and sharp peaks. The dependence of quality factor  $q_{0...3}$  as function of the number of free parameters in the polynomial is shown in figure 3.18. From figure 3.18 we see that the best estimates for spectral derivatives are obtained when a polynomial with 7 degrees of freedom is used.

We have tested a modified version of the procedure just outlined: in stead of the logarithm of the spectrum, the product of the spectrum with frequency was modelled using a

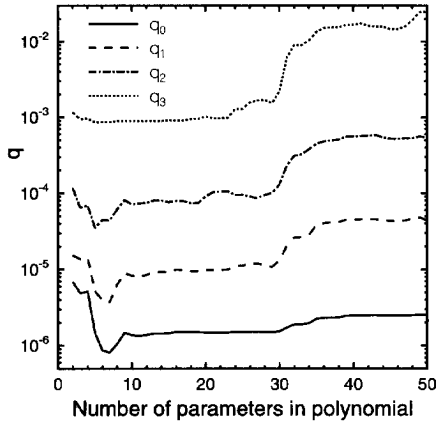


Figure 3.18: Quality factors for smoothing via polynomial fitting

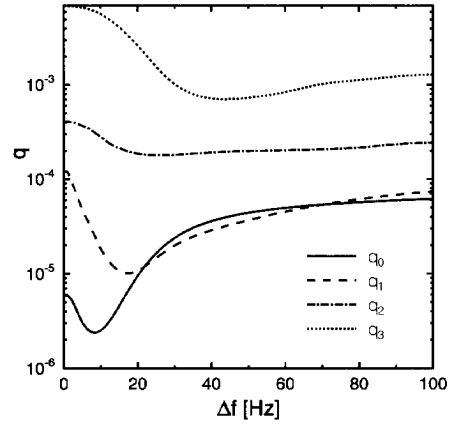


Figure 3.19: Quality factors for smoothing via convolution

polynomial. In this way cross-spectra can be modelled. The quality factors found in this test were slightly worse than the quality factors in the log-log model.

2. In the second method, the estimates for differentiated spectra are convolved against a window function  $W(f, \Delta_j f)$  with fixed width  $\Delta_j f$ . The  $j$ -th order derivative (functional form as in formula 3.65) is constructed from the  $j - 1$ -th order derivative (also type 3.65) as follows:

$$f^j \frac{d^j S(f)}{df^j} \Big|_{\text{model}} = W(f, \Delta_j f) * \left( f \frac{d}{df} \left( f^{j-1} \frac{d^{j-1} S(f)}{df^{j-1}} \Big|_{\text{model}} \right) \right) \quad (3.67)$$

We have done a test to find out which window width gives the best suppression of artificial wiggles. The dependence of quality factor  $q_0 \dots q_3$  as function of window width  $\Delta_j f$  in Hz is shown in figure 3.19. From this plot we see that the quality factors for zeroth up to third order spectral derivatives have minima. The locations of these minima are adopted as window widths for smoothing derivatives of spectra.

We have used the AR-coefficients, which were found in section 3.8 in the analysis of 100.000 samples of a turbulence measurement, to generate a set of 100.000 samples via relation 3.31. This set has turbulence-like statistics, and a known spectrum. The estimates for zeroth up to third order derivatives of this test signal, found via method 1, are shown in figures 3.20, 3.21, 3.22 and 3.23. The estimates obtained via the second method are given in figures 3.24, 3.25, 3.26 and 3.27. We see that polynomial fitting of the estimate for the power spectrum leads to estimates for the derivatives without oscillations, even in the (high frequency) range where the theoretical AR-spectrum actually does have oscillations. In our turbulence measurements we expect to find smooth spectra. As a consequence we also expect smooth derivatives of spectra. Therefore it may be that, though the coefficients of the AR model used in this test were

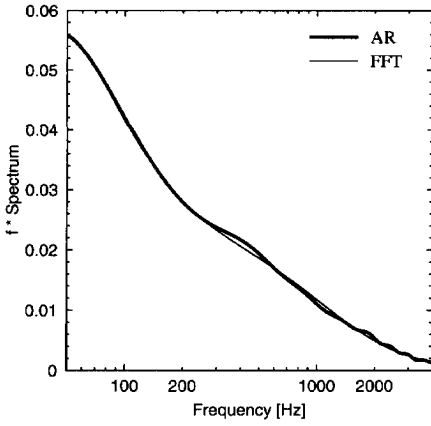


Figure 3.20: FFT-based (method 1: log-log polynomial fitting) and theoretical (AR) estimates: co-spectrum

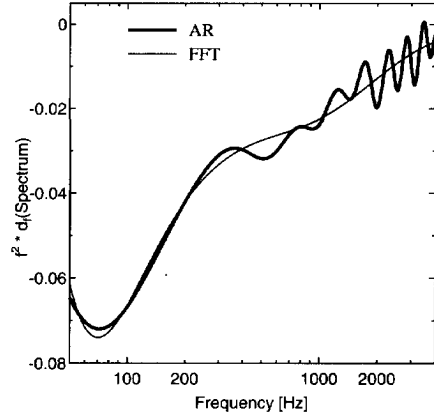


Figure 3.21: First derivative

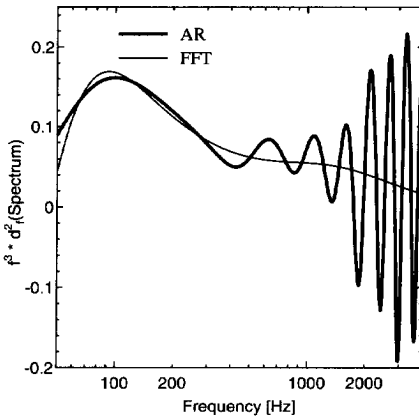


Figure 3.22: Second derivative

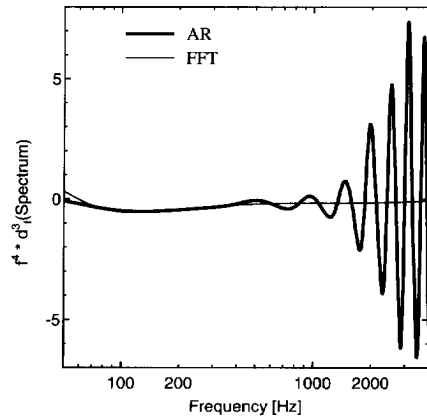


Figure 3.23: Third derivative

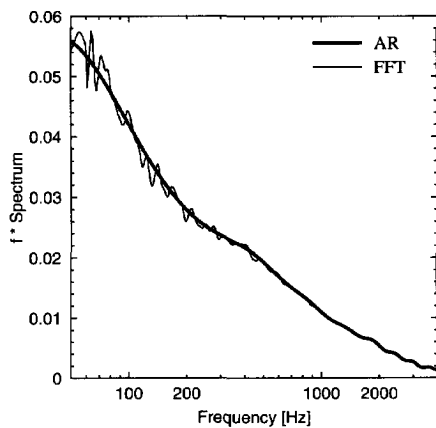


Figure 3.24: FFT-based (method 2: smoothing by convolution) and theoretical (AR) estimates: co-spectrum

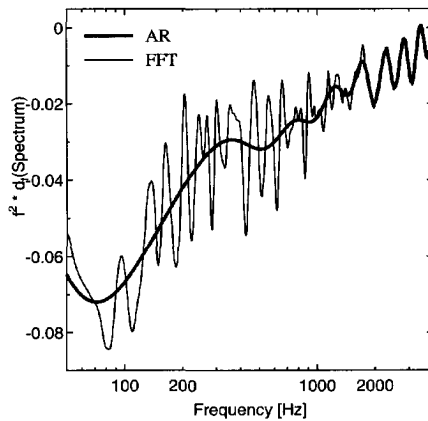


Figure 3.25: First derivative

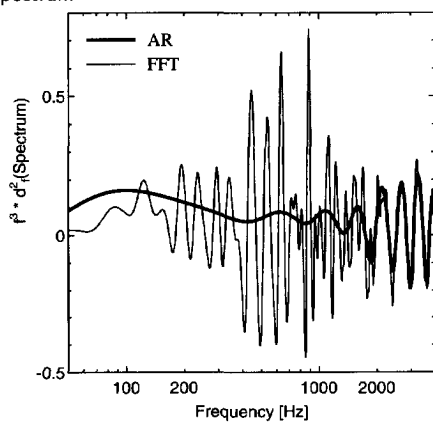


Figure 3.26: Second derivative

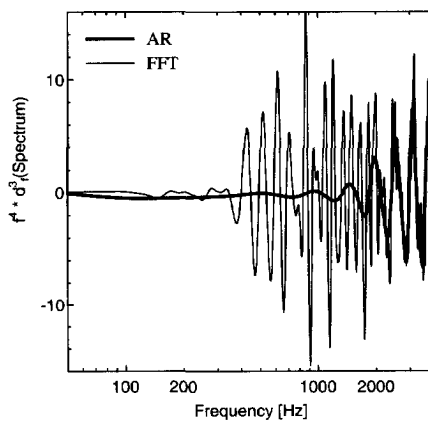


Figure 3.27: Third derivative

calculated from real turbulence data, the wiggles in the high frequency range of the derivatives of the spectra do not actually represent physics. Further research will have to be carried out to clarify this problem.

Wiggle suppression via convolution leads to relatively good estimates in the high frequency range, and still strong (incorrect) oscillations in the lower and middle frequency range. These oscillations stem from a lack of power of the smoothing procedure which was used to transform the periodogram into a cospectrum: at the lower frequencies the smoothing involves only very few contributors to the periodogram.

Neither method leads to satisfactory estimation of the spectral derivatives.

### 3.9.2 Differentiating AR-based spectra

The autoregressive estimates are differentiated analytically. Though we have the AR-spectrum in analytical form, analytical differentiation can still give unwanted amplification of sharp peaks. The origin of these peaks can be a too high order of the AR-model. If e.g. the co-spectrum itself has a significant narrow peak in a certain region, then the Cic-criterion for AR order selection will make sure that this peak is modelled. The exact *shape* of the peak, however, might not be significantly extractable from the dataset. To find the shape of a peak one needs more information than to find if there is a peak at all. This implies that the number of available AR-parameters, that is significant to estimate the derivative of a spectrum, is smaller than the number of parameters that is necessary to model the spectrum itself.

To take into account this theorem, we lower the order of the AR-model as follows: the penalty factor in Cic-criterion 3.32 (equalling 3 when the model is used to estimate zeroth order derivatives of the spectrum) is increased for higher order derivatives. The penalty factor provides a balance in the order selection criterion between the relative fall of the residual with the number of model-parameters and the ratio of the number of model parameters to the number of samples used to find the model. Therefore an increased penalty factor will make that a residual improvement (by taking a higher order model) will have to pass an increased threshold to actually lead to an increased order estimate.

We applied the AR-method to estimate spectral derivatives, as presented in this section, on the dataset which was used in the former section on FFT-based estimates. An increase of the penalty factor with an order of magnitude (penalty factor 30) did not lead to a higher suggested AR-model order (analysis performed on the same turbulence dataset as used in previous subsections). This suggests that the drop of the residual with the number of parameters is substantially stronger than the influence of the penalty term in the Cic-criterion.

The AR-model which has been used for testing in this section, was constructed from measured turbulence data. We see that the AR-based estimates for the higher order spectral derivatives have strong oscillations. Earlier (section 3.4.2) we expected turbulence spectra (and consequently their derivatives) to be smooth. It therefore is not clear whether the oscillations really represent structure in the spectrum of the measured data, or whether they are artefacts of AR-modelling. To solve this problem we suggest to remove sharp structures from the estimates for the derivatives of the spectrum by convolving it against a spectral window function of which the width is a constant fraction of the frequency. Without theoretical justification we take a

window with 5 percent width.

Estimates of zeroth-, first-, second-, and third order derivatives, found via AR-estimation plus convolution, have been shown in figures 3.24, 3.25, 3.26 and 3.27 (and in figures 3.20, 3.21, 3.22 and 3.23).

### 3.9.3 Conclusion

From the FFT-based and AR-based estimates for the derivatives of the cospectrum we can see the following:

Estimates for derivatives produced via convolution FFT suffer from oscillations in the low frequency range. FFT-based estimates found via polynomial fitting of the log-log-power spectrum inadequately model structures in the high frequency range of the spectrum of our model dataset. As discussed in section 3.9.2, it is not clear whether the oscillations, which are present in the derivatives of the spectrum of the test data, had been present in the derivatives of the spectrum of the original measured dataset. Therefore we have no fundamental reason to assume that the wiggles, which are not modelled by the polynomial method to estimate spectral derivatives, are an indication of this method's inadequacy to estimate the *true* spectral derivatives of a measured turbulence signal.

The AR-results shown in figure 3.24 follow the spectrum of the mathematical test dataset (plus the spectral derivatives) better than the estimates constructed with the polynomial method.

A solid theoretical frame for the assessment of the correctness of either method to suppress the blowing up of artificial wiggles in higher order derivatives ('FFT + polynomial fitting' or 'AR + smoothing') is still lacking and will need attention in future studies. Therefore we will use and show the results of both methods to estimate spectral derivatives when we will be analysing turbulence data later in this study. The 'true' spectral derivatives will be somewhere between the two estimates.

# Chapter 4

## Comparison of theory with DNS

### Introduction

In the chapter 2 we have developed a theory for the unaliasing of one-point measurements of weakly anisotropic, homogeneous turbulent flow (relations 2.119, 2.120, 2.121, 2.122, 2.133 and 2.134) and in chapter 3 we have devised two different methods for the estimation of the terms in those relations. To assess the combination of theory and practical estimation method, we will apply it to a situation for which we can independently check the resulting estimates. For this check we need full three-dimensional velocity fields, resolved down to Kolmogorov's length scale. Such complete and detailed fields have not been measured. Therefore we need to subside to artificial flows. In our case we will make use of a Direct Numerical Simulation (DNS) of grid generated turbulence. The numerical model is described in section 4.1. Simulations will cover the flow from the grid to 50 meshsizes downstream of the grid. In section 4.2 we will make an analysis of the data generated by the DNS, in terms of time averaged velocity and vorticity values. Next we consider which part from the full domain between the grid and 50 meshsizes downstream the grid can be used to test the unaliasing relation. In section 4.3 we will calculate wavenumber spectrum  $\bar{\Psi}$  directly from the simulated velocity fields. In section 4.4 an indirect estimate for  $\bar{\Psi}$  is given via unaliasing of one-point spectrum  $\bar{\Theta}$ . A comparison of the two methods will be discussed in section 4.5.

The term "grid", with two different meanings, can lead to confusion when one is reading this chapter. Therefore we will call the physical grid, at the inflow of the tunnel, the *grid* and the set of nodes, on which the relevant quantities are calculated numerically, the *mesh*.

### 4.1 Description of the model

The DNS-code which is used in this chapter to test the unaliasing relations is based on a DNS-code for a channel. This code has been developed at Laboratory for Aero- and Hydrodynamics, Delft University of Technology (see e.g. van Haarlem et al. (1998)). Pourquié has implemented the inflow conditions for the turbulence generating grid bars. He has also written a parallelised version of the vector code, such that it runs on the CRAY-T3E supercomputer of Delft University

of Technology (Pourquié et al., 1997).

### 4.1.1 Specification of the DNS method

Important details of the DNS-code are the following:

- The code discretises the following set of equations:

$$\frac{\partial \mathbf{u}}{\partial t} + \mathbf{u} \cdot \nabla \mathbf{u} = \frac{1}{\rho} \nabla p + \frac{1}{\text{Re}} \nabla^2 \mathbf{u} \quad \text{Navier-Stokes equation} \quad (4.1)$$

$$\nabla \cdot \mathbf{u} = 0 \quad \text{incompressibility condition} \quad (4.2)$$

where  $\mathbf{u}$  is velocity,  $p$  is pressure and  $\text{Re}$  is a Reynolds number, based on the mean velocity in the channel  $U_{\text{mean}}$  (about half the velocity through the grid apertures), the mesh size  $M$  and the viscosity  $\nu$ :

$$\text{Re} \equiv \frac{U_{\text{mean}} M}{\nu} \quad (4.3)$$

- Discretisation is done with a second order accurate finite volume method on a staggered mesh.
- Advective and diffusive terms are advanced in time through a second-order Adams-Bashforth scheme.
- Continuity is enforced by a pressure correction method, which results in a Poisson's type of equation for the pressure. The Poisson equation is solved via FFT in the two lateral directions, and via tridiagonal matrix equations in the mean flow direction.
- Boundary condition in lateral direction: we have adopted periodic boundary conditions in the two lateral directions. This boundary condition, which is not a very realistic one, is a compromise. The realistic boundary condition of no normal velocity would lead to an inhomogeneous flow with approximate homogeneity near the centre-line of the testsection, but our unaliasing theory, which we are testing in this chapter, assumes homogeneity. To artificially increase homogeneity the domain is considered periodic in the two lateral directions.
- Boundary condition in mean flow direction (figure 4.1): At the inflow boundary of the DNS domain the velocity is set to unit velocity in mean flow direction for all nodes lying in the gaps in the turbulence generating grid, and to zero for the nodes on the grid bars. The boundary condition at outflow sides is a so-called convective boundary condition:

$$\frac{\partial \mathbf{u}}{\partial t} + U_{\text{mean flow}} \frac{\partial \mathbf{u}}{\partial x} = 0 \quad \text{combined with} \quad \frac{\partial p}{\partial x} = 0; \quad (4.4)$$

where  $x$  is the coordinate in mean flow direction.



### 4.1.2 Specification of the calculation

At the inlet of the channel we use a turbulence generating grid with four bars in both lateral directions (see figure 4.1). This is considerably less than the 18 bars, which are used in the windtunnel experiments (see section 5.5). By giving the bars a width of  $0.25M$  we obtain a grid-solidity of 44 percent (the solidity of a grid is defined as the fraction of the grid's surface, which is covered by bars and which consequently blocks the flow). This is at the edge of Bradshaw and Pankhurst's criterion to prevent the flow from developing persistent structures (see section 5.5.2). With this solidity, the unit velocity through the apertures at the inlet gives a mean velocity in the tunnel of  $U_{\text{mean}} = 0.55$ . The physical domain's size is  $50M \times 4M \times 4M$

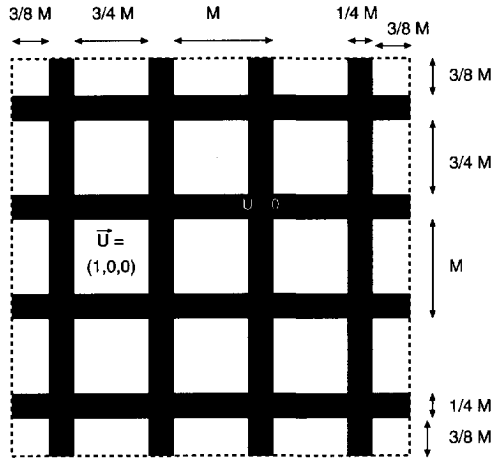


Figure 4.1: Inflow conditions for DNS of a windtunnel.

(figure 4.2). Numerical nodes are placed on a rectangular mesh, with equal spacing in all three directions. To investigate the influence of (refinement of) the numerical mesh, we will carry out two runs with different meshes: in the first simulation (called simulation A) we will use  $600 \times 48 \times 48$  mesh-nodes; in the second simulation (simulation B) we will use  $1000 \times 80 \times 80$  mesh-nodes. We will run simulations at  $Re = 1000$ . With relation 4.3 this condition determines viscosity  $\nu$ . With this known viscosity we will be able to estimate Kolmogorov's lengthscale  $\eta$  from the decay of kinetic energy in the simulations via relation 1.3. A rough estimate for  $\eta$  is found from relation 1.2 by setting the constant of proportionality equal to 1 and by taking macrolengthscale  $L$  equal to  $M$ . In this way we find  $\eta = 0.006M$ . Later we will see that for our simulation the proportionality constant in relation 1.2 is about 10, giving  $\eta = 0.06M$ . This value of  $\eta = 0.06M$  corresponds with a distance  $x/M = 10$  in relation 1.16 for grid-generated turbulence, which was found by Batchelor.

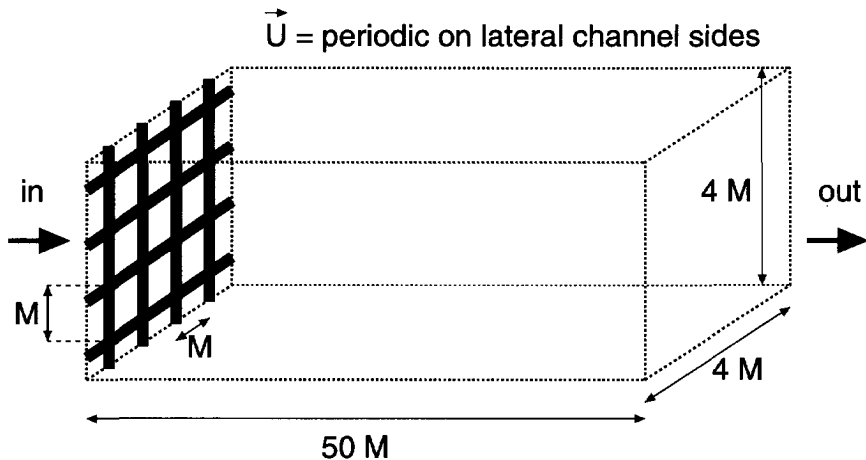


Figure 4.2: Domain for DNS of a windtunnel.

## 4.2 Characteristics of the DNS simulations

In this section we will discuss the general flow characteristics for simulations A and B as described in section 4.1. Before we started collecting data from the simulations, we have first let the model run during a time  $T$  such that  $UT > 2 \times 50M$ . This was done to allow the model to become independent from the initial laminar flow field. To calculate mean values and variances in simulation A, we have averaged quantities during a time period in which the mean flow travels 4.4 times the numerical domain. This corresponds with a time  $364 M/U_{\text{mean}}$ . In simulation B we collected data during a time period in which the mean flow travels 3.3 times the numerical domain. This corresponds with a time  $273 M/U_{\text{mean}}$ . We found that the longest time scales, associated with large scale fluctuating motions are equal to  $11 M/U_{\text{mean}}$  for simulation A and  $16.5 M/U_{\text{mean}}$  for simulation B. We assume that observations done with a time delay corresponding with twice the characteristic time for large scale motions, are independent. From this assumption we see that the number of independent realizations, over which quantities are averaged, amounts to at least 18 for simulation A and to 8 for simulation B.

The development of the variance of the (absolute) velocity as a function of the distance from the grid is shown in figure 4.3.

We have fitted decay relation 5.18 from section 5.7.3.2 to these data. The best fit was found for  $x_0/M = -0.39$  and  $n = 1.91$ . The exponent  $n$  in this relation is relatively high when compared with the values found in other studies (where  $n$  is found to be slightly larger than 1, see section 5.7.3.2). We have the impression that the decay exponent is a function of the solidity of the grid. In the windtunnel experiments on grid-turbulence, which will be presented in chapter 7, we have used a grid with solidity 55 percent, which is much larger than in most studies and somewhat larger than in the DNS of this chapter (44 percent). In the windtunnel we find a decay exponent of 2.49.

From the decay of the velocity variance we can estimate energy dissipation  $\epsilon$ . The derivative of

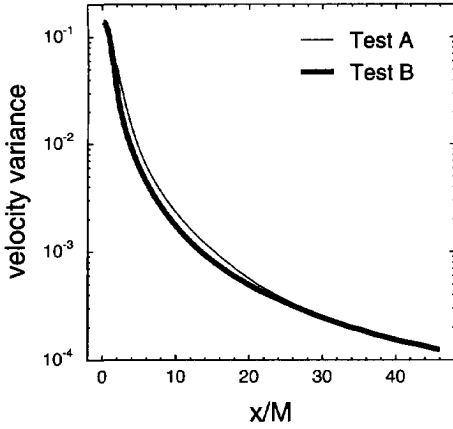


Figure 4.3: Development of the velocity variance

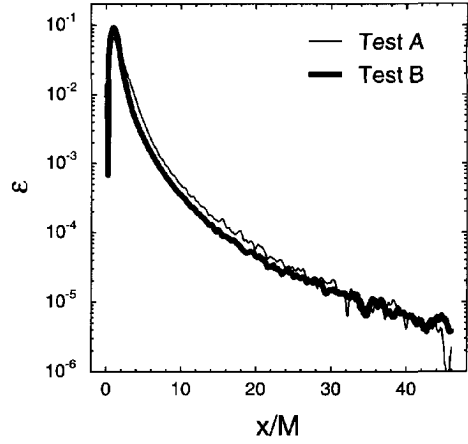


Figure 4.4: Development of the energy dissipation

the velocity variance as a function of the distance from the grid gives us the amount of kinetic energy that the flow loses when it travels a unit distance. The mean flow velocity gives the amount of unit lengths which the decaying flow is travelling per second. Consequently the energy dissipation is given by the following relation:

$$\varepsilon = \frac{1}{2} U_{\text{mean}} \frac{d \left( \overline{u'}^2 \right)}{dx} \quad (4.5)$$

The estimated values are given in figure 4.4. The estimation of dissipation  $\varepsilon$  involves differentiation. Differentiation of the velocity variance data from simulations A and B leads to amplification of small variations in the curves in figure 4.3. This is the reason why the curves in figure 4.4 have some small fluctuations. Kolmogorov's length scale (see section 1.1) is estimated via relation 1.3. The estimates, expressed in mesh-widths  $dx$  used in the calculation, are shown in figure 4.5. We see from figure 4.5 that in simulation A Kolmogorov lengthscale  $\eta$  is smaller than numerical resolution  $dx$  throughout the domain. This implies that in simulation A not all lengthscales present in the flow are fully resolved. Comparison of results of simulation A with experiments is therefore not advisable. Nevertheless, we continue with simulation A. Simulation A may not be physically correct, but it may still provide us with sufficient numerical data, meeting the restrictions which we had set in our unaliasing theory (homogeneity and small anisotropy).

In simulation B the  $\eta$  is only larger than  $dx$  beyond  $x/M = 20$ . We can therefore compare the outcomes of simulation B with experiments in the zone  $x/M > 20$ . The question remains if such a comparison with experiments is allowed, given the fact that in the region  $x/M < 20$  the flow is not well resolved.

The growth of macroscale  $L$ , estimated by means of relation 1.4, is shown in figure 4.6. In figure 4.7, the mean flow distribution as obtained in simulation B is given. We see that a jet-like lateral inhomogeneity is visible to  $x/M = 10$ . The jet-shaped regions transform to long bands, oriented in the mean flow direction.

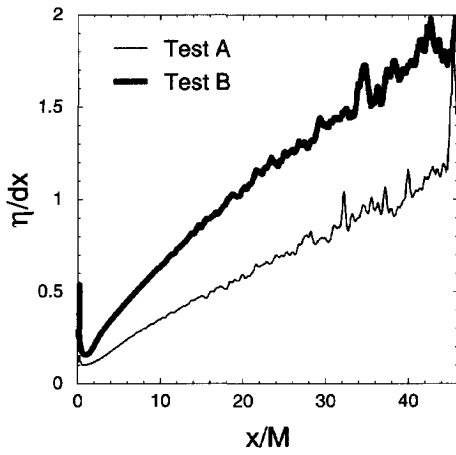


Figure 4.5: Development of the Kolmogorov length-scale expressed in numerical mesh length  $dx$

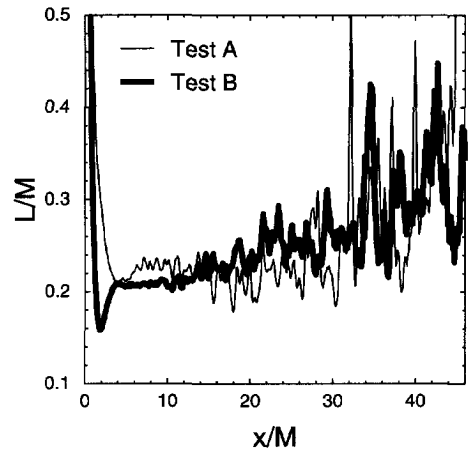


Figure 4.6: Development of the macroscale

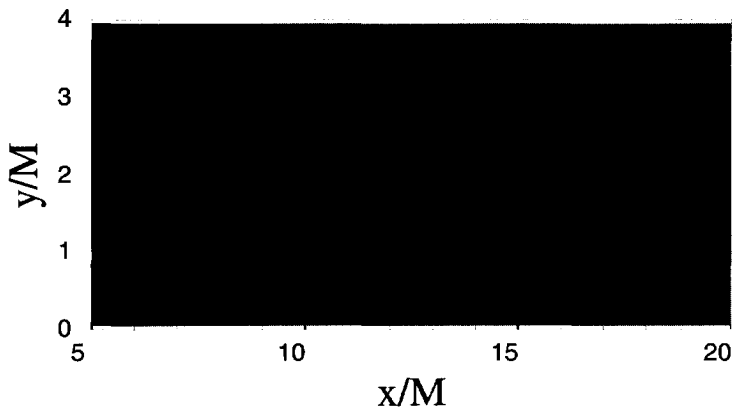


Figure 4.7: Simulation B: development of the mean flow. The contour plot gives qualitative insight into the regions where the mean velocity has a constant value.

### 4.2.1 Lateral homogeneity of the velocity variance

To see whether simulations A and B yield lateral homogeneity, we plot the logarithm of the velocity variance in a cross-section parallel to the mean flow (figures 4.8, 4.9 and 4.10). The choice for a logarithmic plot is made to better illustrate lateral variations over a wide range of variance levels. While observing these cross-sections please keep in mind that the coordinates on the axes are unequal: the ratio of the units is about 1 to 7. From figure 4.8 we see

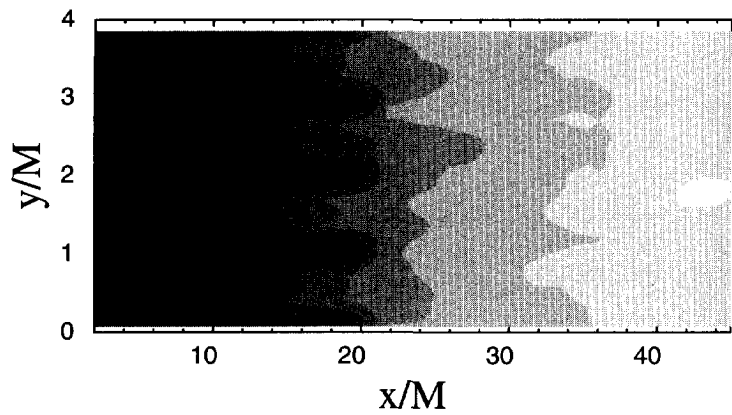


Figure 4.8: Simulation A: development of (the logarithm of) the variance of the velocity

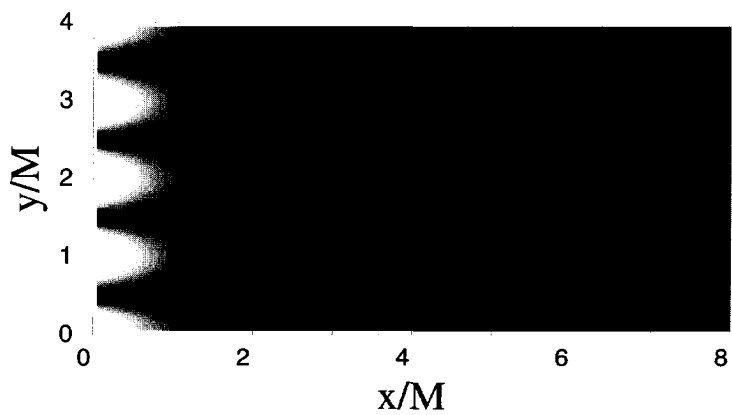


Figure 4.9: Simulation B: development of (the logarithm of) the variance of the velocity: the zone close to the grid

that according to simulation A turbulence energy does not become laterally homogeneous until  $x/M > 20$ . Figures 4.9 and 4.10 from simulation B suggest that simulation A has overestimated the distance at which lateral homogeneity is attained, because in simulation B the velocity variance reaches lateral homogeneity at  $x/M = 4$ . In the tests, which we did on our windtunnel

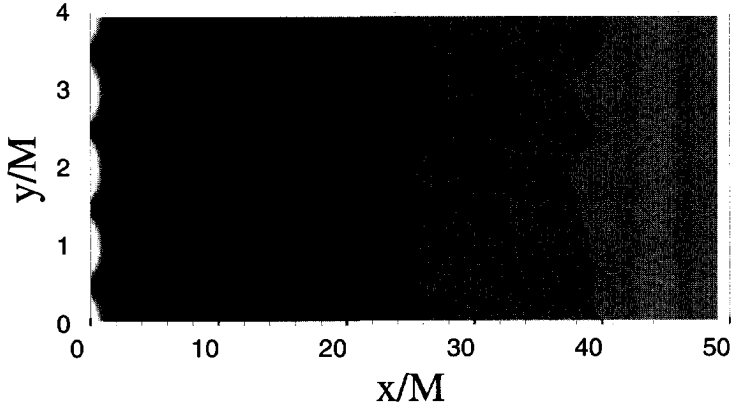


Figure 4.10: Simulation B: development of (the logarithm of) the variance of the velocity

(see figure 5.30 in section 5.7.3.2), we did not find strong lateral inhomogeneity of the velocity variance, which we do see in the DNS-results of simulation A (figure 4.8). Therefore we have a preference for simulation B to simulation A, since the former agrees better with measurements.

#### 4.2.2 Lateral homogeneity of the anisotropy

In addition to the lateral homogeneity of the velocity variance, we will also consider the lateral homogeneity of the rescaled normalised anisotropy invariants of the Reynoldsstress tensor (see appendix C for the definitions of these invariants). Estimates for the rescaled third invariant in a crosssection parallel to the mean flow are presented in figures 4.11 (simulation A) and 4.12 (simulation B). Associated character plots are given in figures 4.13 and 4.14 (the origin in the plots represents isotropy). In agreement with the results from figure 4.8, we find from

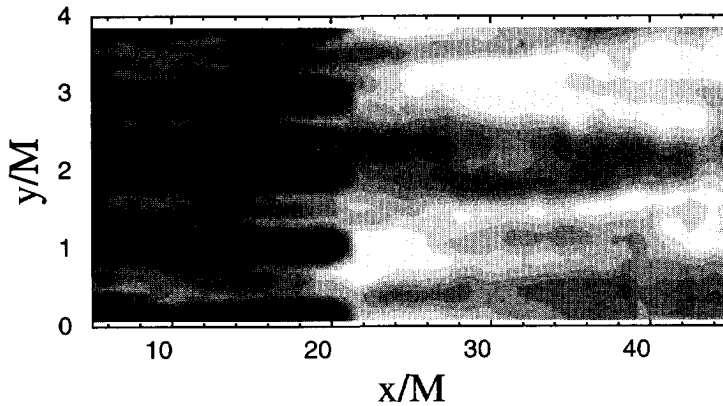


Figure 4.11: Simulation A: development of the rescaled third anisotropy invariant

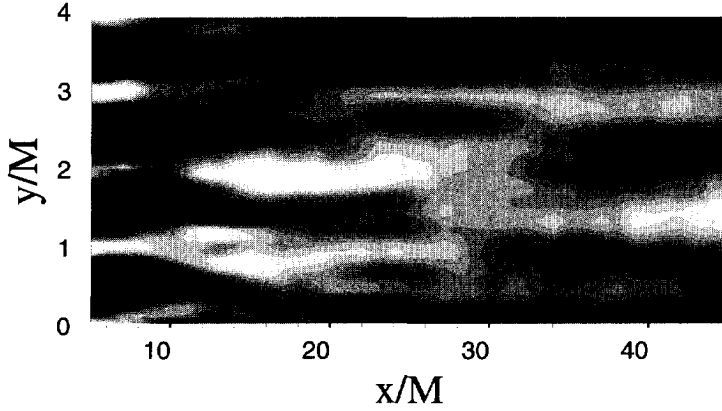


Figure 4.12: Simulation B: development of the rescaled third anisotropy invariant

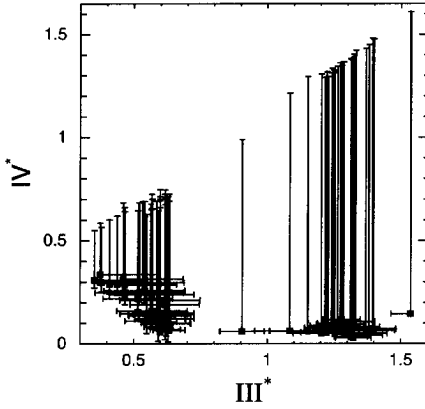


Figure 4.13: Simulation A: character plot for the full computational domain

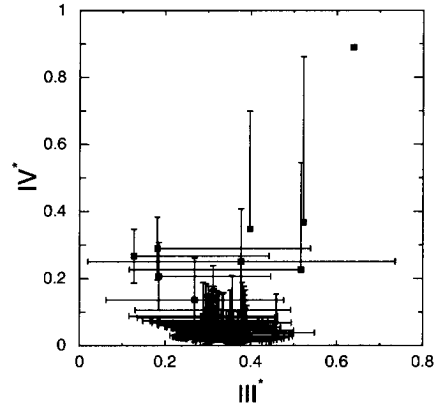


Figure 4.14: Simulation B: character plot for the full computational domain

figure 4.11 that in simulation A the anisotropy character of the flow persists until about  $x/M = 20$ . From there in simulation A the lateral inhomogeneity drops to a much lower level than in the first  $20M$  behind the grid. In simulation B we see that the region behind the grid in which lateral inhomogeneity of the anisotropy character shows a jet-like structure, reaches to  $x/M = 15$ . This is much further than the point where the velocity variance becomes laterally homogeneous. This shows that mean flow dynamics is more efficient in levelling out inhomogeneities in the absolute turbulent energy field, than in the distribution of that energy over the three dimensions. Furthermore we see that in simulation B, after  $x/M = 15$ , the lateral inhomogeneity of the third invariant merely changes from "jets" positioned exactly behind the apertures of the grid, to more or less arbitrarily positioned regions, with a preference for elongation in the mean flow direction. The preference for long bands need not be problem, as long as the probability of their

occurrence is homogeneous. The persistence of those bands on fixed locations after taking the mean value of a great many realizations of the flow may be. This tendency of the third invariant to correlate in longitudinal bands becomes even more apparent when one realizes that the units on the axes in the plot differ by a factor of 7. The character plots show that both for simulation A and for simulation B the anisotropy character is dominantly but not purely axisymmetric (the axis was checked to be the mean flow direction).

### 4.2.3 Magnitude of the anisotropy

Figures 4.11 and 4.12 merely give qualitative information on the distribution of the third invariant. More quantitative information can be found in figures 4.15 and 4.16. The thickness in vertical direction of the black bands in these figures represent one-standard-deviation intervals for the third invariant. From the results plotted in figure 4.15 for the third anisotropy invariant

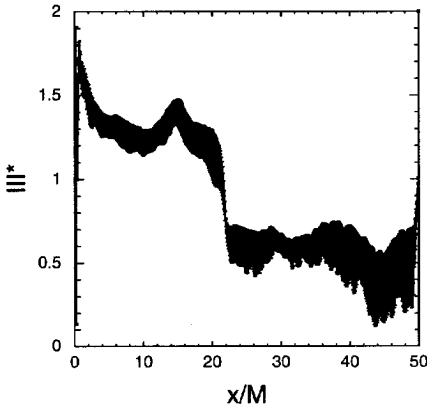


Figure 4.15: Simulation A: one standard deviation intervals for the rescaled third anisotropy invariant

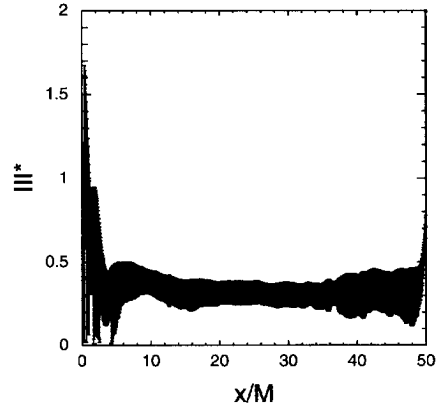


Figure 4.16: Simulation B: one standard deviation intervals for the rescaled third anisotropy invariant

in simulation A, we see that, throughout the domain, one can expect to find a third invariant larger than 0.5. Such a value for  $III^*$  cannot be considered a small deviation from isotropy. We therefore conclude that simulation A gives turbulence with an anisotropic character, which is too large to be of use for the checking of our unaliasing theory, which assumes that the character of the flow deviates only from isotropy by a small parameter. Therefore simulation A will not be used further to test the unaliasing model. Simulations A and B only differ by their spatial resolutions of the flow field. The poor performance of simulation A compared with simulation B must therefore be attributed to this difference. The resolution in simulation A must be too coarse to allow small scale structures to play the crucial diffusive role, which they do play in better resolved simulation B.

In simulation B the third invariant behaves better: for most  $x/M$  it takes values between 0.25 and 0.4. Although this may still be a bit on the large side in order to represent a first order



expansion around isotropy, nevertheless we will use data calculated with simulation B to test the unaliasing model from chapter 2. The results will be discussed in the sections below.

### 4.3 Direct estimation of tensor $\bar{\Psi}$

In this section we will construct direct estimates for wavenumber spectrum  $\bar{\Psi}$ . Here 'direct' means that we just substitute three-dimensional velocity fields in definition 2.65 of  $\bar{\Psi}$ . This is opposed to the indirect estimates, which we will construct via application of the unaliasing theory to simulated one-point measurements. Indirect estimates will be constructed in the following section.

The unaliasing theory is applicable to fully homogeneous fields. From the results found in the former sections we know that in simulation B at  $x/M \sim 30$  the flow is more or less independent from the inflow conditions at the grid, "fairly" homogeneous (laterally) and "weakly" anisotropic. Unfortunately, the flow is strongly inhomogeneous in the mean flow direction. Therefore we cannot use instantaneous vector fields from the simulation to test the unaliasing theory. To resolve the problem of streamwise inhomogeneity, we record all consecutive times (one thousand slices) of the velocity field at  $x/M \sim 30$ , in planes normal to the mean flow direction, on regular time intervals. In the time delay between the recordings of consecutive slices, the mean flow crosses a distance, which is 90 percent of the mesh width of the numerical mesh. We use Taylor's hypothesis 1.13 to convert the recording times of the slices to  $x$ -coordinates. Thus we make a three-dimensional vector field  $\mathbf{u}(\mathbf{x})$ , which is fully homogeneous in the mean flow direction, and which gives information about the behaviour of turbulent gridflow at  $x/M \sim 30$ .

To calculate wavenumber spectral tensor  $\bar{\Psi}$  from  $\mathbf{u}(\mathbf{x})$  we take the following steps:

- The domain of  $1000 \times 80 \times 80$  (staggered) velocity vectors is transformed to a regular orthogonal mesh, where the velocity vectors reside in the centrepoints of the numerical cells, by taking the averages of the values of velocity components on either side of each centre.
- To allow for the calculation of several estimates of the spectrum, which then can be averaged to get better statistical accuracy, the domain is cut into 100 equal subdomains of  $40 \times 40 \times 40$  points. Even though the width (and the height) of the domain is 80 mesh points, no spanwise correlation over a distance larger than half the channel width (and height) may contribute to the spectrum. The reason for this restriction is the periodic boundary condition, which wraps the edges in spanwise direction.
- For each  $40 \times 40 \times 40$  subset of the velocity field we calculate the Fourier transform  $\hat{\mathbf{u}}(\mathbf{k})$  using 3D Fast Fourier algorithm C06FJF from the NAG library (with tapering).
- We calculate the mean value of  $\left( \hat{\mathbf{u}}(\mathbf{k}) \otimes \hat{\mathbf{u}}(\mathbf{k})^* \right)$  over the 1000 subsets. This gives us spectral tensor  $\bar{\Phi}^t(\mathbf{k})$ , defined in relation 2.25. From spectral tensor  $\bar{\Phi}^t(\mathbf{k})$  we estimate  $\bar{\Psi}(\mathbf{k})$  via integration over the surface of spheres with radius  $k$ . This integration is done by sorting  $\bar{\Phi}^t(\mathbf{k})$  by the length  $k$  of wavevector  $\mathbf{k}$  in 325 bins. The step between the bins is one tenth of the smallest wavenumber associated with a  $40^3$  subdomain. Estimates for  $\bar{\Psi}$

in bins into which no  $\bar{\Phi}'(\mathbf{k})$  is mapped, are found by interpolation between neighbouring non-empty bins. The number of contributions of  $\bar{\Phi}$  to the different  $\bar{\Psi}$ -bins is shown in figure 4.17.

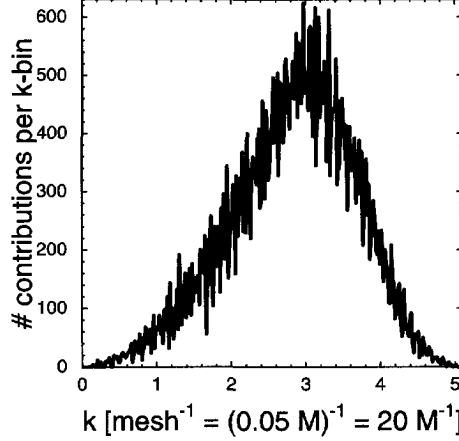


Figure 4.17: Number of contributions  $\Phi(k_1, k_2, k_3)$  to a bin of  $\Psi(|k| \pm 0.5dk)$

Following the above method we find direct estimates for the trace and the third and fourth rescaled anisotropy invariants of wavenumber spectral tensor  $\bar{\Psi}$  (definitions of anisotropy invariants can be found in appendix C). These estimates are shown in figures 4.18, 4.19, 4.20 and 4.21. In these plots the wavenumber is based on the wavelength expressed in numerical meshlengths  $dx = 0.05M$ . The smallest wavenumber is 0.09 and corresponds with a diagonal wave (in the direction of  $(1, 1, 1)$ ) with length  $2M$  in all three directions. The corresponding character plot is shown in figure 4.22.

From figure 4.19 we see that nearly all of the fluctuation energy can be found in waves with a wavenumber smaller than  $k \sim 0.7$ , which corresponds with wavelengths larger than  $0.45M$ . This preference of the fluctuating energy for long waves can also be seen in figure 4.18, where for the shorter waves the energy falls with the thirteenth power of the wavenumber. This feature does not correspond with grid-generated turbulence in practice, where, for the higher wavenumbers, the exponent of decay does not become stronger than  $-4$ , and where there is a large portion of the spectrum with a  $-5/3$ -exponent (see our results in chapter 7). The large exponent in our DNS-spectra may be related to turbulence, which is not fully developed. This suggestion can be verified with a set of energy spectra at several distances from the grid. Hinze (Hinze, 1975, p.262) shows that, if the high wavenumber range in the spectrum is in equilibrium, then that part of the spectrum is 'self-preserved'. One can test the high wavenumber range of the spectrum for self-preservation by rescaling the spectra with dissipation  $\epsilon$  and viscosity  $\nu$  (Hinze, 1975, p.223). For a self-preserving turbulent flow this scaling will make the spectra to collapse on a single curve. In our simulation we have not collected spectra at different positions from the grid, and we therefore can not give evidence if the fast decay of the spectrum in the simulation is related to the turbulence not being fully developed.

Concerning the anisotropy of  $\bar{\bar{\Psi}}$ , the direct estimation method provides us with the following information: from figures 4.20, 4.21 and 4.22 we see that for every wavelength the contribution to the fluctuating velocity field is moderately anisotropic (invariants mostly smaller than 0.3) and axisymmetrically elongated (definitions of invariants and character plot are given in appendix C). Elongation was checked to be in the mean flow direction (by observation of  $\bar{\bar{\Psi}}$ 's eigenvectors).

The absolute value of the swirl-fraction (defined in relation 2.39) was estimated to be smaller than  $10^{-12}$  for all wavenumbers. From this estimate we conclude that the flow in our DNS contains no net swirl. This conclusion is consistent with the boundary conditions and the dynamical equations in the simulation: they are invariant under reflections in two planes along the mean flow, perpendicular to the (periodic) boundaries of the "simulation tunnel".

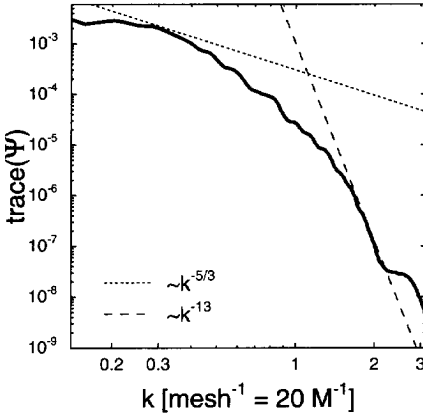


Figure 4.18: Direct estimate for the trace of the wavenumber spectral tensor: double logarithmic plot.

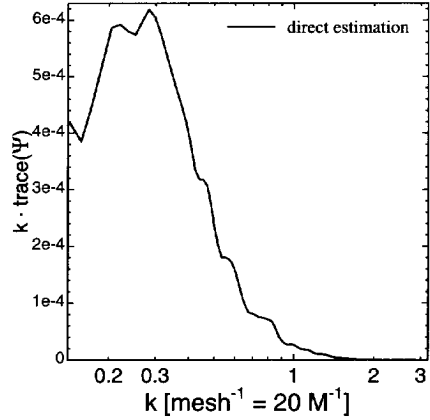


Figure 4.19: Direct estimate for the trace of the wavenumber spectral tensor: the surface is proportional to the energy content

## 4.4 Indirect estimation of tensor $\Psi$ with unaliasing theory

In this section we consider estimates of wavenumber spectral tensor  $\bar{\bar{\Psi}}$  via simulated one-point measurement. We will first compute one-point spectral tensor  $\bar{\bar{\Theta}}$  from our DNS-data. Then we will apply the unaliasing theory, developed in chapter 2, to tensor  $\bar{\bar{\Theta}}$  to construct estimates for wavenumber spectral tensor  $\bar{\bar{\Psi}}$ .

### 4.4.1 Estimation of one-point spectrum $\Theta$

In section 3.6.4 it was argued that by using AR-based spectra one can only estimate diagonal terms in the cospectral tensor. Not only the AR-method to estimate spectral derivatives, but

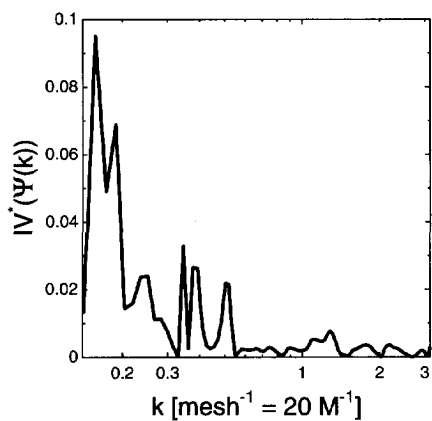


Figure 4.20: Direct estimate for the rescaled fourth anisotropy invariant of the wavenumber spectral tensor

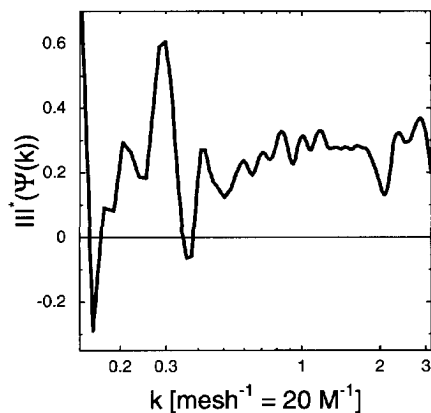


Figure 4.21: Direct estimate for the rescaled third anisotropy invariant of the wavenumber spectral tensor

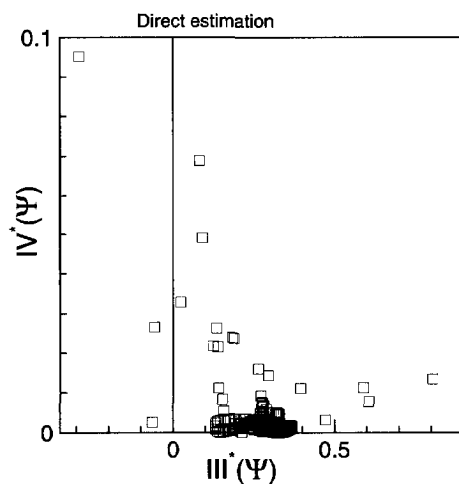


Figure 4.22: Character plot for the direct estimates of the wavenumber spectral tensor

also the double-logarithmic polynomial method presented in section 3.9.1 is restricted in its application to diagonal elements. Off-diagonal terms in a spectral tensor indicate that the principal axes of the tensor do not coincide with the axes of the frame of reference. In our DNS we have taken the axes of reference along the mean flow, and along the two lateral directions. In ideal isotropic turbulence, any orthogonal frame of reference is a frame of eigenvectors. In the frame of eigenvectors the spectral tensor does not have off-diagonal elements, which allows for the reduction of the calculation to diagonal elements. In the former section we have shown that wavenumber spectral tensor  $\bar{\Psi}$  is not isotropic, but fortunately has its principal axes along the frame of reference, which we have chosen for the simulation. Consequently we can safely restrict the calculation of spectral tensors to their diagonal elements.

The dataset of  $1000 \times 80 \times 80$  velocity vectors, which was constructed using Taylor's hypothesis in section 4.3, is partitioned into 64 rectangular subsections of  $250 \times 20 \times 20$  nodes. For each subsection, velocity vectors along the  $20 \times 20$  rows of 250 nodes in mean flow direction are considered to be recordings of one-point measurements (which, in fact, they are).

Velocity vectors along the 400 rows are used to construct two different estimates for  $\bar{\Theta}$  and its first, second and third derivatives. The first construction is made via the FFT-based method explained in section 3.9.1: a polynomial is fitted to the smoothed double-logarithmic plot of the diagonal elements of the spectrum. The autoregressive method of section 3.9.2, which implements analytic differentiation of a fitted AR-model, is used to generate the second estimate of  $\bar{\Theta}$ . The estimates for  $\bar{\Theta}$ 's trace and rescaled third and fourth anisotropy invariants, which are thus found, are presented in figures 4.23, 4.24, 4.25, 4.26, 4.27 and 4.28. A detailed look at the plot of the AR-results for the rescaled anisotropy invariants of the one-point spectrum reveals that, for certain low wavenumbers, no estimates are given. These omissions are caused by the large values of these estimates: they are close to their one-dimensional values (the right side of the character plot).

Spectra  $\bar{\Psi}$  and  $\bar{\Theta}$ , for which we now both constructed direct estimates, represent different quantities. Our study is the first to provide a means to relate these two spectra. This means that until now researchers had to restrict their interpretations of one-point measurements to contemplations of  $\bar{\Theta}$ , hoping that it would somehow still reflect the character of  $\bar{\Psi}$ . We therefore compare the figures for  $\bar{\Theta}$  with the direct estimates for  $\bar{\Psi}$ , which were constructed in the former section, to see which aspects of  $\bar{\Psi}$ 's character are correctly revealed by  $\bar{\Theta}$ , and which significant differences can be found. We draw the following conclusions:

- The energy content in  $\bar{\Theta}$  is much smaller than in  $\bar{\Psi}$ . This difference may be attributed to the absence of lateral fluctuations in  $\bar{\Theta}$ , which do contribute to the direct estimate for  $\bar{\Psi}$ . According to figures 4.7 and 4.12 the flow is not fully homogeneous in the lateral direction, and the inhomogeneities have a preference for long, streamwise coherency. The consequence of this streamwise ordering of lateral inhomogeneities is that the mean velocity of lines of vectors in the mean flow direction will differ from line to line. When the spectrum is estimated from a (simulated) one-point measurement, then the mean value of the velocity *along that specific line* is subtracted from the line of velocity vectors. In this way, the fluctuation of the mean velocity vector from line to line, which represents energy, will be discarded. As a result, the energy found in  $\bar{\Theta}$  will be smaller than in  $\bar{\Psi}$ . The reason to subtract the mean along a line, instead of the mean of the full velocity field

is that the same procedure is normally applied to real one-point measurements, where one has the velocity only on a line.

- The strong exponent in the high wavenumber segment of the direct estimate for the wavenumber spectral tensor (found to be -13), is found back in the one-point spectral tensor (figures 4.18 and 4.23).
- At low frequencies ( $k < 0.7 \Rightarrow \lambda \equiv 2\pi/k > 0.45M$ ), the autoregressive estimates give much higher values for the energy than the FFT-based estimates. This difference can be caused by either of the two estimation procedures:
  - The FFT-based method shoots a polynomial through the double-logarithmic plot of the spectrum, and consequently takes the risk of losing relevant energy.
  - Furthermore, the FFT-based method incorporates high-pass filtering followed by tapering. Both filtering and tapering suppress the low wavenumber part of the spectrum.
  - The AR-based method of spectral estimation is based on (partial) correlation coefficients, which are distributed linearly, and where the minimum delay is taken to be the delay between two neighbouring samples. The longest structures in the signal take place on scales which are an order of magnitude larger than the longest partial correlation coefficient in the AR-model. As an example we give a fourth order linear AR-model:

$$u(t) = a_1u(t - \tau) + a_2u(t - 2\tau) + a_3u(t - 3\tau) + a_4u(t - 4\tau) + \text{white noise} \quad (4.6)$$

where  $\tau$  is Kolmogorov's timescale. The consequence of the adopted linear distribution of partial correlation coefficients is that the long structures in the signal must still be consequences of these short correlations, with a maximum delay of  $4\tau$ . The contributions to the correlation function, associated with the terms in this model decay exponentially with delay. Hence it is mathematically correct that, even at a delay equal to the characteristic time of the largest, slowest structures, the correlation function is non-zero. One can consider the coefficients in model 4.6 the generators of the correlation function in the full domain of interest, and claim that the full correlation function is modelled.

Logarithmically distributed partial correlations may be useful to circumvent this problem:

$$u(t) = a_1u(t - c^0\tau) + a_2u(t - c^1\tau) + a_3u(t - c^2\tau) + a_4u(t - c^3\tau) + \text{white noise} \quad (4.7)$$

where  $c$  is a positive constant. When we take  $c = 10$  we have the following model:

$$u(t) = a_1u(t - \tau) + a_2u(t - 10\tau) + a_3u(t - 100\tau) + a_4u(t - 1000\tau) + \text{white noise} \quad (4.8)$$

we see that the model parameters of a logarithmic AR-model give the model a memory over a much wider range of timescales than a linear AR-model. Unfortunately there is no theory about logarithmic AR-models. We constructed a logarithmic AR-model, where the coefficients were solved using the Yule-Walker method. The resulting spectral estimates gave much better representation of the energy at low wavenumbers than the conventional AR-method. To our regret, the

estimates were not as smooth as the classic AR-estimates. Therefore we could not apply the logarithmic autoregressive model to the estimation of spectral derivatives. Consequently we will not use logarithmic autoregressive modelling in this study.

- There is a strong difference between the estimates for the anisotropy characters of  $\bar{\Psi}$  and of  $\bar{\Theta}$ . The axisymmetry, which was found for all wavenumbers in the direct estimate for  $\bar{\Psi}$  (figure 4.22), is conserved in the FFT-based estimate for  $\bar{\Theta}$  (figure 4.27): in either character plot all estimates are on the lower boundary of the plot. The AR-based estimates, which have larger inaccuracies than the FFT-based estimates, show a band of estimates which are "nearly axisymmetric" (figure 4.28). For high wavenumbers ( $k > 1 \Rightarrow \lambda < 0.3M$ ) the FFT- and AR-based estimates in figures 4.25 and 4.26, for respectively the fourth- and third invariants, agree.

Where the direct estimate for the wavenumber spectral tensor indicated an elongated axisymmetric anisotropy (the third invariant in figure 4.21 is positive), the one-point spectral tensor's anisotropy character tends to "pancake" anisotropy when the wavelength is smaller than  $0.5M$  (the third invariant in figure 4.26 is negative). This is the first time in this research that we actually see the effects of aliasing in one-point measurements: One-point measurements estimate a tendency in small structures to *suppress* the velocity in the mean flow direction. On the other hand, the direct estimate of what really are small structures, found via a full three-dimensional "measurement" of the velocity vector in all points of the domain, indicates that in reality the small scale movements are *favoured* in the mean flow direction.

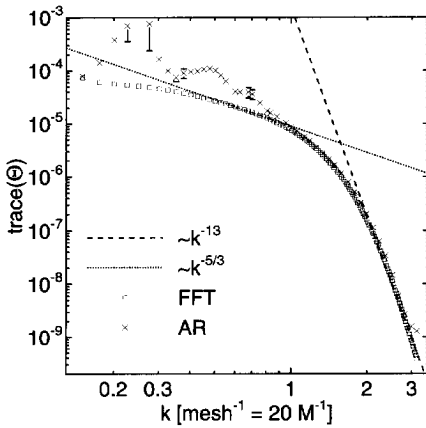


Figure 4.23: Estimates for the trace of the one-point spectral tensor: double logarithmic plot

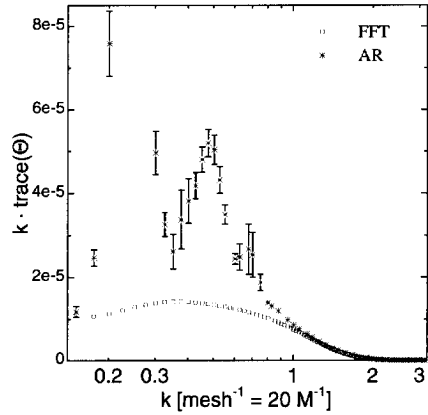


Figure 4.24: Estimates for the trace of the one-point spectral tensor: the surface is proportional to the energy content

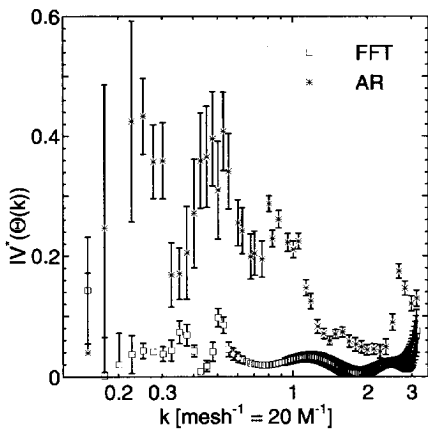


Figure 4.25: Estimates for the rescaled fourth anisotropy invariant of the one-point spectral tensor

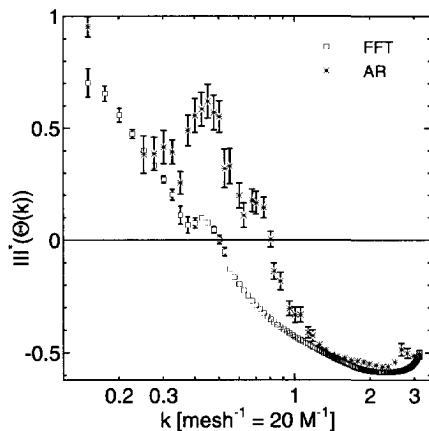


Figure 4.26: Estimates for the rescaled third anisotropy invariant of the one-point spectral tensor

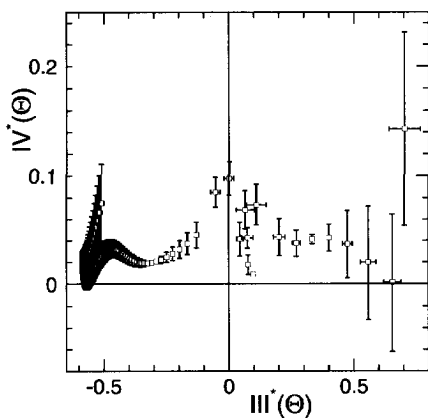


Figure 4.27: Character plot for the one-point spectral tensor: FFT-based estimates

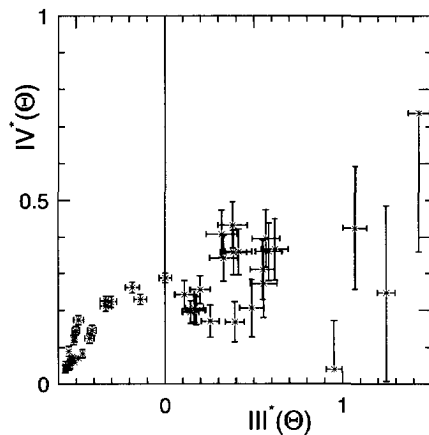


Figure 4.28: Character plot for the one-point spectral tensor: AR-based estimates



#### 4.4.2 From $\Theta$ to $\Psi$

Relations 2.122, 2.133 and 2.134 are used to estimate  $\bar{\Psi}$  from  $\bar{\Theta}$ . To find out which terms in these relations are most significant, we name the terms in these relations *Term 1* to *Term 14* as follows:

$$\begin{aligned} \Psi_{11} = & \underbrace{-\frac{1}{5}k^3\Theta_{11}'''}_{\text{Term 1}} + \underbrace{k^2 \left( \frac{4}{15}\Theta_{11} - \frac{1}{5}\Theta_{22} - \frac{1}{5}\Theta_{33} \right)''}_{\text{Term 2}} - \underbrace{k \left( \frac{4}{15}\Theta_{11} + \frac{1}{5}\Theta_{22} + \frac{1}{5}\Theta_{33} \right)'}_{\text{Term 3}} \\ & + \underbrace{\frac{2}{5}(\Theta_{22} + \Theta_{33})}_{\text{Term 4}} - \underbrace{\frac{2}{5}k \int_k^\infty x^{-2}(\Theta_{22} + \Theta_{33})dx}_{\text{Term 5}} \end{aligned} \quad (4.9)$$

$$\begin{aligned} (\Psi_{11} - \Psi_{22}) = & \underbrace{-\frac{2}{15}k^3\Theta_{11}'''}_{\text{Term 6}} + \underbrace{k^2 \left( \frac{2}{5}\Theta_{11} - \frac{2}{15}\Theta_{22} - \frac{2}{15}\Theta_{33} \right)''}_{\text{Term 7}} \\ & + \underbrace{k \left( -\frac{2}{5}\Theta_{11} + \frac{16}{15}\Theta_{22} \right)'}_{\text{Term 8}} - \underbrace{\frac{22}{15}\Theta_{22} + \frac{2}{3}\Theta_{33}}_{\text{Term 9}} \\ & + \underbrace{\frac{2}{5}k \int_k^\infty x^{-4}(3x^2 + 2k^2)\Theta_{22}dx}_{\text{Term 10}} - \underbrace{\frac{2}{5}k \int_k^\infty x^{-4}(x^2 + 2k^2)\Theta_{33}dx}_{\text{Term 11}} \end{aligned} \quad (4.10)$$

$$\begin{aligned} (\Psi_{22} - \Psi_{33}) = & \underbrace{-\frac{16}{15}k(\Theta_{22} - \Theta_{33})'}_{\text{Term 12}} + \underbrace{\frac{32}{15}(\Theta_{22} - \Theta_{33})}_{\text{Term 13}} \\ & - \underbrace{\frac{8}{5}k \int_k^\infty x^{-4}(x^2 + k^2)(\Theta_{22} - \Theta_{33}) dx}_{\text{Term 14}} \end{aligned} \quad (4.11)$$

We estimate terms 1 to 14 as follows: the 64 estimates for  $\bar{\Theta}(k)$ ,  $\frac{d}{dk}\bar{\Theta}(k)$ ,  $\frac{d^2}{dk^2}\bar{\Theta}(k)$  and  $\frac{d^3}{dk^3}\bar{\Theta}(k)$ , which were constructed in the former section, are used to estimate terms 1 to 14 and their respective accuracies. The resulting indirect estimates (found via unaliasing) for wavenumber spectral tensor  $\bar{\Psi}$  are given in figures 4.29 (double-log energy plot), 4.30 (surface-proportional energy plot), 4.31 (fourth anisotropy invariant), 4.32 (third anisotropy invariant), 4.33 and 4.34 (character plots). The ratio of the absolute value of terms 1 to 14 to the trace of  $\bar{\Psi}$  is presented in figures 4.35 to 4.42.

From the relative contributions of terms 1 to 14 in figures 4.35 to 4.42 we draw the following conclusions:

- The data in figures 4.41 and 4.42 points out that the flow has no preference for either lateral direction: the relative contribution to the energy of the difference between fluctuations in the lateral directions is not more than a few percent. As a result terms 12, 13 and 14 are negligible.
- From figure 4.36 we see that terms 1 and 6, which represent the third (and highest order) derivative of the one-point spectrum and which are equivalent up to a factor, dominate

the AR-based estimates for structures with wavelength larger than  $0.3M$ . Moreover, the error-bars associated with these terms in this region are so large that the AR-estimates are completely spoilt in this wave-region. In figure 4.35 we see that, according to the FFT-based estimates, the third order derivative of the one-point spectrum dominates the energy of the wavenumber spectrum. This implies that, in this particular simulation:

$$\Psi_{11} \simeq -\frac{1}{5}k^3\Theta_{11}''' \quad (4.12)$$

- In general we can conclude that the higher the order of a derivative involved in a term, the more important the relative contribution of that term to the energy content of the wavenumber spectral tensor. This implies that the construction of an accurate method for the estimation of spectral derivatives is crucial for the applicability of the unaliasing theory. The necessity for good estimation procedures for higher order derivatives is a drawback for the applicability of the unaliasing model to the DNS-data in this study: differentiation is difficult because small wiggles tend to grow rapidly in differentiation.

When we observe the indirectly estimated wavenumber spectrum's energy and its anisotropy, we find:

- The energy distribution of the indirect estimate of  $\bar{\Psi}$  (figures 4.29 and 4.30) does not show resemblance with its direct estimate (figures 4.18 and 4.19), though the exponent of decay in the high wavenumber range ( $\sim k^{-13}$ ) is found back.
- The axisymmetry of the spectrum is correctly estimated: virtually all point in figures 4.33 and 4.34 are found on the lower boundary of the diagram.
- In qualitative sense we can say that application of the unaliasing theory on one-point measurements gives a better characterisation of the structures in the flow, than the one-point spectral tensor. From figures 4.33 and 4.34 we see that nearly all structures are axisymmetrically elongated. This is an improvement to the on-point spectrum, which showed a tendency for the small scale structures to adopt a "pancake"-shaped velocity distribution.
- The anisotropy character of  $\bar{\Psi}$ 's indirect estimate does not make a quantitative match with its direct estimate. The invariants of the indirect estimate fluctuate much stronger with wavenumber than those of the direct estimate.
- There is much scatter in the autoregressive estimates. The low scatter in the AR-estimates in the low-wavenumber range is related to unrealistically high estimates for the energy in this region.
- A few points in figures 4.33 and 4.34 lie outside the bounding curves of the character plot. This indicates that the unaliasing theory does not intrinsically guarantee realisability: estimated diagonal elements of the spectrum can become negative.

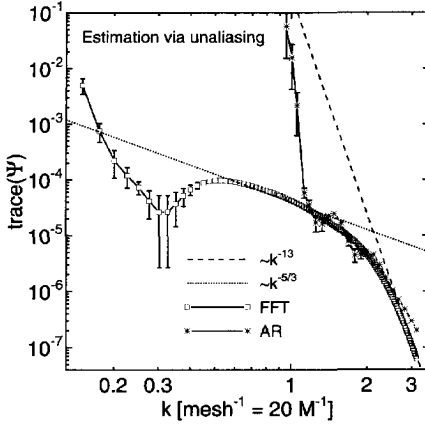


Figure 4.29: Indirect estimates for the trace of the wavenumber spectral tensor, found via unaliasing of the one-point spectral tensor: double-log plot

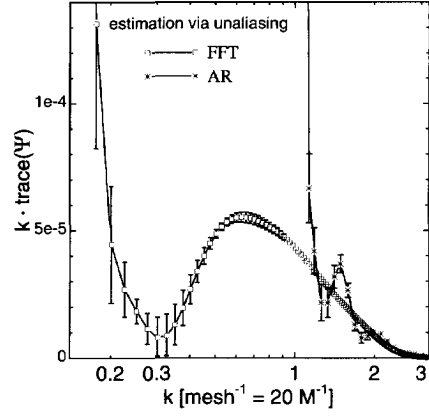


Figure 4.30: Trace( $\Psi$ ), surface is proportional to the energy content

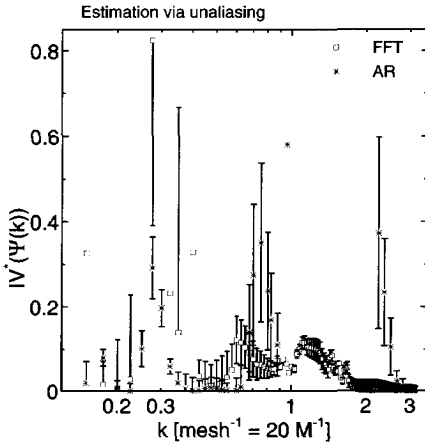


Figure 4.31: Indirect estimates for the rescaled fourth anisotropy invariant of the wavenumber spectral tensor

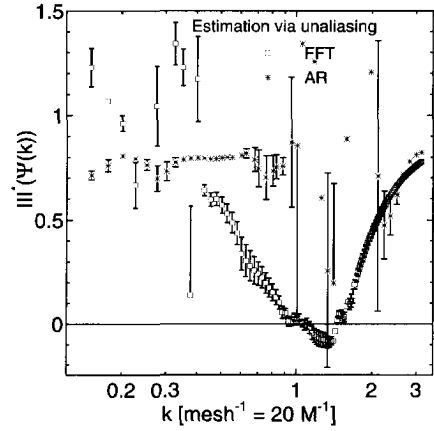


Figure 4.32: Indirect estimates for the rescaled third anisotropy invariant of the wavenumber spectral tensor

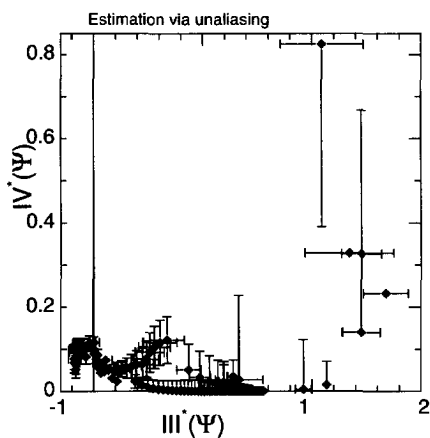


Figure 4.33: Character plot for the indirect estimates of the wavenumber spectral tensor: FFT-based estimates

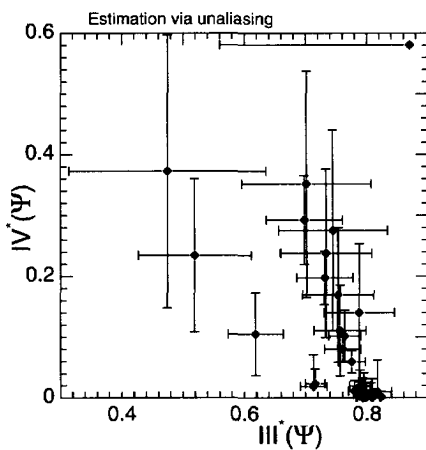


Figure 4.34: Character plot for the indirect estimates of the wavenumber spectral tensor: AR-based estimates

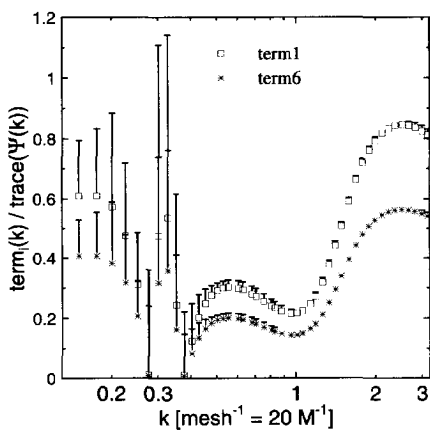


Figure 4.35: Ratio of the norm of terms 1 and 6 to  $\text{Trace}(\Psi)$ : FFT-based estimates

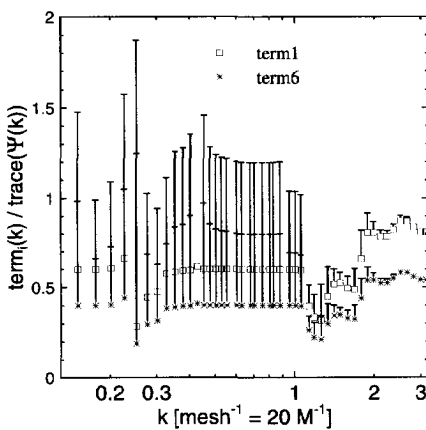


Figure 4.36: Ratio of the norm of terms 1 and 6 to  $\text{Trace}(\Psi)$ : AR-based estimates

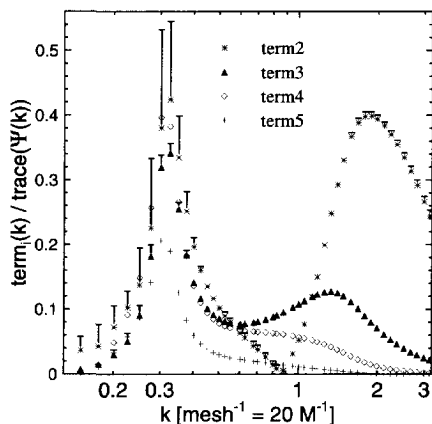


Figure 4.37: Ratio of the norm of terms 2,3,4 and 5 to  $\text{Trace}(\Psi)$ : FFT-based estimates

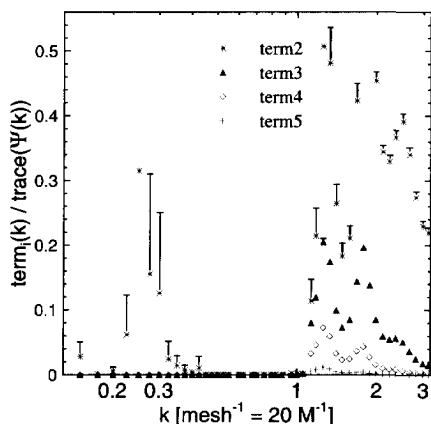


Figure 4.38: Ratio of the norm of terms 2,3,4 and 5 to  $\text{Trace}(\Psi)$ : AR-based estimates

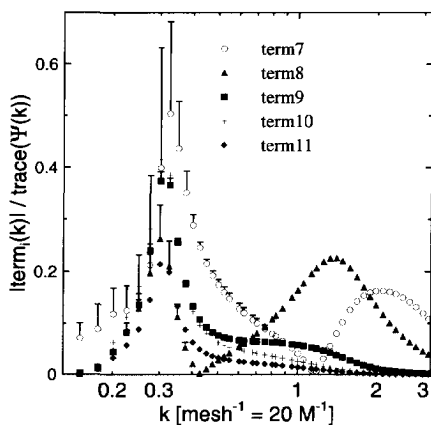


Figure 4.39: Ratio of the norm of terms 7,8,9,10 and 11 to  $\text{Trace}(\Psi)$ : FFT-based estimates

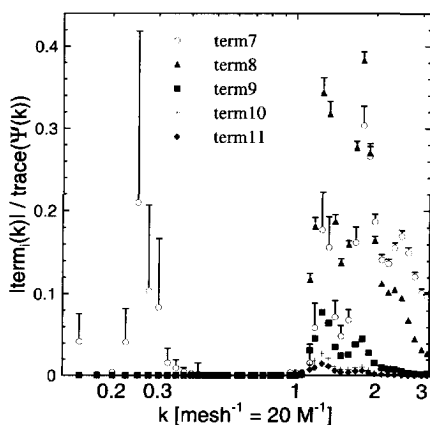


Figure 4.40: Ratio of the norm of terms 7,8,9,10 and 11 to  $\text{Trace}(\Psi)$ : AR-based estimates

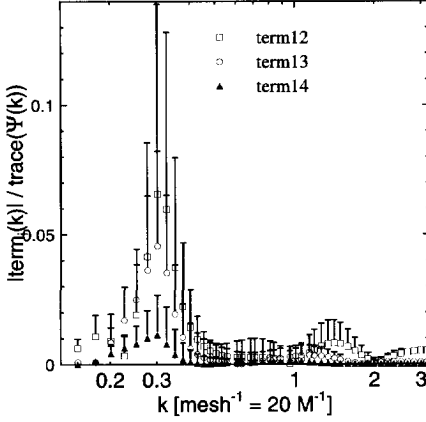


Figure 4.41: Ratio of the norm of terms 12,13 and 14 to Trace( $\Psi$ ): FFT-based estimates

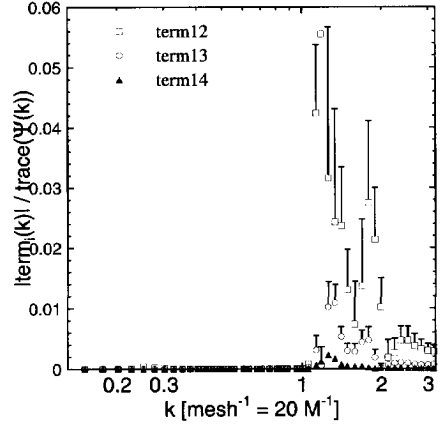


Figure 4.42: Ratio of the norm of terms 12,13 and 14 to Trace( $\Psi$ ): AR-based estimates

### 4.4.3 Asymptotic theory

In the former subsection we have seen that application of the full unaliasing relations to DNS-data does not give satisfactory result. We will now try to find asymptotic relations for  $\bar{\Psi}$  as function of  $\bar{\Theta}$ , when the wavenumber is large. In the high wavenumber part of the spectrum, we describe spectra  $\bar{\Theta}$  and  $\bar{\Psi}$  with axisymmetric power laws:

$$\Theta_{11}(k) = \frac{1}{3} \text{Trace}(\bar{\Theta}) (1 + III^*(\bar{\Theta})) k^n \quad (4.13)$$

$$\Theta_{22}(k) = \Theta_{33}(k) = \frac{1}{3} \text{Trace}(\bar{\Theta}) \left(1 - \frac{1}{2} III^*(\bar{\Theta})\right) k^n \quad (4.14)$$

$$\Psi_{11}(k) = \frac{1}{3} \text{Trace}(\bar{\Psi}) (1 + III^*(\bar{\Psi})) k^n \quad (4.15)$$

$$\Psi_{22}(k) = \Psi_{33}(k) = \frac{1}{3} \text{Trace}(\bar{\Psi}) \left(1 - \frac{1}{2} III^*(\bar{\Psi})\right) k^n \quad (4.16)$$

After substitution of these models for  $\bar{\Theta}$  and  $\bar{\Psi}$  at high wavenumbers in unaliasing relations 4.9 and 4.10 we find:

$$III^*(\bar{\Psi}) = 2 \frac{\Psi_{11} - \Psi_{22}}{\Psi_{11} + 2\Psi_{22}} \quad (4.17)$$

$$= \frac{4 \left( -n^3 + 4n^2 + 2n - 6 - \frac{6}{n-1} \right) + 2III^*(\bar{\Theta}) \left( -2n^3 + 14n^2 - 3n + 6 + \frac{6}{n-1} \right)}{5 \left( -n^3 + n^2 - 10n + 12 + \frac{12}{n-1} \right) + III^*(\bar{\Theta}) \left( -5n^3 + 20n^2 + 8n - 30 - \frac{30}{n-1} \right)} \quad (4.18)$$

With  $n = 13$ , the value, which we found in the high wavenumber range of the DNS-spectra, this relation gives:

$$III^*(\bar{\Psi}, n = 13) = 0.91 \frac{1 + 1.20III^*(\bar{\Theta})}{1 + 1.14III^*(\bar{\Theta})} \simeq 0.91 \left( 1 + 0.06III^*(\bar{\Theta}) \simeq 0.91 \right) \quad (4.19)$$

From the last equality we see that in our simulation the exponent of the high wavenumber spectrum is so high that the third invariants of  $\bar{\Theta}$  and of  $\bar{\Psi}$  are almost decoupled: the unaliasing relations suggest an estimate for the third invariant of  $\bar{\Psi}$  of about 0.91, independent from which third invariant one may have found in one-point spectrum  $\bar{\Theta}$ . This is a characteristic of this particular simulation and it may explain why the unaliasing theory applied to our DNS-data gives poor results.

In many experiments one finds an exponent  $n = -5/3$  in the high wavenumber region of the spectrum (inertial subrange). With  $n = -5/3$  relation 4.18 gives:

$$III^*(\bar{\Psi}, n = -\frac{5}{3}) = 0.22 \frac{1 + 1.64III^*(\bar{\Theta})}{1 + 0.30III^*(\bar{\Theta})} \simeq 0.22 \left( 1 + 1.34III^*(\bar{\Theta}) \right) \quad (4.20)$$

This relation for a  $-5/3$ -spectrum depends non-trivially on the third invariant of the one-point spectrum.

Asymptotic analysis may also be developed for the low wavenumber region. In this region the turbulent energy depends on wavenumber via a fourth power:  $\bar{\Psi}(k \downarrow 0) \sim k^4$  (see e.g. Batchelor (1953, p.37)). This fourth order dependence of the energy calls for the inclusion of terms up to and including fourth order terms in the expansion of the unaliasing relations. We leave this laborious work to a future study.

## 4.5 Discussion and conclusion

Concerning the DNS-study, which was carried out in this chapter, to compare direct and indirect estimation of the wavenumber spectral tensor we draw the following conclusions:

- Axisymmetry is conserved throughout the analysis, but quantitative agreement between the two estimates is absent. In general terms we see that application of the unaliasing theory gives a more realistic vision on the anisotropy character present in the flow than the "unrefined" spectral tensor of one-point measurements.
- One gets the impression that the problems are stronger for the low wavenumber range than for the high wavenumber range. Only for high wavenumbers the two methods of estimation (FFT and AR) agree. From this inconsistency in the estimation procedure we infer that no statement about the low wavenumber range in this specific simulation will make sense unless a more robust way to estimate spectral derivatives for long waves is developed.
- The comparison of direct estimates of the wavenumber spectral tensor and indirect estimates via application of the unaliasing theory to simulated one-point measurements is not satisfactory.

Possible causes for the poor performance of the unaliasing method in the DNS-simulation in this chapter are:

- **Too coarse numerical mesh** Velocity gradients can only be represented with a limited accuracy. At the inflow side of the DNS-domain it may be necessary for a good simulation of turbulent flow, to have a high resolution of the velocity field, in order to catch all details of the chaotic generation process of the fluctuating part of the flow. With a coarse resolution, the shortest waves, with a wavelength of two numerical mesh lengths, will be easily dissipated by the numerical evolution scheme. Mesh refinement will help to solve this problem of unwanted dissipation of relevant small lengthscales, before they have helped to generate an equilibrium in the spectrum.
- **Poor statistics** The test in this chapter included only a few macroscales. We could have collected much more 2D-slices of velocity vectors. Not to estimate the spectrum for even bigger structures (since they are limited in spanwise direction), but to get better statistics for the lower wavenumbers. This proposition was not adopted in view of the unrealistically large computational resources that would be needed in the effort, regarding the numerical setup in our laboratory.
- **Reynolds number too low** Maybe a Reynolds number of 1000 is too low for gridflow to produce significant turbulence. To solve this problem, one will (once again) have to use a finer mesh, or a spectral model.
- **Too coarse turbulence generating grid** In spanwise direction there were only four grid cells. With the periodic boundary conditions the maximum correlation length in spanwise direction amounted to a mere  $2M$  (larger correlation distances than  $2M$  are wrapped via the boundaries to give a shorter correlation distance than  $2M$ ). This largest correlation length is not much larger than the largest observed macroscale in the flow ( $\sim 0.4M$ ). The macroscale is not per definition the largest scale in the flow. Consequently there will be structures in the flow, with (large) sizes such that their dynamical behaviour is influenced by the periodicity of the boundaries. The small number of laterally independent large scale structures will give these structures a poor dynamics. This reduced dynamics may have reduced the development of small scale structures, which could explain the strong drop of the spectrum at the high wavenumbers.
- **Lateral inhomogeneity** In the list of conclusions about one-point spectrum  $\bar{\Theta}$  in section 4.4.1 it was explained that the lateral inhomogeneity of the mean velocity, which is organised in bands along the mean flow direction, will reduce the contribution of large scales to the wavenumber spectrum.
- **Too strong decay** The spectrum was found to decay with frequency following a  $k^{-13}$ -behaviour. The consequence of this large exponent is that this exponent will turn into an extra multiplicative factor with each differentiation. A third order derivative is the highest order in the unaliasing theory. In a  $k^{-13}$ -spectrum the relative importance of this term will be larger than the same term in a  $k^{-5/3}$ -spectrum by a factor  $13^3/1.67^3 = 475$ . This is a large factor. In the following chapter we will perform measurements, where we expect to find  $k^{-5/3}$ -behaviour. It may well be that in these measurements the relative importance



of the higher order derivatives, which are clearly difficult to estimate, is substantially less than in the DNS of this chapter. Therefore we still have hope that the unaliasing theory will be applicable to data from windtunnel measurements. An indication that this conjecture may be correct is given at the end of the former section. There the difference in asymptotic behaviour for high wavenumbers is studied in the relation between third anisotropy invariants of  $\bar{\Theta}$  and  $\bar{\Psi}$ . It was shown that with an exponent of -13, the two invariants are almost decoupled, whereas with an exponent of -5/3 the relation is non-trivial.

- **Limited validity of Taylors hypothesis** To obtain a flow-field which is fully homogeneous, Taylor's hypothesis was invoked to glue slices of velocity vectors in a plane normal to the mean flow, at a constant distance from the grid at the inlet, but at different times, together to a 3D field. In the actual flow we have seen that e.g. the variance of the fluctuating velocity decays with the square of the distance from the grid. Taylor's hypothesis is clearly invalid on the large scales: we assumed it to be correct over a lengthscale which equals the total length of the domain. As long as this assumption is not used to estimate the correlation function for relatively long separations there should generally not be any problem. The unaliasing theory however assumes that the flow is incompressible. A consequence of the application of Taylor's hypothesis may be that the resulting 3D velocity field contains some artificial compressibility. Maybe this has its repercussions on the estimates for  $\bar{\Psi}$ .

From the above discussions we conclude that the unaliasing theory still has a good chance to adequately transform one-point spectra to a wavenumber spectrum in real life. Even if the performance of the theory will be as bad as in this chapter, then still qualitative insight into the underlying 3D character of the real flow is to be gained. Therefore we will use the theory in the following chapter about windtunnel measurements to interpret the data.



# Chapter 5

## Metrology and experimental setup

### Introduction

No matter how abstract or complex a physicist constructs a theory, his model will always have to give an account to nature: by adding units to his statements he relates his ideas to phenomena that can be perceived with the senses. In this chapter we will describe the tools and constructions that we use in this research to extend our senses to be able to better "hear the things speak". The goal of our setup is to create grid-generated turbulence, which in section 1.3 was chosen as the reference flow of this study. We will describe the setup and the instruments that are used to collect time-series of turbulent velocity. These time-series will be used in chapter 7 to test the unaliasing relations developed in chapter 2.

The outline of this chapter is as follows: In the first section we describe the analogue filters, which we will use to eliminate high frequency noise from the electronic signals. Then we will report how basic quantities like pressure, temperature and relative humidity will be observed. Apparatus measuring these quantities will be called *peripheral apparatus*. In subsequent sections we will describe the calibration facility for hotwire probes, the four hotwire probe itself, the grid that will be used to generate turbulence in our windtunnel, the windtunnel itself and its testsection.

Throughout this chapter there will be emphasis on determination of measurement accuracies of the respective devices. We found that there is neither a theoretical model nor commercial software for the analysis of samples with estimated variances and covariances. Without such a model it is not possible to estimate the significance of estimated parameters. Without knowledge of the significance of estimated parameters it does not make sense to discuss differences from other estimates or models. To fill this gap we have derived a practical relation for the inclusion of (co-)variances of samples in standard weighted least squares curve-fitting routines. This derivation is presented in appendix A.

## 5.1 Analogue filtering and electronic signal conditioning

To eliminate aliasing all electronic signals from peripheral apparatus (pressure transducers, thermometers, hygrometer) are fed to DIFA programmable elliptic filters (type SICOS). There is a second reason to filter these signals: the peripheral signals are used to correct anemometer signals for drift in temperature and pressure. Noise in pressure and temperature signals will introduce noise in the corrected anemometer signals. This noise in the corrected anemometer signals may be misinterpreted as turbulence.

All filters introduce a phase-shift in periodic signals (see Priestley (1981)). When this phase-shift depends non-linearly on frequency (as in conventional Butterworth- and Chebychev- filters), then the corresponding time-shift will be different for high frequencies than for low frequencies. Suppose we would apply such non-equal time-delay filters to the hotwire signals. In this case the non-linear calibration model for hotwires (discussed in section 6.5.4) can no longer be used to analyse probe signals composed of components with different frequencies. To eliminate this problem, equal time delay filters (ETD) from SICOS are used to filter the hotwire signals. These filters have a phase-shift which is linear with frequency.

Filtered signals are conditioned to make the dynamic ranges of the signals match the range (-10 Volt to 10 Volt) of the a/d-board. Conditioning is done by home-made offset/gain amplifiers, which have been tested for cross-talk and for spurious oscillations. Conditioned signals are digitised by a 16 channel (single ended, i.e. signals are measured relatively to a ground signal) 12 bit Keithley Instruments DAS40 a/d-board. The two least significant bits of the readings done by the a/d-board appeared to be reproducible but to have an offset which is channel dependent. To prevent interference of this channel-dependent offset with the interpretation of samples, every electronic device was connected to a unique a/d-channel both during calibration and during other measurements. Channel cross-talk was found to be negligible between a/d-channels to which apparatus was connected by means of coaxial cables. Open channels (not connected to an apparatus) did show some cross-talk.

## 5.2 Peripheral apparatus

In this section a description will be given of simple apparatus which will be used throughout the experiments presented in this thesis (pressure transducers, thermometers, relative humidity sensor). Different researchers often draw different conclusions from different results observed in basically the same experiment. To reduce this source of error emphasis will be put on the calibration of the apparatus.

Experimentation software has been written in Borland PASCAL 7.0 to allow for sampling under DMA (Direct Memory Access, which is fast). With this software, samples can be recorded a user-specified number of times at a user-specified frequency. The program can use the recorded set of samples to estimate the set's mean values and (co-)variances of the deviations around these mean values. Calibration relations can be fit to the collection of these mean values and variances of samples (see section A for the principle of  $\chi^2$ -fitting). These fitted calibration relations can be stored for future use in calibration files. Other experiments can refer to the

fitted calibration relations in these files and apply them. In this way experiments "inherit" information from former (calibration) experiments.

### 5.2.1 Measurement of pressure

Pressure differences up to 15 mm H<sub>2</sub>O are measured with help of two Setra type 239 electronic transducers. These transducers are (statically) calibrated against a Betz manometer, which is described in section D.1. The relation between the output of the transducer and the pressure difference offered (by suction of air from the tubing interconnecting both manometers) can be described by a linear relation. An RMS-deviation of 0.5 Pascal was found at  $\chi^2 \sim 5$ . The high value for  $\chi^2$  was found to be caused mainly by hysteresis in the electronic transducer (the calibration consists of two sequences of samples: one taken with increasing pressure, and one recorded with decreasing pressure, see figure 5.1). Repetitions of this calibration on different

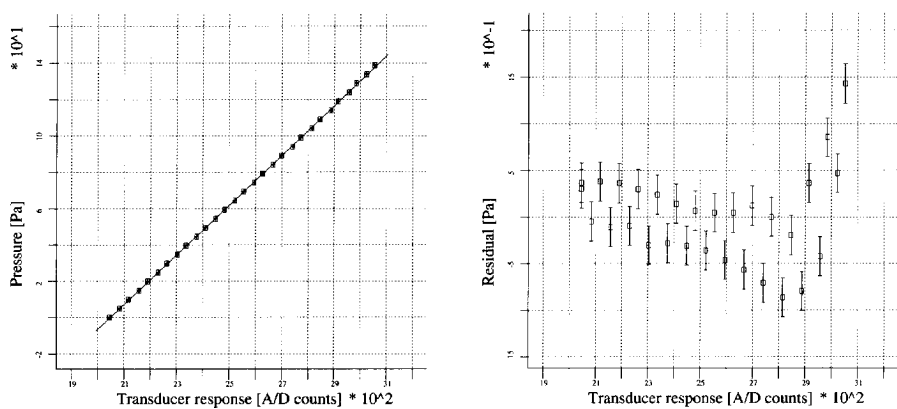


Figure 5.1: Calibration curve of electronic pressure transducer.

days revealed that the transducers' linearities are stable, but that the zeroth-order terms drift from day to day, possibly due to temperature effects. To solve this problem the transducers are placed in boxes isolated with 5 cm thick polystyrene foam. Moreover, zeroth-order calibration terms are always freshly measured before any experiment is started.

The maximum response frequency of the system consisting of pressure box plus connecting tubes plus pressure taps in the windtunnel (see figure 5.2) is estimated as follows: To model the effect of viscous friction, we assume developed Stokes-flow in all segments of the system. This is a simplification, which overestimates the influence of wall friction. As a consequence we will find a value for the cut-off frequency which will be too low. This estimate will therefore be a safe estimate when we want to know which fluctuations we can expect the system to measure. For Stokes-flow (velocity  $u$ , viscosity  $\rho$ ) in a tube with length  $L$  and diameter  $D$  we can relate nett flow  $Q$  (to be contained in the transducer) to the pressure difference  $\Delta p$  over the tube (combine

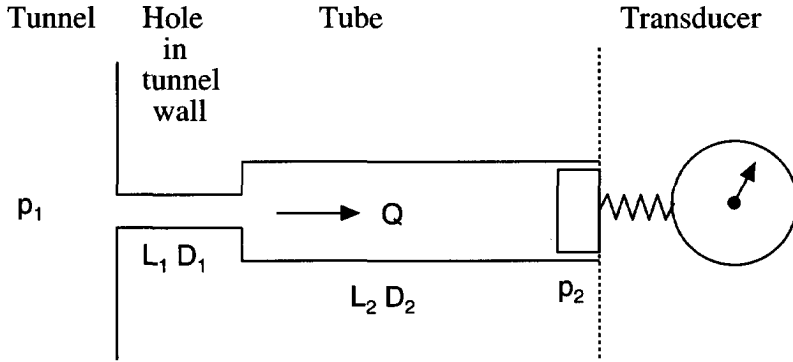


Figure 5.2: Schematic view of a pressure transducer connected to the windtunnel.

relation 6.47 in White (1986) with  $\Delta p = \rho gh$ :

$$\Delta p = \frac{1}{2} \rho u^2 \frac{L}{D} 64 \frac{v}{u D} \equiv c Q \quad (5.1)$$

$$c \equiv 128 \frac{\nu \rho L}{\pi D^4} \sim 0.0006 \frac{L}{D^4} \quad \text{for air.} \quad (5.2)$$

Characteristics of the pressure valve are  $L_1 = 1$  cm and  $D_1 = 1$  mm, which leads to  $c_1 = 6 \cdot 10^6$  Pa m<sup>-3</sup> s. The tube has characteristics:  $L_2 = 3$  m and  $D_2 = 5$  mm, which gives  $c_2 = 3 \cdot 10^6$  Pa m<sup>-3</sup> s.

The change of pressure in the pressure transducer is linearly proportional to the volume flow:

$$\frac{\partial p_2}{\partial t} = \frac{\partial p_2}{\partial \text{volume}} \frac{\partial \text{volume}}{\partial t} = \alpha Q \quad (5.3)$$

$$\alpha \equiv \frac{\partial p_2}{\partial \text{volume}} = 1.5 \cdot 10^{10} \text{ Pa m}^{-3} \quad (\text{for our transducer}) \quad (5.4)$$

To model instationary effects, we add inertia forces to the right hand side of equation 5.1:

$$p_2 - p_1 = (c_1 + c_2)Q + \rho \left( L_1 \frac{\partial u_1}{\partial t} + L_2 \frac{\partial u_2}{\partial t} \right) \quad (5.5)$$

$$= (c_1 + c_2)Q + \frac{4\rho}{\pi} \left( \frac{L_1}{D_1^2} + \frac{L_2}{D_2^2} \right) \frac{\partial Q}{\partial t} \quad (5.6)$$

$$= \frac{c_1 + c_2}{\alpha} \frac{\partial p_2}{\partial t} + \frac{4\rho}{\pi \alpha} \left( \frac{L_1}{D_1^2} + \frac{L_2}{D_2^2} \right) \frac{\partial^2 p_2}{\partial t^2} \quad (5.7)$$

$$= \frac{1}{\omega_1} \frac{\partial p_2}{\partial t} + \frac{1}{\omega_2^2} \frac{\partial^2 p_2}{\partial t^2} \quad (5.8)$$

where angular frequencies  $\omega_1$  and  $\omega_2$  are defined by:

$$\omega_1 \equiv \frac{\alpha}{c_1 + c_2} \quad \text{cut-off by friction} \quad (5.9)$$

$$\omega_2 \equiv \sqrt{\frac{\pi\alpha}{4\rho \left( \frac{L_1^2}{D_1^3} + \frac{L_2^2}{D_2^3} \right)}} \quad \text{cut-off by inertia} \quad (5.10)$$

Let us now assume that pressure  $p_1$  in the windtunnel and pressure  $p_2$  in the transducer are periodic with the same frequency:

$$p_1(t) = \tilde{p}_1 e^{i\omega t} \quad (5.11)$$

$$p_2(t) = \tilde{p}_2 e^{i\omega t} \quad (5.12)$$

where amplitudes  $\tilde{p}_1$  and  $\tilde{p}_2$  are complex numbers. Via substitution of these periodic functions into relation 5.8 we find the following relation for the suppression of pressure by the tubing system:

$$\left| \frac{\tilde{p}_2}{\tilde{p}_1} \right| = \left[ 1 + \left( \frac{2}{\omega_2^2} + \frac{1}{\omega_1^2} \omega^2 \right) + \frac{\omega^4}{\omega_2^4} \right]^{-0.5} \quad (5.13)$$

Inertia cut-off frequency  $f_1 = \frac{\omega_1}{2\pi}$  is 50 Hz, and friction frequency  $f_2 = \frac{\omega_2}{2\pi}$  is 250 Hz. We see that inertia forces dominate friction forces by a factor of 5, even though the friction forces are overestimated by the assumption of developed Stokes-flow. The frequency of 50 Hz matches the fastest structures seen on an oscilloscope.

To measure the difference between total and static pressure we use a Pitot-static tube, which is described in appendix D.2.

Air density is used in Bernoulli's law 1.20 to relate pressure differences to velocities. This quantity depends on temperature, on atmospheric pressure and on relative humidity. A mercury barometer is used to measure atmospheric pressure. The relative humidity element of a Vaisala HMI-33 combined temperature (Pt100)/humidity sensor was calibrated following a procedure outlined in the sensor's manual. The measurement of temperature is outlined in the following subsection.

### 5.2.2 Measurement of temperature

Many observational methods in fluid dynamics and in anemometry are temperature dependent (rumour has it that every measuring device is at least a thermometer). The main reason why we want to measure temperature in our study are its influences on the heat exchange of hotwires and on air density. For this accurate knowledge of temperature is essential.

In this subsection we will study static and dynamic response of four different thermometers. The results will be used to make a selection of which thermometer will be used in the rest of this research.

To measure temperature we need a reference. Let us adopt a mercury thermometer as standard. The output of a Philips PM-2535 system multimeter (capable of measuring temperature

and humidity) is compared to the readings of a mercury thermometer. The (very) close agreement between these two instruments (differences less than 0.1 Kelvin) is the reason why we take the multimeter (which can be read automatically) as reference for the calibration of other thermometers.

### 5.2.2.1 Static thermometer calibration

Two home-made Pt100 temperature sensors, a Vaisala HMI-33 combined temperature (Pt100) and humidity sensor and the Philips PM-2535 system multimeter were put in a closed oven with their sensors put closely together. The output of the four thermometers was recorded in the range from 20°C to 30°C (temperature traverses were made both upward and downward).

Though the variances in the samples (internal errors) taken by the two home-made Pt100 sensors were found to be smaller than those in the samples taken by the Vaisala, the external errors (deviations from fitted curves) were much larger. This contraposition can be explained as follows: The Vaisala suffers from high frequency noise, which can be filtered out. After analogue filtering of the thermometer signal, the external error in samples of the Vaisala was 0.1°C. It appeared that a wireless telephone at three meters distance of the thermometers caused the signals of the home-made thermometers to show jumps of 0.6 Volt, the Vaisala signal was not affected. The capricious behaviour of the home-made apparatus motivates our choice to use the Vaisala thermometer in the rest of this research.

### 5.2.2.2 Dynamic thermometer response test

The reaction times of the thermometers referred to in the former section have been measured as follows: All thermometers have been put in an oven, which was set to a temperature of 30°C. After half an hour the thermometers had reached the temperature of the oven and their signals were constant. At this point the thermometers were taken out of the oven, and placed in a windtunnel, which was set to a velocity of 5 m/s. The signals of the thermometers were recorded. To these temperature/time signals functions were fit of type:

$$T(t) = T_{\text{ambient}} + (T_{\text{oven}} - T_{\text{ambient}})e^{-\frac{t}{\tau}} \quad (5.14)$$

where time constant  $\tau$  gives the reaction time of the thermometer.

For the two home-made thermometers reaction times were 280 seconds and 160 seconds respectively. The Vaisala's reaction time was 320 seconds. The reaction test was repeated after the protective head was removed from the Vaisala sensor to enhance its response. Without protective head, the Vaisala had a reaction time of 70 seconds. This is an improvement in sensitivity by a factor five, when compared to the sensor with protective head.

The most important application of a thermometer in this research will be the monitoring of ambient temperature during hotwire measurements. Variations in room temperature on a timescale faster than one minute are considered to be irrelevant. We conclude that our thermometers are able to follow the slow variations in ambient temperature needed to correct the hotwire measurements.



At this point we have calibrated thermometers, a hygrometer and two pressure transducers. In the coming sections we will use these apparatus to examine the behaviour and characteristics of our windtunnel facilities.

## 5.3 The hotwire calibration unit

A special calibration unit has been devised and built to allow for an *in situ* calibration of (multi-) hotwire probes. The calibration unit consists of a miniature wind tunnel (see figure 5.7 for a schematic view) fitted in a frame (figure 5.5) which can pitch and yaw with respect to a hotwire probe, which is mounted in a fixed position. The frame is mounted on an arm which can be swung in and out of the testsection (see figures 5.3, 5.4 and 5.6). Before we carry out an experiment in which a hotwire probe will be used, we install the hotwire probe in the testsection, place the calibration unit in front of the probe (the swing-arm is fixed into its position in the testsection using an electromagnet). Then we calibrate the probe and remove the calibration unit. In this way no electric connection to and from the hotwires needs to be changed during calibration with respect to measurement. This *in situ* calibration is to be preferred to calibration where the probe has to be taken out of the experimental setup. It so happens that hotwire response (and consequently the value of calibration data) is very sensitive to changes in electric connection (see the discussion in section E.4.3). Therefore a calibration outside the measurement position should be considered as unreliable. Instead of a movable calibration jet, we also could have implemented a pitch/yaw facility for the hotwire probe itself. An installation to move the probe would have to remain in the testsection after calibration, and would cause flow distortion. Flow distortion by obstacles is the theme of this research, which is why we want to eliminate all distortions other than those deliberately made. For that reason we have preferred the pitch/yaw construction for the calibration tunnel above a construction to move the probe.

### 5.3.1 Construction of the miniature windtunnel

The flow in the miniature windtunnel (see figure 5.7) is forced by a centrifugal fan. The air is first blown into a 36 cm long cylinder settling chamber (inner diameter 17 cm) in which five wire gauzes with increasing mesh refinement have been placed. On the central part of the first gauze a round plate has been placed, to break the jet coming from the fan and force the flow to use the full diameter of the tube. The array of wire gauzes is implemented to reduce turbulence and to remove possible velocity non-uniformities (see Groth and Johansson (1988) and Laws and Livesey (1978)). From the settling chamber the air enters the contraction, which contracts the flow to an outflow at the nozzle with 6 cm diameter. The effect of the contraction is to reduce the fluctuation level of the flow and to improve its homogeneity and isotropy (Comte-Bellot and Corrsin, 1966).

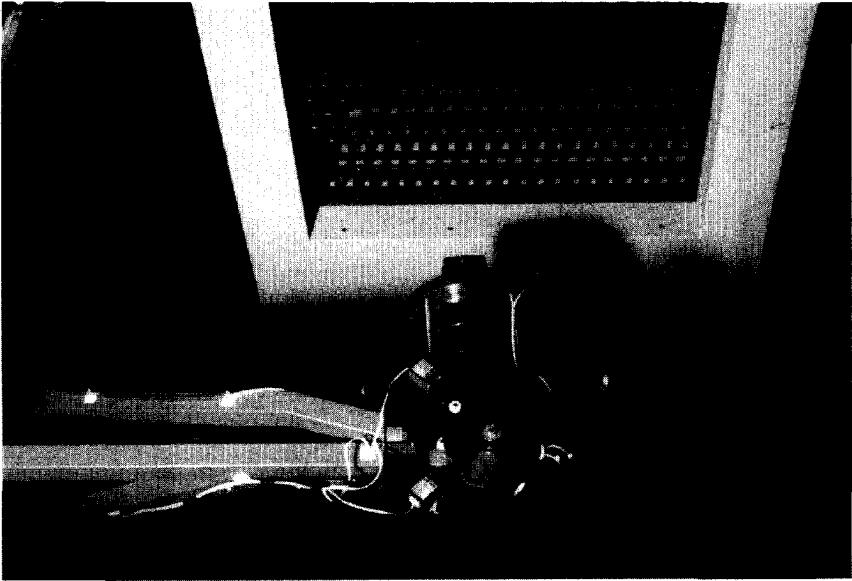


Figure 5.3: Hotwire calibration unit mounted in the testsection.

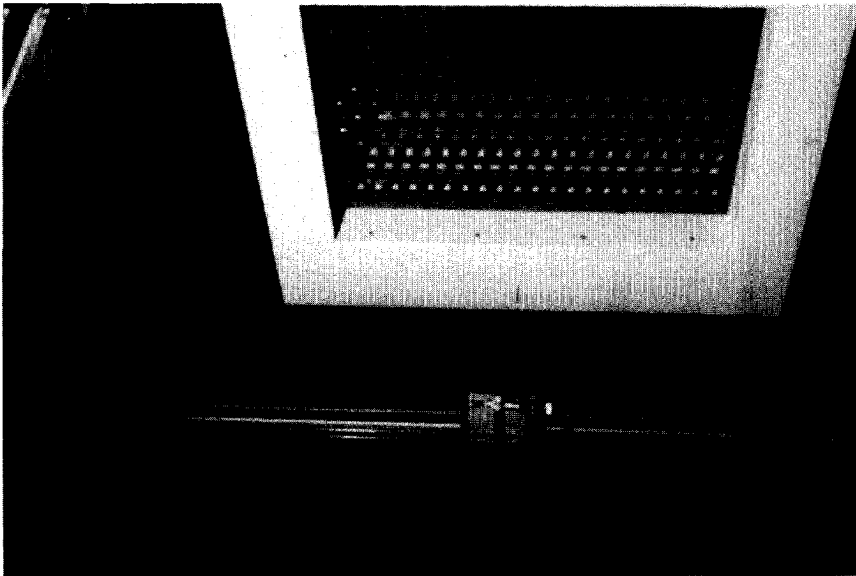


Figure 5.4: Hotwire calibration unit swung outside the testsection.

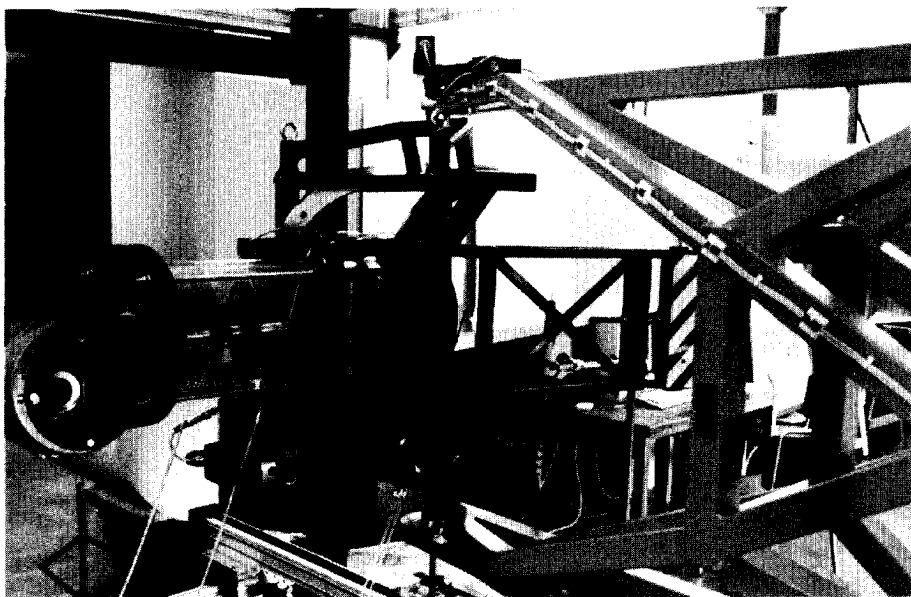


Figure 5.5: Hotwire calibration unit: pitch/yaw facility.

### 5.3.2 Calibration of contraction pressure

A relation between the contraction pressure of the calibration unit and the pressure difference over a Pitot tube (see section D.2) placed in the calibrator's jet is established in the range from 0 m/s to 16 m/s (33 samples). One would expect that this contraction pressure and Pitot pressure difference may at most differ by a constant factor. Nevertheless a third order polynomial gave a significantly better RMS deviation than a linear relation, i.e. better by a factor 2.5: from 0.85 Pa to 0.35 Pa and with  $\chi^2$  dropping from 8.9 to 1.3. The velocity inaccuracy (based on the average calibration velocity of 8 m/s) dropped from 11 cm/s to 4 cm/s). Although the origin of the non-linear relation between contraction pressure and Pitot pressure difference is unclear, we adopt this third-order relation for future use. With this relation we can calculate the actual velocity in the calibrator's jet by observation of the contraction pressure difference.

### 5.3.3 Mean flow homogeneity check

We have measured the velocity profile of the miniature windtunnel's jet (6 cm total diameter) using a Pitot-tube. This velocity profile at 3 cm downstream of the nozzle is presented in figure 5.8 (an interval  $U \pm \sigma_U$ , i.e. one standard deviation, is shown). Only the plateau in the middle 4 cm of the jet are shown (the centreline can be found at  $y=3$  cm). Near the edges of the jet the mixing layers enter the jet and thus lead to a lower mean flow. We see that the lateral profile is seriously inhomogeneous: The local mean velocity deviates from the average velocity (averaged over the central zone of the profile) with an RMS of 8 cm/s, i.e. about seven

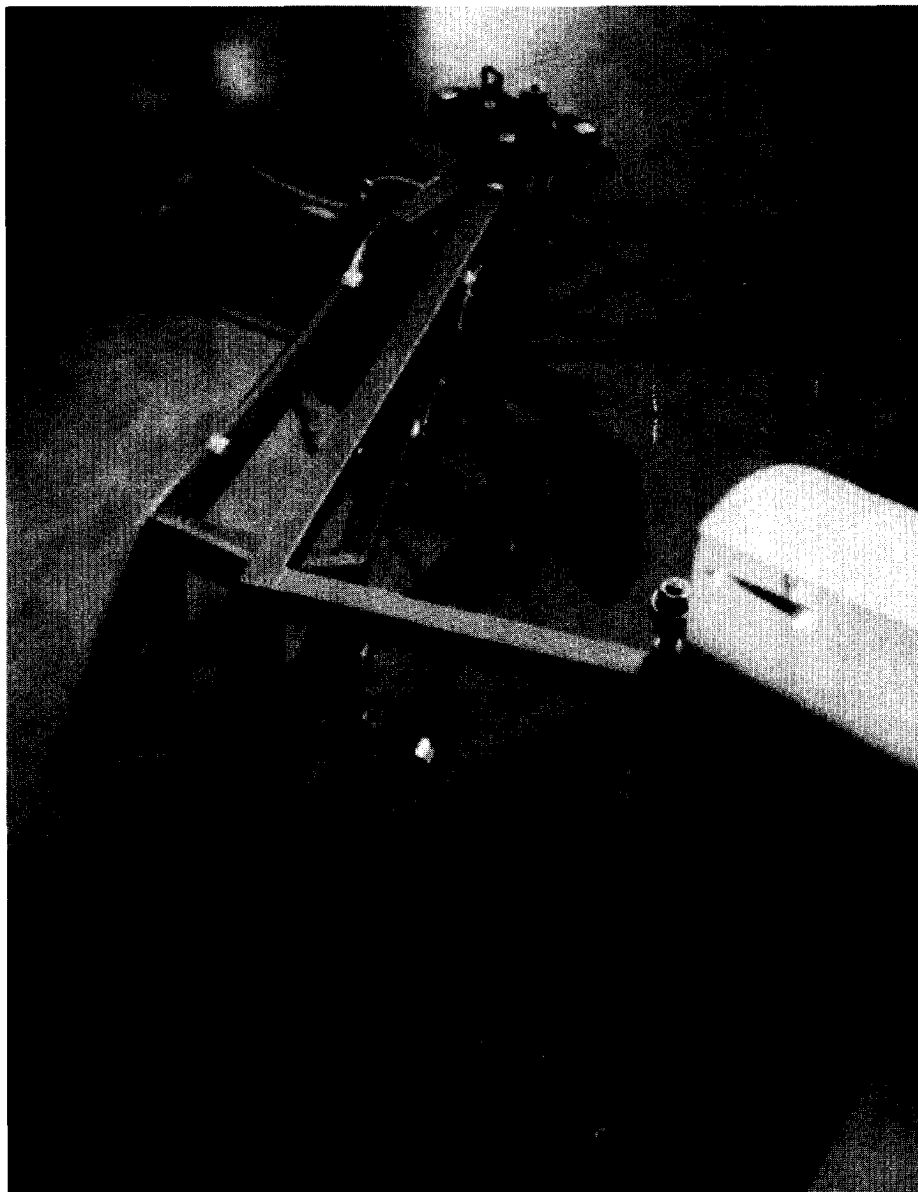


Figure 5.6: Hotwire calibration unit plus swing arm.

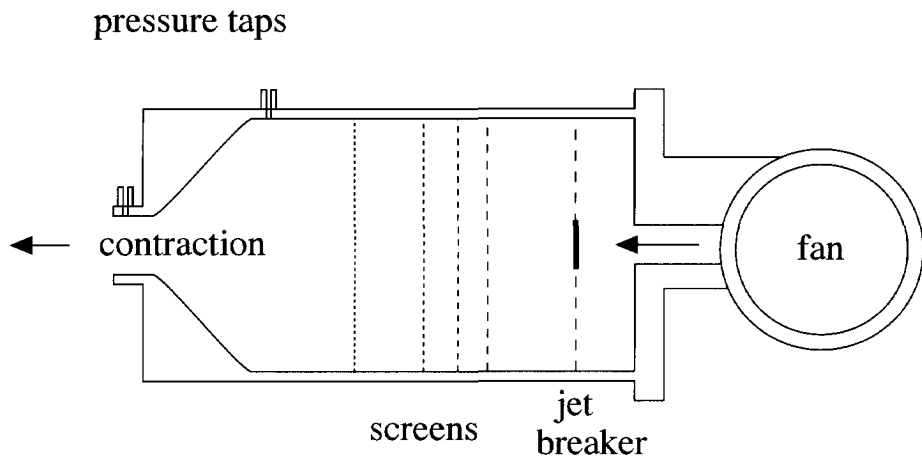


Figure 5.7: Hotwire calibration unit: the tunnel.

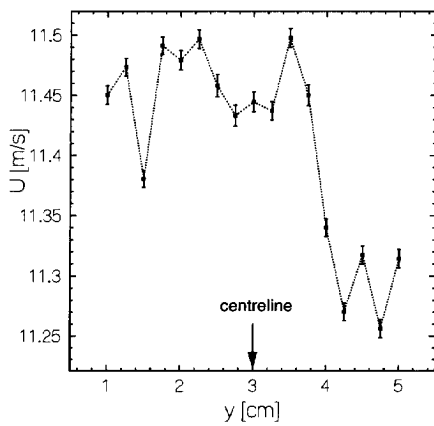


Figure 5.8: Raw lateral wind profile of calibration tunnel.

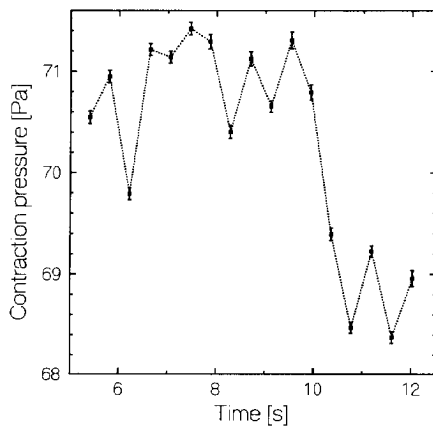


Figure 5.9: Contraction pressure drift.

promille. The fan of the calibration tunnel is driven by ordinary, non-stabilised AC-current. Changes in net-voltage will directly influence the fan's power, and consequently its air-flow. To see whether this effect has had significant influence on the homogeneity measurement, we have plotted the tunnel's contraction pressure, which has been recorded for each sample of the homogeneity measurement, in figure 5.9. There is a clear correlation between figures 5.8 and 5.9. To eliminate fan power drift from the calibration tunnel's homogeneity measurement we apply the following correction (via Bernoulli's law) to the data:

$$U_{i,\text{corr}} = U_i \sqrt{\frac{p_{1,\text{contr}}}{p_{i,\text{contr}}}} \quad (5.15)$$

where  $p_{\text{contr}}$  denotes the contraction pressure difference, and where subscript 1 refers to the initial measurement.

The effect of this correction on the homogeneity measurement is shown in figure 5.10. The RMS

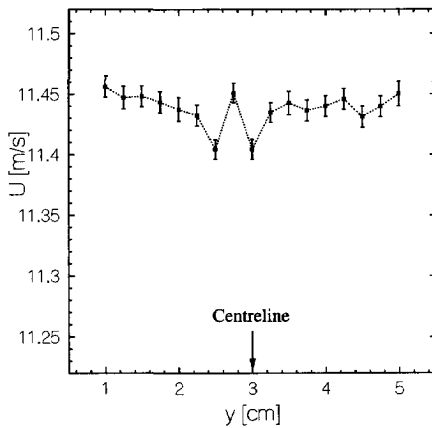


Figure 5.10: Calibration tunnel's lateral mean flow profile, after correction for contraction pressure drift.

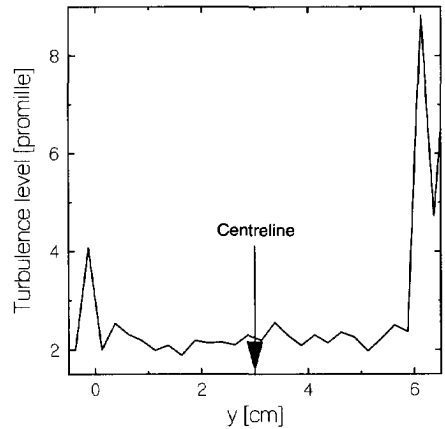


Figure 5.11: Calibration tunnel's lateral fluctuating flow profile.

of the deviations of the local (mean) velocities from the average of the mean velocity profile over the plateau of the jet (middle four centimetres) decreases from 8 cm/s in the uncorrected case to 1.4 cm/s after correction (an improvement by a factor of 6). Even after correction for pressure drift, the velocity profile is not flat within the measurement accuracy. This may be attributed to variations of pressure *during* the recording of a set of raw samples, which are used to calculate one calibration point. When we will use the calibration unit to calibrate probes, we aim at an accuracy of 10 percent in a measurement of the turbulent velocity. When we use a mean flow of 10 m/s with a grid to generate 5 percent turbulence (which for our future turbulence measurements will be shown to be a low estimate), then we have an RMS velocity of  $u' = 0.5$  m/s. Ten percent of this RMS velocity is 5 cm/s. Homogeneity of the calibration tunnel (1.4 cm/s) appears to be better than the required accuracy (5 cm/s). Therefore there is no need to try to correct the profile for pressure drift during the collection of samples. We conclude that

(concerning mean flow homogeneity) our calibration facility is a proper tool to calibrate probes.

### 5.3.4 Turbulence level check

After the mean flow homogeneity check, we check the calibration tunnel for its turbulence level. At 0.5 cm distance from the outlet, with a mean velocity of 10 m/s, we use a single hotwire, perpendicular to the flow, to measure the turbulence level. This measurement is shown in figure 5.11. Over nearly the full range of the calibration tunnel's orifice, turbulence level is below 2.2 promille (2.2 cm/s). The increase in turbulence level near the boundaries of the jet is caused by the mixing layer between the jet and the ambient air. In the previous subsection we have estimated that the desired accuracy for the calibrator is 5 cm/s. We conclude that at 0.5 cm from its outlet the calibration jet has sufficiently low turbulence level to allow for the calibration of probes for our experiments.

A second turbulence level test has been performed at a distance of 3 cm of the orifice. The portion of the jet in which turbulence level was below 2.2 promille decreased from nearly 100 percent of the jet's width to 50 percent. The mixing layer apparently grows rapidly.

### 5.3.5 Pitch and yaw facility

The calibration tunnel can make a pitching movement by sliding over a gearing ring (pitch range: -40 to +40 degrees, see figure 5.5). The constellation of tunnel and gearing ring can yaw around a vertical axis (yaw range dependent on pitch angle). Pitch and yaw movements are driven by DC-motors. Stepper motors, which are commonly used (see e.g. Lemonis (1995, p.31)), have not been used in this case because they generate electromagnetic pulses. These pulses can spoil signals from hotwire probes. A rubber band is used to constantly pull the calibration unit into one yaw direction, thus eliminating yaw-hysteresis. The accuracies of pitch and yaw movements have been measured. Pitch accuracy is  $0.15^\circ$  and yaw accuracy is  $0.1^\circ$ . To check if the measurements of pitch and yaw are stable (time-independent) the facility was set to make random motions during two hours. Pitch and yaw angles were found to remain within their previously measured accuracies. Let us consider a mean flow in the calibration unit of 10 m/s. The consequence of a pitch inaccuracy of  $0.15^\circ$  is then a velocity inaccuracy of 2.5 cm/s. This is still falls within the desired calibration accuracy of 5 cm/s (see subsection 5.3.3). A ditto reasoning holds for the yaw accuracy.

To compare our calibration facility with other set-ups we obtained a similar calibration dataset for a four wire subminiature probe from Mr. G. Lemonis from ETH Zürich (range: 2 m/s to 10 m/s) and we collected a calibration dataset for our four wire probe (range: 2 m/s to 16 m/s). We applied a fifth order direct full four wire calibration model (relation 6.28) to both datasets (see section 6.5.6). The RMS residual of our calibration was 5 cm/s, the residual of Lemonis' set was 17 cm/s. To bring our and Lemonis' calibration data to the same velocity scale, and thus make them comparable, we multiply Lemonis' velocities by a factor of 1.6. After this commensurability mapping, our residual is five times smaller than the RMS residual of Lemonis' calibration. We assume that inaccuracies in the calibration samples have their origin in the positioning inaccuracy of the calibrator, and not in inaccuracies in estimating the static hotwire

voltage or in estimating the calibration jet's velocity. From this assumption we conclude that our calibration setup is five times more accurate than the facility in Zürich.

From the above test of calibration facilities we conclude that our setup meets our requirements which we had set to a calibration (i.e. to enable us to measure turbulent flow with ten percent accuracy in the turbulent velocities). The setup in Zürich is not sufficiently reliable to be used to calibrate a probe for this type of turbulence measurement.

## 5.4 The four hotwire probe: design

In our laboratory we constructed a four hotwire probe for the measurement of turbulent velocities. The reason why we use a four wire probe instead of a three wire probe is given in chapter 6. One is also referred to this chapter for the principles of hot-wire anemometry and for the calibration and signal interpretation method, which we have developed. The probe is shown in figures 5.12, 5.13 and 5.14. We used  $2.5\mu\text{m}$  thick platinum plated tungsten wire. The four wires had 0.5 mm long sensing zones on which the platinum was etched off.

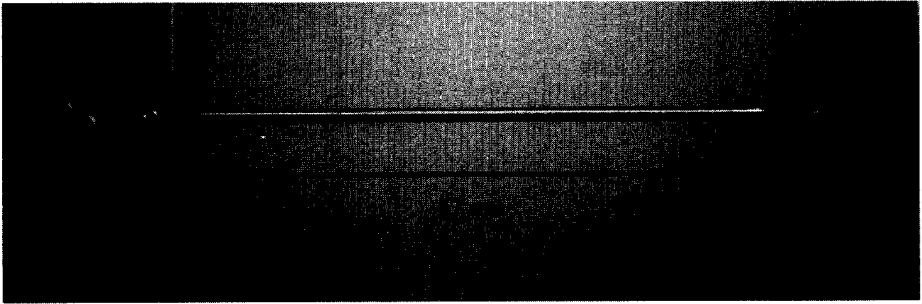


Figure 5.12: The four hotwire probe.

To see if the prongs and the stem of the probe distort the flow around the probe significantly we fit Jørgensen's law (see sections 6.3.2 and G) to a calibration dataset. Parameter  $k$  measures how strong flow, which is parallel to the wire, is altered in direction by the prongs such that the wire feels normal, and thus cooling, flow. An ideal probe has  $k = 0$ . Parameter  $h$  measures to which extent the wire's position can be considered a stagnation point of the probe. For an ideal probe parameter  $h$  takes value 1. We find that for our probe  $k = 0.2$  and  $h = 1.2$ . We draw the following conclusions:

- Parallel cooling parameter  $k$  is identical to the value found by Jørgensen. From this value for  $k$  we deduce that the prongs of our probe are sufficiently thin not to distort the flow any worse than other hotwire probes.
- In our case binormal cooling parameter  $h$  deviates from ideal value 1 about twice as much as the value  $h = 1.08$  found by Jørgensen. We conclude that our ceramic elements and the drops of glue between the prongs are relatively large, and consequently distort the flow more than was the case in the original study by Jørgensen.



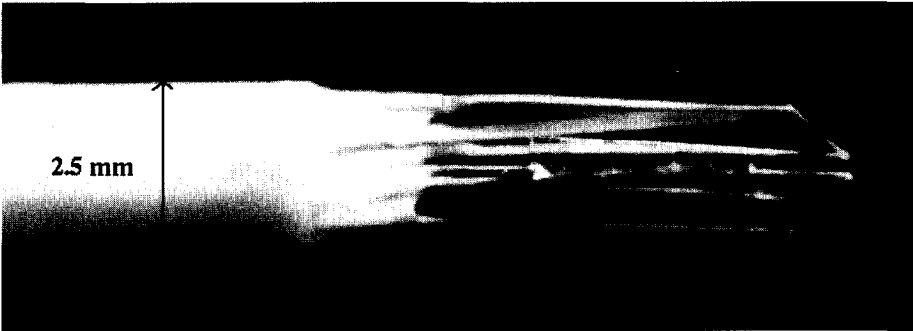


Figure 5.13: The four hotwire probe: detail.

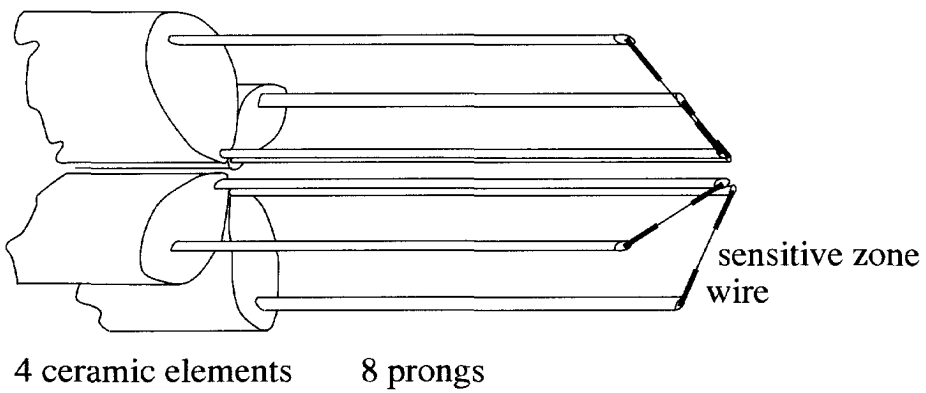


Figure 5.14: The four hotwire probe: design.

- The differences of dimensionless parameters  $h$  and  $k$  from their ideal values is small compared to 1. If this would not be the case, then the relation between a velocity vector and its response would be difficult to invert. The calibration model which we will use (see section 6.5.4) relates the response of the locally distorted flow to the undistorted calibration flow. Therefore with our calibration method we will interpret the probe's response to large scale (large when compared with lateral sizes of the probe) flow in a correct manner.

We do not take into account the possible difference in the effect of local distortion between large scale flow (the mean flow) and small scale fluctuations (small when compared with sizes of the probe). Therefore, we can use our probe only to measure flow structures which are larger than the width of the constellation of ceramic elements, i.e. 2.5 mm.

Analysis of Lemonis' calibration dataset (see end of section 5.3.5) with Jørgensen's law yielded  $k = 0.3$  and  $h = 1.2$ . In Lemonis' case flow blockage by the probe's stem (characterised by the deviation of  $h$  from 1) is equally serious as in our case. Prong interference (i.e. the value of  $k$ ) is 50 percent stronger than in our case. This difference in  $k$  to our opinion comes from a different wire mounting: in our probe only the central part of the wire is made sensitive; in Lemonis' probe the whole filament is sensitive from prong to prong. As a consequence the wires in Lemonis' probe will have stronger influence from their prongs than the wires in our probe. Lemonis' probe distorts the flow in its neighbourhood relatively stronger than our probe does, but in view of the probe's smaller dimensions (1 mm width) the *absolute* distortion is smaller than in our case.

Four equal CTA bridges from Dantec Electronics (type 56C17) are used to operate the four wire probe (see figure 6.1 for the electronic circuit of a CTA-bridge). Throughout this research an overheat ratio of 1.6 is used for all wires. The characteristics of the wires are made less susceptible to drift by operating the wires at overheat ratio 1.8 during 24 hours prior to their first use.

## 5.5 The grid

To generate turbulence we pass homogeneous laminar flow through a grid (see figure 5.20). A set of jets is formed and when there are enough grid cells (we suggest at least 15 cells in each direction) the set of interacting jets evolves to a homogeneous turbulent flow. Our grid (18 \* 23 cells) consists of flat metal strips woven in a square pattern. The strips are fixed in wooden frames. Strips have width 13 mm and the meshsize  $M$  is 4 cm. In the coming subsections we will first estimate the turbulence characteristics, which we expect to find in turbulence generated with our grid. Then we will check the flow behind the grid for homogeneity of mean and fluctuating velocity.

### 5.5.1 Expected flow characteristics

From relation 1.16 we can see that the value for Kolmogorov's lengthscale (see section 1.1) in our experiments is a quarter of a millimetre at  $x/M=31$ , which is at the downstream end of the

testsection (with  $M=4$  cm and with highest velocity  $U=16$  m/s). Given the probe's diameter of 2.5 mm, we cannot resolve all small scale structures in the flow behind our grid. This is not necessarily a reason to reject our probe as measuring instrument for grid turbulence, since it may be that the non-resolvable structures contain very little energy, and do not play a role in dynamical processes.

To see if we will miss contributions to the flow, which carry an appreciable amount of energy, we estimate Taylor's microscale  $\lambda$  (see section 1.1). Via relation 1.17 we find that  $\lambda$  will grow to 3 mm at the downstream end of the testsection. This lengthscale is larger than the size of the probe. We will see in section 5.7.3 that the best part of the testsection for performing experiments is the rear end. We therefore conclude from the estimates of the smaller characteristic turbulence lengthscales that our four wire probe can be used to resolve turbulent grid flow in our setup, as long as we restrict ourselves to structures larger than Taylor's microscale.

In a test we have found that at  $x = 20M$  correlation length  $L$  (see section 1.1) is about half the meshsize of the grid, i.e.  $L=2$  cm. Via relation 1.15 we find that at the rear end of the testsection ( $x/M=31$ ) the correlation length is 23 mm, which is an order of magnitude larger than the size of the probe. From this test we conclude that our grid will produce flow with a dynamical range (i.e. from the correlation length down to Taylor's microscale) of one order of magnitude.

The grid has a solidity of 54 percent (fraction of the grid's surface which blocks the flow). Bradshaw and Pankhurst (1964) have found that grids with solidities larger than 43 percent can have a pattern of trailing vortices of various sizes in the flow from the grid. These vortices can remain present in the flow over a long distance and influence flow statistics, mainly connected with boundary layer disturbance (but we have no boundary layers) and with inhomogeneity (which we will check in the following section). Despite the fact that our grid has solidity larger than the highest recommended solidity, we nevertheless expect no problems for the following reasons: We will not measure in boundary layers, and flow homogeneity will be assured by careful adjustment of the grid bars.

### 5.5.2 Homogeneity check

The lateral homogeneity of the mean flow behind the grid has been measured with a Pitot-tube. Velocities were corrected for windtunnel drift using the method described in section 5.3. The profile is presented in figure 5.15 (the two lines correspond with a tolerance band of  $\pm$  one standard deviation around the measured mean value). The first characteristics which we see from the profile shown in figure 5.15 are the "devil's horns": two peaks of high velocity at the edge of the grid. Furthermore, even in the central zone the mean velocity profile has deviations from uniformity that are larger than the tolerance level. These results imply that the mean flow behind the grid is inhomogeneous. Next we plot the width of the mesh cells in figure 5.16. There is a remarkable resemblance between the mesh-width shown in figure 5.16 and the local mean velocity shown in figure 5.15.

To get the agreement between these two plots we had to double the values of the mesh widths of the first and of the last cells. An explanation why this doubling of the width of the extreme grid cells improves the correspondence between mesh width and mean velocity is the following (see figure 5.17): Consider two-dimensional grid-flow. Flow coming through a central grid cell

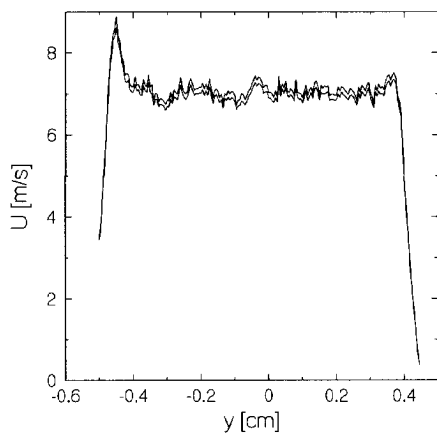


Figure 5.15: Lateral wind profile behind the grid.

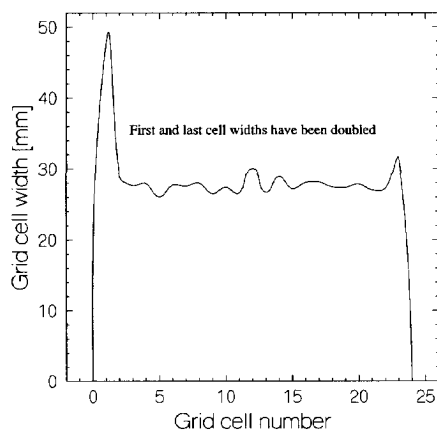


Figure 5.16: Mesh width of the grid.

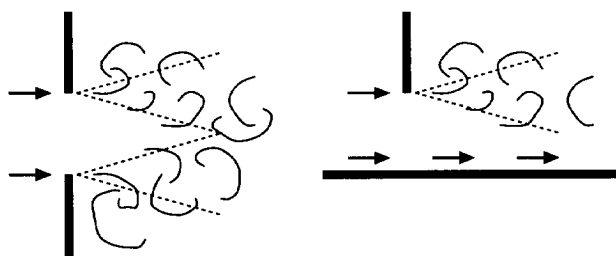


Figure 5.17: Difference between flow through a central grid cell and flow through a cell at the edge. The dashed lines represent developing mixing layers.

will develop two mixing layers. In those mixing layers the jet coming through the cell meets the still air behind the grid's strips. These interactions are strong, and consequently there is a large pressure-drop over the grid. On the edge of the grid, the cells start at the wall of the outlet of the tunnel. The wall is more or less smooth and behind the grid on one side of the cell there is no still air waiting for the jet to interact with (though a small boundary layer will develop). We can map this situation with a wall on a situation without a wall: construct the mirror-image of the grid in the wall and eliminate the wall (see figure 5.18). The new situation has (roughly) the

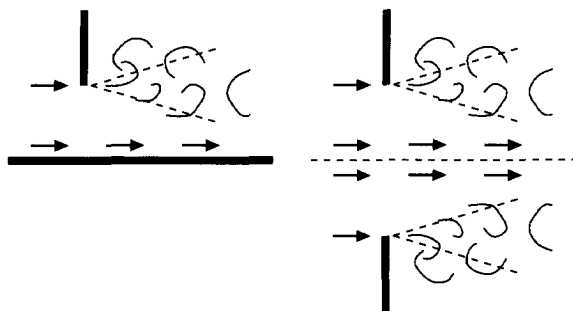


Figure 5.18: Left: grid cell at the edge; Right: central grid cell with mean flow as in situation on the left.

same dynamic equations and boundary conditions as the original situation has (when restricted to the original area). Therefore in the original area the solution of the equations of motion will be the same as in the original situation with a wall. Earlier in this section we have found that mean grid flow is very sensitive to the size of the grid cells. This leads us to the conclusion that in order to make flow through the grid cells on the edge match the flow through the central cells, the width of the cells on the edge has to be half the width of the central cells.

We have modified the grid such that the extreme grid cells have width half as large as the central cells (see figures 5.19 and 5.20). Accuracy of the cell width is 0.1 mm. The lateral wind profile of the grid after modification is shown in figure 5.21. The adaptations have clearly improved the grid's characteristics: In contrast with what was shown in figure 5.15 the central zone's mean velocity inhomogeneity in figure 5.21 are smaller than the tolerance limits. There is still global inhomogeneity (velocities tend to be higher near the edges than in the centre), but the differences are limited to a few percent. We draw the conclusion that the mean flow characteristics of our grid are now satisfactorily homogeneous.

## 5.6 The windtunnel

The windtunnel that will be used in this research has a closed loop (the return section of the tunnel and the fan are placed in the cellar of the building). Total length measured over the centreline amounts 53 meters. The tunnel is drawn schematically in figure 5.22. The tunnel's fan is driven by a Ward-Leonard system. When no grid has been placed, the tunnel can reach a maximum velocity of 40 m/s. With the grid placed, the maximum mean flow drops by 50 percent to 20 m/s. Directly behind the contraction a segment has been removed from the tunnel, to

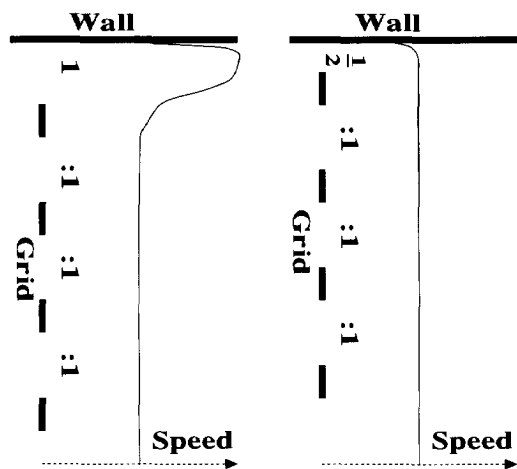


Figure 5.19: Modification of the grid to yield homogeneous mean flow.

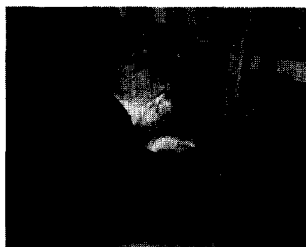


Figure 5.20: Modification of the grid.

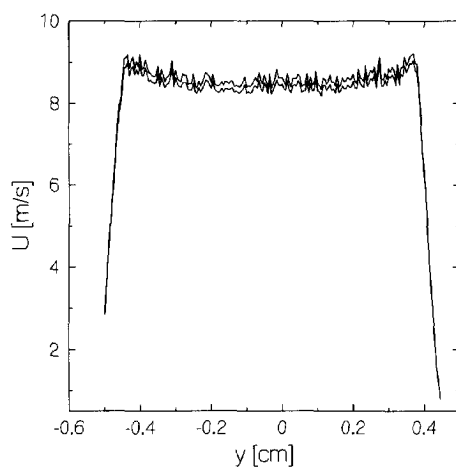


Figure 5.21: Lateral wind profile behind the grid after modification.

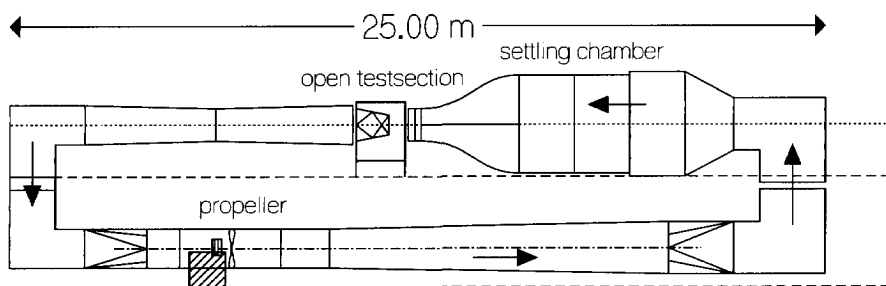


Figure 5.22: The windtunnel.

allow for the installation of a testsection. The gap is 1.5 meters long and the cross section of the outlet from the contraction is 70 cm (vertical) by 90 cm (horizontal). The tunnel's return inlet (behind the testsection) has a cross section measuring 1.1 meters by 1.1 meters. The edges of the return inlet are smoothly rounded.

The tunnel has no climate control, no velocity control (only the fraction of the maximum power on the motor can be set, by hand).

The tunnel's basic resonance frequency, calculated from the length over the centreline (53 m/s) and the speed of sound (340 m/s) is 6.4 Hz (infrasonic). This is sufficiently low not to interfere with turbulence spectra. Higher order harmonics however may be relevant.

## 5.7 The testsection

An open windtunnel testsection has been devised to allow for three dimensional traversings with sensors. In this part of the report we will outline the design of this testsection and present some measurement results. At the end of this section we will present the set-up, which will be used to produce stagnating flow.

### 5.7.1 Specification of testsection and traversing mechanism

The design of the testsection is illustrated in figures 5.23 and 5.24. The construction is as follows: A probe holder is mounted on a vertical hollow elliptic rod (3 cm by 5 cm). A belt is attached to this probe holder and closed through the vertical rod. A D/C driven motor can displace belt and probe holder along the rod over a distance of 100 cm. This vertical axis of displacement will from now on be called the z-axis. The ends of the z-axis are mounted on two slides that can make a displacement in the lateral direction over (mechanically coupled) linear modules. This axis of displacement will be called the y-axis (total y-displacement is 100 cm). The four ends of the two linear y-modules have been mounted on slides that can move in the tunnel's axial direction by means of (coupled) linear traversing modules: the x-axis (100 cm full displacement). The quadruple implementation of linear x-modules, and the double implementation of y-modules have been adopted to get a stable, reproducible displacement of the

probe. Single implementations of linear modules would have led to a construction susceptible to elastic vibrations, and consequently inaccurate positioning and orientation of the probe. The accuracies in  $x$ ,  $y$  and  $z$  have been found to be 0.25 mm (principally due to hysteresis). This accuracy is of the order of the Kolmogorov scale and less than the expected Taylor microscale (see section 1.3). Hence we conclude that the traversing mechanism of the testsection is sufficiently accurate for our experiments.

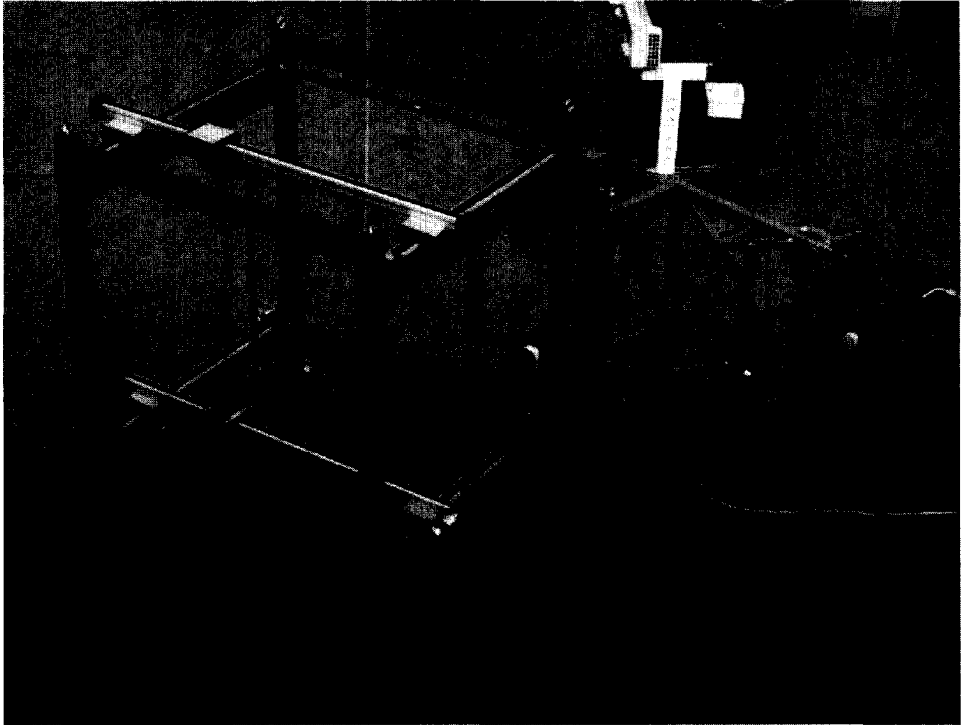


Figure 5.23: Design of the testsection: general overview.

### 5.7.2 Laminar velocity profile in the testsection

The laminar velocity profile in the testsection (i.e. the velocity profile without a grid) has been measured using a Pitot-tube. Profiles are measured in horizontal planes at respective vertical distances from the centreplane: -31.5 cm (not shown), -21.5 cm (not shown), 0 cm (see figures 5.25 and 5.26), 21.5 cm (figure 5.27) and 31.5 cm (figure 5.28). An average tunnel velocity of 8 m/s has been used. Corrections for contraction pressure drift have been applied to the Pitot pressures (relation 5.15). The fringes in the plots, at the edges of the jet, are artificial contributions of the plotting routine.

The central plane has been scanned twice. During the first measurement (shown in figure 5.25) the traversing mechanism scanned the plane regularly in rows along the  $y$ -axis. In the second



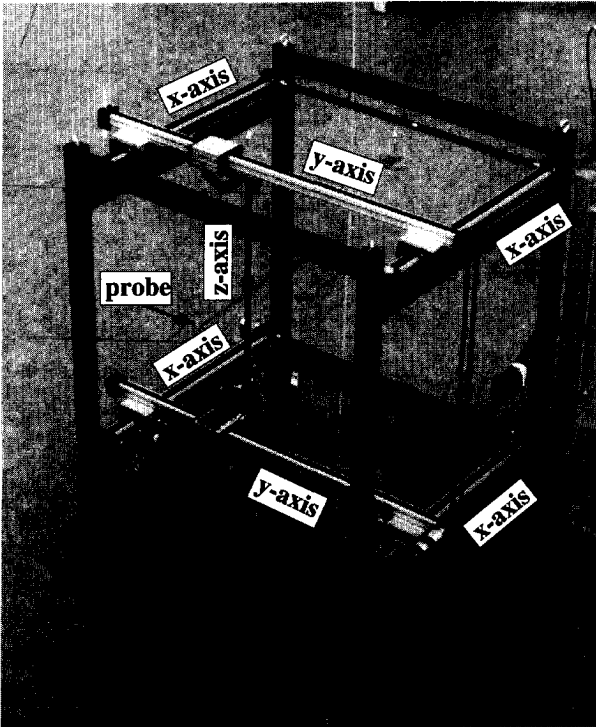


Figure 5.24: Design of the testsection: definition of the axes.

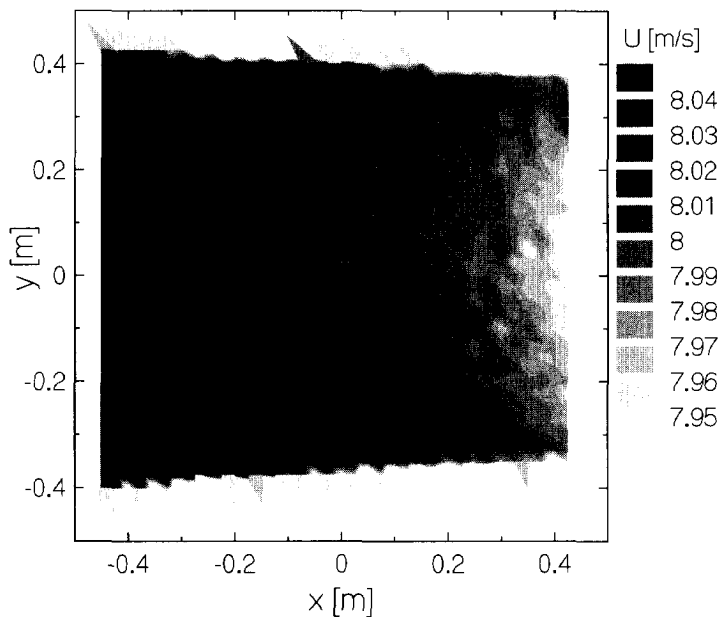


Figure 5.25: Laminar velocity profile in the horizontal centreplane, regular sampling of the grid.

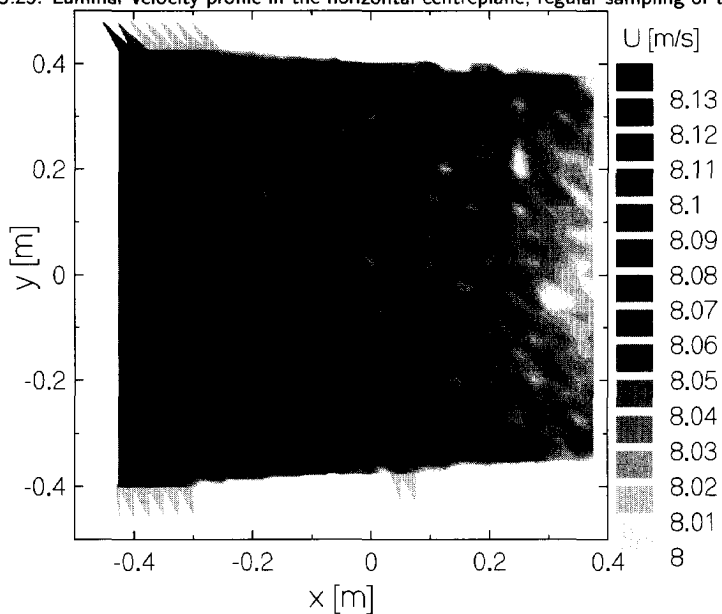


Figure 5.26: Laminar velocity profile in the horizontal centreplane, random sampling of the grid.

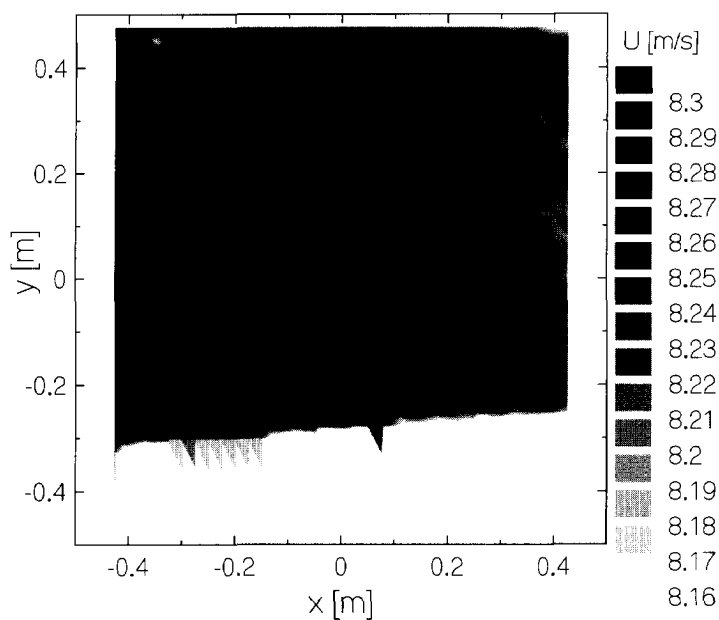


Figure 5.27: Laminar velocity profile in the horizontal plane 21.5 cm above the centreplane, random sampling of the grid.

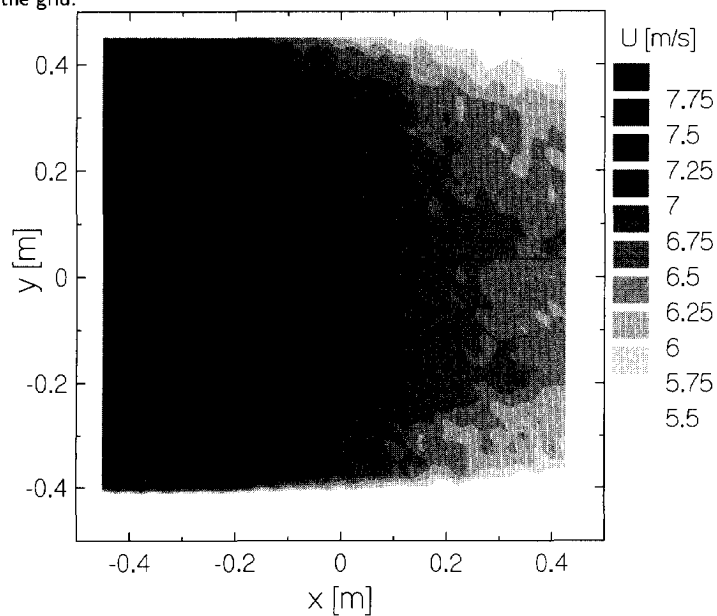


Figure 5.28: Laminar velocity profile in the horizontal plane 31.5 cm above the centreplane, random sampling of the grid.

experiment (figure 5.26), the grid of points in the central plane was scanned at random. The aim of this second test was to eliminate correlations between sampling position and drifting quantities (e.g. atmospheric pressure).

The (random) scatter in the randomly sampled data is 0.75 percent, which is a bit larger than the scatter in the regularly sampled data, which is 0.5 percent. This difference may be attributed to instabilities in the tube system connected to the Pitot-tube. During sampling the tubes were supposed to be still after a certain settling time. This delay was sufficient in the regular scan, but in the random scan, which involved larger traverses, the tubes were not fully still during sampling.

Qualitatively the results in the randomly sampled data are equivalent to the results of the regularly scanned samples. This indicates that inhomogeneities suggested by the regular scan are not artefacts introduced by drifting quantities or by an instable measuring system, but that they truly represent spatial differences. We see from figures 5.25 and 5.26 that in the testsection the laminar velocity drops by one percent. Results of the random scan suggest that the flow has slight asymmetric inhomogeneity: flow is stronger for negative  $y$ , which is on the side opposite the calibration facility. This asymmetric inhomogeneity is smaller than the inhomogeneity in the flow direction.

The results of measurements in horizontal planes situated 21.5 cm (figure 5.27) and 31.5 cm (figure 5.28) below the central plane agree with those obtained in horizontal planes above the central plane, and therefore these two planes are not shown here.

Axial lines in figures 5.25, 5.26, 5.27 and 5.28 also belong to vertical planes. We can get an impression of the velocity distribution in the vertical centre-plane by making a combination of those lines from the horizontal profiles which have central lateral coordinate. Observe the central axial lines of the profiles at  $z=21.5$  cm (13.5 cm off the edge) and at  $z=31.5$  cm (3.5 cm off the edge). Even without making a plot we can see in the horizontal centre-plane that these central lines match the lines  $y=31.5$  cm (13.5 cm off the edge there is only a small decay of the velocity) and  $y=41.5$  cm (3.5 cm off the edge the mixing layer comes by in full extent) respectively. We conclude that the intrusion of the mixing layer at the top and the bottom of the jet in the testsection is equally strong as the intrusion of the mixing layers at the sides of the jet.

From the laminar measurements we conclude that we have to take into account a small velocity gradient along the tunnel's centreline. The crosssection of the return inlet at the end of the testsection is twice as large as the crosssection of the windtunnel contraction's outlet. The larger return inlet may cause the flow to expand somewhat. To satisfy continuity the flow has to decelerate (in our experiments we can neglect compressibility effects). This response to a difference in crosssection is possibly the cause of the observed inhomogeneity of the laminar flow. Nevertheless we can say that the mean flow's response to the wider return inlet is very modest: a full response would have led to a mean velocity drop of 50 %, whereas the observed drop is only 1 %. This is in agreement with our experience with a modified return inlet, which had the same shape (and consequently the same diameter) as the inlet into the test section. With the modified return inlet the velocity profiles were exactly the same as with the old return inlet (even the fluctuating contributions to the velocity did not alter by the modification). In the testsection the increase of the mixing layer at the boundary of the laminar jet does not influence the homogeneity of the bulk-flow 'plateau' in the middle.

5.7.3 Velocity profiles of gridflow

After checking the laminar flow in the testsection for its homogeneity, we consider turbulent grid flow. Homogeneity is checked both for the mean flow and for the fluctuating velocity. We use the same mean velocity as in the laminar tests in the former subsection.

5.7.3.1 Mean grid flow

The mean velocity profile across the horizontal centreplane, measured with a Pitot-tube, is shown in figure 5.29. In this figure the origin is 76.5 cm behind the grid (meshsize is 4 cm). We immediately see from figure 5.29 that the mean grid flow has stronger inhomogeneities

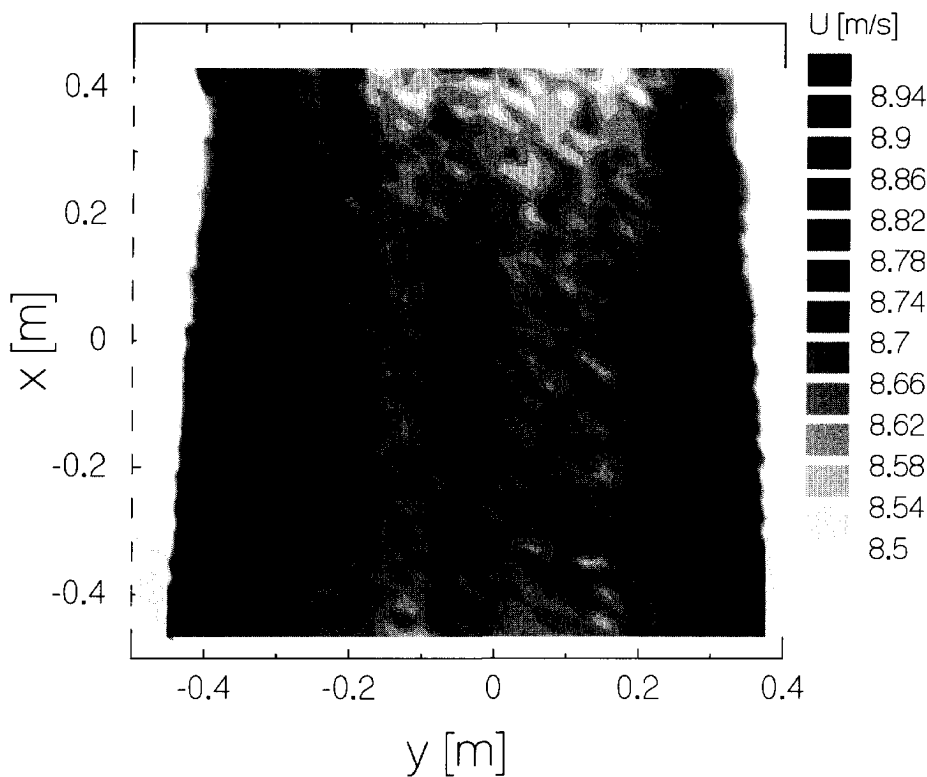


Figure 5.29: Gridflow: Mean velocity profile in the horizontal centreplane.

adjacent to the mixing layer (region outside the central 50 centimetre of the central plane) than the laminar profile. In the central plateau (50 centimetre width) the mean grid flow is relatively homogeneous, though the scatter (1.2 percent) is the double of the random scatter in the (regularly scanned) laminar flow profile (shown in figure 5.25). Part of this difference comes from systematic effects: despite our carefully made modifications to the grid (see section 5.5)

we see in figure 5.29 that a small inhomogeneity in  $y$ -direction can be found to extend in  $x$ -direction throughout the cross-section. Such a streamwise correlation (not seen in the laminar data) must be effects of the grid. Apart from this minor difference, when restricted to the plateau the mean grid flow's homogeneity matches the laminar flow's homogeneity.

### 5.7.3.2 Fluctuations in grid flow

We measured the ratio of fluctuating and mean velocities with a single hotwire probe. The velocities estimated from the hotwire signal are corrected for drift in the windtunnel's velocity using the contraction pressure with use of relation 5.15.

The lateral profile of the fluctuation level, defined as the ratio of the fluctuating velocity to the mean velocity, (at 29 cm or 7.25 meshsizes  $M$  behind the grid) is shown in figure 5.30. In this figure we plotted two bands with width  $\pm$ -one standard deviation: one band in which the signal from the pressure transducer connected to the wind tunnel's contraction has been low-pass filtered (1 Hz) and one band in which the pressure signal has not been filtered. When the signal of the pressure transducer connected to the windtunnel's contraction is not filtered, the estimated fluctuation level is significantly larger than when the signal is filtered (fluctuations in the pressure signal enter the hotwire's velocity estimates via relation 5.15). This confirms the necessity of filtering, which we conjectured in the introduction of section 5.2. From the central part of the scan with filtered pressure signal we conclude that the fluctuation level of the grid flow is homogeneous in the lateral direction.

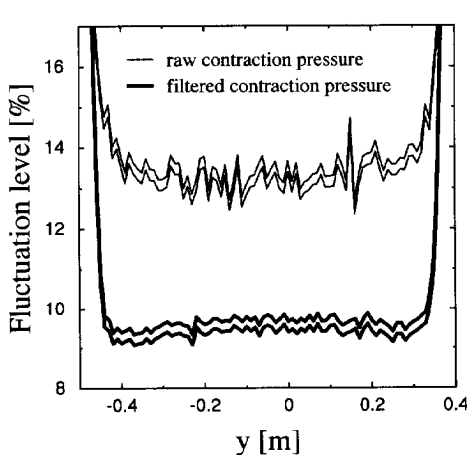


Figure 5.30: Gridflow: Lateral fluctuating velocity profile. Intervals of  $\pm$  one standard deviation are shown for the fluctuation levels.

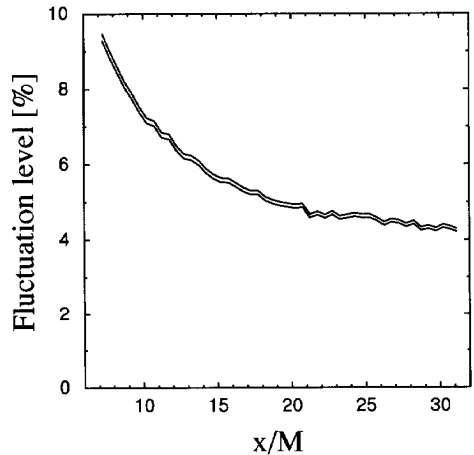


Figure 5.31: Gridflow: Fluctuating velocity profile along the centreline.

The fluctuation profile along the centreline of the jet is presented in figure 5.31. We see that the fluctuation level decays by 64 percent to less than half its initial level from one side of the testsection to the other. This is a serious inhomogeneity, which is caused by the short distance

between the grid and the testsection. In section 1.3 we have seen that in literature one reports gridflow to become homogeneous and isotropic after a distance between  $10M$  and  $40M$  from the grid. The range of our experiment is from  $7M$  to  $31M$ , which is partly below the first estimate for the distance of full development, and well below the second estimate. As a consequence of our measurement we can confirm the estimate by Comte-Bellot and Corrsin: grid generated turbulence is not homogeneous (in axial direction) before at least 31 meshsizes away from the grid.

To compare our measurements with the findings of Batchelor, we fit relation 1.14 for the decay of grid-turbulence (from here called Model 1) to our data:

$$\frac{u^2}{U^2} = a \frac{M}{x - x_0} \quad \text{Model 1} \quad (5.16)$$

We find  $a=487$  and  $x_0/M=1.07$ . The resulting fitcurve ( $\chi^2 = 12$ ) and residuals are shown in figure 5.32. The residuals in figure 5.32 show a large systematic contribution. In combination

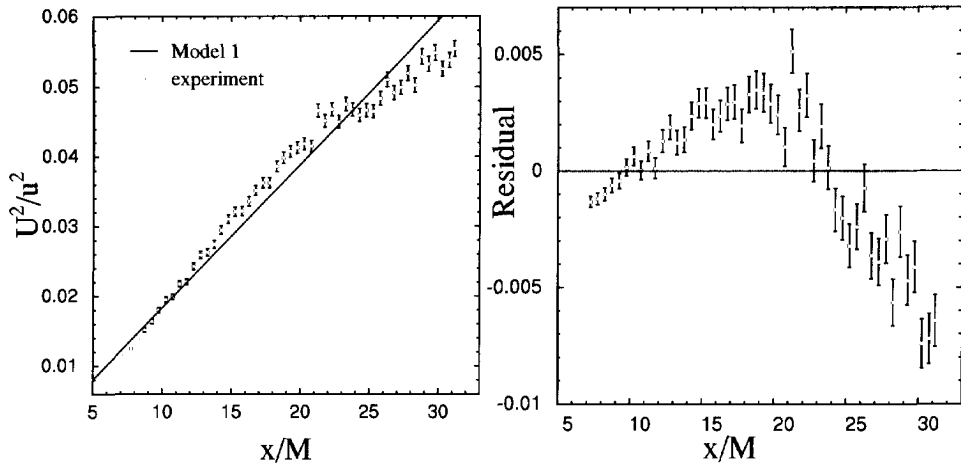


Figure 5.32: Comparison of fluctuating velocity along the centreline with model 1.

with the large value for  $\chi^2$  this suggests that we should use a different model.

We propose the following modification to model 1: There can be low frequency contributions to the fluctuations caused by phenomena other than turbulence, e.g. resonance of the tunnel. These fluctuations (called  $u_0$ ) need not decay and as a consequence they will give a constant term. This term can be accounted for via Pythagoras' law. The new model is called model 2:

$$\frac{u^2}{U^2} = \frac{u_0^2}{U^2} + a \frac{M}{x - x_0} \quad \text{Model 2} \quad (5.17)$$

With this model we find  $a=297$ ,  $x_0/M=3.68$  and  $u_0/U = 2.57$ . Model 2 plus residuals are shown in figure 5.33 ( $\chi^2 = 2.8$ ). When compared with the residuals in model 1, the residuals in model 2 are smaller by a factor 2. The value for  $\chi^2$  however is large, and we see that the residuals still have significant systematic deviations. This means that a model must exist better than model 2.

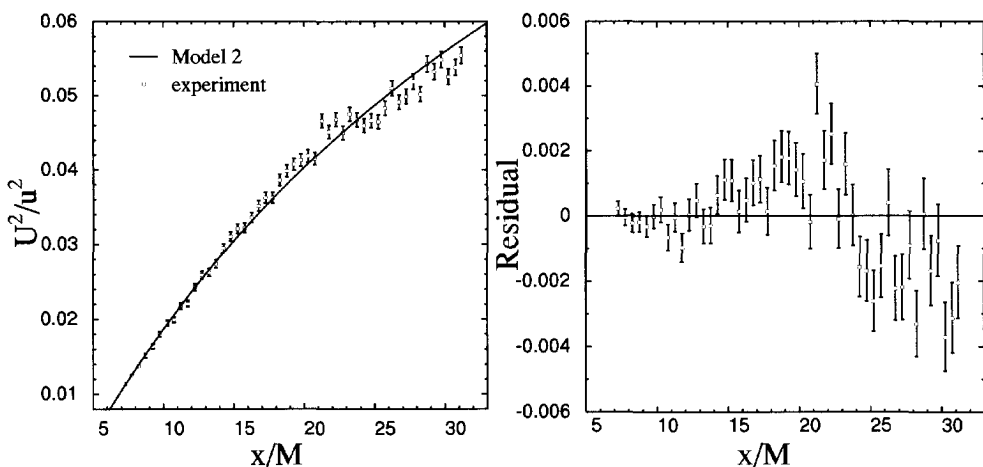


Figure 5.33: Comparison of fluctuating velocity along the centreline with model 2.

In the construction of model 1 Batchelor (1953) has assumed that the square of the fluctuation level decays as the reciprocal of the distance to the grid. On page 137 in his book Batchelor (1953) gives a more general model, which we combine with model 2 to yield model 3:

$$\frac{u^2}{U^2} = \frac{u_0^2}{U^2} + a \left( \frac{M}{x - x_0} \right)^{-n} \quad \text{Model 3} \quad (5.18)$$

Batchelor points out that exponent  $n$  in relation 5.18 for the decay is a discriminator for the behaviour of the Reynolds numbers based on the fluctuating velocity and either the macroscale or Taylor's micro scale: if  $n$  is larger than one, then these Reynolds numbers will increase with distance to the grid and vice versa.

We find  $a = 2.13 \cdot 10^4$ ,  $x_0/M = -2.56$ ,  $u_0/U = 3.87$  and  $n = 2.49$ . Model 3 and residuals are presented in figure 5.33 ( $\chi^2 = 1.3$ ). The residuals are random, and  $\chi^2$  has a reasonable value. We conclude that model 3 is significantly better than model 2, and that model 3 describes our data with sufficient accuracy. From the fitted exponent of decay  $n = 2.49$  we infer that Reynolds numbers  $Re_L$  and  $Re_\lambda$  decrease with  $x$ . Batchelor reports that though "data about the value of  $x/M$  at which the decay law 5.16 ceases to be valid is rather meagre (...) the energy begins to decay more rapidly (...) between  $x = 120M$  and  $x = 200M$ ". Data of our measurement contradict this hypothesis: already in the initial period of decay we have rapid decay.

The plot in figure 5.35 gives a representation of models 1, 2 and 3 in the range from  $5M$  to  $60M$ . The extrapolation of the model to positions beyond the range of the testsection is made to allow for the bringing up of suggestions for improvement of our setup for future studies on grid flow. Figure 5.35 suggests that repositioning the testsection 1.2 meters ( $=30M$ ) further downstream from the contraction will improve homogeneity to a large extent. This is not the case: estimated inhomogeneity of the *turbulent* fluctuations, which in the current situation drop by 79 percent, will still fall by 40 percent (according to model 3) when the setup is moved.



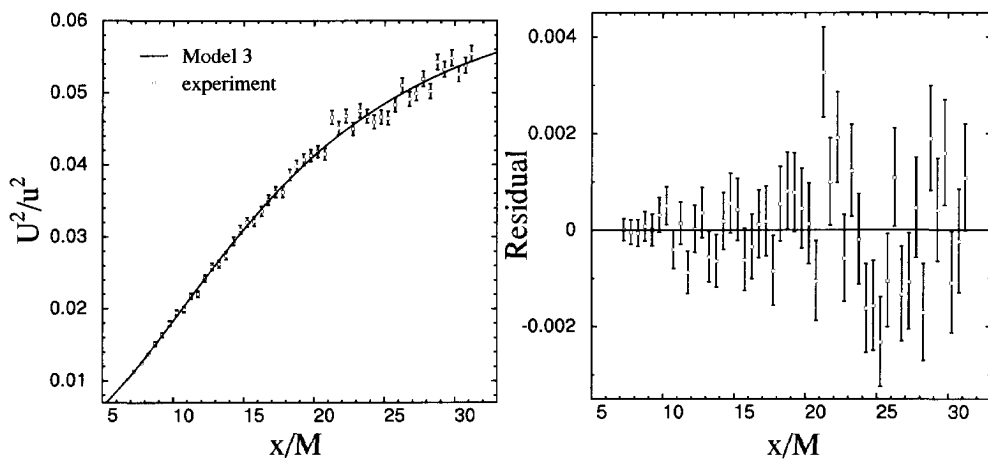


Figure 5.34: Comparison of fluctuating velocity along the centreline with model 3.

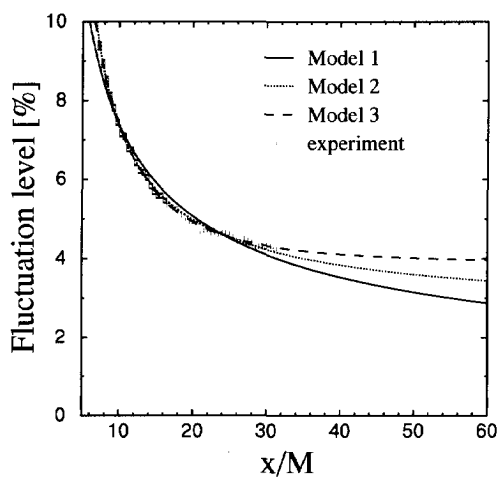


Figure 5.35: Extrapolation of models 1, 2 and 3

To see if our assumption that low frequency, non-decaying contributions distort our observation of the fluctuating velocity as turbulence, we place a four hotwire probe in the centre of the testsection and record its response to grid generated turbulence during 15 minutes at 2 kHz (low-pass filtered at 800 Hz). We construct the full complex cross-spectrum of the velocity samples. The scalar energy spectrum is shown in figure 5.36. Rescaled fourth- and third aniso-

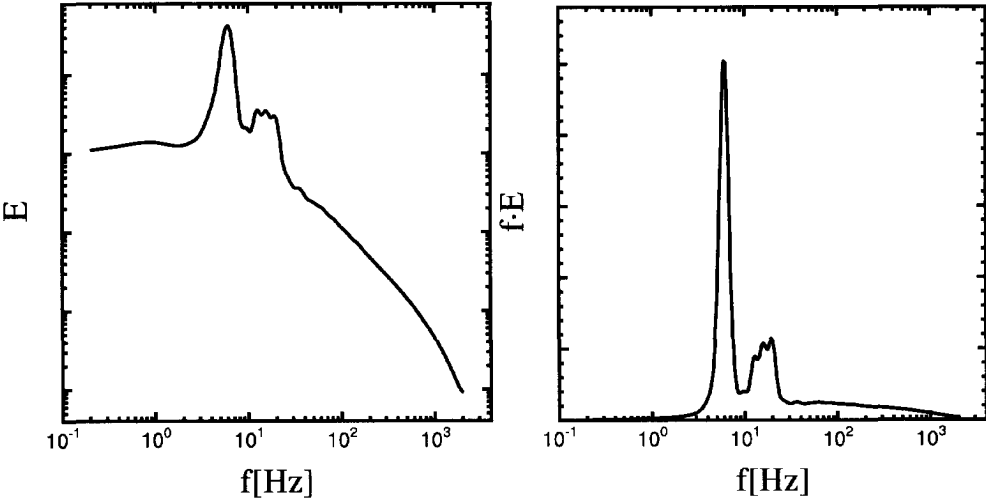


Figure 5.36: Grid turbulence at 25 M: Energy spectrum

trophy invariants (definition C.13) corresponding with the spectral expansions are presented in figure 5.37. The swirl-fraction (definition 2.39) is presented in figure 5.38.

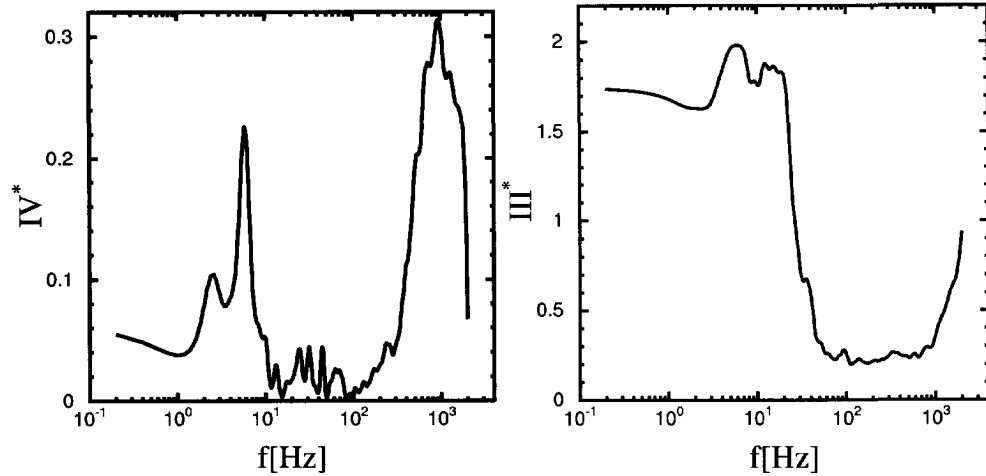


Figure 5.37: Grid turbulence at 25 M: Rescaled anisotropy invariants of cross spectra

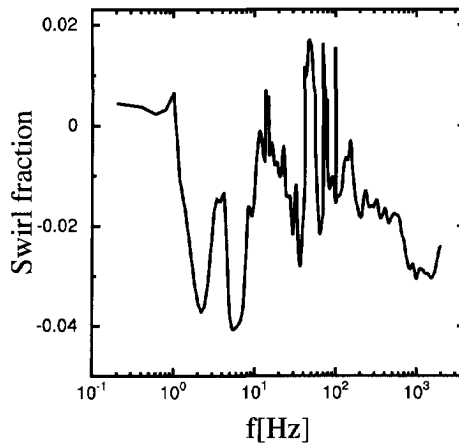


Figure 5.38: Grid turbulence at 25 M: Swirl fraction of cross spectra

We see from the plot of the turbulent energy (figure 5.36) that there is a large contribution to the fluctuation level at the low frequencies. The highest peak in the energy spectrum closely matches the resonance frequency of the tunnel, which we predicted in section 5.6 (6.4 Hz). From the anisotropy invariants (figure 5.37) we can infer (see appendix C) that the structures associated with these low frequency fluctuations (slower than 40 Hz) are one dimensional waves, which confirms our hypothesis. Analysis of the components of the correlation spectrum has shown that the orientation of the one-dimensional low frequency waves is along the tunnel's core line.

The swirl fraction is sufficiently low to allow for the assumption that our grid turbulence is not circularly polarised.

#### 5.7.4 The velocity terminator

To study the distortion of turbulent flow we constructed a velocity terminator, which can be mounted in the flow. The terminator, which is shown in figure 5.39, consists of a vertical flat plate (1.2 meters long), with width  $D = 16$  cm, mounted perpendicular to the tunnel's mean flow direction, with a small hole in the centre. The hole is intended for positioning the four wire probe on the stagnation line upstream of the plate, with its axis oriented along the mean flow. Adhesive tape is used to make an airtight connection between the probe and the terminator.

The edges of the terminator have undulating skirts leading downstream from the edges. By mounting the terminator with skirts an artificially stabilised wake is added to the plate. The idea behind this modification is to reduce the influence of fluctuations from the wake. The undulations in the skirts are intended to prevent the flow leaving the terminator from forming a regular vortex street. The length of the skirts (in streamwise direction) positions the Kutta condition, associated with the wake-generated oscillating circulation around the plate, far downstream the zone in which the distortion experiment is done. Vortices behind the terminator would induce an oscillating motion of the upstream stagnation line in the lateral direction. Such oscillations,

which may interact with the grid turbulence, would make it difficult to assess which mechanism influences turbulence: the solid plate and mean flow gradients of the flow along the plate, or wake oscillations.

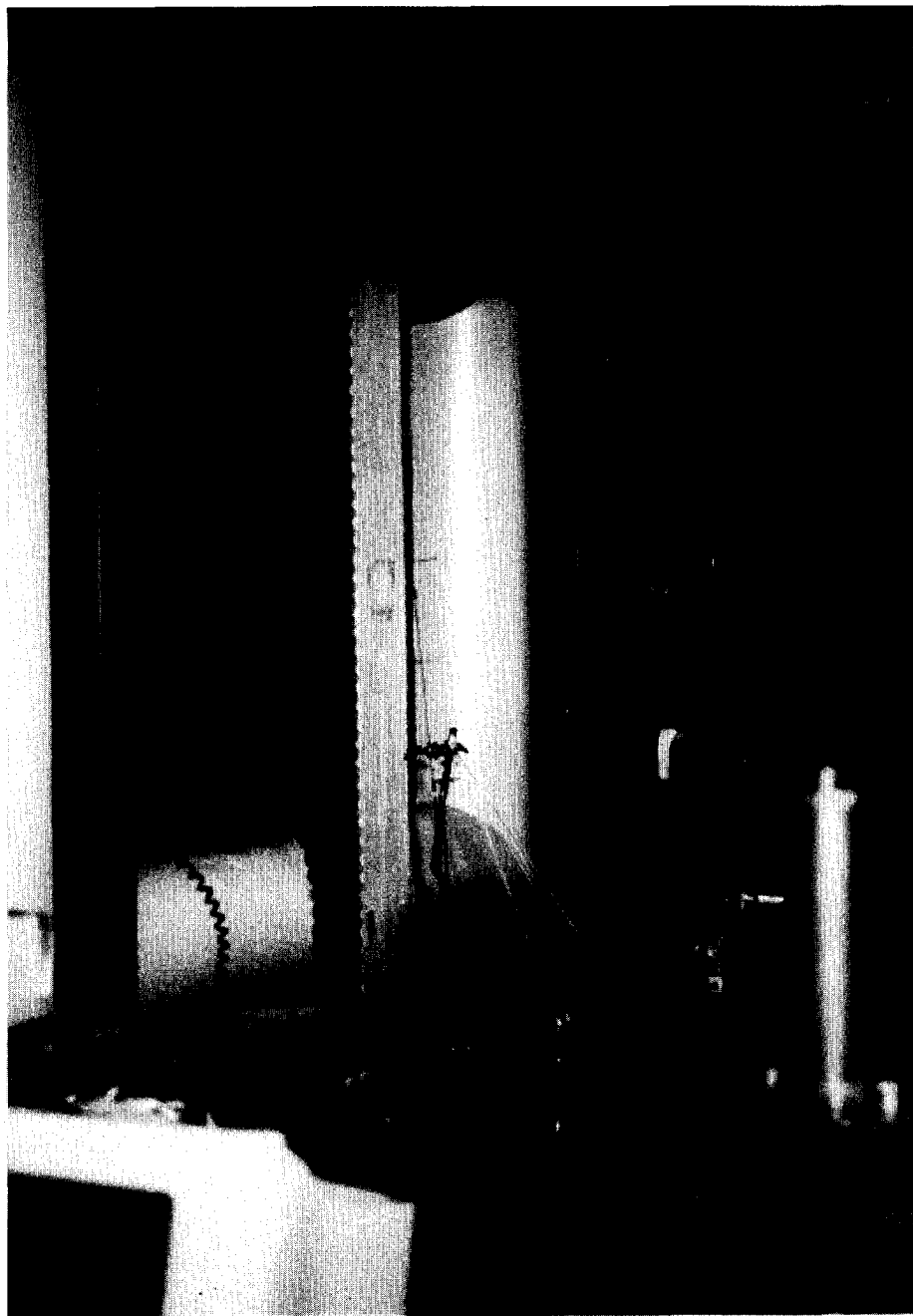


Figure 5.39: The terminator mounted in the testsection.



# Chapter 6

## Hot-wire anemometry

### Introduction

In this chapter we will outline the principles of hot-wire anemometry. We will also develop a calibration and signal interpretation method for the four-wire probe described in section 5.4. Concerning hot-wire anemometry Kovasnay (1959) wrote:

"During the 30 years of hot-wire turbulence research, the improvement in technique has been impressive and the published data on turbulence has increased steadily. Nevertheless, it still has more of the caprice of an art, than the complete reliability of a convenient routine laboratory procedure"

In his valuable book Perry (1982) added to this:

"Although further improvements have occurred, the statement is still true to a large extent. It is this 'caprice of an art' which leads many people not only to worry about the calibration of the instrument but also the calibration of the person carrying out the measurements."

Seventeen more years later I have come to the conclusion that Kovasnay's and Perry's statements are still valid. Hot-wire anemometry is far from being a 'plug-'n-play'-method.

I will first give a short qualitative account of the development of hot-wire anemometry. Then, in section 6.2 the principle of a constant temperature hot-wire anemometer (CTA) is explained. In section 6.3 a qualitative discussion on the dependence of the hot-wire voltage on different physical parameters is provided. Compensation of the hot-wire signal for temperature drift of the cooling fluid will be addressed in section 6.4. The calibration procedures for hot-wire probes, proposed in literature, will be outlined in section 6.5. A suggestion to use an indirect calibration method is made and explained. The procedures given in sections 6.4 and 6.5 will be tested in section 6.6.

## 6.1 Historical background

More than a century ago scientists were concerned about the heating induced in certain materials when electric current is flowing through them (see Forbes (1884)). They did efforts to eliminate this effect, via which valuable energy was dissipated and which could lead to unpleasantly high temperatures in conductors (see Oberbeck (1895) and Boussinesq (1901)).

After a while several people (Kennelly et al. (1909), Bordoni (1912) and King (1914)) realized that the immersion of a conductor with temperature dependent resistance in a fluid- or in air flow can provide a method to measure the fluid velocity. The principles are:

- Let an electric current go through the conductor, which as a result heats up.
- The fluid is cold, and will convect heat from the conductor.
- Measure the loss of heat of the conductor by monitoring the resistance of the conductor.
- Eliminate all dependences of the heat loss signal on physical parameters *other* than velocity (e.g. temperature of the fluid).
- Calibrate the remaining voltage/velocity-vector relation.

The last two items in this list are far from being trivial.

The first type of hot-wire anemometer that was developed, kept the probe at a constant electric current (CCA). This principle can be used to measure fluid velocity in static or in slowly varying situations. The major breakthrough in hot-wire anemometry came with the invention of the electron tube, which could be used to build an amplifier. The frequency response of a CCA is poor (-3dB at 650 Hz), which was soon (1912) recognised by Harper (1912). Therefore Dryden and Kuethe (1929), who wanted to measure velocity fluctuations, used a compensating amplifier in the CCA-circuit to improve response. Ziegler (1934) obtained a constant temperature anemometer (CTA) by integrating a feedback amplifier in the anemometer circuit. With carefully chosen cables, the anemometer system could now have its -3dB-point up to 100 kHz. The principle of CTA had already been used in 1912 by Morris (Morris, 1912), but frequency response in Morris' CTA was dependent on the researcher's physical condition since the feedback loop was manually driven.

Today Ziegler's CTA is still state-of-the-art. Since the development of the CTA in 1934, a lot of effort has been put into the development of a calibration procedure, and of a probe manufacturing technique. The effort to find a calibration procedure has led to a vast quantity of calibration methods. Most of these procedures have either been developed on theoretical grounds and have no relation to real experiments (unrealistic assumptions are made in some of the models), or they are outdated by the introduction of computers (see section 6.5). The effort to make a probe has been more fruitful than the quest for a calibration method. It has yielded subminiature probes, which are capable of the detection of all nine velocity gradients of atmospheric turbulence lengthscales of the size of Taylor's microscale (Tsinober et al., 1992).



## 6.2 CTA-circuit

In this section a review is given for the functioning of a Constant Temperature hot-wire Anemometer (CTA).

Basis of the hot-wire is a piece of wire with temperature dependent resistance. For the materials mostly used (tungsten, platinum), the relation between resistance  $R_w$  of the wire and temperature  $T$  can be assumed to be linear at least within the range of temperatures which we will be considering ( $T \in [300\text{ K} - 500\text{ K}]$ ) (the second order coefficient in this expansion differs from the first order coefficient by a factor  $\sim 10^4$ ):

$$\frac{R_w(T)}{R_w(T_0)} = 1 + \alpha_{T_0}(T - T_0) \quad (6.1)$$

The suffix  $T_0$  of  $\alpha$  indicates that  $\alpha$  depends in principle on  $T_0$ .

The wire is placed in an electric circuit according to the scheme presented in figure 6.1. Resistor  $R_2$  represents resistances of cables, contacts, prongs and additional internal resistances in the anemometer. Amplifier  $A_2$  is included to decouple output reading from the CTA-circuit; its amplification is here taken to be 1. The anemometer works according to the following steps:

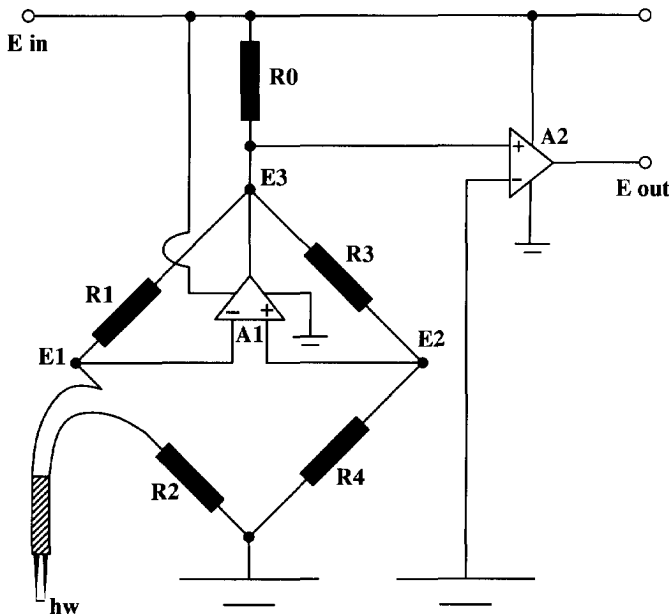


Figure 6.1: Circuit of a constant temperature anemometer

1. Input voltage  $E_{in}$  induces an electric current through the Wheatstone bridge with components  $(R_1, R_2 + R_{hw}, R_3, R_4)$ .
2. If voltage  $E_1$  is smaller than  $E_2$ , then differential amplifier  $A_1$  will increase  $E_3$ .

3. As a consequence of this,  $E_1$  will be larger, resulting in a larger current through the hot-wire, which will heat up.
4. The warmer hot-wire has larger resistance, bringing the Wheatstone bridge more in balance.
5. Steps 2 to 4 repeat until equilibrium is achieved.
6. The reverse process corrects the bridge if the hot-wire becomes too hot.

The bridge with feedback-coupling pursues equilibrium by keeping the resistance of the hot-wire at a constant value. This implies that the wire maintains its temperature. Usually the amplification of amplifier  $A_1$  is taken to be large, resulting in quick frequency response. Apart from frequency response, there is another advantage of CTA-anemometers: the constant temperature of the wire leads to a constant heat loss of the wire to other parts of the probe. In constant current anemometers heat loss was a function of velocity, and therefore hard to model.

Hot-wire voltage  $E_{hw}$  can be extracted from output voltage  $E_{out}$  as follows:

$$E_{hw} = \frac{R_4 R_{hw}}{(R_3 + R_4)(R_{hw} + R_2)} E_{out} \quad (6.2)$$

## 6.3 Cooling of a wire

In this section the dependence of the output signal on relevant physical quantities is outlined qualitatively. The question whether or not certain relations that will be given in this section can be used quantitatively for calibration will be answered in sections 6.4, 6.5 and 6.6.

We first consider the cooling of an element  $dl$ , taken from an infinitely long heated wire, placed perpendicularly to a uniform flow (subsection 6.3.1). Then the sensitivity of the wire's voltage to flow direction will be introduced (subsection 6.3.2). Finally, something is said about the difference between a real hot-wire and an element taken from a long wire (subsection 6.3.3).

### 6.3.1 Normal cooling of an element

Imagine a small element  $dl$  of a thin (diameter  $d$ ) wire, which is heated electrically (voltage  $E_{hw}$ , current  $I$ ) to a uniform temperature  $T_{hot}$  and resistance  $R(T_{hot})$ , and which is placed in a cooling flow with temperature  $T_0$  (velocity  $U$ , dynamic viscosity  $\mu$ , pressure  $p$  and density  $\rho$ ). The wire's axis is normal to the flow.

An ideal hot-wire with operational resistance  $R(T_{hot})$  in equilibrium at temperature  $T_{hot}$  dissipates all heat  $\phi$  [W] that is produced by the electric current to the flow:

$$\phi = E_{hw}^2 / R(T_{hot}) = dl h \pi d (T_{hot} - T_0) \quad (6.3)$$

where  $h$  [ $WK^{-1}m^{-2}$ ] is the heat transfer coefficient. Using relation 6.3, we can calculate this heat transfer coefficient from the voltage  $E_{hw}$  over the wire.

Many physical quantities influence the exchange of heat from the wire. The introduction of dimensionless characteristic numbers allows for comparison of the relative contributions of the different flow processes to the transfer of heat. The following dimensionless numbers play a role:

- Nusselt's number, defined as  $Nu \equiv \frac{hd}{k}$  (where  $k [WK^{-1}m^{-1}]$  is the fluid's heat conduction coefficient), characterises the exchange of heat. It is Nusselt's number which is measured by the hot-wire anemometer.
- Reynolds' number, defined as  $Re \equiv \frac{\rho U d}{\mu}$  characterises the importance of inertia-forces over viscous forces. Quantity  $\mu [kg m^{-1} s^{-1}]$  is the dynamic viscosity.
- Prandtl's number, defined as  $Pr \equiv \frac{c_p \mu}{k}$  (with  $c_p [J kg K^{-1}]$  the specific heat of the fluid at constant pressure). This number gives the ratio of viscous to thermal diffusion.
- Grashoff's number, defined as  $Gr \equiv \frac{g \rho^2 d^3 \beta (T_{hot} - T_0)}{\mu^2}$  (with:  $g [ms^{-2}]$  gravitation-acceleration,  $\rho [kg m^{-3}]$  density,  $\beta [K^{-1}]$  coefficient of cubic expansion of the gas), characterises buoyancy effects.
- Eckert's number, defined as  $E \equiv \frac{U^2}{c_p (T_{hot} - T_0)}$ , is a measure for the importance of compressibility.
- Overheat ratio, defined as  $a \equiv \frac{T_{hot} - T_0}{T_0}$ . The fact that tungsten rusts above 300 degrees Celsius (Lowell, 1950) limits the overheat ratio for non-coated tungsten hot-wires. Platinum and platinum-iridium do not oxidise, but they have a very low temperature coefficient of resistance.
- Mach's number, defined as  $Ma \equiv \frac{U}{u_{sound}}$ , where  $u_{sound}$  represents the speed of sound in the fluid.
- Elongation of the wire, defined as  $\frac{dl}{d}$ , where  $dl$  is the length of the filament, and where  $d$  is its diameter. Heat leakage to the prongs depends on this parameter.
- Knudsen's number, defined as  $Kn \equiv \frac{\lambda}{d}$ , with  $\lambda$  the molecular mean free path. This number indicates whether or not continuum approximations can be made for the interaction between the fluid and the wire.
- Thermal conductivity ratio, defined by  $\frac{k}{k_w}$ . In this relation  $k_w$  is the wire material's heat conduction coefficient.

Altogether we can say that heat exchange from a wire to a fluid depends on all these characteristic numbers:

$$Nu = f(Re, Pr, Gr, E, a, Ma, \frac{dl}{d}, Kn, \frac{k}{k_w}). \quad (6.4)$$

Fingerson and Freymuth (1983, p.111) worked out an example for air flow around a wire with  $d = 4\mu m$ ,  $dl = 1.25mm$ ,  $T_{hot} = 250^\circ C$ . They found that for this configuration buoyancy effects are negligible for velocities above 5.2cm/s (i.e. no dependence on Gr). They

also indicate that for air Prandtl's number can be assumed to be constant. Although for the example  $Kn \simeq 0.02$ , which indicates some molecular slip-flow, it is allowed to use continuum theory as long as compressibility effects are small. Mach's and Eckert's numbers are only relevant for high velocity or low density flow. The thermal conductivity ratio may represent temperature inhomogeneities on and around the wire. This parameter is mostly used to estimate the importance of leaking of heat to the prongs. For a tungsten wire in air flow the thermal conductivity ratio is smaller than  $10^{-3}$  and as a consequence it is negligible. The example of Fingerson and Freymuth is representative for the experiments which will be performed in this study. Therefore we can reduce relation 6.4 to:

$$Nu = f(Re, a, \frac{dl}{d}) \quad (6.5)$$

Parameter  $\frac{dl}{d}$  represents aerodynamic prong-effects. Information about the velocity of the fluid is now hidden in Re.

The reason why King's publication (King, 1914) has become a classic, is that King gave a ready to use functional form for relation 6.5:

$$Nu = A' + B'Re^{0.5} \quad (6.6)$$

in which  $A'$  and  $B'$  are calibration constants. Relation 6.6 is therefore called King's law.

Following the direction indicated by King, many researchers have wrought out subtle modifications to relation 6.6 (see Collis and Williams (1959); Kramers (1946)). The modification to relation 6.6 which today is still the most popular is the replacement of fixed exponent 0.5 by a variable calibration constant  $n$ , so that:

$$Nu = A' + B'Re^n. \quad (6.7)$$

Although King did not make this modification, people also refer to relation 6.7 as "King's law", a nomenclature which will be adopted in the current study either.

The expression of Collis and Williams (1959), which more accurately includes changes in fluid properties with temperature, is:

$$Nu = (A' + B'Re^n) \left(1 + \frac{a}{2}\right)^{0.17} \quad (6.8)$$

### 6.3.2 Directional sensitivity of an element

In the previous subsection we saw how a hot-wire probe responds to a cooling flow oriented perpendicularly to the wire. In this section we will consider the dependence of the wire's signal to the direction of the flow with respect to the wire.

It is common to adopt a version of King's law (relation 6.7), which is formulated for physical quantities, instead of for dimensionless characteristic numbers ( $A$ ,  $B$  and  $n$  are again calibration constants):

$$E_{hw}^2 = A + BU_{eff}^n \quad (6.9)$$

$U_{\text{eff}}$  is called the effective cooling velocity. It represents the magnitude of the (fictive) velocity in a given direction (perpendicular to the wire, in the plane of both wire and probe), for which the flow induces the same cooling as by the actual velocity vector. The question now is: what is the relation between the flow-velocity vector and this effective velocity?

The effective cooling velocity depends both on the wire's orientation and on the velocity-magnitude of the cooling flow. A concept which is most often adopted is the following: for every given speed of the flow, the relation between the effective cooling velocity and the wire's orientation is the same:

$$U_{\text{eff}} = ||\mathbf{u}||f(\text{flow and wire orientations}) \quad (6.10)$$

where function  $f$  expresses angular sensitivity of the wire.

For small deviations from flow normal to the wire (up to 30 degrees) one has observed that the effective cooling velocity is simply the velocity component normal to the wire:

$$U_{\text{eff}}^2 = U_{\perp}^2 \equiv U_n^2 + U_b^2 \quad (6.11)$$

For a definition of the directions used, see figure 6.2. This relation is known as the Cosine Law.

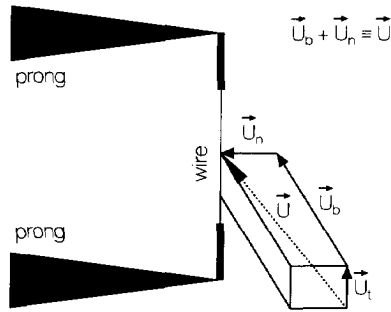


Figure 6.2: Definition of velocity contributions

We have seen that an ideal hotwire does not respond to flow parallel to the wire, and that its response to normal flow does not depend on the direction from which this normal flow comes (i.e. the probe does not feel any difference between  $U_n$  and  $U_b$ ). A study in more detail (Jørgensen, 1971), which was extended to larger angles, revealed that a hot-wire actually experiences also some cooling by the velocity component parallel to the wire (component  $U_t$  in figure 6.2). Moreover it appeared that flow normal to the wire, in the plane of both the wire and the probe (component  $U_n$ ), is slightly blocked by the stem of probe. This was seen as an increase in cooling when the direction of the flow was changed from  $U_n$  to  $U_b$ , which is not only normal to the wire but also normal to the probe-axis. Relation 6.11 was therefore extended to:

$$U_{\text{eff}}^2 = U_n^2 + k^2 U_t^2 + h^2 U_b^2 \equiv U_{\perp}^2 + k^2 U_t^2 + (h^2 - 1) U_b^2 \quad (6.12)$$

which is known as Jørgensen's Law. Constants  $k$  and  $h$  are calibration constants. Typical values are (Jørgensen, 1971):  $k \sim 0.2$  and  $h \sim 1.08$ .

### 6.3.3 Non-ideal effects

The previous sections have given us a qualitative insight into the velocity-response of an ideal hot-wire probe in the flow of a medium under stationary physical conditions (density, temperature, etc.). In this section some remarks are made concerning real, non-ideal situations.

- Hot-wires are mounted on prongs. In some cases, when e.g. gold plating of prong-tips and of the external parts of the wire is used, only a small part of the wire heats up and is thus sensitive to cooling flow. This is done to reduce heat-loss of the wire to the prongs, and to reduce aerodynamic influences of the prongs on the hot-wire cooling. Very small probes can only be as small as they are when the whole wire is made sensitive, which means no plating of the external parts of the wire. Jørgensen's law 6.12 assumes that the wires in a probe have an effective cooling velocity, of which the directional variation is the same for all absolute flow velocities. This assumption is invalid for probes suffering from prong-effects. Moreover, the functional relation between flow velocity and effective cooling velocity is bound to be complex for probes with aerodynamically interfering prongs. In this study we will use gold-plated prong-tips. Jørgensen's law will not be used to analyse turbulence measurements.
- Both hot-wire materials and the electric connections (welded or soldered) between the wire and the prongs are subject to aging and pollution. This means that the properties of a probe drift as a function of time and therefore they must be monitored carefully. Regular calibration can help solve this problem. Prior to use, wires are usually artificially aged by a period of operation at higher overheat ratio (e.g.  $a = 0.8$ ) than will be used in real experiments (e.g.  $a = 0.6$ ).
- The resistance of a typical hot-wire is a few Ohms. This makes it difficult to measure a probe's characteristics in one set-up and subsequently decouple the probe and install it in a different place with different cables in the electronic circuit to perform the measurement. The change in contacts and in cable-resistances can e.g. spoil carefully performed calibrations. Therefore calibration and measurement must be done at the same place.
- A hot-wire averages the velocity field over its length. Velocity gradients leading to large velocity differences over the probe's wires can therefore cause misinterpretations of the probe's signals, because of the non-linearity of the velocity/voltage calibration (see Wyngaard (1968, 1969); Hirota et al. (1988)). This effect will become significant in flows where mean gradients over the size of the wire are significant, or when waves are measured with wavelength smaller than the wire length. We will not study sharp gradients, nor will we try to resolve structures smaller than the wires (which usually have length 1 mm). In our study Taylor's microscale is estimated to be larger than 1 mm. Therefore with our probe we will not have problems due to the length of the wires. Citriniti and George (1996) have pointed out that a hot-wire anemometer probe reduces spatial aliasing of turbulent velocity fluctuations because of the filtering property of the probe sensing element.
- A long, thin wire has non-uniform temperature distribution. This complicates heat transfer relations involved. By taking the length of the wires more than 200 times the diameter,

we reduce temperature inhomogeneity effects at the ends of the wire to a relatively small contribution of the total cooling of the wire.

- Wires that are not tightly mounted to their prongs adapt their orientation to the flow, which gives unwanted directional variations.
- Multi hot-wire probes must be built such as to reduce thermal cross-talking by the wires. This phenomenon will give coupled fluctuating signals, which a researcher unaware of this problem may incorrectly interpret as anisotropy of the Reynolds stress tensor.
- Some researchers (Wyngaard, 1969) reduce the number of prongs in their probes by using one central prong for all wires on the probe. Though this practice may be comfortable for the manufacturer of the probe, such an implementation will lead to severe cross-talk between the signals of the wires. By using eight prongs for four wires we prevent this source of error.
- The wires of a multi-wire probe are a distance  $d$  apart. Consequently, the signals of the different wires of the probe are not responses to the same flow (see (Wyngaard, 1969; Park and Wallace, 1993; Zhu and Antonia, 1995, 1996)). This effect will become a problem if the flow has local (mean or instantaneous) velocity gradients. Gooden (1995) has found that the errors in Reynolds stress are proportional with the square of the separation  $d$  measured in Taylor's microscales  $\lambda$ . He also found that these errors are small for nearly isotropic flow. Gooden's results are confirmed by our calculations for an isotropic spectral contribution, which are presented in appendix F. We found that wire separation leads to an underestimation of the longitudinal spectra and to an overestimation of the lateral spectra. This artificially induced misinterpretation of the anisotropic character of the flow is axisymmetric: isotropic turbulence is interpreted to be turbulent with a smartie-like axisymmetric anisotropy. This colouring of the turbulence character is shown to become appreciable for waves with wavelength smaller than six times the wire-separation.

## 6.4 Temperature drift of the fluid

Hot-wire anemometers work by virtue of heat exchange. Therefore it will not sound surprising that a temperature drift in the flow will cause immediate change in the heat exchange from the wire to the fluid and consequently in the measured velocity. This effect, which is of utter importance, is often incorrectly accounted for. Many researchers rely on ready to use methods from literature. Their confidence in these methods makes these researchers apply them without any checking or calibration of the relations involved.

The best method to overcome temperature corrections is to keep temperature constant during both calibration and measurement. Not every laboratory has air-conditioned wind tunnels, which makes this ideal method in many cases to a dream. Therefore we have to apply corrections. Adequate temperature correction is the first step in the process of interpreting hot-wire voltages in terms of velocities.

In this section we will first derive the relations for the dependence of hot-wire signals on temperatures of wire and fluid. Then we will make an inventory of the correction methods proposed in literature and test these.

### 6.4.1 Temperature dependence of the signal

Relation 6.3 gives a model for the dissipation of energy by a hot-wire at temperature  $T_{\text{hot}}$  in a fluid at temperature  $T_0$ . Fingerson and Freymuth (1983, p.123) show, by careful bookkeeping of all fluid temperature dependences, that Collis and Williams' relation 6.8 (with  $n = 0.45$ ) leads to the following relation for heat exchange  $\phi$ :

$$\phi \sim \left( A(T_{\text{hot}} + T_0)^{0.8} + BU^{0.45} \right) \left( 1 + \frac{aT_0}{2} \right)^{0.17} (T_{\text{hot}} - T_0) \quad (6.13)$$

They applied both relations 6.3 and 6.13 to air flow with  $T_{\text{hot}} \sim 230^\circ\text{C}$  and  $T_0 \sim 23^\circ\text{C}$ . They examined an increase in ambient temperature by 50K within a velocity range from 6m/s up to 100m/s and found that the velocities calculated by both methods do not differ more than 3 percent. This makes clear that relation 6.13 for the heat exchange differs negligibly from relation 6.3. In the current study we adopt relation 6.3 for the heat transfer. This choice is made because the relation is simpler than relation 6.13 and nearly equally accurate. Moreover, relation 6.13 is based on King's law. Later in this chapter we will show that the combination of King's law and Jørgensen's law cannot be used for quantitative interpretation of hotwire signals. This is an extra reason why we do not want to adopt relation 6.13.

Let us compare total output signals  $E_{\text{out}}(T)$  and  $E_{\text{out}}(T_{\text{ref}})$  (as provided by relations 6.2 and 6.3) of the anemometer for two different situations, the former when the cooling fluid has temperature  $T$ , and the latter when it has temperature  $T_{\text{ref}}$ . We accomplish this by taking the ratio of the two output signals:

$$E_{\text{out}}(T_{\text{ref}}) = E_{\text{out}}(T) \sqrt{\frac{T_{\text{hot}} - T_{\text{ref}}}{T_{\text{hot}} - T}} \quad (6.14)$$

Combination of this relation with relation 6.1 for the resistance of a wire as a function of temperature gives:

$$E_{\text{out}}(T_{\text{ref}}) = E_{\text{out}}(T) \sqrt{\frac{R(T_{\text{hot}}) - R(T_{\text{ref}})}{R(T_{\text{hot}}) - R(T)}} \quad (6.15)$$

Relations 6.14 and 6.15 provide us with the anemometer signal which we would have measured in case the fluid would have had temperature  $T_{\text{ref}}$ , whereas in reality it had temperature  $T$ .

The latter relation 6.15 has been proposed by Kanevce and Oka (1973). Lomas (1986) claims that this relation will provide better ambient temperature correction than the former 6.14. The reason he gives is the following: when relation 6.14 is used, one has to estimate  $T_{\text{hot}}$ . This is not an easy thing to do. When relation 6.15 is used, we need to know the resistance  $R(T_{\text{hot}})$  of the wire at operational temperature. This parameter is set to the Wheatstone-bridge in the anemometer by the researcher and consequently known. Furthermore one needs to know the cold resistance of the wire at different ambient temperatures. In a simple experiment one can



measure the relation between the total cold resistance of the probe and temperature. From relation 6.15 we see that the temperature dependence of the *total* output signals of the anemometer is independent from the values of any resistance in the anemometer bridge other than the hot-wire's; even parasite resistances from cables, contacts and prongs do not enter the relation! This would make relation 6.15 better applicable than relation 6.14. Relation 6.15 however suffers from a subtle incompleteness, which renders it an inappropriate tool. In appendix E both models for the dependence of the signal on ambient fluid drift are examined. It is shown that relation 6.15 has to be extended to:

$$E_{\text{out}}(T_{\text{ref}}) = E_{\text{out}}(T) \sqrt{\frac{R_{\text{total}}(T_{\text{hot}}) - R_{\text{total,cal}}(T_{\text{ref}}) + \Delta_1}{R_{\text{total}}(T_{\text{hot}}) - R_{\text{total,cal}}(T) + \Delta_1}} \quad (6.16)$$

Subscript "cal" means that the cold resistance as function of temperature is determined in a calibration.  $\Delta_1$  represents the sum of two contributions: The first contribution to  $\Delta_1$  is the difference in contact and internal resistances between the CTA and the Ohmmeter used to measure the cold resistance. The second contribution to  $\Delta_1$  concerns the bridge's resistance which is set by the user. It is formed by two contributions: 1: mis-indication on the anemometer's front panel of the resistance to which the bridge is adjusted and 2: the respective parasite resistance inside the anemometer. In appendix E it has been shown that  $\Delta_1 \sim 0.3\Omega$ .

The fact that Lomas had forgotten resistance  $\Delta_1$  in relation 6.15 makes his claim that this relation would be better in practical applications than relation 6.14 an incorrect statement.

#### 6.4.2 Correction for temperature drift

Both relation 6.14 and relation 6.16 can in principle be used to correct hot-wire samples for ambient temperature drift. In appendix E a discussion is presented on why the resistance method is rejected and why and how we adopt relation 6.14 to correct for ambient fluid temperature drift. The method to determine  $T_{\text{hot}}$  directly by calibration is outlined in subsection E.1.3.

### 6.5 Velocity calibration methods

Now that we have some insight into the behaviour of a real hot-wire probe, we will see how this knowledge can be used to calibrate hot-wire probes, and to interpret their signals.

There is a major difficulty that has to be observed when one tries to translate hot-wire responses to velocity: We have seen that a wire is sensitive roughly to the velocity normal to its axis. This introduces ambiguities in the solution for the wind vector. With a three wire probe with perpendicular wires aligned with the coordinate axes all wind with absolute velocity  $u$  aligned with any of the eight diagonal vectors  $(\pm 1, \pm 1, \pm 1)$  (one in each octant, see figure 6.3) will cause the same set of hot-wire responses. Many signal interpretation techniques that have been reported in literature stem from the pre-computer era. Calculative labour had to be limited by restriction of calibration procedures to simple relations. Therefore many researchers adopted qualitative relations 6.9 and 6.12 in quantitative sense. These methods, implementing physical

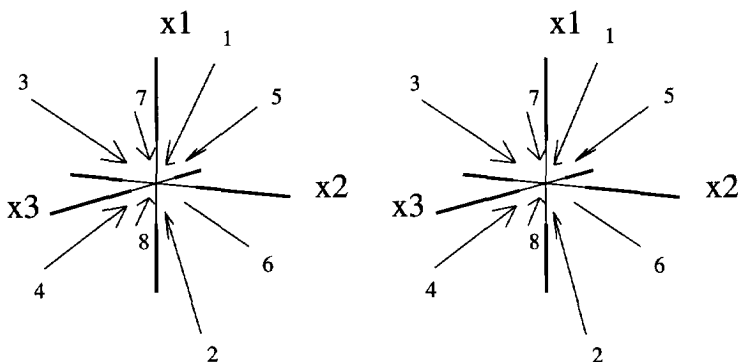


Figure 6.3: Three wire probe with eight velocity vectors inducing the same response

laws for the cooling of a wire, lead to the concept of an effective cooling velocity. They are addressed to in the first subsection.

The look-up table method and a recently developed method will be treated in subsequent subsections.

In subsections 6.5.5 and 6.5.6 suggestions are made to simplify labour even more by fitting the wind velocity vector directly as function of hot-wire voltages using orthogonal polynomials.

In section 6.6 the performance in practical applications of several of these calibration models will be tested and compared.

A recently developed calibration and interpretation method is based on neural network theory. This method has its origin in the Technische Universität Berlin, Institut für Luft- und Raumfahrt, Fachgebiet Luftfahrtantriebe (Prof.Dr.-Ing.J. Hourmouziadis, fax + 49 30 314 79448). In a brochure (1998) this group reports that their neural method would be a major improvement to polynomial methods, especially in the probe response regions with strong non-linearity. The neural network method will not be addressed in this thesis.

### 6.5.1 Effective velocity methods

Effective cooling velocity methods deduce wind velocity from hot-wire response by careful analysis of the physics involved in the cooling process of a wire. In relation 6.9 the effective cooling velocity has been defined as the magnitude of the (fictive) velocity normal to the wire, needed to induce the same cooling as induced by the actual wind velocity vector. This concept was introduced to make a connection between models for the normal cooling of a wire and models for the directional sensitivity of a wire. The application of methods using this concept is outlined in this subsection.

In section G a method is given to estimate the parameters  $A, B, n, k$  and  $h$  plus orientation angles  $\theta$  and  $\phi$  of a wire, which are involved in the physical relations for the hot-wire response (King's law and Jørgensen's law).

Jørgensen's law 6.12 can be used to relate the effective cooling velocity (which is a simple function of the hotwire response) to the velocity vector components in the laboratory's Cartesian frame of reference:

$$U_{\text{eff}} = \sqrt{c_1 U_1^2 + c_2 U_2^2 + c_3 U_3^2 + c_4 U_1 U_2 + c_5 U_1 U_3 + c_6 U_2 U_3} \quad (6.17)$$

Coefficients  $c_i$  are expressions in terms of the wire and probe orientation and in terms of sensitivities  $h$  and  $k$ . Many researchers obtain (by careful selection of hot-wire orientations, usually under the approximations  $h = 1$  and  $k = 0$ ) values for  $c_i$  in expression 6.17, such that the set of response equations can be solved in a simple analytic way. However, it is not always possible to measure directly of a probe a wire's orientation with accuracy sufficient to be used for calibration purposes. Another difficulty is introduced by the intrinsic uncertainty of the wire's orientation following from mounting the wire on a probe.

We can calculate coefficients  $c_i$  in Jørgensen's law 6.17 from the parameters which were estimated in section G. In certain cases (Marasli et al., 1993) one estimates coefficients  $c_i$  by fitting Jørgensen's law 6.17 directly to a calibration dataset, without first estimating  $\theta$ ,  $\phi$ ,  $h$  and  $k$ .

Two ways to use a probe's calibration constants (and functions) to estimate the velocity vector from the probe's response will now be presented: The first method is based on the interpretation of mean and fluctuating parts of the response. The second method focuses on the analysis of instantaneous samples.

### 6.5.1.1 Signal interpretation via Reynolds decomposition

Hot-wire probes are often used to measure both mean velocity and turbulence quantities. Many people have assumed in their analysis that the mean of a hot-wire signal is related to mean velocity, and that the root-mean-square of the fluctuating component is related to turbulence superimposed on the mean velocity. Such a procedure can be only considered partly correct when the hot-wire calibration would be linear. This is not the case (as was shown in an article by Parthasarathy and Tritton (1963), who point out that "one gets the impression that sometimes it is overlooked"). Even then, the RMS of the fluctuating velocity will contribute to the time averaged response equations, which are often considered to be equations for the mean velocity. To distinguish between mean and fluctuating components of a hot-wire's response in terms of velocity components, one makes a Reynolds decomposition of velocity components and of hot-wire signals into mean and fluctuating parts. Expressions for mean velocity and for Reynolds stresses are obtained by combining Reynolds decomposition with Taylor series expansion of relation 6.17 for small velocity fluctuations around the mean velocity. The Taylor series for relation 6.17 is combined with its time average: The latter is subtracted from the former. This gives an equation for the fluctuating velocity component.

Taylor expansion of the effective cooling velocity can easily lead to errors (e.g. Saustrup Kristensen's calculations (Saustrup Kristensen, 1973)). It is surprising that it was not until 1975 that in a moment of brilliance a scientist (Rodi, 1975) has come up with the cunning plan to apply a lineariser to match hot-wire response with the *square* of the effective cooling velocity, instead of with the effective cooling velocity itself. This step allows one to by-pass the Taylor's expansion in the relation between hotwire signals and the velocity vector, which

was mentioned in the former paragraph. Although Rodi (like Acrivlellis some years later (Acrivlellis, 1977)) persevered in Saustrup Kristensen's errors in the Taylor's expansion of the old method, his suggestion was good. Jørgensen's relation now took the form:

$$U_{\text{eff}}^2 = c_1 U_1^2 + c_2 U_2^2 + c_3 U_3^2 + c_4 U_1 U_2 + c_5 U_1 U_3 + c_6 U_2 U_3 \quad (6.18)$$

Despite the progress in analysis of hot-wire data some researchers continued to use relation 6.17 with  $k = 0$  and  $h = 1$  (Kastrinakis and Eckelmann, 1983), facing problems with cross-talk of Reynolds stresses due to neglected terms in Taylor expansions.

One way to find the mean velocity vector and the Reynoldsstresses from the Reynolds decomposition of relation 6.18 is the following: Perform six recordings of (mean and RMS of) the response of a single wire. Use this single-wire probe in six different (known) orientations. When the stochastics of the flow have been the same during all six measurements, then these six measurements with a single wire probe have provided us with enough independent equations of type 6.18 to be able to calculate the mean velocity vector and the Reynoldsstress. A technique similar to the method just explained is used by Gooden (1995) to analyse X-wire measurements.

### 6.5.1.2 Instantaneous signal interpretation

Implementation of a non-linear multi-equation solver on a computer makes it possible to directly use relations 6.9 and 6.18 (or relation 6.12) to find full velocity information from the instantaneous responses of the wires on a three-wire probe.

When the laws of King and of Jørgensen are used for calibration, then a probe is calibrated indirectly, i.e. the response of the wires is modelled as function of the wind velocity vector in stead of vice versa. In such indirect cases one has to invert these relations to interpret hot-wire samples in terms of velocity vectors. We have written a program to solve the velocity from the response of 3-wire probes (the response of a 4-wire probe is interpreted via combination of subprobe estimates according to either method described in section 6.5.5). Rootfinding routine "c05pcf" from the NAG-library is used to iterate from an initial guess for the velocity vector to a solution of the nonlinear probe response model.

Tests have shown that convergence of the rootfinding procedure depends critically on the initial guess for the velocity vector. Depending on the situation, up to eight different velocity-vectors can induce the same response on a 3-wire subprobe. We used a frontal (zero pitch and yaw, see definition 6.30) velocity of 4 m/s as initial guess. Sometimes the rootfinding procedure gave a velocity vector outside a certain cone of acceptance (situated around the frontal vector). In such cases this vector was not accepted as velocity estimate, but instead it was twisted to a frontal wind vector and fed as new initial guess to the rootfinding routine. This was repeated until proper convergence was achieved (i.e. within the calibration range). If no convergence to acceptable estimated was found, then the subprobe result was tagged "suspect".

It so happens (especially when one of the wires gave a low signal) that several solutions of the response equations can be found close to one another, rendering the rootfinding procedure helpless. This is the reason why we did not get 100 percent match between simulated (mathematically perfect, i.e. no noise was added to the signal) calibration datasets and the inverses of

their exact models.

When calibration velocities themselves were used as initial guesses, then a perfect match between dataset and inverted model was found. This method (of using the calibration conditions as primary guesses for the calculation of the model accuracy) ascribes tempting accuracy on the probe. This is deceptive since no such perfect initial guesses will be present when one uses the model to process data from real measurements.

The performance of the effective velocity method to find velocity information from the response of a four-hot-wire probe is examined in section 6.6.

## 6.5.2 Look-up table method

Hot-wire responses  $E_i$  (index  $i$  counts the wires) that have been corrected for temperature drift contain information on wind velocity, which we want to extract from them. To reduce the size of a multi-wireprobe one places the prongs closely together and drops the idea to plate portions of the wire close to the prongs. As a result, the constants in Jørgensen's law will become strongly velocity dependent. Also, the presence of prongs in the neighbourhood of sensitive parts of wires leads to complicated relations between real wind velocity and the effective cooling velocity. This can render Jørgensen's law 6.12 completely inadequate.

Perry (1982, p.4-5) remarks that:

"...one cannot assume that the 'effective' angle of an inclined wire can be measured directly from an image of the filament. This leads to a different philosophy of calibration as outlined in chapter 8. Broadly speaking, this philosophy is to ignore the heat transfer laws, remove the complicating effects of linearisers and ignore the details of wire angles. One simply fits a Taylor series to the voltage versus known velocity component expanded about some operating point..."

This strong statement finds its basis in a development in hot-wire data analysis that has been elaborated parallel to that of the effective cooling velocity method.

Willmarth and Bogar (1977) developed a method for the calibration of X-wire probes for measuring two velocity components  $u$  and  $v$ . They recorded the response of both wires to wind chosen on a regular grid of 20 absolute velocities times 20 yaw-angles of the probe. Via interpolation of the calibration data, they could interpret experimental data obtained in experiments. This method, which can be extended to three-dimensional flow, is called a *look-up table method*. A disadvantage however is, that the calibration dataset needed for 3D-flow and a four-wire probe requires a full 3D-calibration, which takes considerably more time than the calibrations needed to apply King's law in combination with Jørgensen's law. Look-up table methods do not suffer from inaccuracies in and assumptions made by effective angle methods. This advantage, combined with simplicity, is why the look-up table method has gained terrain over the effective velocity method (Johnson and Eckelmann, 1984; Browne et al., 1989; Lueptow et al., 1988; Wubben, 1991). A problem with this method is that it is indirect: an interpolation process inverting the relation between probe response and wind velocity is needed for every sample. Another problem is the following: bad calibration samples introduce systematic errors in their neighbourhoods when local interpolation schemes are used.

### 6.5.3 Lemonis' indirect subprobe method

Lemonis (1995), who used a 21-wire probe, was aware of the problem with the King/Jørgensen method, referred to in the introduction to the former subsection. His method of data-processing, which (like the look-up-table-method) abandons the effective cooling velocity concept, is presented in this subsection.

In Lemonis' model the point of departure is the fact that hot-wire response  $E_i$  is the consequence of a wind velocity  $U_j$  (for the case of four wires):

$$E_i = f_i(U_1, U_2, U_3) \quad i = 1..4 \quad (6.19)$$

by building functions  $f_i$  as a linear combination of linearly independent 3D Bernstein-Bézier polynomials  $B$  as follows:

$$f_i(U) = \sum_{k=0}^{k'} \sum_{l=0}^{l'} \sum_{m=0}^{m'} c_{iklm} B_k^{k'}(u_1) B_l^{l'}(u_2) B_m^{m'}(u_3) \quad (6.20)$$

$$B_k^{k'}(x) \equiv \frac{k'!}{k!(k'-k)!} x^k (1-x)^{k'-k} \quad (6.21)$$

$$u_n \equiv \frac{U_n - U_{n,\min}}{U_{n,\max} - U_{n,\min}} \quad (6.22)$$

Coefficients  $c_{ijklm}$  are found by application of a least-squares routine (see subsection A.1) fitting relation 6.20 to a calibration data-set. Subscripts  $_{\min}$  and  $_{\max}$  refer to minimum and maximum values of a quantity within the calibration data-set.

Lemonis' method has as merit that it does neither lean on specific laws which might be too limited to model the response of multi-hotwire probes nor on knowledge of the exact orientations of the wires.

The choice for Bernstein-Bézier polynomials is unclear to me. These polynomials are linearly dependent on other kinds of polynomials (e.g. Legendre-, ordinary- and Chebychev polynomials). They therefore span the same functional space as the other polynomials do. Functions which are orthogonal on their domain speed up numerical least-squares methods to solve coefficients  $c_{ijklm}$ . Unfortunately Bernstein-Bézier polynomials are not orthogonal on their domain.

The response of a four-wire probe defines a set of four non-linear equations in velocity components  $U_j$  through relation 6.19. This overdetermined set is split into four determined three-equation sub-probe systems. This is done by neglecting of the equation for the wire with the number corresponding with the respective subprobe from the four-equation set.

Lemonis' calibration relation 6.19 needs the exact wind velocity vector as input and provides the user with information concerning the hot-wire probe's response: it outputs to you the response of the probe (= what you have) as function of its input: the velocity vector (= what you do not yet have, but would like to know). This system has to be inverted. Three-wire sub-probe systems are solved using a non-linear multi-dimensional rootfinding routine. Lemonis uses a non-linear equation solver from the IMSL computer-library. Sub-probe results are then combined into a full probe result by taking the arithmetic mean (Lemonis and Dracos, 1994) (add and divide by four).

In section 6.6 the practical performance of the indirect Lemonis model is studied and compared with the indirect King/Jørgensen model, the direct 4-wire subprobe model and the full 4-wire model.

#### 6.5.4 Full 4-wire indirect model

Relation 6.19 for the response of a four-wire probe can be inverted without using subprobes. Assume that the four response functions of the wires are comparable in magnitude (i.e. the wires are roughly the same). Assume also that the errors in the four hotwire signals have the same expectation value. In this case we find the best estimate for velocity  $U$  at the point where the following quantity  $Q^2$  has a minimum:

$$Q^2 \equiv \sum_{i=1}^4 \left( E_{i,\text{measured}} - f_i(U_1, U_2, U_3) \right)^2 \quad (6.23)$$

A nonlinear minimisation routine (E04FCFF from NAG) is used to solve this equation. In relation 6.19 we use Chebychev polynomials (defined in relation 6.26) instead of Bernstein functions. This is done to facilitate computation. Like the Bernstein functions in section 6.5.3, these Chebychev functions are taken orthogonal on the datarange.

The inversion of calibration relation 6.19, which is needed in indirect methods to interpret measured responses in terms of velocities, is time consuming. We will see direct data-processing methods, which give explicit expressions for the velocity as function of the response of the probe, in the following two subsections.

Test results of the indirect full 4-wire method are presented in section 6.6.

#### 6.5.5 Direct method: subprobe model

The concept of fitting abstract functions to hot-wire calibration data can be taken even further than presented in the former subsection. Tsinober et al. (1992) presented a study in which they directly fitted velocity components as function of hot-wire voltages. Three-dimensional orthogonal fourth order Chebychev functions are used to map three hot-wire responses in subprobe  $j$  on three velocity components (indicated with index  $i$ ). A triple of hot-wire responses in a subprobe is written as:  $(E_{j,1}, E_{j,2}, E_{j,3})$ , where  $(E_{j,1})$  refers to the first wire in subprobe  $j$ ,  $(E_{j,2})$  to the second wire and  $(E_{j,3})$  to the third. The four subprobes give the following estimates:

$$\begin{aligned} U_{j=1,i} &= f_{1,i}(E_2, E_3, E_4) \quad i = 1..3 \\ U_{j=2,i} &= f_{2,i}(E_1, E_3, E_4) \quad i = 1..3 \\ U_{j=3,i} &= f_{3,i}(E_1, E_2, E_4) \quad i = 1..3 \\ U_{j=4,i} &= f_{4,i}(E_1, E_2, E_3) \quad i = 1..3 \end{aligned} \quad (6.24)$$

$$f_{j,i}(E_{j,1}, E_{j,2}, E_{j,3}) = \sum_{k+l+m=0}^4 c_{j,iklm} T_k(e_{j,1}) T_l(e_{j,2}) T_m(e_{j,3}) \quad (6.25)$$

where Chebychev functions  $T_k(x)$  and their rescaled (to make the functions orthogonal on the interval spanned by the dataset) arguments  $e_{jn}$  are defined by:

$$T_k(x) \equiv \cos(k \arccos(x)) \quad (6.26)$$

$$e_j \equiv -1 + 2 \frac{E_j - E_{j,\min}}{E_{j,\max} - E_{j,\min}} \quad (6.27)$$

Coefficients  $c_{iklm}$  are found by least squares fitting (see subsection A.1) relation 6.24 to a calibration data-set. Subscripts  $\min$  and  $\max$  refer to minimum and maximum values within the calibration data-set.

The summation in relation 6.25 is such that the total degree of the product polynomial (defined as the sum of the degrees of the factor-polynomials) does not exceed four.

### 6.5.5.1 Combination of subprobe results

Like in the former subsection, the four sub-probe results are combined into a full probe result. Tsinober et al do not give information on how they have accomplished this. One way to come to a combined estimate for the four-wire probe is to take the mean value of the four subprobe estimates. In this case, if one subprobe's estimate is instable (i.e. it has an unrealistic value), then the combined estimate is instable either. We give two suggestions for a stable method (insensitive to the divergence of one subprobe result) to combine four sub-probe results into a full probe result. These methods are:

- Any three subprobe results have in common that there is one particular wire of which they all have used the response. A curved plane is formed in the three dimensional velocity vector space by those velocity-vectors that all induce the same response on a single wire. Linearise the four planes of constant wire response through the four subprobe results. The orthogonal distance in velocity space to a plane of constant wire response is proportional to a difference in wire response. The intersection of the four planes defines a tetrahedron. Take the point at which the quadratic sum of distances to the four planes is minimal. This minimises the squared sum of suggested external measurement-errors (differences between samples and model) in the wire responses. When we take the random errors, which enter all four hot-wire readings during their estimation via d/a sampling, to be independent, then we can calculate the composed error in the set of four wire readings via Pythagoras' law. The subprobe combining method just described is the method which needs the least compound error to relate the four wire voltages to a velocity vector. Therefore we expect this method to give a good estimate for the velocity.
- The former method shows similarity with taking the centre of the largest sphere (in three dimensional velocity space) that can be fitted into the tetrahedron spun by the four subprobe estimates for the velocity vector. In this case the suggested external measurement-errors in the wire-responses are the same for all four wires (i.e. the differences between the measured hot-wire voltages  $E_i$  and the responses  $f_i(\mathbf{u})$  (via the calibration model  $f_{1..4}$ ) of the wires to the final estimate for the velocity vector  $\mathbf{u}$  has the same value for all four



wires). A 2D equivalent of this three dimensional problem of finding which velocity vector corresponds best with a set of non-collocated velocity vectors estimated by subprobes is shown in figure 6.4.

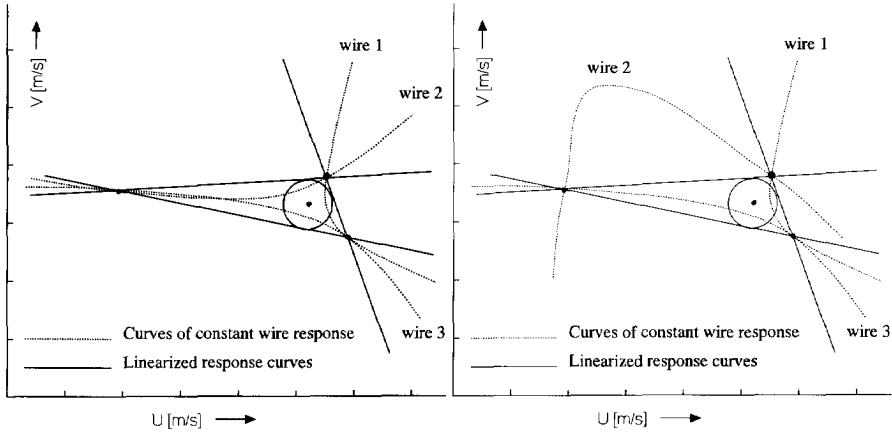


Figure 6.4: 2D-equivalent of subprobe combination method by a tetrahedron. Left a situation in which the method succeeds, right an unsuccessful situation.

Curvature of the calibration curves must be small on the scale of the set of four subprobe estimates. Otherwise, the planes of constant wire response may not be linearised. This means that the subprobe-results must not differ too much from one another. From the calibration model one can calculate the curvature and see if linearisation is allowed. In practice both combination methods converge even if one sub-probe result deviates very much from the other three. The indirect full 4-wire calibration method from section 6.5.4 takes the curvature in the response curves into account. As a consequence we expect the indirect full 4-wire method to give better velocity estimates than the direct subprobe model.

In section 6.6 the performance of the direct 4-wire subprobe model is studied and compared with the indirect King/Jørgensen model, the indirect Lemonis model and the full 4-wire model.

### 6.5.6 Direct method: 4-wire model

Let us define two functional spaces of velocity vectors, which are covered by the functions defined by:

$$u_i = f_i(E_1, E_2, E_3, E_4) = \sum_{k+l+m+n=0}^N c_{iklmn} T_k(e_1) T_l(e_2) T_m(e_3) T_n(e_4) \quad (6.28)$$

$$u_i = f_i(E_1, E_2, E_3, E_4) = \sum_{k=0}^N \sum_{l=0}^N \sum_{m=0}^N \sum_{n=0}^N c_{iklmn} T_k(e_1) T_l(e_2) T_m(e_3) T_n(e_4) \quad (6.29)$$

The difference between these two classes of functions is that functions in the first have a *total* degree of the product polynomial which is restricted, and that those in the second class have an

upper limit to the degree of the composing factor functions. In hot-wire literature both methods are used. To our opinion the latter model is less optimal than the former model: in the latter model many coefficients are needed for products of relatively high order contributions by all four factor polynomials. These product functions model a higher order effect in a higher order effect in a higher order effect. The first model does not include such unimportant terms.

Either of the two functional spaces contains the space span by the combinations of subprobe-functions given in relation 6.25 as a subspace. Therefore a model based on the functions of relation 6.28 is *à priori* better than the model based on functions given in relation 6.25. The system to find the velocity-vector is overdetermined: with four wire-responses we have to model three velocity components. Therefore weighted  $\chi^2$ -fitting can make sure that a hot-wire giving less stable response in a certain region will contribute less to the full probe result in this particular region. This can happen in velocity-regions where the orientation of one wire is much more parallel to the flow than the orientations of the other three wires.

Application of the full 4-wire direct model can enlarge the cone of acceptance within which velocity-vectors can be properly modelled, when compared to the cone of acceptance of any of the four three-wire subprobes: these subprobes have different cones of acceptance, and these cones are merged when all four wires are used in the full 4-wire model.

## 6.6 Test of calibration methods

Several models have been presented in the former sections for hot-wire response and calibration. In this section we will test and compare these velocity estimating methods. The models that we will test are: the King/Jørgensen model, the Lemonis model, the direct subprobe model and the full 4-wire model.

### 6.6.1 Test of laws of King and Jørgensen

To see the applicability of the hot-wire response models of King and Jørgensen both simulations and measurements have been performed. These mathematical and experimental tests will be described in detail in this subsection.

In the simulations we determine the sensitivity of the model for small changes in model parameters and temperatures. To estimate these sensitivities we first model the response of a probe with realistic characteristic parameters. These responses are then analysed by the same model, which in sequence is instructed to disregard certain characteristics, by assuming ideal values for these characteristics.

In the measurements we analyse data from a 4-wire calibration in which the response of the probe has been recorded in a full 3D orientation/velocity scan. The validity of the effective cooling velocity concept is checked.

To test the King/Jørgensen model we have written three computer routines. The operational principles of the second routine are outlined in appendix G. In our programs, polar angles ( $\theta, \phi$ )

represent a wire's orientation (see figure 6.5 for the definition of  $\theta$  and figures 6.6 and 6.7 for the definition of  $\phi$ ). Polar angle  $\theta$  is the angle between the hotwire and the  $x_3$ -axis and  $\phi$  gives the rotation angle of the wire around this  $x_3$ -axis measured from the  $x_1$ -axis.

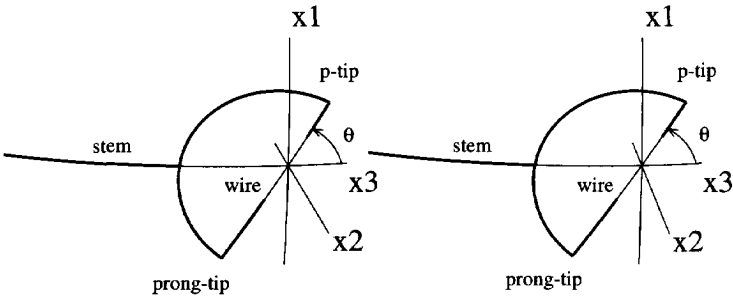


Figure 6.5: Definition of angle  $\theta$  between a wire and the  $x_3$ -axis

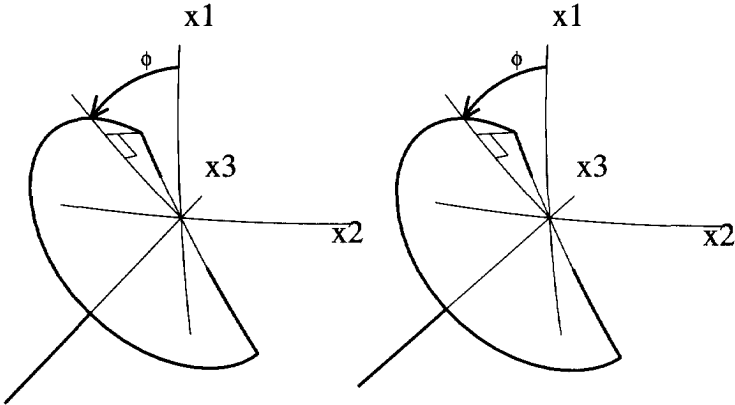


Figure 6.6: Definition of angle  $\phi$ . The probe is seen from an angle from behind.

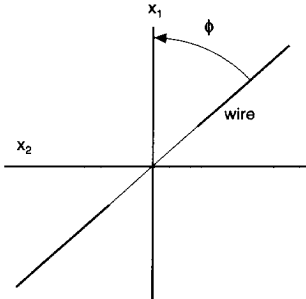


Figure 6.7: Definition of angle  $\phi$ . Frontal view of the probe.

The programs can perform the following tasks:

- Simulate the response of a 4-wire probe to air-flow with a given velocity-vector and given temperature. The responses of these wires are modelled conform relations 6.9 and 6.12. Constants  $(A, B, n, k, h, \theta, \phi, T_{\text{hot}})$  can be specified for each wire individually. In this list constants  $(A, B, n)$  refer to King's law 6.9 and  $(k, h)$  to Jørgensen's law 6.12.  $T_{\text{hot}}$  is the operation temperature of the wire. The stem of the probe is supposed to be along  $\theta = 0$ , which is the  $x_3$ -axis.
- Extract coefficients  $(A, B, n, k, h, \theta, \phi)$  from two calibration datasets: The first calibration gives the response of the probe to flow with a constant direction, but with different velocities. The second calibration is done at constant velocity, but with varying orientations of the flow.  $T_{\text{hot}}$  is assumed to be known. See appendix G for details of these two steps.
- Estimate the wind vector from a given set of four wire responses according to the method outlined in section 6.5.1.2. This is mainly a non-linear rootfinding routine, taken from a numerical library, which uses the parameters provided by the former routine (or a user-specified set of parameters) in the laws of King and of Jørgensen.

#### 6.6.1.1 Mathematical tests

In this test we study the sensitivity of the King-Jørgensen model for small errors in model parameters (mis-estimates of the wire orientations, wrong values of  $k$  and  $h$ , wrong hot-wire temperatures). To find these sensitivities we simulate a four wire probe, with realistic characteristics, and generate simulated calibration data. We also generate two different measurement files with the response of the probe to isotropic turbulence. These two datasets are constructed to see the influence of the direction of the mean flow. We simulate one measurement of frontal flow (from here called *dataset A*), and one measurement with a mean velocity, which is more at the edge of the calibration dataset (from here called *dataset B*). The interpretation of the calibration data depends on the assumptions, which one is prepared to make with respect to the laws of King and of Jørgensen, and to the effect of ambient temperature drift on the responses of the wires. By varying the interpretation of the calibration data, we generate different methods to interpret the two simulated measurements of isotropic turbulence. To assess the consequences of the different assumptions in the interpretation of the calibration data, we measure the quality of the interpreted measurements with the rescaled normalised anisotropy invariants of the Reynoldsstress tensor (see appendix C for their definition). These invariants are good measures of the quality of an interpretation method, because the final use of hotwire probes in this research will be to estimate the anisotropy of turbulent flow.

All tests are described in detail in the list of tests presented below. General specifications, valid for all tests, are the following:

- In the (simulated) calibrations the velocity ranges from 2 m/s to 10 m/s (step 1 m/s) at pitch- and yaw-angles ranging from -30 degrees to 30 degrees (step 7.5 degrees). The frontal direction of the probe is taken along the  $x_3$ -axis. Pitch- and yaw-angles are related

to velocity vector  $\mathbf{u}$  via the following set of equations ( $u$  is the length of  $\mathbf{u}$ ):

$$\begin{aligned} u_1 &= u \cos(\text{pitch} + \pi/2) \\ u_2 &= u \sin(\text{pitch} + \pi/2) \sin(\text{yaw}) \\ u_3 &= u \sin(\text{pitch} + \pi/2) \cos(\text{yaw}) \end{aligned} \quad (6.30)$$

- We use Jørgensen's typical values (Jørgensen, 1971) for tangential and binormal cooling:  $h = 1.08$  and  $k = 0.2$ . In King's law we use  $n = 0.5$  from King (1914). Coefficients  $A$  and  $B$  are chosen such that the output signal ranges from 2 Volt to 4 Volt in the velocity range from 0 m/s to 10 m/s:  $A = 4$  and  $B = 5$ . These values are characteristic for the anemometers that are used in this study.
- Furthermore, unless otherwise stated, we use  $\theta = 45^\circ$  and  $\phi_{1..4} = (0^\circ, 90^\circ, 180^\circ, 270^\circ)$ .
- A (simulated) probe, with characteristics conform the values given in this list, is used to simulate the response to isotropic "turbulence". Test data includes 5000 samples consisting of a mean flow plus 3D isotropic Gaussian noise with an RMS vector length of 5 % of the mean velocity.
- In dataset A the mean flow is 6 m/s and directed along zero pitch and yaw ( $u' \sim 30$  cm/s). In the second dataset (dataset B) the mean velocity vector is  $\mathbf{u}_{\text{mean}} = (1, 2, 5)$  m/s (which makes an angle of  $24^\circ$  with the  $x_3$ -axis). Rescaled third and fourth anisotropy invariants of the Reynoldsstress tensors of both test datasets are found to be  $III^* = -0.0145$  and  $IV^* = 0.0000$ . These are the characteristics of the turbulence *before* the simulated response was calculated.

To simulate mis-estimates in model parameters, we deliberately changed some of the calibration constants. The magnitudes of these modifications mimic realistic systematic errors. We used the tampered calibrations to interpret the "turbulent signals" of datasets A and B.

The tests are listed in the following table. The corresponding rescaled third and fourth invariants of the normalised anisotropy tensor (see section C) are shown in figure 6.8. The RMS value of the difference between true velocities and estimated velocities is called  $\delta u$ . Rescaled anisotropy invariants are listed in table 6.1.

**1. No tampering:** The true calibration constants are used to interpret the test dataset.

As a first test of the King/Jørgensen model we use the model to interpret the simulated calibration data. We find a difference of 9.55 cm/s, which is nearly two percent when compared with the calibration's mean velocity.

Results of the interpretation of datasets A and B are given in table 6.1.

**2. Neglecting  $k$  and  $h$ :** In this test we assume that the cosine law (relation 6.11) correctly models the effective cooling velocity. We know that this model can be refined to the Jørgensen model (used to generate the response of the probe), where coefficients  $h$  and  $k$  are used to model blockage of the flow by the probe's stem, and distortion of the flow by the prongs. Here we will see if these refinements are necessary.

3. **Wrong angles of wires:** We record the response of a probe which has wire orientations  $\theta_{1..4} = (47^\circ, 43^\circ, 43^\circ, 44^\circ)$  and  $\phi_{1..4} = (358^\circ, 91^\circ, 177^\circ, 277^\circ)$ . We analyse these samples as if they had been recorded with a probe which has orientations  $\theta_{1..4} = 45^\circ$  and  $\phi_{1..4} = (0^\circ, 90^\circ, 180^\circ, 270^\circ)$ . In this way we simulate what will happen if we assume in our analysis that we successfully constructed a probe according to specifications, whereas in reality we have a probe with wire orientations slightly different from the ideal values.
4. **Wrong wire temperatures:** Calibration constants are based on reference temperature  $T_{\text{ref}} = 20^\circ\text{C}$ . The four wires have temperatures  $T_{\text{hot}} = (205^\circ\text{C}, 190^\circ\text{C}, 220^\circ\text{C}, 180^\circ\text{C})$ . The response of the probe to velocities of datasets A and B is taken at ambient temperature  $T = 25^\circ\text{C}$ . In the analysis of these data we assume that  $T_{\text{hot}} = 200^\circ\text{C}$  for all four wires. This type of error can in practice result from estimating  $T_{\text{hot}}$  from the overheat ratio of the anemometer bridge and a theoretical temperature coefficient of resistance. Relation 6.14 is used to correct for temperature drift.
5. **Neglecting temperature drift** Calibration constants are based on reference temperature  $T_{\text{ref}} = 20^\circ\text{C}$ . The four wires have temperatures  $T_{\text{hot}} = 200^\circ\text{C}$ . The response of the probe to velocities of datasets A and B is taken at ambient temperature  $T = 25^\circ\text{C}$ . In the analysis of these data we assume that  $T = T_{\text{ref}} = 20^\circ\text{C}$ , in other words: we assume that temperature drift is not important. This assumption is often made by researchers. In this test we will see the implications if the assumption in a situation where temperature *does* drift.

Test	Dataset	$\delta u$ [cm/s]	$III^*$	$IV^*$
1	A	$3.3 \cdot 10^{-2}$	$-1.44 \cdot 10^{-2}$	0.000
1	B	$2.1 \cdot 10^{-1}$	$-1.06 \cdot 10^{-1}$	0.002
2	A	12.1	$1.01 \cdot 10^{-1}$	0.000
2	B	36.2	$-3.05 \cdot 10^{-1}$	0.071
3	A	22.5	$1.52 \cdot 10^{-1}$	0.029
3	B	55.2	$7.81 \cdot 10^{-1}$	0.007
4	A	2.65	$2.40 \cdot 10^{-2}$	0.006
4	B	4.20	$-4.50 \cdot 10^{-2}$	0.003
5	A	48.8	$-1.43 \cdot 10^{-2}$	0.000
5	B	45.1	$-2.80 \cdot 10^{-2}$	0.001

Table 6.1: Results of the mathematical tests of the King/Jørgensen model.

Based on these tests we can make the following remarks:

- It is remarkable that when correct calibration constants are used to analyse flow of which the mean is not aligned with the probe (test 1<sup>b</sup>), then the estimated invariants are incorrect, though the RMS deviation of the velocity is small. Incorrect invariants can be caused by a distorted calibration function, but a distorted calibration function is likely to induce mean velocity errors as well.
- From the tests 4 and 5 we see that the estimated anisotropy character of a turbulent flow, which is analysed with the King/Jørgensen model, is not significantly sensitive to the

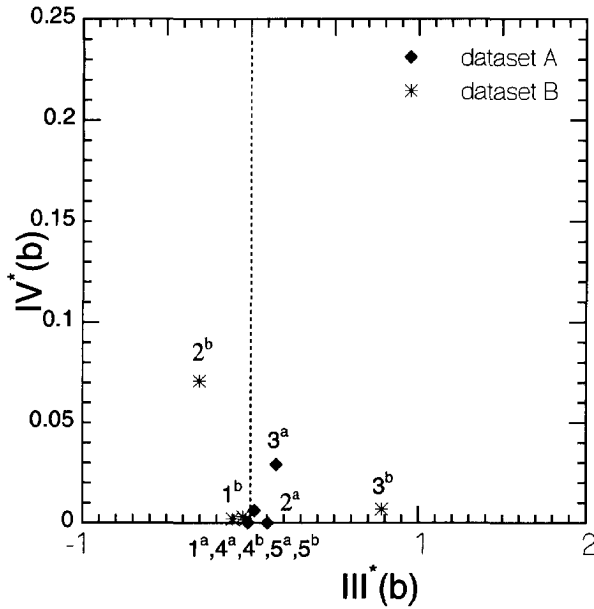


Figure 6.8: Anisotropy estimates for isotropic flow found with slightly modified calibration constants in the King/Jørgensen model.

correctness of the method which is used to compensate ambient temperature drift: the invariants have a small value, even though temperature was corrected for in a wrong manner.

- In the tests concerning wire angle variations and tangential- and binormal sensitivities (tests 2 and 3), true and estimated anisotropy characters differ significantly. Deviations are significant but small when the probe is aligned with the mean flow. When the probe is not aligned with the mean flow, then the estimated anisotropy character has no relation with the true character.

The above conclusions can be important for the assessment of the value of other studies: Michard *et al.* (1987) have measured the decay of grid-generated turbulence in a wind-tunnel. Turbulence was made anisotropic with propellers. One expects the nonlinear terms in the equations of motion to level out the anisotropy with time. Nevertheless it appears that the flow persists in its being anisotropic. The character of anisotropy is found to transform from cigar-like to pancake-like. Michard *et al.* did not mention which measurement technique they have used to measure their velocities. In case they have used hot-wire probes, it would be interesting to know which tests they have done to guarantee that they correctly determined the character of the flow. As we have seen in this subsection, artificial anisotropy is easily introduced in the estimates.

### 6.6.1.2 Physical test

After we had performed the mathematical sensitivity-tests presented in the former subsection, we have tested the applicability of the data-reduction program to real measurements as follows:

- We performed a full 3D calibration of a 4-wire probe in the velocity range 2 m/s to 10 m/s (step 1 m/s) at pitch- and yawangles ranging from -30 degrees to 30 degrees (step 7.5 degrees).
- Coefficients in King's law were found using only the samples taken at zero pitch- and yaw-angles.
- Coefficients in Jørgensen's law were found using those samples taken at an absolute velocity of 6m/s of which the velocity vector does not deviate more than 30 degrees from zero pitch- and yaw-angles (i.e.  $\theta \leq 30^\circ$ ).
- In one plot we compare King's law (with coefficients found in the second step of this list) with the effective cooling velocities associated with the calibration samples used in the third step. The result is presented in figure 6.9.
- The former step is repeated for *all* calibration samples with an effective cooling velocity less than 10 m/s. Results are given in figure 6.10.

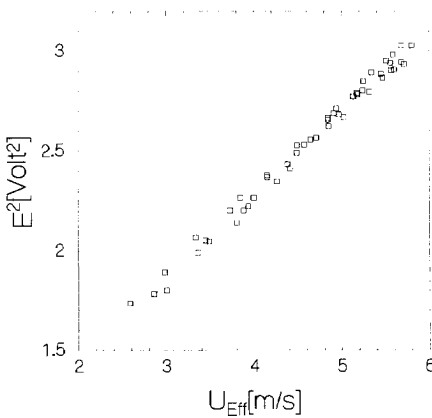


Figure 6.9: Test of the effective cooling velocity concept. The curve represent King's law. Only calibration samples taken at 6 m/s within a 30 degree cone are shown.

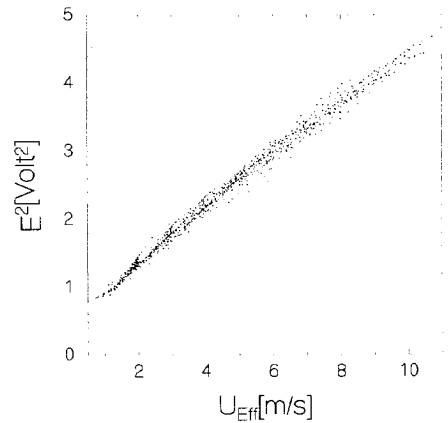


Figure 6.10: All calibration samples are shown.

Figure 6.9 suggests that application of the laws of King and Jørgensen is not such a bad idea after all. All points are within reasonable distance from the curve marking King's law, and there is no systematic scatter. If we would interchange the axes and rescale the anemometer



output, then figure 6.9 is comparable with the results presented in a recent study by Gieseke and Guezennec (1993, figure 5), who conclude from the figure that validity of this approach to model a wire's response for practical use is confirmed.

When we plot all calibration samples (figure 6.10) we see that scatter in points is dramatically increased when compared with figure 6.9 (from 0.2 m/s to 0.5 m/s deviation in the effective cooling velocity). Moreover, we see bands associated with samples taken at constant absolute velocity. This systematic behaviour gives rise to unacceptably large errors in the model. Many points show a deviation larger than 0.5 m/s. The angular sensitivity appears to be velocity dependent: if a constant angular sensitivity would have been applicable, then the data in figure 6.10 would have collapsed on a single curve, whereas in reality there are systematic deviations, corresponding with angular calibrations at different velocities. The conclusion of Gieseke and Guezennec that one can calibrate a multi-wireprobe with a linear velocity-calibration and a 2D angular calibration is not justified.

From this test we conclude that the effective velocity concept does not lead to a quantitatively accurate interpretation of hotwire measurements. Nevertheless we can use this method to find qualitative characteristics of a probe:

- From wire orientation angles  $\theta$  and  $\phi$  (estimated with the procedure presented in appendix G) we can see to which accuracy the manufacturer has managed in placing the wires according to specifications. Knowledge about the wires' orientations can also be used to closely examine samples for which the interpretation routine does not converge: one can see if flow is too parallel to a wire to give useful response. The response of such a wire can then be discarded.
- From constant  $h$  we can see if the stem of the probe causes serious flow blockage: the more  $h$  is larger than 1, the stronger the blockage.
- From constant  $k$  we can see to which extent the prongs interfere with the flow around the wire: the larger  $k$ , the stronger the prong interference. Stem- and prong-interference lead to bad measurement. Knowledge of  $h$  and  $k$  can help to assess the correctness of the assumption that the probe does not influence the measurements.

## 6.6.2 Test of other indirect- and direct calibration methods

In this subsection we assess the applicability of Lemonis' indirect calibration method, the indirect full four wire method, the direct combined subprobe model and the full four wire model.

First we will use these models to calculate calibration constants for the mathematical calibration data composed in the first mathematical test of the King/Jørgensen model in section 6.6.1.1. Then we will use these models with their respective constants to interpret the signals of datasets A and B from section 6.6.1.1. RMS deviations between model and estimated velocities are computed and rescaled third and fourth anisotropy invariants of the estimated Reynolds stresses are given in character plots. This is the same presentation as used in the former subsection.

After the mathematical tests are done, we apply the calibration methods that are studied in this section to analyse a real calibration dataset.

### 6.6.2.1 Mathematical test of indirect methods

To test Lemonis' indirect method we used fourth order polynomials. To initiate the set of equations in the indirect method we used (0,0,6) m/s as starting value. Lemonis' method (described in section 6.5.3) is applied to all four three-wire subprobes in the four-wire probe individually (tests I1/I4). To combine subprobe estimates into a final velocity estimate the least squares method of section 6.5.5.1 is used (test I5). The indirect full 4-wire model (see section 6.5.4) is studied in test I6. In tests I1/I6 *all* calibration samples are used. To see the effect of restriction of the calibration to samples that can be found within a certain cone, we have redone the tests with those calibration samples where polar angle  $\theta$  is not larger than  $32^\circ$  (tests I7/I12). The RMS-deviations of the interpreted and original samples in datasets A and B are shown in table 6.2.

Test	probe	calibration range	RMS-error(A)	RMS-error(B)
I1	subprobe 1	all samples	0.15 [cm/s]	1.8 [cm/s]
I2	subprobe 2	all samples	0.15 [cm/s]	11.7 [cm/s]
I3	subprobe 3	all samples	0.15 [cm/s]	1.1 [cm/s]
I4	subprobe 4	all samples	0.15 [cm/s]	2.0 [cm/s]
I5	combination of subprobes	all samples	0.15 [cm/s]	1.0 [cm/s]
I6	full 4-wire model	all samples	0.06 [cm/s]	0.65 [cm/s]
I7	subprobe 1	$32^\circ$ -cone	0.15 [cm/s]	1.6 [cm/s]
I8	subprobe 2	$32^\circ$ -cone	0.15 [cm/s]	11.1 [cm/s]
I9	subprobe 3	$32^\circ$ -cone	0.15 [cm/s]	0.2 [cm/s]
I10	subprobe 4	$32^\circ$ -cone	0.15 [cm/s]	1.9 [cm/s]
I11	combination of subprobes	$32^\circ$ -cone	0.15 [cm/s]	0.5 [cm/s]
I12	full 4-wire model	$32^\circ$ -cone	0.02 [cm/s]	0.19 [cm/s]

Table 6.2: Velocity mis-estimates by different indirect models

The anisotropy characters estimated by these tests are shown in figure 6.11. We see from this figure that individual subprobes can mis-estimate the anisotropy invariants of dataset B (which has true rescaled invariants  $III^* = -0.0145$  and  $IV^* = 0.0000$ ) by differences of 0.1 to 0.3. The combined subprobe model (based on the full calibration set) yields reasonable estimates. The indirect full four wire model, of which the calibration functions are calculated using the samples within a cone, gives the best results:  $III^* = -0.0164$  and  $IV^* = 0.0000$  for dataset A, and  $III^* = -0.0189$  and  $IV^* = 0.0005$  for dataset B. The deviations of these estimated invariants from the "true" values are of order 0.005. This is even smaller than the inaccuracies with which we managed to give test datasets A and B an isotropic character. We studied the influence of using the (known) true velocities as starting points on the results of the tests of the indirect calibration method (RMS deviation and invariants). All ten tests were redone with this less honest inversion method. The differences with the former method were found to be negligible for datasets A and B.

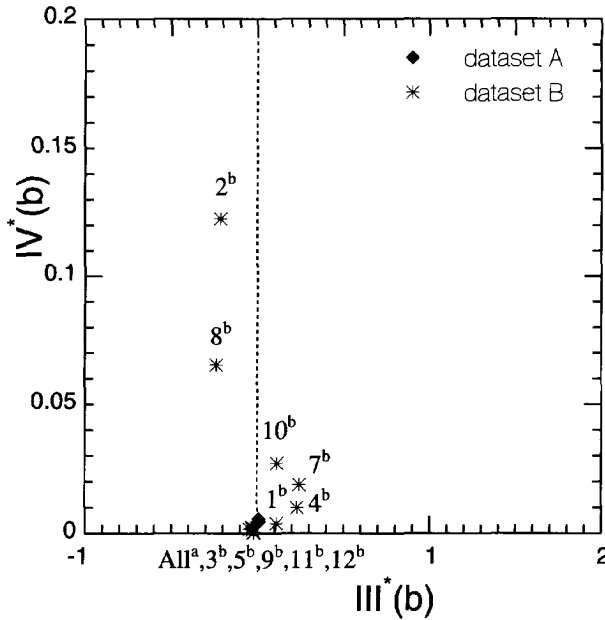


Figure 6.11: Character plot for test data processed with indirect calibration model.

### 6.6.2.2 Mathematical test of direct methods

In way similar to the tests of the indirect calibration methods described in the above paragraph, we tested the direct (single and combined) sub-probe model (see sections 6.5.5 and 6.5.5.1), using relation 6.28 with order  $N = 5$ . In tests D1/D4 we studied individual three-wire subprobes. In test D5 the combined subprobe model is studied. Tests D6/D10 are concerned with the same tests as in D1/D5, but with restrictions of the calibration data to a cone  $\theta \leq 32^\circ$ . Tests are listed in table 6.3:

Estimated anisotropy invariants of tests D1 to D5 (using calibration constants based on the full calibration set) are presented in figure 6.12. Results of tests D6 to D10 (calibration coefficients found using only the calibration samples within a  $32^\circ$ -cone around the probe-axis) are shown in figure 6.13.

Based on the tests just presented, we can draw the following conclusions:

- From figures 6.12 and 6.13 we see that no individual subprobe estimates the invariants of either dataset within an accuracy of 0.1. It may even happen (subprobes 2 and 3) that the estimated invariants have no resemblance to the true invariants.
- Limitation of the calibration samples to a  $32^\circ$ -cone improves the estimation of anisotropy invariants. Even then the combined subprobe model leads to errors in the invariants of more than 0.1, which is about ten percent full scale.

Test	probe	calibration range	RMS-error(A)	RMS-error(B)
D1	subprobe 1	all samples	8.3 [cm/s]	8.8 [cm/s]
D2	subprobe 2	all samples	7.4 [cm/s]	32.8 [cm/s]
D3	subprobe 3	all samples	8.1 [cm/s]	31.0 [cm/s]
D4	subprobe 4	all samples	7.5 [cm/s]	10.5 [cm/s]
D5	combination of subprobes	all samples	4.0 [cm/s]	14.4 [cm/s]
D6	subprobe 1	32°-cone	2.9 [cm/s]	8.5 [cm/s]
D7	subprobe 2	32°-cone	3.4 [cm/s]	14.2 [cm/s]
D8	subprobe 3	32°-cone	2.9 [cm/s]	8.1 [cm/s]
D9	subprobe 4	32°-cone	3.3 [cm/s]	7.4 [cm/s]
D10	combination of subprobes	32°-cone	0.5 [cm/s]	4.6 [cm/s]

Table 6.3: Velocity mis-estimates by different direct models

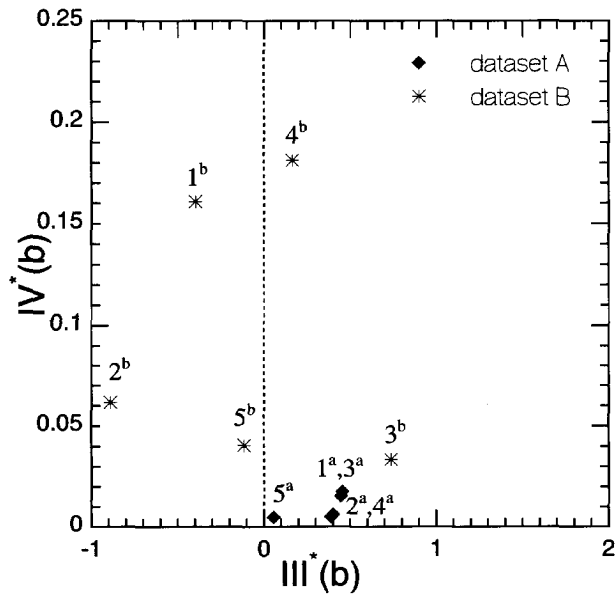


Figure 6.12: Character plot for test data processed with direct calibration model based on all calibration samples, (combination of) 3-wire subprobes.

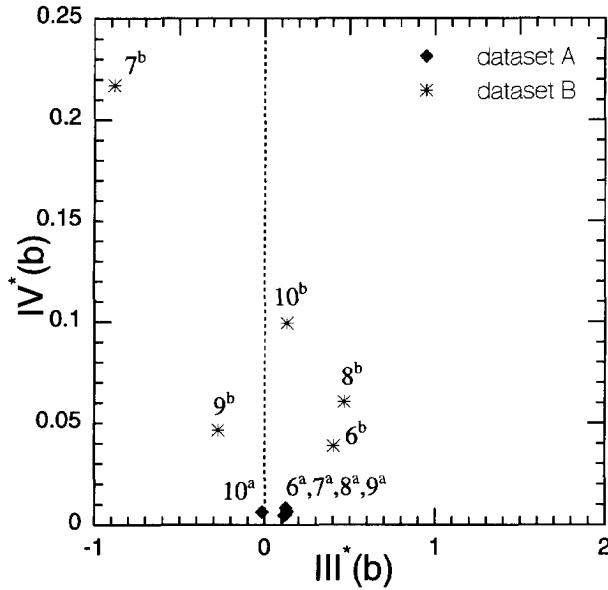


Figure 6.13: Character plot for test data processed with direct calibration model based on calibration samples within 30 degree cone, (combination of) 3-wire subprobes.

- The conclusions made by Tsinober et al. (1992), who use the direct subprobe model to analyse measurements of turbulence structures, possibly suffer from this artificial anisotropy, which may be introduced into the estimated velocities by their calibration model. Close examination of their calibration data can help minimise this source of error.

The direct full four-wire model is studied in tests D11/D15. The effects of cone-limiting and of using different model orders ( $N$  in relations 6.28 and 6.29) are examined. We also have a look at the difference between application of relations 6.28 and of relation 6.29. The tests of the full four-wire model are listed in table 6.4. Anisotropy invariants have been plotted in

Test	model relation	model order	calibration range	RMS-error(A)	RMS-error(B)
D11	(6.28)	N=5	all samples	4.6 [cm/s]	5.9 [cm/s]
D12	(6.28)	N=5	32°-cone	0.4 [cm/s]	2.4 [cm/s]
D13	(6.28)	N=7	32°-cone	0.2 [cm/s]	2.0 [cm/s]
D14	(6.29)	N=3	all samples	3.0 [cm/s]	7.5 [cm/s]
D15	(6.29)	N=3	32°-cone	0.3 [cm/s]	3.2 [cm/s]

Table 6.4: Velocity mis-estimates by the direct full 4-wire method

figure 6.14. We see that full 4-wire models, based on calibration samples within a 32°-cone, correctly estimate the isotropic character of dataset A, which contains 'turbulent flow' around the mean calibration velocity vector. Dataset B contains simulated turbulence around a mean vector closer to the edges of the calibration domain than the samples in dataset A. Even the

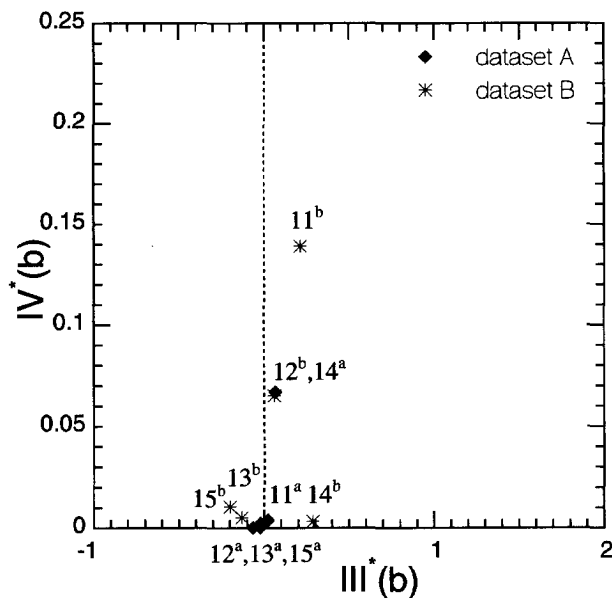


Figure 6.14: Character plot for test data processed with direct full 4-wire calibration model.

best estimates for anisotropy invariants of dataset B have differences with the true invariants of magnitude 0.1.

The indirect model used in indirect test I12 gives better estimates for the anisotropy invariants than the full 4-wire model used in direct test D12. The RMS residual of the calibration data modelled with the former model is 1.27 cm/s, the latter model gave 0.179 cm/s. Though the direct model leads to a smaller RMS residual in the calibration data, the indirect model gives better estimates for the Reynolds stress anisotropy. One possible explanation for this difference can be the following: the domain of the indirect calibration functions is homogeneously covered with calibration samples. This constant density of calibration samples in the domain will lead to calibration functions which will not favour certain velocity ranges in modelling accuracy to other velocity ranges. The domain of the direct method, i.e. the three- or four-dimensional space of values within which the probe responses can be found, is inhomogeneously covered with calibration samples. This is the immediate consequence of the non-linearity of the calibration functions: the image of a linearly distributed set (in this case the velocities) gives a non-linearly distributed set (the responses of the probe). As a consequence it can happen that the calibration function will be very accurate around the mean calibration velocity vector, and poorer for velocities with a larger deviation from this mean. This will give a distorted mapping to the velocity space. To see if this plays a significant role in the current analysis, we plot the residuals of the indirect calibration model of test I12 and of the direct calibration model of direct test D12 as function of the deviation  $U_d$  of the calibration velocity from the mean calibration velocity. These residuals are shown in figure 6.15. It appears that in average sense the residuals of the direct model are smaller than the residuals of the indirect model, irrespective of  $U_d$ . This falsifies our conjecture that the non-linear distribution of the responses, via distorted mapping

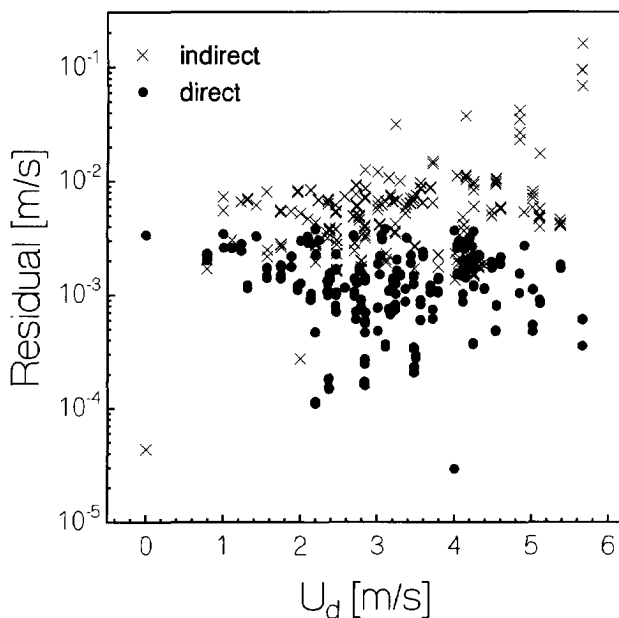


Figure 6.15: Residuals of calibration models as function of the deviation of the calibration velocity vector from the mean calibration velocity vector.

to the velocity space, induces the artificial anisotropy.

A different explanation may be the following: it can be that the direct calibration function has wiggles between the calibration samples, and therefore incorrectly models velocity in the calibration range. In such a case the calibration samples themselves do not suffer from the wiggles.

### 6.6.2.3 Physical tests

To see to which extent the mathematical tests in sections 6.6.2.1 and 6.6.2.2 represent reality, we apply the calibration methods from those sections to a calibration dataset, which is found in a measurement. In this calibration we measured the response of a four-wire probe to flow with pitch and yaw angles ranging from  $-30^\circ$  to  $30^\circ$  with steps of  $7.5^\circ$ , and with velocities ranging from 2 m/s to 16 m/s with steps of 2 m/s.

The indirect calibration functions (order 4) represented the hotwire response with an accuracy of (RMS external error) 0.002 Volt. For different wires  $\chi^2$  took values 2.2 to 3.6. These large values for chisquare possibly are to be attributed to a too small estimation for the internal errors, resulting from a too fast sampling (samples were not independent). If this explanation is correct, then the estimates for the internal errors must be doubled to make model and experimental data correspond to one another.

The indirect methods yielded the following RMS velocity deviations between calibration data

and estimates: Individual three wire subprobes gave RMS errors up to more than 1 m/s. The combined subprobe model gave 37 cm/s. The full 4-wire model gave 4.8 cm/s.

The direct combined subprobe model (order 4, restriction to a  $32^\circ$ -cone) led to velocity modelling with accuracy 14 cm/s. The accuracy was about 50 cm/s for a single 3-wire subprobe. The direct full four wire model (order 4), restricted to a  $32^\circ$ -cone, represented the calibration velocities with an RMS deviation of 3.7 cm/s.

## Conclusion

From our study of hot-wire anemometry we draw the following conclusions:

- Cooling laws for hotwires (laws of King and Jørgensen) only provide *qualitative* information about a probe: in particular manufacturing accuracy and relative importance of flow distortion by prong and stem. These laws give a too idealised representation of hotwires for quantitative calibration.
- Temperature correction of hot-wire data is best done with a factor, which is the squareroot of the ratio of temperature differences. The method which uses a similar factor, based on the squareroot of the ratio of resistance differences is shown to be equally accurate, but less practical in use. The operational temperature of the wire, which plays a vital role in the correction factor, should be determined by optimisation of this parameter such that samples taken at different temperatures and various velocities collapse on a single curve.
- When one uses direct calibration methods, then one should only use those samples which are found within a certain cone of acceptance.
- Hotwire should be calibrated *in situ*. Differences in resistance between calibration setup and measurement setup can spoil the value of the calibration.
- In practice three wire probes are incapable of giving accurate estimates for either the velocity vector, or for the anisotropy of the Reynoldsstress. A fourth wire is to be used, and the method of data reduction should use the redundant information of the fourth wire in an integrated way, not via subprobes. The curvature of the response functions plays an essential role (see figure 6.4) in the estimation process: In the analysis of a measured calibration dataset, the indirect combined subprobe model gives velocity estimates which have RMS inaccuracies which are an order of magnitude larger than the error in estimates made by the indirect full four wire method.
- The indirect polynomial method, combined with the least squares method to combine subprobe estimates, adequately models the velocity/hotwire response relation. The indirect full four wire method gives the best data reduction method for four wire probe signals (when compared with the other indirect and direct methods given in this chapter).
- In a test on simulated isotropic turbulent flow, the indirect full four wire model gives rescaled Reynoldsstress anisotropy invariants which do not deviate from isotropy more



than 0.005 (on a full scale of  $III^* \in [-1, 2]$  or  $IV^* \in [0, 1]$ ). These deviations are smaller than the accuracy of the test. Therefore, we will use this reconstruction method to analyse our measured data later in this study.

- We have performed a mathematical test on isotropic turbulence. The direct full 4-wire method gave good estimates for the Reynoldsstress anisotropy only when the mean flow was close to the mean calibration velocity vector (the model estimated  $III^*$  and  $IV^*$  with an accuracy of 0.01, which is good). Turbulence around a mean velocity vector which makes an angle of  $24^\circ$  with the mean calibration velocity vector was incorrectly modelled with a direct full 4-wire model: the estimated  $III^*$  and  $IV^*$  deviated from their true isotropic values by no less than 0.1. This inaccuracy is unacceptable in our case, where we will use a 4-wire probe to see and analyse first order deviations from anisotropy. Though the velocity residuals of the direct full 4-wire calibration method are smaller than the velocity residuals of the indirect full 4-wire method, the indirect method is to be preferred above the direct method.



# Chapter 7

## Experiments on turbulent stagnation-point flow

### Introduction

In this chapter we will use the experimental equipment, which we described in chapters 5 and 6, to collect time series of real life turbulent flows. We will use these time series to test the unaliasing relations for one-point spectra, which we developed in chapter 2, via the practical estimation methods developed in chapter 3. The type of turbulence on which we will focus our attention is grid-generated turbulence. This flow type was chosen as our reference flow in section 1.3, and we have already used it (unfortunately not with too much of success) in the DNS in chapter 4. As explained in section 1.6, we will place a long flat plate normal to the mean flow (see section 5.7.4 and figure 5.39) and follow the turbulence on the stagnation line as it approaches the plate. This is done to create a non-axisymmetric anisotropic turbulence that requires an essentially anisotropic unaliasing method.

We will commence by estimating the mean flow upstream of the terminator (section 7.1). This mean flow will give us insight into the amount of strain that is offered to the turbulence. Next we will present the results of one-point measurements of grid-generated turbulence in our wind-tunnel. This is done in section 7.2. The one-point spectrum will be estimated and discussed in section 7.3. A comparison will be made with the theoretical RDT-models which were reviewed in section 1.6. The relative importance of the terms contributing to the wavenumber spectrum is studied in section 7.4. In this section we will also present our estimates for the wavenumber spectrum. The main results of this chapter will be summarised in section 7.5.

### 7.1 Mean flow upstream of the terminator

Before we will study the influence of the terminator on turbulence properties, we will first check its effect on the mean flow. The terminator, (described in section 5.7.4), with width  $D = 16$  cm, is placed at a distance of 154 cm (about  $10D$  or  $38.5M$ ) downstream of a turbulence generating grid (see section 5.5). The mean flow is measured with a Pitot-tube in the horizontal centre-

plane (parallel to the flow, normal to the plate and dividing the plate in two equal parts). This is done for four geometries, with and without the terminator in position and also with and without the turbulence generating grid positioned. The ratio of the laminar mean velocity when the terminator is positioned to the laminar velocity without terminator is shown in figure 7.3. The equivalent of this figure for turbulent grid flow is given in figure 7.4. Figures 7.3 and 7.4 only differ in smoothness, but apart from this they are identical. This is to be expected: the fluctuations in the turbulent case lead to scatter in the samples. We conclude that the introduction of turbulence does not seem to influence the mean flow around the terminator.

To see if the general character of the mean flow around the terminator agrees with simple theoretical models, we calculate the potential flow solution of two-dimensional flow ( $u, v$ ) around an infinitesimally thin flat plate with width  $D$ , placed in the origin and aligned with the  $x$ -direction. The upstream flow is aligned with the  $y$ -axis (one has to keep in mind that this orientation of the frame of reference in the construction of a potential flow solution differs by  $90^\circ$  from the frame of reference in our experiment). By mounting the plate with skirts we have forced the presence of a wake behind the plate and shifted the associated Kutta-condition from close to the plate to relatively far downstream. To see the influence of the wake on the mean flow upstream of the plate we consider two solutions, one without a wake behind the plate, and one including an infinite wake.

The (complex) solution for potential flow without a wake ( figure 7.1) is (see Milne-Thomson (1938, page 172)):

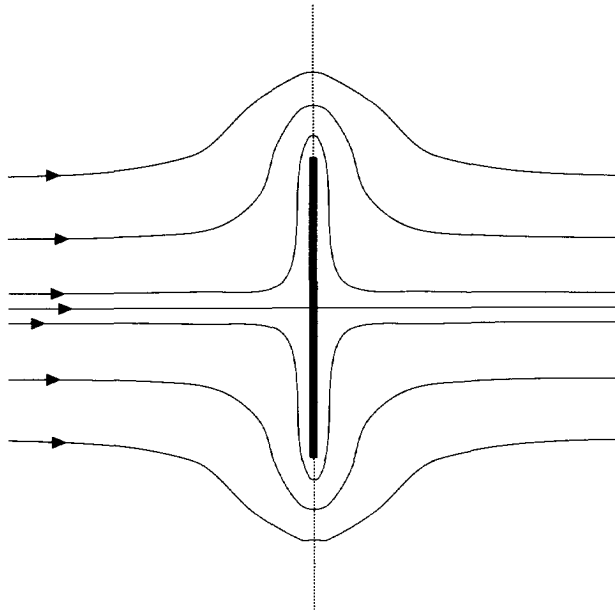


Figure 7.1: Potential flow around a plate without wake

$$u - iv = -\frac{dw}{dz} \quad (7.1)$$

$$w = \phi + i\psi = -\frac{iU}{4} \sqrt{4z^2 - D^2} \quad (7.2)$$

$$z \equiv x + iy \quad (7.3)$$

where  $U$  is the upstream velocity, which is along the  $y$ -axis, and where  $\phi$  and  $\psi$  are respectively the potential and the streamfunction. The far field approximation of this solution gives dipole behaviour, which is characterised by a decrease with distance of the plate's influence on the velocity field proportional with  $r^{-2}$ .

The potential flow solution for flow around a flat plate with an infinite wake behind the plate (see figure 7.2) is (the so called "Helmholtz free streamline solution") is taken from Batchelor (1967, p.497) and it reads:

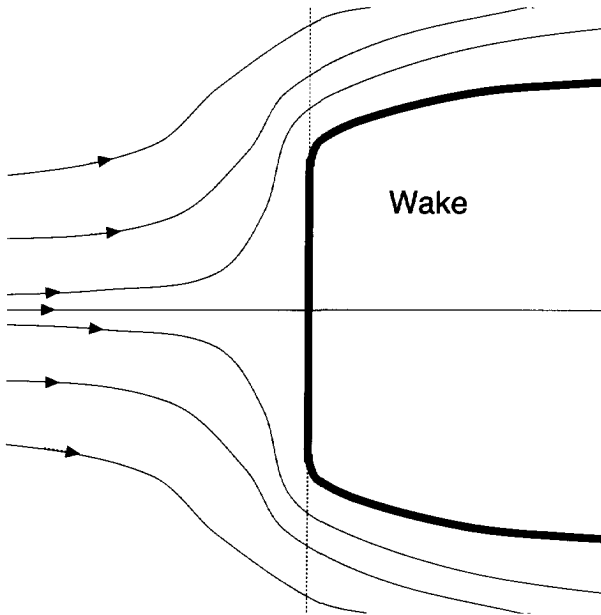


Figure 7.2: Potential flow around a plate with wake

$$z = \frac{D}{\pi + 4} \left( 2iy + y(y^2 - 1)^{0.5} + \frac{1}{2}\pi i - \log \left\{ y + (y^2 - 1)^{0.5} \right\} \right) \quad (7.4)$$

$$u - iv = \frac{Ui}{y} - U \left( 1 - \frac{1}{y^2} \right)^{0.5} \quad (7.5)$$

$$y \equiv \left( \frac{w}{kU} \right)^{0.5} \quad (7.6)$$

The pressure in the wake is assumed to have the same value as the pressure far upstream of the plate. Inside the wake the velocity is set zero. This implies that on the separation line

between the flow and the wake the velocity equals  $U$ . The separation lines can be shown to be paraboles. The inclusion of the wake effectively can be interpreted as a monopole contribution to the velocity field. This leads to a far field (upstream) decrease with distance of the plate's influence on the velocity field proportional with  $r^{-1}$ , instead of the  $r^{-2}$ -behaviour following from relation 7.2.

The two potential flow solutions (without and with a wake) are shown in figures 7.5 and 7.6. The length of the velocity vector (relative to its value at minus infinity) is plotted on the same scale as the Pitot-tube measurements. The value of the mean flow velocity on the stagnation line is plotted in figure 7.7. The Pitot-tube measurements are plotted, along with the potential flow solution. The fit-model shown in this figure will be defined later.

From figure 7.7 we can see that the near field has a good agreement with the wake-potential flow up to a distance  $x = 0.3D$  away from the plate. In the near field the flow feels that behind the plate there is a large cavity and from this position in the near field the cavity seems "infinite". The influence of the plate on the flow decreases with distance following an  $x^{-1}$ -dependence. Further away from the plate ( $x > 0.3D$ ) the effect of the plate shifts more and more from the wake-potential solution to the non-wake potential, indicating that (of course) the wake is finite.

Later in this chapter we will construct estimates for the change in anisotropy character of turbulent flow along the stagnation line of the terminator. We will try to make a connection between these changes and the integrated strain of the mean flow along the stagnation line following the results of the RDT theory discussed in section 1.4. This means that we have to estimate the mean strain. In the former paragraph we have shown that the actual plate flow can be qualitatively described as plateflow with a finite wake. One can construct a potential flow solution with a wake of finite size using Riabouchinsky's method (Milne-Thomson, 1938, p.322) for flow around two parallel flat plates placed one behind the other and with free streamlines joining the edges of the plates. By varying the distance between the plates one can tune this model to the measured velocities and get an estimate for the size of the wake. A second method to model a finite wake is Roshko (1954)'s method. In this method the ratio of the velocity on the free streamline behind the plate to the upstream free velocity is fixed to a value between 0 and 1. Neither method to model a finite wake will be used in this study, because we can estimate the integrated strainrates directly from the mean velocity on the stagnation line via relation 1.48. To estimate the mean velocity on the stagnation line we will fit a curve to the measured values and differentiate it. We adopt a simple functional form with linear behaviour in the near field and with quadrupole behaviour in the far field to model the fast decrease of the plate's influence. The quadrupole contribution makes the function fall off faster with distance to the plate than both potential flow solutions presented in this section. Nevertheless it is included because we found much better correspondence with the measurements and less systematic residuals. We find:

$$\frac{u(x/D)}{U} = 1 - \frac{1}{1 + 1.18x/D + 0.172(x/D)^2 + 0.653(x/D)^3} \quad (7.7)$$

This function is illustrated in figure 7.7. In the following sections relation 7.7 for the mean velocity along the stagnation line is substituted in asymptotic expressions 1.52 and 1.53 for the distortion of fluctuating velocity components.

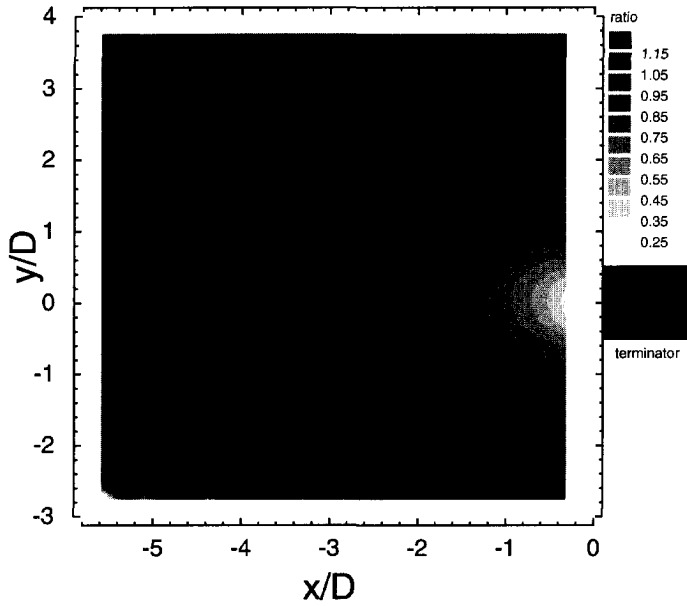


Figure 7.3: Pitot-tube measurement of laminar flow: ratio of mean velocity with and without terminator

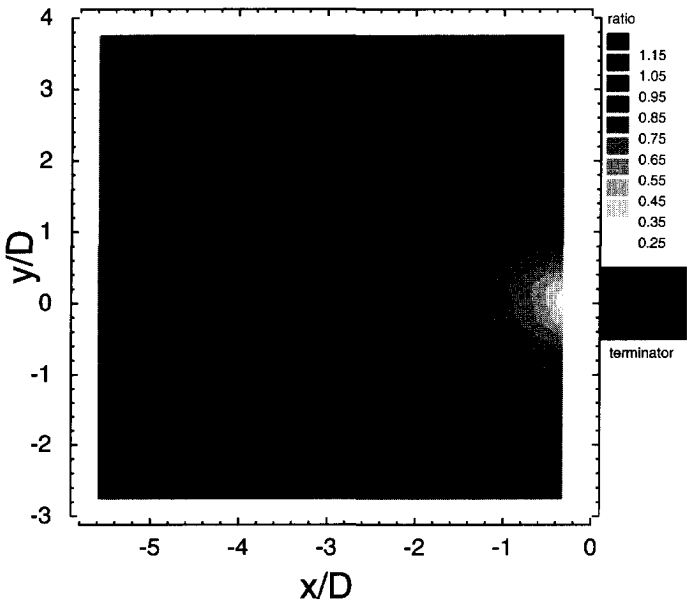


Figure 7.4: Pitot-tube measurement of turbulent flow: ratio of mean velocity with and without terminator

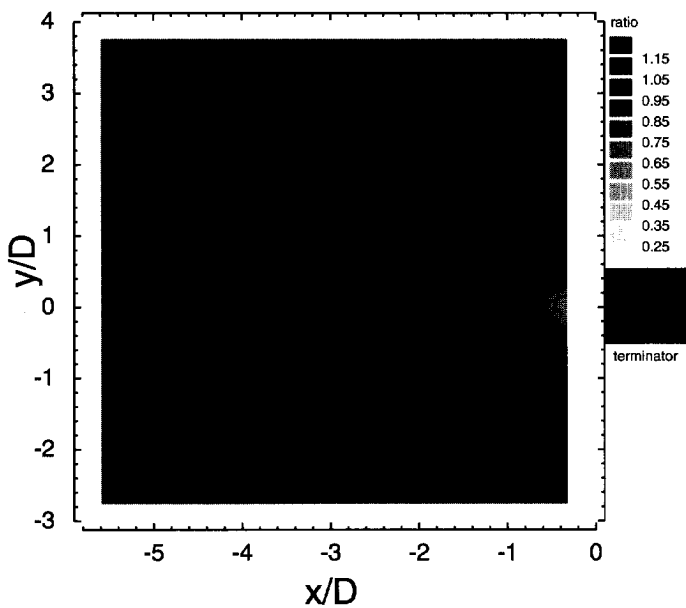


Figure 7.5: Wakeless potential flow solution for ratio of mean velocity with and without terminator.

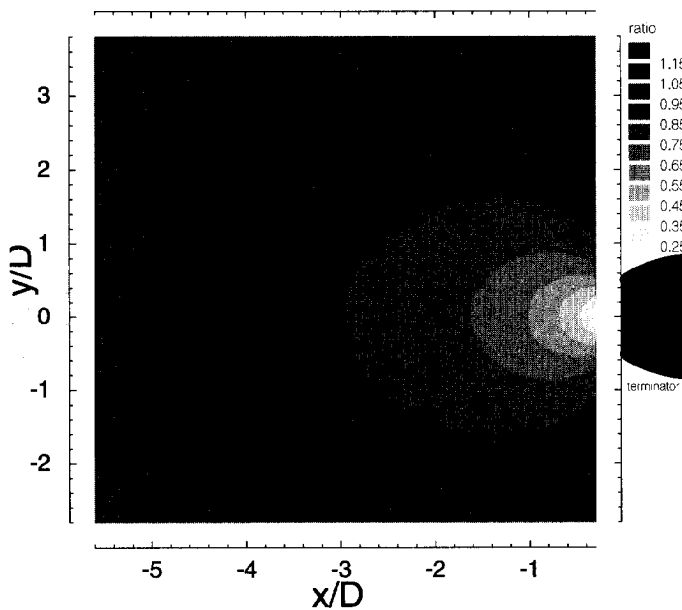


Figure 7.6: Helmholtz' potential flow solution (with wake) for ratio of mean velocity with and without terminator



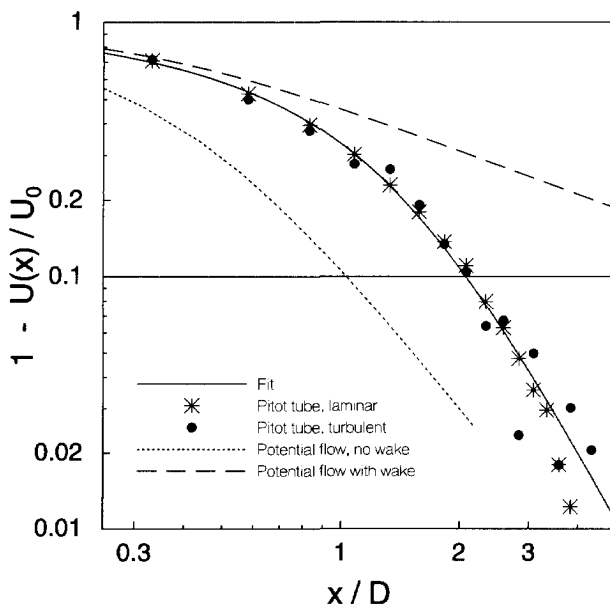


Figure 7.7: Mean flow on the stagnation line of the terminator: Pitot-tube measurements, hotwire measurements and potential flow solution

$x$ [cm]	1	2	3	4	5	7	9	11	13	16	19	22	26	30	35
$x/D$	0.06	0.13	0.19	0.25	0.31	0.44	0.56	0.7	0.8	1.0	1.2	1.4	1.6	1.9	2.2
$1 - U_x/U_\infty$	0.93	0.86	0.81	0.76	0.71	0.62	0.55	0.47	0.42	0.33	0.26	0.21	0.17	0.12	0.09

Table 7.1: Positions on the stagnation line relative to the stagnation point at which the velocity vector is measured

## 7.2 Hotwire measurements on the stagnation line

For our measurements we have used the four-wire probe described in section 5.4. It is calibrated following the full-4-wire indirect method described in section 6.5.4. Temperature drift has been compensated with help of the method presented in section 6.4.2. The electronic signals from the hotwires have been conditioned using ETD-filters at 8 kHz, DC-offset and gain (see section 5.1). We have recorded time-series of the velocity vector at 15 positions on the stagnation line of the terminator. In these experiments the probe was fixed with its measuring volume at 119 cm ( $\approx 29.75 M$ ) behind the grid ( $M=4$  cm). To select a position relative to the stagnation point, the plate was traversed in streamwise direction over the probe using the hole described in section 5.7.4. The positions at which measurements have been taken are listed in table 7.1. Two sequences were recorded: one at a mean undisturbed velocity of 14 m/s (run A) and one at 9 m/s (run B). Per run signals were recorded at 20 kHz during 90 seconds. After application of the calibration, the samples in each record were corrected for mean velocity drift of the wind-tunnel during the sampling of the record with help of relation 5.15 (a variation of  $\pm 3\%$  was observed

in run A and  $\pm 2\%$  in run B). In this way we have eliminated a major portion of non-turbulent fluctuations from the signal, but the resonant sound effects may still be present in the data. Their intensity was small when compared with the mean velocity of the tunnel and their frequency was much lower than the turbulent fluctuations. Therefore we will neglect the resonance of the tunnel in the analysis of our measurements. To eliminate mechanical vibrations from the electric contraction pressure the pressure-signal is passed through a 1 second analogue elliptic low-pass filter.

In the analysis of the hotwire measurements we noticed that the fraction of samples lying outside the calibration function of the probe is very large in the region  $x/M < 0.5$ . At a distance equal to half the plate diameter ( $D/2$ ) off the stagnation point the outlier fraction was 1 percent, increasing rapidly with approaching distance to the plate to 100 percent in the stagnation point. Limited validity of the calibration function can account for part of this phenomenon: velocities have to be higher than 2 m/s and fall within a cone of angle 30-degrees around the stagnation line. The sharp drop to zero of the mean velocity on the stagnation line combined with amplification of the fluctuations by vortex-stretching can lead to local velocities beyond the range of the calibration.

Vortex-shedding behind the plate as a possible cause for the failing of the calibration function close to the plate is rejected on the following ground: The Strouhal number, which characterises oscillations, is defined as:

$$\text{Str} \equiv \frac{fD}{U} \quad (7.8)$$

where  $f$  is an oscillation frequency,  $D$  is a characteristic length of the cause of the oscillations and  $U$  is the flow velocity. For vortex-shedding behind a flat plate the Strouhal number is 0.14. From this relation we expect shedding frequencies to be around 13 Hz in run A and 8 Hz in run B. A comparison of spectra of the velocity in situations with and without the terminator did not show isolated peaks at these frequencies.

A crude solution for the samples outside the calibration range is to simply tag those outliers as 'bad' and either ignore them or estimate their values by interpolation between neighbouring samples inside the calibration range. This method however will introduce systematic errors: samples which in reality are outside the calibration are then mapped back inside the calibration range. To prevent bias in the interpretation of the hotwire measurements from this mechanism we reject all records where the fraction of outliers is larger than one percent. In practice this means that we reject all records taken at positions less than half the plate diameter away from the plate (6 records per run of 15 records). In the remaining nine records per run we replaced those samples that were outside the calibration by the respective preceeding samples.

### 7.3 Estimation of the one-point spectral tensor

The calibrated data, collected in the hot-wire experiments described in the previous section, are used to estimate the diagonal components of one-point spectrum  $\bar{\Theta}$ . Off-diagonal components are negligible since the coordinate axes in the experiment coincide with the principal axes of  $\bar{\Theta}$ . The fluctuation level is found to be about 7 percent, indicating that condition 1.12 for

applicability of Taylor's hypothesis is satisfied. We therefore used Taylor's hypothesis 1.13 to translate the time-spectra into spatial spectra. The wavelength computed via relation 1.13 from a frequency  $f$  will from now on be called the "structure size":

$$\text{upstream structure size } [D] \equiv \frac{U_\infty}{fD} \quad (7.9)$$

The label "upstream" is added to indicate that the upstream velocity is used in Taylor's hypothesis for all points on the stagnation line, even where the local mean velocity was substantially lower. The reason why this was done is that, in their washing past the plate, eddies do change in size, but not in frequency. Labelling structures by frequency therefore allows for the following of the life of those structures along the stagnation line. If we would use the local velocity in Taylor's hypothesis then such comparison of structures before and after their reaction to the plate would not be possible. The actual structure size can be estimated from the upstream structure size by multiplication with the ratio of the local and the upstream velocities.

For structures smaller than  $2D$  (which comprise the full set of scales in which we are interested) we found no significant differences between the FFT-based estimates for the one-point spectrum and the AR-based estimates. Therefore we limit the graphical presentation of the estimates for the one-point spectrum to FFT-estimates. The results of the analysis of run B can be summarised in a simple formulation: they confirm all the results of run A and gave no extra information. The inclusion in run B of estimates for smaller structure sizes than in run A is not considered to be relevant, because the spectral estimates for those small scales suffer from the finite distance between the hot wires in the probe (see appendix F). Consequently we restrict the graphical presentation of results from the hot-wire experiments to run A.

In some of the plots of our results we compare quantities with their upstream values. In such plots we have adopted the fifteenth record in each run, taken at  $x/D = 2.2$ , as reference for upstream values. From table 7.1 we see that in this last point the deviation of the mean velocity from its extrapolated value far away from the plate is 9 percent. This deviation from the asymptotic value, which is present in our reference point, will lead to an underestimation of the true distortion in records closer to the plate. As a measure for the distance to the plate we will use distortion parameter  $\mathcal{D}$ , defined as the relative change in mean velocity compared with its upstream value:

$$\mathcal{D}(x) \equiv 1 - \frac{U(x)}{U_\infty} \quad (7.10)$$

The positions on the stagnation line corresponding with values of the distortion parameter can be read from table 7.1 on page 193.

In appendix F it was shown that hot-wire separation influences the interpretation of hot-wire signals. We have seen that the velocity distribution associated with structures smaller than six times the wire separation in the probe is aliased onto a distribution which appears squeezed in the mean flow direction, with a deviation in the estimate for  $\text{III}^*$  from its actual value of 0.1 or larger. In our study this means that we can expect such artificial distortion in structures smaller than  $0.04D$ , which form only a very small portion of the structure sizes in our analysis.

To see if our measurements meet expectations we have included in our plots the asymptotic RDT-estimates for extremely large and extremely small scales (see section 1.6). We have plotted

relation 1.53 found by Batchelor and Proudman for the small scale structures and relation 1.52 found by Hunt for the large scales. We have also plotted the velocity evolution tensor (relation 1.50) and its inverse, the vorticity evolution tensor (relation 1.48). Though it was devised for the study of vorticity distortion, the latter is nevertheless included in the study of velocity distortion, because in section 1.6 it was found that this tensor has the same far field behaviour as Hunt's solution for the distortion of the velocity of large structures. From rapid distortion condition 1.33 we see that in our situation the RDT solution of Batchelor and Proudman is applicable to structures of size  $L$  within the range:

$$0.07 \ll L[D] \ll 1 \quad (7.11)$$

The validity of Hunt's quasi-steady solution is restricted to much larger structures.

Figure 7.8 shows the relative values of the diagonal components of  $\bar{\Theta}$  when compared with their upstream values. In the three plots on the left these relative values are shown as a function of the distortion parameter; five different (upstream) structure sizes are followed along the stagnation line. On the right the ratio of local and upstream values of  $\Theta_{ii}$  is plotted as a function of the upstream structure size. The absolute change in one-point spectrum  $\bar{\Theta}$  is presented in figure 7.9 as a function of both the distortion parameter and of the upstream structure size. The trace and the rescaled anisotropy invariants are shown for the same five structure sizes as used in figure 7.8 (see appendix C for the definition of anisotropy invariants). The development of the character plot (see figure C.2 for the definition) as a function of the distortion parameter is shown in figure 7.10. Slow distortion effects like diffusion and dissipation may influence measurements close to the stagnation point, which may result in attenuation of energy especially in the small scales. Nevertheless we expect that RDT accounts for the relative changes in the ratios of the three components of velocity fluctuations to one another. To analyse this we have plotted the ratios of the principal components of the one-point spectrum to its trace in figure 7.11.

The sizes of the structures, which we generated in our experiment, are mostly smaller than the width of the plate. This is the reason why we will be mainly discussing the correspondence of our measurements with theoretical predictions from small scale RDT-asymptotics.

From the estimates for one-point spectrum  $\bar{\Theta}$  presented in figures 7.8 to 7.11 we conclude the following:

From the two plots of the kinetic spectra energy on the top of figure 7.9 we see that the energy is not conserved per structure size. When the plate is approached, the large scales gain energy while the small scales lose energy. From figure 7.8 we see that this structure-size dependent reaction to the plate is supported by all three velocity components: amplification of the large scales and attenuation of the small scales. This result is the opposite of the findings of Bearman (1972), who found amplification of kinetic energy in the small scales and attenuation of energy in large scales. Dissipation and diffusion, which eliminate energy from the small scales and which let coherent structures grow in size, may play a role.

The thick lines in the left three plots in figure 7.8 give the RDT-estimates for asymptotically small and large scales. The predictions of these theories for the reaction of the fluctuations in the three principal directions to the approach of a plate were confirmed by the experiments of Bearman (1972). In our case, only in the middle plot, for lateral fluctuations, we find confirmation of the theories of Batchelor and Proudman, while for the larger scales the reaction to

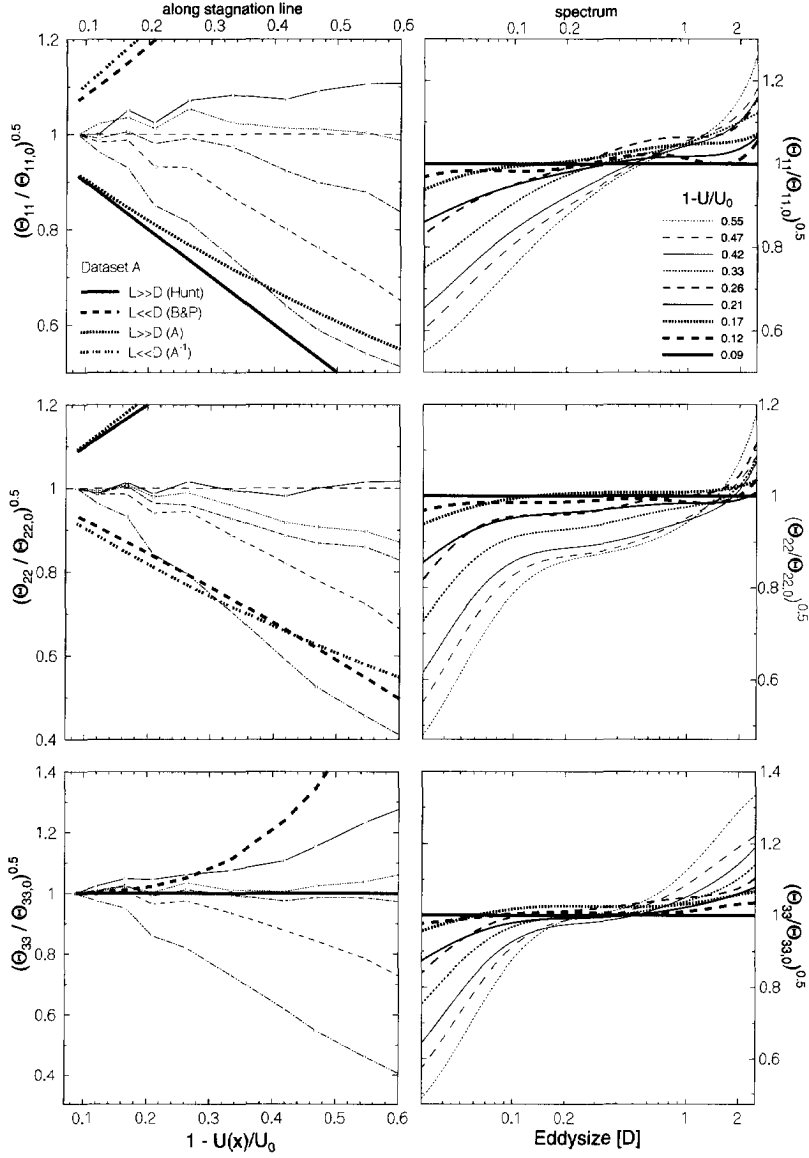


Figure 7.8: Relative distortion of one-point spectrum  $\bar{\Theta}$ . Velocity components along the coordinate axes are shown for dataset A. Left: The lines represent the following upstream structure sizes along the stagnation line:  $\text{---} = 1.6D$ ;  $\text{---} = 0.6D$ ;  $\text{---} = 0.2D$ ;  $\text{---} = 0.07D$ ;  $\text{---} = 0.03D$ . Right: spectra at various points on the stagnation line.  $U_\infty = 14\text{m/s}$ . FFT-based spectra. The thick lines in the figures on the left refer to asymptotic RDT-relations.

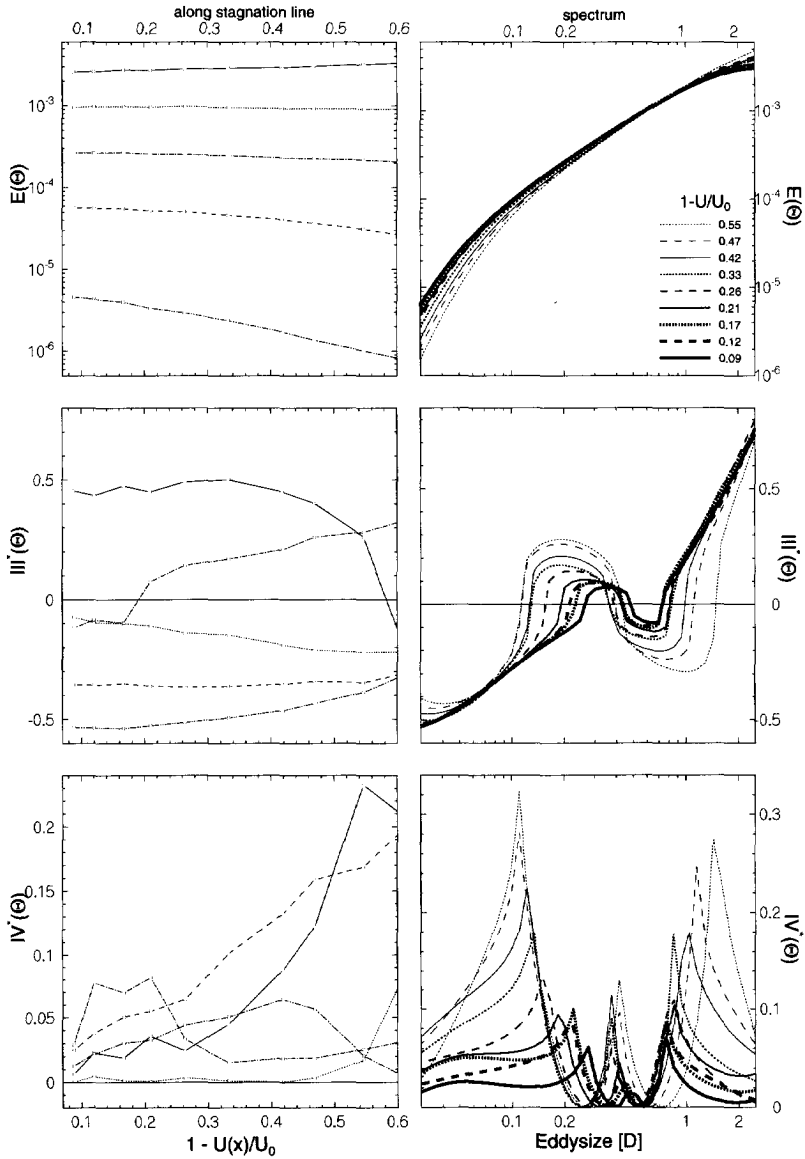


Figure 7.9: Absolute distortion of one-point spectrum  $\bar{\Theta}$ . Kinetic energy and anisotropy invariants are shown for dataset A. Left: The lines represent the following upstream structure sizes along the stagnation line:  $\text{—}$  =  $1.6D$ ;  $\text{- -}$  =  $0.6D$ ;  $\text{...}$  =  $0.2D$ ;  $\text{- . -}$  =  $0.07D$ ;  $\text{— — —}$  =  $0.03D$ . Right: spectra at various points on the stagnation line.  $U_\infty = 14\text{m/s}$ . FFT-based spectra

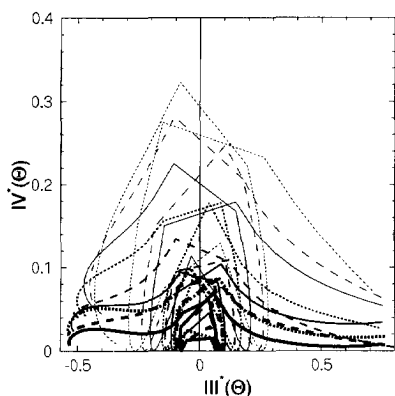


Figure 7.10: Character plot of one-point spectrum  $\bar{\Theta}$  for dataset A

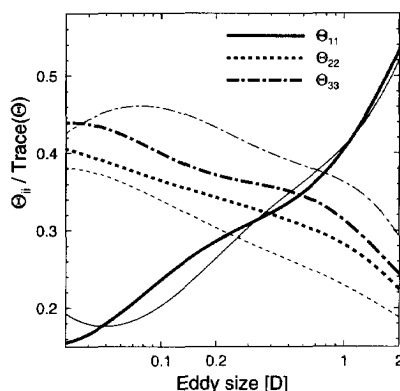


Figure 7.11: FFT-estimate for the relative contribution of the diagonal elements of the one-point spectrum to its trace. The thick lines refer to the record 15 of run A (most upstream of the plate) and the thin lines correspond with record 7 (close to the plate).

the plate becomes more and more indifferent. For the longitudinal fluctuations the RDT-models had predicted the exact inverse of what we have observed: amplification of the small scales and attenuation of the large scales. A similar mismatch between theory and measurement is observed for the vertical fluctuations: the small scales were expected to be amplified, while the large scales were expected to be indifferent to the plate.

There is a possibility that the reaction of the energy spectrum to the plate reflects the non-validity of RDT-conditions. If this is correct, then the small eddies in the flow can lose energy during the passage of the plate. Nevertheless the influence of the mean flow gradients on the three components of velocity fluctuations, which now is only part of the dynamics involved, may follow the RDT predictions. If this assumption is correct can be seen from figure 7.11, where the ratio of the three diagonal components of the one-point spectrum to its trace is plotted. The first striking characteristic of this figure is that the reaction to the approach of the plate (represented by the difference between thick and thin lines) is to a large extent insensitive to the size of the structure! The fraction of longitudinal fluctuations is mostly constant and the fraction of vertical fluctuations grows at the cost of the fraction of lateral fluctuations. Only for the very small structures ( $< 0.06D$ ) there is a slight amplification of longitudinal fluctuations at the cost of vertical fluctuations. This reaction of the smallest scales confirms the small scale RDT-theory of Batchelor and Proudman. By regarding the diagonal components of the one-point spectrum as fractions of the kinetic energy spectrum we have found better correspondence with small scale RDT-asymptotics and with Bearman's experimental results: attenuation of lateral fluctuations and amplification of vertical fluctuations. What remains unsolved is why the longitudinal fluctuations take a constant fraction of the energy in such a large portion of the spectrum.

The widening loops in character plot 7.10, which are supported by the four lower plots in figure 7.9, reflect what we see from figure 7.11: the upstream axisymmetry of vertical and lateral fluctuations around the mean flow direction is broken by the plate. The complexity of the loops in the character plot are a representation of the complexity of the initial, upstream anisotropy of the turbulence and not of the influence of the plate. Initially small scale structures have a preference for the two lateral directions and the large scales prefer the mean flow direction.

A possible explanation for the differences between our and Bearman's measurements is the calibration of the hot-probe. In the present study we have made an extensive effort to eliminate all thinkable sources of systematic errors in the estimation of instantaneous velocity vectors and in the estimation of the anisotropy character associated with a collection of samples. Bearman (1972) does not explain how he calibrated his probe and consequently we cannot discuss his method. Since we have discussed here the results of only two experiments (run A and run B), it would be interesting to see to which extent our results can be reproduced in the future by other researchers.

For large structures the energy does not follow the  $k^4$ -behaviour predicted by relation 1.8 from Batchelor and Proudman. This is one of the characteristics which is introduced by the aliasing effect in one-point spectra, which was discussed in chapter 2. In the following sections we will unalias the one-point spectrum, and check if the large scale behaviour of the energy spectrum has better correspondence with theory.

## 7.4 Estimation of the wavenumber spectral tensor

In the last section of chapter 3 we have decided on two methods to estimate the terms in expressions 4.9, 4.10 and 4.11 for the diagonal elements of wavenumber spectrum  $\bar{\Psi}$ : 'FFT + polynomial fitting' and 'AR + smoothing'. In this section we will estimate the terms in the expressions for  $\bar{\Psi}$ , study their relative importance and add them. The results will be discussed.

The toughest challenge of the two methods spectral estimation methods was shown to be the estimation of higher order derivatives of the one-point spectrum. The expressions for the wavenumber spectrum depend on zeroth to third order derivatives of the one-point spectrum. Consequently we want to see in how much in practical applications our estimates for the wavenumber spectrum are affected by the weakest point of our methods to estimate spectral derivatives. Therefore we have plotted the ratio to the trace of  $\bar{\Psi}$  of all individual terms in the expressions for the wavenumber spectrum. The results for the most upstream point in run A ( $x/D = 2.2$ ) are plotted in figure 7.12. Terms are grouped per equation (4.9, 4.10 or 4.11). To see if a different anisotropy leads to a shift in which terms dominate the unaliasing relations, the terms are also plotted for  $x/D = 0.56$ . These plots are shown in figure 7.13. From the plots of the relative importance of the terms in  $\bar{\Psi}$  we conclude that there is little resemblance between the FFT-based estimates and the AR-based estimates. The lack of correspondence is worse for higher order derivatives. Unfortunately the higher order derivatives dominate the trace of the wavenumber spectrum both close to the plate and far upstream. The DNS-study presented in chapter 4 suffered from the same problem. This directly makes clear that an in-depth study in the estimation of spectral derivatives is called for (as was stated in section 3.9.3).



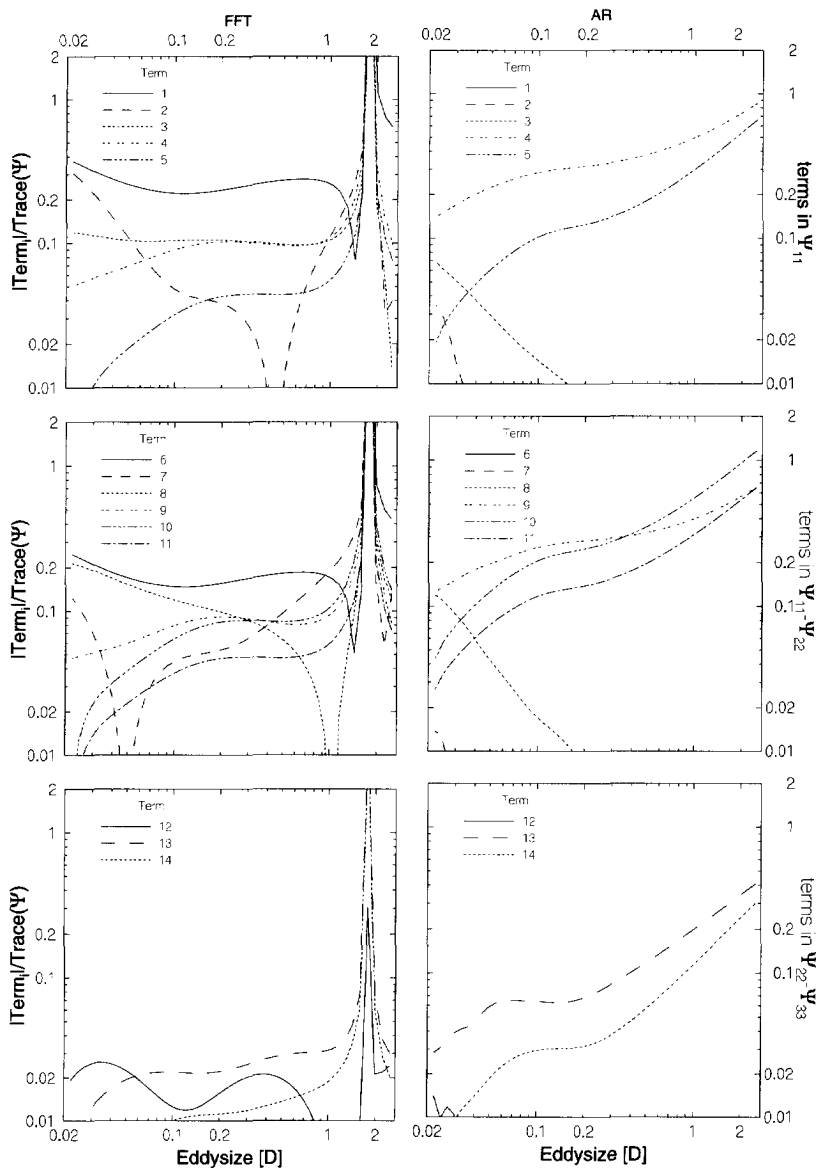


Figure 7.12: Ratio of terms in expressions 4.9, 4.10 and 4.11 for components of  $\tilde{\Psi}$  to the trace of  $\tilde{\Psi}$ . Terms and traces for dataset A are evaluated at  $x/D = 2.2$ .

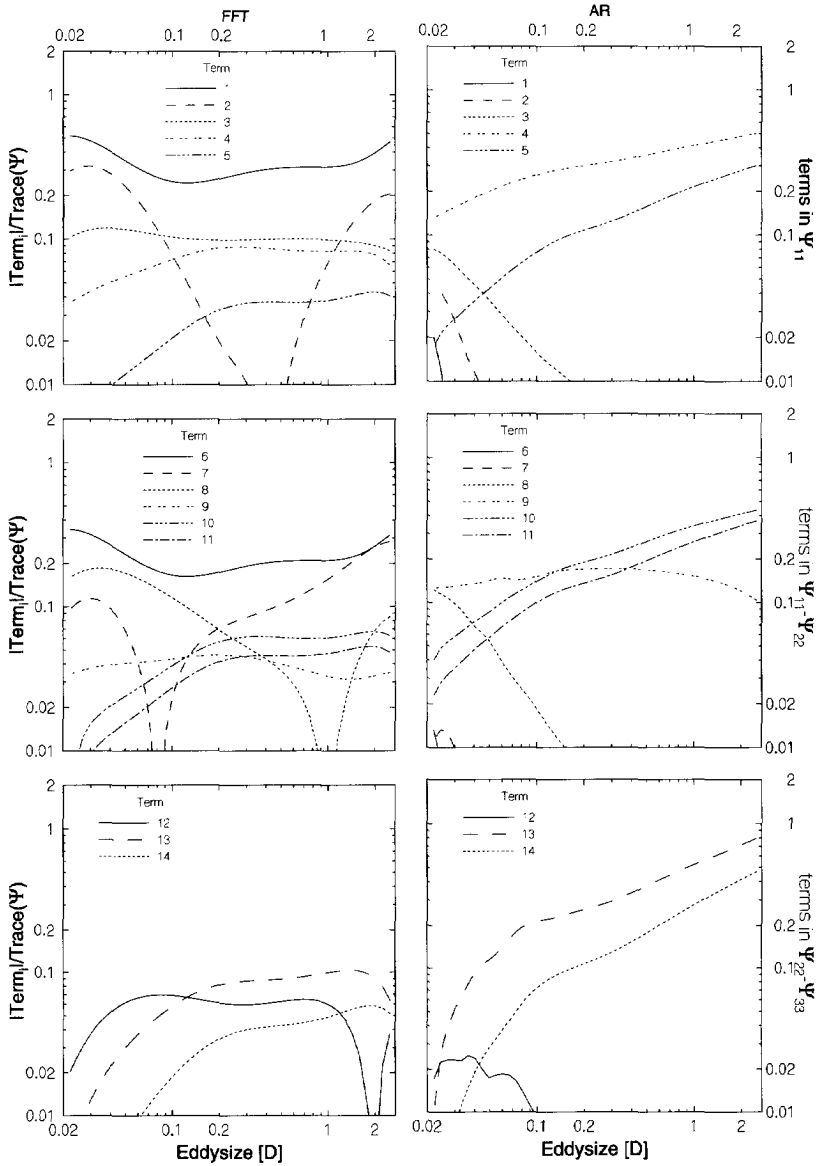


Figure 7.13: Ratio of terms in expressions 4.9, 4.10 and 4.11 for components of  $\tilde{\Psi}$  to the trace of  $\tilde{\Psi}$ . Terms and traces for dataset A are evaluated at  $x/D = 0.56$ .

From the estimates for the terms in  $\bar{\Psi}$  we have constructed estimates for wavenumber spectrum  $\bar{\Psi}$  itself (like with the one-point spectrum we show only run A; differences between FFT and AR estimation methods for spectral derivatives have led to the inclusion of plots for both implementations). The results are presented as follows: The relative change of the diagonal elements of  $\bar{\Psi}$  as a function of the distortion parameter is shown in figure 7.14 for five different upstream structure sizes. Spectra of diagonal components of  $\bar{\Psi}$  are given in figure 7.16. The evolution along the stagnation line of the energy and of the anisotropy invariants is followed in figure 7.15. Spectra of the energy and of the anisotropy invariants are presented in figure 7.17. Character plots of  $\bar{\Psi}$  are shown in figure 7.18. The ratios of the diagonal components of  $\bar{\Psi}$  to its trace are plotted in figure 7.19.

In classic theory the analysis of one-point spectra in terms of unaliased wavenumber spectra is restricted to isotropic turbulence. This limitation reduces the spectral range in which the consequences of classic theory can be tested to high wavenumbers, where one expects to find a more or less isotropic distribution of energy over the structure sizes. Consequently one can only make estimates for one independent scalar function of the (actual) wavenumber: e.g. the energy (see e.g. (Tennekes and Lumley, 1972, page 263) and (Batchelor, 1953, page 143)). Statements on the anisotropy character of anisotropic turbulent flow are beyond the scope of classic theory.

Application of our unaliasing theory to the one-point spectra of turbulence approaching a flat plate on the stagnation line gives us the following insight in the behaviour of spectra for anisotropic turbulence:

All characteristics which we found in the former section in the reaction of the one-point spectrum to the approach of the plate are also exhibited by both the FFT-based estimates and the AR-based estimates for the wavenumber spectrum: amplification of large scale amplitudes, attenuation of all three directions of small scale fluctuations, no change with the plate's approach of the fraction of longitudinal fluctuations in the kinetic energy (only for the very small scale there was a slight increase) and an increase of the fraction of vertical fluctuations at the cost of the fraction of lateral fluctuations. The correspondence between our estimates for the wavenumber spectrum and RDT-asymptotic models is equally good as the correspondence between RDT and our one-point spectra. This means that only the relative behaviour of the velocity components agrees with small scale RDT-estimates.

When we compare figure 7.14 for the relative distortion of the components of the wavenumber spectrum with the corresponding plots for the one-point spectrum on the left in figure 7.8, we see that the wavenumber spectrum discriminates stronger between the reaction to the plate of the large scales and of the small scales than estimated by the one-point spectrum. This difference can be attributed to the aliasing in one-point spectra, which smears out the characteristics over the spectrum, thus eliminating sharp contrasting characteristics between different lengthscales. Consequently we can say that this is exactly what we expected to find.

The FFT- and AR-estimates for individual components of  $\bar{\Psi}$  agree better than the estimates for the anisotropy invariants. This difference can be explained by recognising that the invariants are estimated by making combinations of the different components and zooming in on their differences. This will automatically lead to an amplification of relative errors. The study of anisotropy invariants is a stronger test for the accuracy of both the measured data and of the unaliasing method than the estimation of components of  $\bar{\Psi}$ .

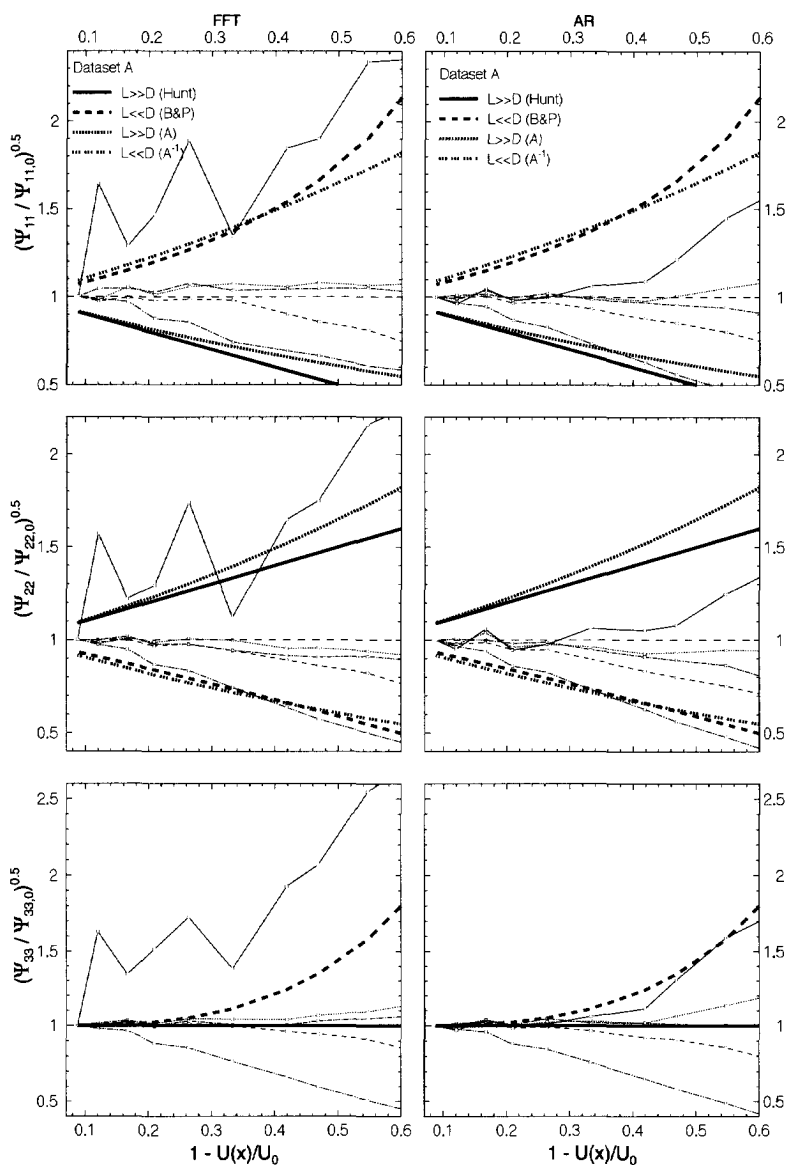


Figure 7.14: Relative distortion of wavenumber spectrum  $\bar{\Psi}$ . Velocity components along the coordinate axes are shown for dataset A. The lines represent the following upstream structure sizes:  $\text{—}$  =  $1.6D$ ;  $\text{---}$  =  $0.6D$ ;  $\text{...}$  =  $0.2D$ ;  $\text{-.-}$  =  $0.07D$ ;  $\text{-.-.-}$  =  $0.03D$ . The thick lines refer to asymptotic RDT-relations.

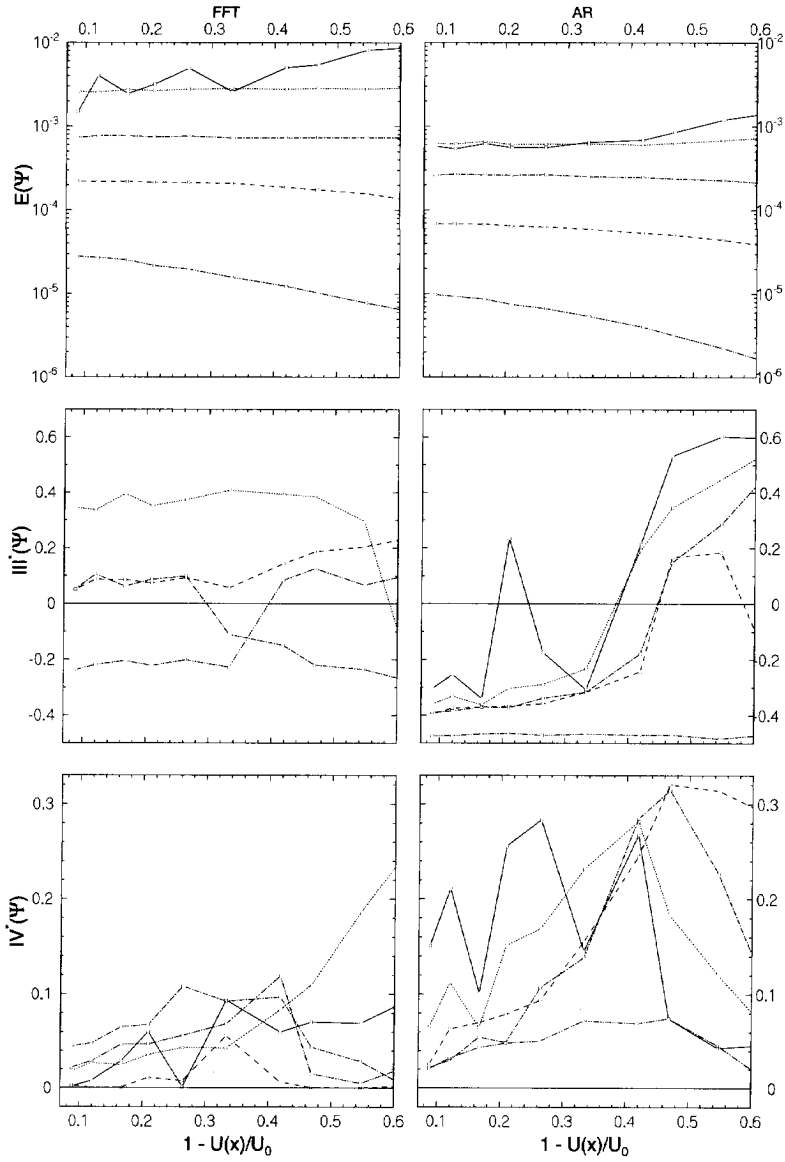


Figure 7.15: Absolute distortion of wavenumber spectrum  $\bar{\Psi}$ . Kinetic energy and anisotropy invariants are shown for dataset A. The lines represent the following upstream structure sizes: — = 1.6D; ..... = 0.6D; --- = 0.2D; -.- = 0.07D; - - - = 0.03D.

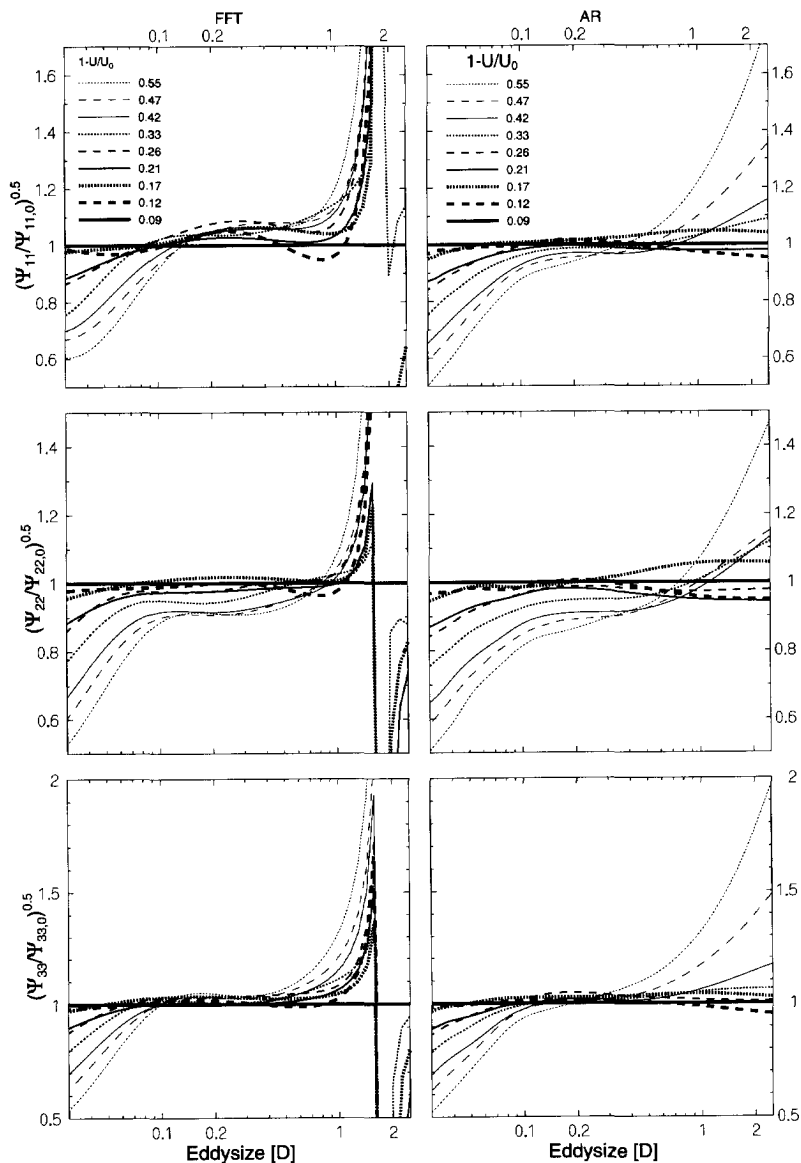


Figure 7.16: Relative distortion of wavenumber spectrum  $\bar{\Psi}$ . Velocity components along the coordinate axes are shown for dataset A.

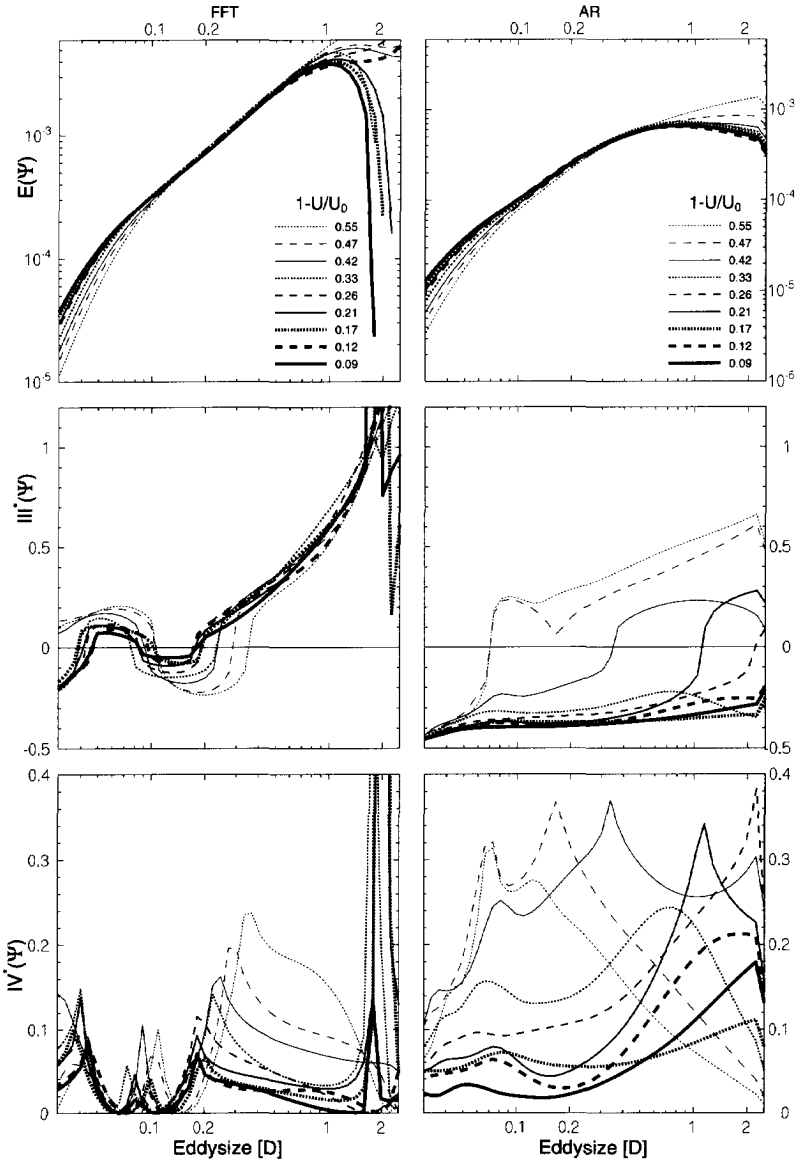


Figure 7.17: Absolute distortion of wavenumber spectrum  $\bar{\Psi}$ . Kinetic energy and anisotropy invariants are shown for dataset A.

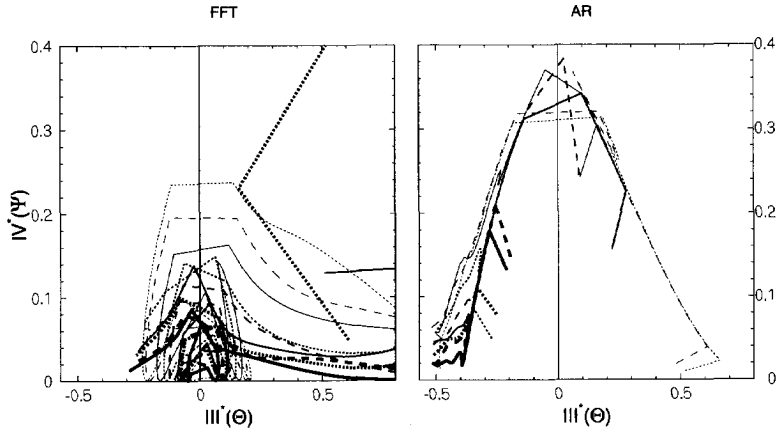


Figure 7.18: Character plots of wavenumber spectrum  $\tilde{\Psi}$  for dataset A. For legend see figure 7.17.

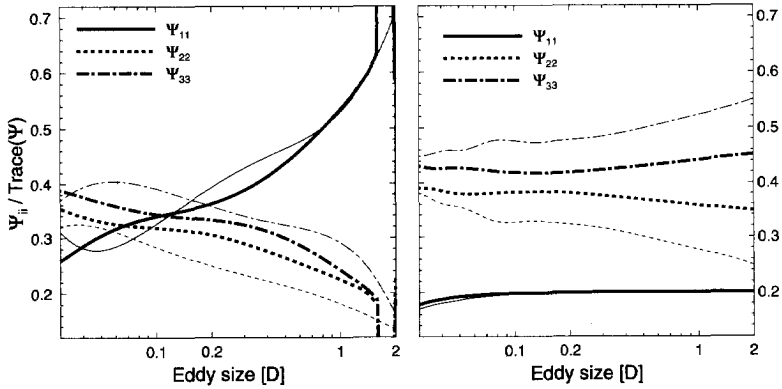


Figure 7.19: Relative contribution of the diagonal components the wavenumber spectrum to its trace. Left : FFT and right: AR. The thick lines refer to record 15 in run A (upstream of the plate) and the thin lines correspond with record 7 (close to the plate).



The big difference between FFT and AR is found in the initial, upstream energy spectrum and its anisotropy. From the plot on the right in figure 7.19 we see that the anisotropy of the AR-based wavenumber spectrum does not depend very much on structure size. This is not what we expect to find because the anisotropy of the one-point spectrum depends so strongly on the wavenumber. The plots of the FFT-estimates for  $\bar{\Psi}$  resemble the corresponding plots of  $\bar{\Theta}$  with the difference that they are shifted to the smaller structure sizes. This agrees with our view of aliasing as a mapping of small scale structures to larger scales. The unaliasing procedure has amplified longitudinal fluctuations and attenuated fluctuations in the two lateral directions. This is conform what we expected from theory: for the one-point spectrum of isotropic turbulence with a  $-5/3$ -power for example we know that lateral fluctuations are overestimated by a factor of  $4/3$ . This factor has to be compensated by unaliasing relations. From the better correspondence of the FFT-based results for  $\bar{\Psi}$  with our expectations we have developed a preference for the FFT-based method above the AR-based method, but without better fundamental understanding of how to estimate spectral derivatives we can only draw qualitative conclusions about  $\bar{\Psi}$ 's nature.

The turbulence which we produced in our windtunnel was generated with a mesh with mesh-size 4 cm. Therefore we would expect to find only eddies with size smaller than a couple of times this mesh-size. The fact that  $\bar{\Theta}$  does ascribe energy to even larger structures once more shows the distorted vision which one gets from turbulence because of the aliasing effect in one-point spectra. In section 1.1 we remarked that Batchelor and Proudman (1956) have developed a theory, which predicts  $k^4$  behaviour for the energy of large scale structures in grid generated turbulence. Our measurements are not concerned with large scale behaviour and therefore we cannot see if in our experiment there is such  $k^4$ -dependence. Nevertheless we see that for the large scales there is a strong drop in energy. Further study, in which our unaliasing theory is used, can reveal the large wavenumber character of the spectrum of grid generated turbulence.

## 7.5 Discussion and conclusion

We have found that, in the modelling of the mean flow around an obstacle, it is essential to correctly model the wake behind the obstacle. The size of the wake largely determines the far field behaviour of the velocity.

To our surprise when the plate was approached all velocity components of small scales were attenuated, while all components of large scales were amplified. For the longitudinal and vertical velocity fluctuations this behaviour is the exact inverse of the theoretical predictions from RDT-models by Hunt (1973) and by Batchelor and Proudman (1954), which were supported by the experimental findings of Bearman (1972). The lateral velocity was observed to obey the RDT models. Concerning the measurements of Bearman we cannot make any remarks, since in his article he does not reveal how his probe is calibrated. In earlier chapters we had found that calibration of a hot-wire probe is a delicate task, which requires more attention than it gets in most studies. We would like to see if future studies will support our results.

We have monitored changes in the relative participation of the three principal directions of velocity fluctuations to the kinetic energy as a function of the distance to the plate. This was done to see if the RDT-predictions were reflected in these quantities. We found that for most struc-

ture sizes the fraction of longitudinal fluctuations was independent of the distance to the plate. Only the very small scales ( $< 0.06D$ ) we observed an increase of the contribution by longitudinal fluctuations. This type of reaction was predicted by small scale RDT asymptotics, but we are surprised about the small portion of the spectrum with this characteristic. For all structure sizes the fraction of vertical fluctuations was found to grow at the cost of lateral fluctuations, a reaction confirming small scale RDT. We could not explain why the influence of the plate on anisotropy did not depend on structure size.

We have applied the two unaliasing implementations (FFT and AR) to the one-point spectra on the stagnation line of the plate and found that both methods showed the same reaction of the wavenumber spectrum to the plate as seen in the one-point spectrum. The only difference between the two methods was the estimate for the upstream spectrum. The FFT-based method to estimate the wavenumber spectrum was found to follow our expectations better than the AR-based method. In chapter 3 we have already shown that the AR-method to estimate spectral derivatives suffers from oscillations for the small scales and is inadequate for application to large scales. The deviations of the AR-estimates from the FFT-estimates can be a consequence of these two problems.

In accordance with expectations, we found that the unaliasing relations attenuate lateral fluctuations and amplify longitudinal fluctuations. We also found that the differences in behaviour between large and small scales were amplified by the unaliasing theory, which confirms the interpretation of the one-point spectrum as a smeared out version of the wavenumber spectrum.

In contrast with the energy of the one-point spectrum, the energy of the wavenumber spectrum was found to fall off rapidly for large structures, i.e.  $k \downarrow 0$ . This observation confirms the notion that we have created grid-turbulence with a finite range of lengthscales. Our data were too limited to find support for  $k^4$ -behaviour, but the anisotropic unaliasing theory admits application to the larger waves.

In textbooks on turbulence, e.g. (Tennekes and Lumley, 1972, page 263) and (Batchelor, 1953, page 143), one-point spectra are only unaliased with isotropic relations. These isotropic relations restrict the unaliasing to the equilibrium range (which is reputed to be isotropic). Our unaliasing method has made it possible to extend the analysis of one-point spectra beyond the mere extraction of the (true wavenumber) scalar energy spectrum. The strong reliance of  $\bar{\Psi}$  on higher order spectral derivatives calls strongly for fundamental research in this area of mathematics. With the present implementations one cannot tell unambiguously what  $\bar{\Psi}$ 's character is, although we conjecture that the FFT-based method provides a good indication.

# Main conclusions and discussion

The aim of this study was to develop and test a method to interpret signals recorded by means of one-point turbulence measurements in terms of physical, three-dimensional structure sizes. The conventional spectrum of one-point measurements (the so-called one-point spectrum) suffers from aliasing, i.e. contributions in the signal from small scales are mapped to large scales. We have constructed an analytic theory, with which one can estimate a three-dimensional turbulent velocity spectrum (called the wavenumber spectrum) from a conventional one-point spectrum. We have tested the validity of our theory by means of a direct numerical simulation (DNS) of grid generated turbulence. From the simulation data we have constructed a one-point measurement and we have used our theory to estimate the wavenumber spectrum. This indirect estimate of the wavenumber spectrum was compared with a direct estimate found via a direct Fourier transform of the three dimensional velocity field. To see the performance of our theory in a practical situation, we have applied our model to hot-wire measurements on the stagnation line of grid generated turbulence that is distorted by a flat plate normal to the mean flow.

The main result of our work is that, under the assumption of homogeneous, weakly anisotropic turbulence, we have developed a set of six equations in closed form to construct an estimate for the symmetric part of the wavenumber spectrum from a given one-point spectrum (relations 2.119, 2.120, 2.121, 2.122, 2.133 and 2.134). This result is based on the assumption that the probability density function for waves of fixed wavelengths to induce velocity in a certain direction can be modelled as ellipsoids. The orientations of the axes of these ellipsoids are allowed to vary freely with the wavelength. In other words, the anisotropies of the small and of the large scales are not required to have the same orientation. The lengths of the axes are restricted by a limitation of the analysis to a first order expansion in a small anisotropy parameter.

It is our belief that this theory is the first theory to exploit *all* information in (the symmetric part of) the one-point spectral tensor in a reconstruction of the wavenumber spectral tensor via unaliasing. The classic unaliasing relations for isotropic turbulence (see e.g. (Tennekes and Lumley, 1972, page 263) and (Batchelor, 1953, page 143)) are recovered in the isotropic limit of our anisotropic relations. With this classic theory one could only estimate turbulent energy in the isotropic part of the spectrum (provided that the spectrum has an isotropic sub-range) and have a qualitative suggestion whether the velocity distribution as a whole was isotropic, elongated or squeezed. Attempts in the past (Sreenivasan and Narasimha, 1978) to construct unaliasing models for axisymmetric turbulence with the axis of symmetry in the mean flow direction lack unambiguity and impose unnecessary restrictions on the nature of the flow.

To quantify flow anisotropy (which can now be estimated with our unaliasing theory), we have rescaled the so-called Lumley-triangle to a plot which we have called a "character plot" (sec-

tion C). This rescaling has been defined such that linear deviations from isotropy can be seen as linear departures from the point in the character plot corresponding with isotropy. In Lumley's original diagram most significantly anisotropic flows are characterised as "fairly isotropic". In our character plot the horizontal parameter (closely related to Lumley's third invariant) gives the (linear) elongation of the velocity distribution. The second parameter gives the (linear) departure from axisymmetry (with two-dimensional flow as its upper limit).

For a practical implementation of our unaliasing theory we have reviewed three methods to construct spectral estimates: Fast Fourier Transform (FFT), Autoregressive models (AR) and Moving Average models (MA). The former two models have been shown to give the best estimate for the spectrum of grid generated turbulence. Both methods are extended so that they can estimate the third derivative of the spectrum, which appears in our unaliasing equations. Based on our results, we have a preference for the FFT-based method for the following reasons. The AR-method minimises the logarithmic difference between the spectra of the model and of the data using a linear frequency axis. Due to this characteristic AR appeared to be an improper tool when a logarithmic frequency axis is used in situations where the frequency range comprises several orders of magnitude. Moreover the estimation of spectral derivatives by means of AR suffers from amplification of (possibly insignificant) little wiggles at each step of differentiation. We have not been able to estimate the accuracy of the estimates for the derivatives of the spectrum.

The practical difficulties, which arise when one tries to estimate spectral derivatives, point out an *intrinsic conceptual problem* in the interpretation of one-point measurements. As long as these practical difficulties will remain unsolved it may well be that turbulence researchers will have to confess that they have little notion of how to physically interpret signals from one-point measurements in terms of the three-dimensional structure of turbulence. A practical solution to this problem may be provided by recently developed measurement techniques like Particle Tracking Velocimetry (PTV) and Particle Image Velocimetry (PIV), which permit the simultaneous estimation of the velocity in a full two-dimensional cross-section of the flow field or even in an array of two-dimensional fields.

To assess applicability of our analytical unaliasing relations to turbulent flow fields we have constructed a mathematical windtunnel by means of a Direct Numerical Simulation of grid generated turbulence. Direct estimates for the wavenumber spectrum (calculated via Fourier transforming three-dimensional velocity fields) and indirect estimates (found via application of our unaliasing relations to simulated one-point measurements) agreed rather poorly, although axisymmetry was observed to be conserved throughout the analysis. The correspondence problem seems to be larger for the smaller wavenumbers. We have found the following possible causes for the lack of agreement: a too coarse numerical mesh in the DNS, poor statistics in connection with a too short time series on which the calculations were based, a too low Reynolds number, a too coarse turbulence generating grid, lateral inhomogeneity, a too strong energy decay of the simulated turbulence and limited validity of Taylor's hypothesis.

Next we have constructed an experimental set-up in a windtunnel for the collection of time series of velocity vectors in one-point measurements in real turbulent flow. This flow is the distortion of grid-generated turbulence by a flat plate placed normal to the flow.

During the calibration of the instruments in our set-up we found out that there is no commercial

data-acquisition software nor a commercial spread-sheet or a data-analysis package, which uses known variances and covariances in the process of fitting a curve through a set of measured data points via weighted least squares. This makes the available commercial software improper tools for scientific use: theories cannot be confirmed or refuted on objective grounds, i.e. based on either *significant correspondence* (the deviations between samples and model are reasonable when compared with the estimated errors) or on *significant differences* (fitmodel and samples differ more than reasonably can be expected via the estimated errors). We have developed a simple relation (relation A.26) for the relative weight of (groups of) experimental samples, with known variances and covariances in two variables. This relation can be readily incorporated in existing software for data analysis via an iterative loop.

For the measurement of turbulent velocity in our setup we have developed a four-hotwire probe. We have shown (see appendix E) that temperature calibration of hot-wires is crucial for accurate velocity measurement. Bearman's correction method, which is based on a ratio of temperature differences, has been shown to effectively eliminate ambient temperature drift provided that the operational temperature of the wire is estimated in a temperature calibration. We found that the separation of the wires in our probe introduces ten percent (or more) anisotropy (i.e. biases of 0.1 in the character plot) in the wavenumber spectrum for structures with sizes smaller than six times the separation of the wires. Based on an investigation of many different calibration methods, we can say that the optimal velocity calibration model for a 4-wire probe is an indirect method, in which the response of each wire is modelled as a function of the velocity vector. Full three dimensional calibration is essential. To estimate the velocity vector from a set of four wire readings one has to *simultaneously* solve the four response equations of the wires for the three unknown velocity components. One should not make sub-probe estimates which are combined later on.

With our calibrated four-wire probe we have performed one-point measurements of the velocity vector on the stagnation line upstream of the plate. The upstream, far field behaviour of the mean flow field (i.e. monopole or dipole) is fully determined by the *wake*. Therefore it is important for the development of quantitatively applicable Rapid Distortion models to include the influence of the wake in the mean flow.

In the one-point spectrum we see that, when the plate is approached, the intensity of the small scale fluctuations is attenuated for all three velocity components while the intensity of the large scales is amplified. This was observed to be the only reaction of the turbulent flow to the distance to the plate discriminating between turbulent length scales. For all structure sizes the relative contributions of the diagonal terms in the one-point spectrum to its trace reacted identically to the distance to the plate: longitudinally the relative contribution was indifferent to the plate's distance and vertically the relative contribution to the trace grew at the cost of lateral fluctuations. The observation that the plate induces the same changes in the anisotropy for all lengthscales contradicts the idea that large scales have different dynamics than small scales. For the small scales our experiment confirms the asymptotic RDT theory by Batchelor and Proudman (1956), which predicts attenuation of the lateral contribution and amplification of both the vertical and the longitudinal contributions (though the behaviour predicted for the longitudinal fluctuations is observed in a much smaller part of the spectrum than the model predictions for the lateral and vertical contributions). The quasi-steady theory for large structures by Hunt (1973) does not agree with our measurements for any structure size. A possible explanation is

that the structures in our experiment are not large enough to allow for a comparison. Furthermore we suspect that there is influence on the measurements from the dynamics of structures that are slowly distorted in the region just in front of the plate. This possible influence of slow dynamics is not incorporated in RDT.

We have used the two methods, which were developed to estimate spectral derivatives (FFT and AR), to construct estimates for the wavenumber spectrum from the one-point spectrum of our hot-wire measurements in front of the plate. The AR-based estimates for the anisotropy of the wavenumber spectrum show very little dependence on the structure size. We have the impression that this is an artefact of the AR-method, which has difficulties in estimating derivatives of a spectrum for large scales. We therefore are inclined to reject the AR-based estimates for the wavenumber spectrum. The FFT-based estimates for the anisotropy character confirm our expectations in two ways: The first confirmation is that the characteristics, which in the one-point spectrum are estimated for large structures, are shifted to the smaller scales by the unaliasing model. The second confirmation of our expectations is that the unaliasing relations attenuate lateral fluctuations and emphasise fluctuations along the mean flow. These characteristics support the suggestion that the FFT-based method to implement our unaliasing relations correctly applies the theory to measured data.

All in all we can say that our study has resulted in the first method in the history of turbulence research, which is capable of employing *all* information in the symmetric part of the spectral tensor of one-point turbulent velocity measurements in a reconstruction of the underlying three-dimensional spectrum. Though practical application of the method has been shown to be far from trivial, the method has filled in a long existing gap in the toolbox for the analysis of turbulence spectra and it is a promising aid for a better understanding of fluid mechanics.

## Recommendations for future study

Future research is suggested to extend the present unaliasing model to include the anti-symmetric part of the spectrum, which is associated with net swirl and net vorticity.

The estimation of derivatives of spectra is an unexplored field of research. Our unaliasing relations can gain much in practical value if there would be a method to estimate with a known accuracy the derivatives of a spectrum.

It would be interesting to study the (un-)aliasing behaviour of one-point measurements when the signal is decomposed in terms of wavelets instead of harmonic functions. The resulting relations can lead to totally different interpretations of one-point measurements than the interpretation provided by our unaliasing relations. If this would be the case, it would be a sign that turbulence researchers have to intensify the discussion about the relation between basic functions and coherent structures in turbulence.

Signal theoreticians are kindly requested to construct methods to estimate cospectra of two variables. Furthermore they are invited to develop theory for a logarithmic AR-model, in which a sample is related to earlier samples with an exponentially increasing delay. The existing AR-models miss the point that in physics interactions between components in the signal are often logarithmically ordered. Furthermore, by assuming that the samples are equally spaced in time,

with infinite precision of the corresponding sampling times, all existing AR-models miss the crucial step that the original signal was *analogue* and was sampled with *finite* accuracy during a *finite* sampling interval. Models are devised to give a mathematical representation of the original, analogue signal, and not of a set of samples.

We are very interested if researchers from other laboratories can experimentally confirm or refute our results for either the small scales or for the large scales in turbulent flow around a plate. The use of subminiature probes as developed by Tsinober et al. (1992) can help to reduce the negative effects of probe interference and of wire separation.

Our model for unaliasing of one-point measurements uses a statistical description for wave-distributions. The model depends on the third derivative of the spectrum and it would be interesting to develop a method for the measurement of turbulent velocity fields such that no unaliasing is required for the estimation of the wavenumber spectrum from measured data. With a rake of one-point sensors as shown in figure 7.20 this may be possible. Three arrays of one-point sensors are placed on perpendicular lines and with exponentially increasing distance. Minimum and maximum separation correspond with the structure sizes in which one is interested.

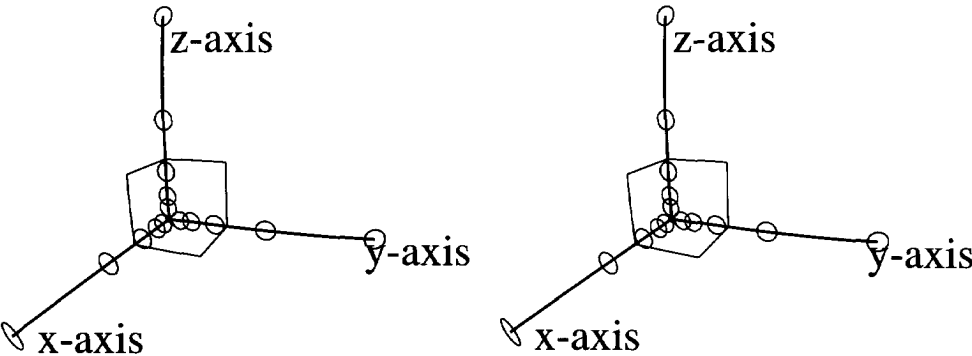


Figure 7.20: Three arrays of one-point sensors with exponentially increasing distance for the estimation of directions of waves.





# Appendix A

## Curve-fitting through data with measurement errors

### Introduction

Physicists often construct models which map one physical quantity (called the "domain") onto a dependent quantity (called the "range"). In this appendix an account is given of  $\chi^2$ -fitting of relations through data with known uncertainties in both domain data and in range data. These uncertainties can be found by (independent) repetition of the experiment followed by analysis of the spread in the resulting probings of the system. For a detailed and indispensable text on how to devise one's experiment such that systematic errors are eliminated where possible and a general view on sound experimenting the reader is referred to the book by Squires (1993). Quantity  $\chi^2$ -, which is a measure for the "badness of fit", weights the deviation from a suggested relation between all datapoints with the datapoints' respective accuracies. This insures the user that inaccurate samples will have little influence on the relation that will be obtained.  $\chi^2$ -Minimisation leads to a suggestion for a particular relation taken from a class of relations. This suggestion fits best the supplied samples according to the  $\chi^2$ -criterion.

In the following sections I will provide expressions for  $\chi^2$  for the cases when:

- No accuracies are known.
- Accuracies are known only for the range quantity.
- Independent error-estimates are known in both domain and range.
- Correlated error-estimates are known in both domain and range. This step will be made via analysis of invariants.

Programs are available (spreadsheets, mathematical libraries, scientific plotting programs) that fit curves through data minimising

$$\chi^2 \equiv \sum_i w_i \left( \Delta(y_i) \right)^2 \quad (\text{A.1})$$

where  $\Delta(y_i)$  are the differences between the range quantity of the measured sample and the fitted model and where  $W_i$  are weights, which can be used to give the more accurate samples relatively stronger influence on the fitting process. For all the above cases of knowledge about error-estimates a link will be made between the respective expressions for  $\chi^2$  and standard weighted least-squares fitting routines. To show the difference between the methods we will apply all methods on the analysis of *one particular dataset* consisting of tens of clusters of raw probings out of which an environment containing three clusters will be considered. We will give plots showing the information which is found when either method is applicable. In these plots we will also show the error-estimates which could be extracted from the respective available information.

After we will have given the relations for  $\chi^2$  something will be said on whether a certain fit-curve makes sense. Finally I will explain two fit-methods: one that is linear in the fit-parameters and the other which is non-linear.

We will suppose that one has measured a collection of  $N$  doublets  $(x_i, y_i)$  and that there is assumed to exist is a relation  $f$  between quantities  $x$  and  $y$  with  $J$  degrees of freedom represented by parameters  $\alpha_j$  ( $j = 1..J$ ).

## A.1 No errors known

No error estimates are known. This may occur when one has discarded raw data. An example of this situation is shown in figure A.1. In this case all samples must be treated equally. The

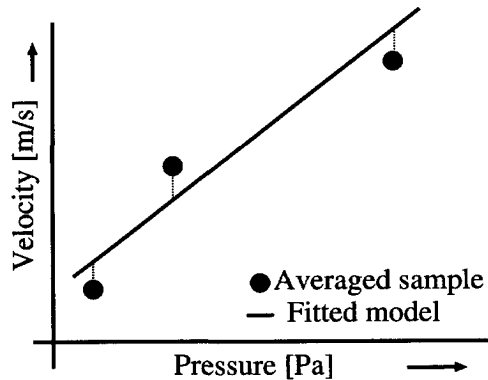


Figure A.1: Distance counting when no error estimates are available

contribution of a sample pair  $(x_i, y_i)$  to  $\chi^2$  is taken to be the square of the difference between the sample's  $y_i$ -value and the function's value evaluated at  $x_i$ . Function  $f_{\alpha_j}$  fits the data best when the sum of squared differences between data and the function's values is a minimum with respect to variation of parameters  $\alpha_j$ , i.e. that

$$\chi^2 \equiv \sum_i \Delta^2(y_i) \quad (\text{A.2})$$

is a minimum, with

$$\Delta(y_i) \equiv f_{\alpha_j}(x_i) - y_i, \quad (\text{A.3})$$

the vertical distance of data-points to the fitcurve. Routines minimising expression A.3 are called *least squares methods*. This methods corresponds with equal weights for all samples in relation A.1:

$$W_i = 1 \quad (\text{A.4})$$

In figure A.1 we see a suggestion for the best relation between pressure and velocity in the region of the three clusters. A curved relation would make a better fit. Without knowledge about the significance of the samples however, we cannot say whether this improvement is still supported by the data.

## A.2 Only y-errors

Often you have knowledge about inaccuracies  $\sigma_{y,i}$  with which  $y_i$  have been measured because you have determined the inaccuracy of the apparatus by calibration. Another possibility is that an estimate for quantity  $y$  is determined by measuring the quantity  $N$  times. Errors in  $x$  are often neglected (too much labour) or forgotten (domain quantity  $x$  is "reliable"). Sometimes their values are really insignificant when compared with the influence of the  $y$ -errors. An example of this situation is shown in figure A.2. If the samples are normally distributed and do not suffer

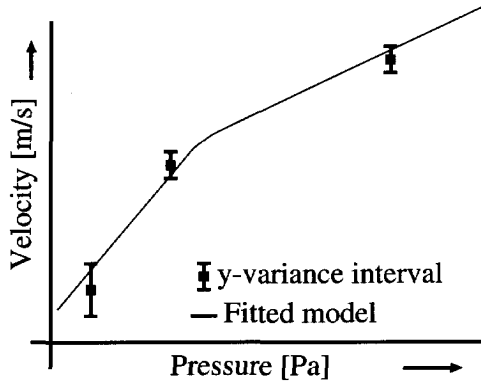


Figure A.2: Distance counting when  $y$ -error estimates are available

from systematic errors, then inaccuracy  $\sigma_y$  associated with mean value  $\bar{y}$  is determined via:

$$\sigma_{\bar{y}} = \frac{1}{\sqrt{N}} \text{RMS}(y - \bar{y}) \quad (\text{A.5})$$

where an overline indicates the mean value.

These inaccuracies  $\sigma_{y,i}$  can be used to weight all samples' contributions  $\Delta(y_i)$  to the badness of fit  $\chi^2$  by measuring the distances of  $f_{\alpha_j}$  to the data-points in units of the local inaccuracies.

This reduces the influence of inaccurate measurements on  $\chi^2$  on the optimisation process. The definition of  $\chi^2$  is now:

$$\chi^2 \equiv \sum_i \left( \frac{\Delta(y_i)}{\sigma_{y,i}} \right)^2. \quad (\text{A.6})$$

We see that, in case only  $y$ -errors are known, the weights in standard weighted least squares routines (relation A.1) are to be taken according to:

$$W_i = \frac{1}{\sigma_{y,i}^2} \quad (\text{A.7})$$

We can now assess from figure A.2 that the available data does support the idea to use a curved type of function: the error-bars are so small that they justify this choice.

### A.3 Uncorrelated $x$ - and $y$ -errors

Suppose that both  $y_i$ 's inaccuracies  $\sigma_{y,i}$  and  $x_i$ 's inaccuracies  $\sigma_{x,i}$  are known. In this section the covariance of the errors is supposed not to be known. This may happen when one uses analogue instruments, which are read independently, but in the same time interval. In this case we can extend the idea given in the former subsection for the case when only inaccuracies in the range quantity were known. We minimise the sum of the squared distances of  $f_{\alpha_j}$  to data-points  $(x_i, y_i)$ , counting both coordinates in units of the respective local inaccuracies  $\sigma_{x,i}$  and  $\sigma_{y,i}$ . In a linear  $xy$ -scatterplot points that lie equally far away from a data-point in  $\chi^2$ -sense form horizontally or vertically oriented ellipses, provided that the errors in  $x_i$  and in  $y_i$  are uncorrelated. An example of the situation when both  $x$ - and  $y$ -errors are known is shown in figure A.3.

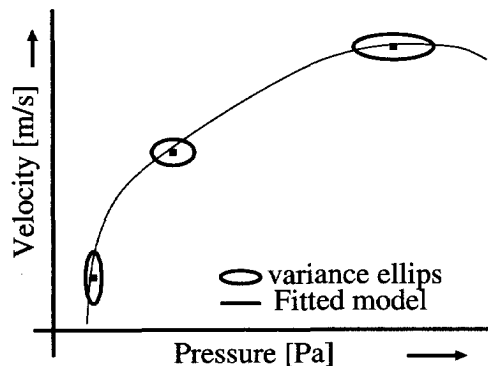


Figure A.3: Distance counting when independent  $x$ - and  $y$ -error estimates are available

For uncorrelated data  $\chi^2$  is now given by:

$$\chi^2 \equiv \sum_i \left( \frac{d(x_i)}{\sigma_{x,i}} \right)^2 + \left( \frac{d(y_i)}{\sigma_{y,i}} \right)^2 \quad (\text{A.8})$$

where  $d(x_i)$  and  $d(y_i)$  are distances to the point on  $f_{\alpha_j}$  which touches the innermost ellipse (as just mentioned) around  $(x_i, y_i)$ . See figure A.4.

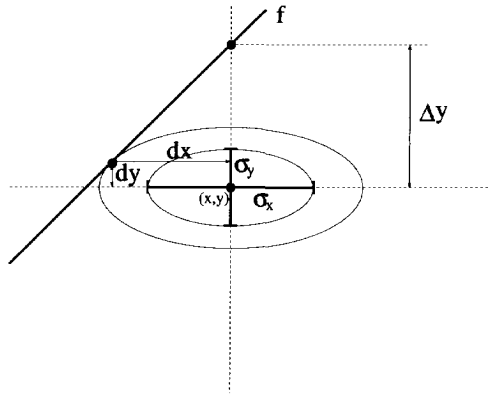


Figure A.4: The distance of a sample to a fitcurve

We will now derive a relation between the expression A.4 for  $\chi^2$  and the weights in standard least squares fitting routines. To achieve this we have to rewrite expression A.8 to one with  $\Delta(y_i)$  instead of  $d(y_i)$ . This is done as follows: The contribution to  $\chi^2$  of one data-point (in which you now place the origin) is constant when the point on the fitcurve  $(d(x), d(y))$  that is closest to the data-point moves over ellipses:

$$\left( \frac{d(x)}{\sigma_x} \right)^2 + \left( \frac{d(y)}{\sigma_y} \right)^2 = c \quad (\text{A.9})$$

for any constant  $c$ , or:

$$d(y) = \pm \sigma_y \sqrt{c - \left( \frac{d(x)}{\sigma_x} \right)^2} \quad (\text{A.10})$$

from which you find the derivative:

$$d'(y) = - \left( \frac{\sigma_y}{\sigma_x} \right)^2 \frac{d(x)}{d(y)}. \quad (\text{A.11})$$

In the point  $(d(x), d(y))$  the fit-function is tangent to the ellipse, since you are looking for the innermost ellipse touching the function. Therefore expression A.11 must equal the function's local directional coefficient  $f'_i$ :

$$d(x) = -f'_i \left( \frac{\sigma_x}{\sigma_y} \right)^2 d(y). \quad (\text{A.12})$$

The fit-curve is supposed to be linear within the horizontal range from the data-point to the curve. The vertical distance of the data-point to the fitcurve can now be calculated:

$$\Delta(y) = d(y) - f'd(x) = \left[ 1 + \left( \frac{f'\sigma_x}{\sigma_y} \right)^2 \right] d(y). \quad (\text{A.13})$$

The horizontal distance to the (locally linear) fitcurve can be found from the vertical distance by the following relation:

$$\Delta(y) = f'\Delta(x). \quad (\text{A.14})$$

Substitution of relations A.14 and A.13 in relation A.8 leads to:

$$\chi^2 = \sum_i \frac{\Delta^2(y_i)}{\left( f'_i \sigma_{x,i} \right)^2 + \sigma_{y,i}^2}. \quad (\text{A.15})$$

This means you can use models based on minimisation of expression A.1 to take into account errors in both  $x$  and in  $y$  when you weight the samples as follows:

$$W_i = \frac{1}{\left( f'_i \sigma_{x,i} \right)^2 + \sigma_{y,i}^2}. \quad (\text{A.16})$$

The problem with weights defined by relation A.16 is that they use the derivative of the function *yet to be found*. This is solved as follows: A first estimate for function  $f$  is found by minimisation of  $\chi^2$  defined by relation A.6. In a series of iterations the derivative of former iterations is used as estimate for  $f'$ . For bijections his method has shown to converge to a stable solution in 5 to 10 iterations, dependent on the variation of  $f'$ .

The extra information provided by the variance ellipses plotted in figure A.3 suggests that the function plotted in figure A.2 is not steep enough in the left hand region of the shown domain segment, and that it is too steep in the right hand region. The curve suggested in figure A.3 has been constructed to include these improvements.

## A.4 Data with correlated errors in $x$ and $y$

Relation A.16 between standard weighted least squares fitting routines and experimental data with measurement errors in both domain-quantity and in range-quantity can be easily extended to data with (partly) correlated errors. This situation is shown in figure A.5.

The step to include covariances in  $\chi^2$ -minimisation will be made by making use of the Mahalanobis distance (see Weinberg (1985)). The Mahalanobis distance  $r_m$  of any point  $p$  to measured

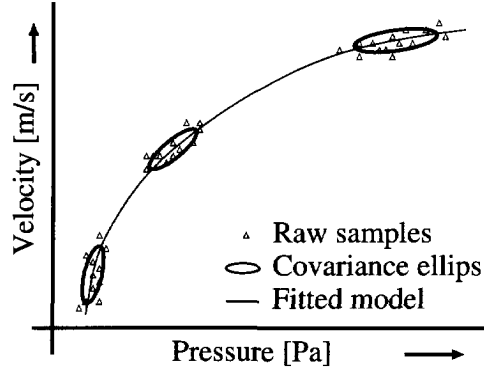


Figure A.5: Distance counting when the full covariance matrix is available

sample  $\mathbf{x}_i$  is defined to be:

$$r_m^2(\mathbf{p}, \mathbf{x}_i) \equiv (\mathbf{p} - \mathbf{x}_i) \cdot \bar{\mathbf{C}}_{\mathbf{x}_i}^{-1} \cdot (\mathbf{p} - \mathbf{x}_i) \quad (\text{A.17})$$

$$\bar{\mathbf{C}}_{\mathbf{x}_i} \equiv \frac{1}{N} \mathcal{E} \left( (\mathbf{x} - \mathbf{x}_i)^t \otimes (\mathbf{x} - \mathbf{x}_i) \right) = \begin{pmatrix} \sigma_x^2 & \sigma_{xy} \\ \sigma_{xy} & \sigma_y^2 \end{pmatrix} \quad \text{covariance tensor} \quad (\text{A.18})$$

$$\mathbf{x}_i \equiv \mathcal{E}(\mathbf{x}) \quad (\text{A.19})$$

Measure  $r_m$  gives the distance of point  $\mathbf{p}$  to sample  $\mathbf{x}_i$  measured in standard deviations. Collections of points with constant standard deviation form ellipses around the measured sample of which the axes are multiples of the eigenvectors of the covariance tensor. As a consequence the errorbars associated with the samples which we consider are to be plotted skewly (see figure A.6). The Mahalanobis distance is invariant to any regular linear transformation  $\bar{\mathbf{A}}$ , i.e. its value does not change if you replace  $\mathbf{p}$  and  $\mathbf{x}_i$  by  $\mathbf{q} \equiv \bar{\mathbf{A}} \cdot \mathbf{p}$  and  $\mathbf{y}_i \equiv \bar{\mathbf{A}} \cdot \mathbf{x}_i$  and substitute the definitions of these new quantities in the covariance tensor.

We now want to find which point  $\mathbf{p}_c$  on fit-curve  $f$  is closest to sample  $\mathbf{x}_i$ , using the Mahalanobis metric. The situation is sketched in figure A.6. To facilitate the calculation we construct a local linearisation  $\mathbf{p}_f$  of fitfunction  $f$  around  $\mathbf{x}_i$ :

$$\mathbf{p}_f = \lambda \mathbf{r} + \mathbf{s} \quad (\text{A.20})$$

where  $\lambda$  is a real number,  $\mathbf{r}$  is a vector in the direction of the fitcurve, and  $\mathbf{s}$  is an arbitrary point on the linearised fitfunction. In  $\mathbf{p}_c$  measure  $r_m$  has a minimum value, and as a consequence its derivative with respect to  $\lambda$  is zero:

$$\frac{\partial r_m^2(\mathbf{p}_c, \mathbf{x}_i)}{\partial \lambda} = 0 \quad (\text{A.21})$$

Substitution of relations A.17 and A.20 into extremum-condition A.21 leads to the following expression for parameter  $\lambda$  in point  $\mathbf{p}_c$ :

$$\lambda(\mathbf{p}_c) = - \frac{\mathbf{r} \cdot \bar{\mathbf{C}}_{\mathbf{x}_i}^{-1} \cdot (\mathbf{s} - \mathbf{x}_i)}{\mathbf{r} \cdot \bar{\mathbf{C}}_{\mathbf{x}_i}^{-1} \cdot \mathbf{r}} \quad (\text{A.22})$$

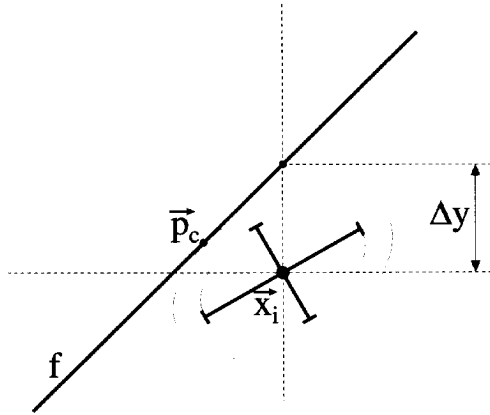


Figure A.6: The distance of a sample with covariance ellipse to a fitcurve

Support vector  $s$  can be any point on the (linearised) fitcurve. To make a link to standard weighted least squares regression methods (see relation A.16) we make the following particular choice:

$$\begin{pmatrix} s_x \\ s_y \end{pmatrix} = \begin{pmatrix} x_i \\ y_i + \Delta y \end{pmatrix} \quad (\text{A.23})$$

where  $\Delta y$  is the vertical distance between sample and fitcurve.

Directional vector  $r$  can be expressed in coordinates via:

$$\begin{pmatrix} r_x \\ r_y \end{pmatrix} = \frac{1}{\sqrt{1 + f_i'^2}} \begin{pmatrix} 1 \\ f_i' \end{pmatrix} \quad (\text{A.24})$$

where  $f_i'$  is the derivative of fitcurve  $f$  at sample  $x_i$ .

With relations A.22, A.23 and A.24 the Mahalanobis distance of measured sample  $x_i$  to fitcurve  $f$  becomes:

$$r_m^2(f, x_i) = \frac{(\Delta(y_i))^2}{(f_i' \sigma_{x,i})^2 + \sigma_{y,i}^2 - 2f_i' \sigma_{xy,i}} \quad (\text{A.25})$$

The expression linking uncertainties  $\sigma_{x,i}$  and  $\sigma_{y,i}$  and (reduced) covariance  $\sigma_{xy,i}$  to weights  $W_i$  in standard fitting routines thus becomes:

$$W_i = \frac{1}{(f_i' \sigma_{x,i})^2 + \sigma_{y,i}^2 - 2f_i' \sigma_{xy,i}}. \quad (\text{A.26})$$

Like with the uncorrelated samples, practical application of this relation in curve fitting routines is done iteratively, since the local derivatives  $f'$  of the function are not available. The denomin-



ator in relation A.26 can be seen as the compound variance  $\sigma^2$  in range quantity  $y$ :

$$\sigma_i^2 \equiv \left( f'_i \sigma_{x,i} \right)^2 + \sigma_{y,i}^2 - 2f'_i \sigma_{xy,i}. \quad (\text{A.27})$$

As an example consider a sample which is composed of individual probings which all lie on a locally linear part of the fitcurve. This can happen if one measures e.g. the response of an anemometer as a function of the pressure drop over the contraction of an instable windtunnel. Common sense says that we have managed to stay on the curve very accurately. We therefore expect a strong weight for this sample. However, both domain quantity  $x$  and range quantity  $y$  have measurement uncertainties associated with the random fluctuation along the fitcurve. In case we would still use relation A.16, then this sample would be given an unexpectedly low weight due to its inaccuracy, even though all composing elements of the sample could be found on the curve. With relation A.26 we see that this correlated variation along the fitcurve justifies a correction of the weight. By taking into account the covariance of the errors we give this sample a heavier weight.

The expression for  $\chi^2$ , which can be optimised with standard weighted least squares routines, is (combine relations A.1 and A.26):

$$\chi^2 \equiv \sum_i r_m^2(f, x_i) = \sum_i \frac{\left( \Delta(y_i) \right)^2}{\left( f'_i \sigma_{x,i} \right)^2 + \sigma_{y,i}^2 - 2f'_i \sigma_{xy,i}} \quad (\text{A.28})$$

The covariance ellipses in figure A.5 (supported by the raw samplings) make clear that the variance ellipses, which were used to construct the curve shown in figure A.3, have given a misleading impression of the character of the derivative of the fit-model. The covariance ellipses compel the fit function to leave the domain at the right hand side in upward direction, instead of in downward direction.

As a conclusion we can say that knowledge of the covariances associated with measured samples and their application in weighted least squares regression is essential for the analysis of measured data. Without this knowledge a discussion on the differences between findings of different scientists or between the results of different models is void, i.e. contradiction cannot be assessed. This means that without knowledge about accuracies all participants in a discussion about differences agree *á priori*.

## A.5 Tuning and quality of a class of fitcurves

In this section we will provide a means to distinguish between good models and bad models, and between good datasets and bad datasets. We will quantify the quality of a fit, give a procedure to detect and remove outliers, demonstrate how the best representative is selected of a class of models for a given dataset and show the importance of making residual plots.

### A.5.1 Quality of a single model

A measure for the success of a fitcurve is  $\chi^2_{\text{reduced}}$  defined as  $\chi^2$  divided by the number of degrees of freedom, i.e. the number of data-points  $N$  minus the number of fit-parameters  $\alpha_j$ ,  $J$ :

$$\chi^2_{\text{reduced}} \equiv \frac{\chi^2}{N - J} \quad (\text{A.29})$$

When external errors  $dx$  and  $dy$  are comparable with measurement accuracies  $\sigma_{x,i}$  and  $\sigma_{y,i}$  then  $\chi^2_{\text{reduced}}$  should be 1. If the fit is poor, then  $\chi^2_{\text{reduced}}$  is much larger than one; the theory represented by the curve makes no sense and one is asked to find a better theory. If the fit-curve overestimates the accuracy of the measurements then  $\chi^2_{\text{reduced}}$  is very small. In such a case the theory is sharper than the measurements and the question rises whether you can perform more accurate measurements? If this is not the case then a totally different type of curve will probably fit equally well.

The question is: Within which range do you accept  $\chi^2$ ? The probability  $q$  to have found a worse (higher) value for  $\chi^2$  is given in Numerical Recipes by (see Press et al. (1992)):

$$q = Q\left(\frac{N - J}{2}, \frac{\chi^2}{2}\right) \quad (\text{A.30})$$

where  $Q$  is the complementary incomplete gamma function. Generally acceptable values for  $q$  are found in the range  $q \in [0.1, 0.9]$ . Under "less-optimal" circumstances one accepts values within the range  $q \in [0.001, 0.999]$ .

### A.5.2 Detection of outliers: the Chauvenet criterion

It may happen that, due to an unknown cause, one or more of the samples deviate strongly from the trend suggested by the other samples. In such cases one can decide to reject those samples. To find such spurious data Chauvenet (1863), an astronomer in the 19-th century, has developed the following criterion: all samples with an individual contribution to  $\chi^2$  larger than a constant factor times  $\chi^2_{\text{reduced}}$  are suspect:

$$\left(\frac{\Delta y_i}{\sigma_i}\right)^2 > (1.42 + 0.301 * \ln(N - J - 4))^2 \chi^2_{\text{reduced}} \quad \text{where } N - J \geq 7 \quad (\text{A.31})$$

where  $N$  is the number of samples, and  $J$  the number of model parameters. Chauvenet based his analysis on the assumption that the samples are normally distributed. From relation A.31 we see that the tolerance of the Chauvenet criterion for deviations increases with the number of free parameters.

The Chauvenet criterion can be repeatedly applied to clean up sets of data. This criterion must be applied with great care to avoid the throwing away of correctly measured samples with relevant, even surprising, information.

### A.5.3 Tuning the number of model parameters

Parameter  $q$  does not point out whether a specific model is the best model for a certain dataset. Within a class of models (e.g. polynomials of arbitrary degree) one can calculate  $\chi^2_{\text{reduced}}$  for a range of models, which differ by the number of model parameters. When  $\chi^2_{\text{reduced}}$  drops substantially by increasing the number of model parameters by one, then the model of higher order is considered to be better than the model of lower order. This process of adding model parameters can be continued until  $\chi^2_{\text{reduced}}$  reaches a more or less constant value (as function of the number of model parameters).

### A.5.4 The importance of residual plots

After the just presented procedure of tuning a class of models to a dataset, one wants to see if the final model gives a good description of the data. The best way to see this is to look at a residual plot (see the right half of figure A.7), in which both the external errors of the samples are shown (the differences  $\Delta(y_i)$  between the data and the model) and the internal errors ( $\sigma_i$  in relation A.27). A model describes the data well when the residuals do not show a systematic behaviour in the residual plot. If the residuals of a tuned class of models are still systematic, then the class of models is inappropriate for description of the data. In such cases one has to develop a different class of models. If the residuals are random, then the value of  $q$  tells if the data is good or bad.

Today assessment of randomness of residuals is left to the eye. Study of the distribution function of the length of groups of neighbouring samples with the same sign of their residual can help to quantify (and hence make more objective) the process of judging models.

An example of a fit-model plus residual plot is presented in figure A.7, where the response is shown of a pressure transducer, when the pressure difference over the transducer (measured with a reference manometer) is first raised from zero to 140 Pascal, and then is lowered from 140 Pascal back to zero. A linear relation is used to model the calibration curve of the transducer. The value of  $\chi^2_{\text{reduced}}$  is 5, which is relatively high. Increasing the number of model parameters to 5 makes  $\chi^2_{\text{reduced}}$  drop to 4. Looking at the figure on the left, with just data and model, we get the impression that the linear model excellently matches the data. The high level of the plateau of  $\chi^2_{\text{reduced}}$  as function of the number of model parameters however suggests that something is wrong. The fit-curve does not reveal two important details of the calibration, which can only be seen from the residual plot:

- The transducer suffers from hysteresis: there is an upper path, associated with the part of the calibration in which the pressure was increased, and a lower path, connected with the response to decreasing pressure. The effect of hysteresis is significant: the half-height of the loop is larger than the internal errors in the samples. The direction of the hysteresis-loop tells if it is the reference manometer or the pressure transducer which has (the larger) hysteresis. The loop is clockwise, indicating that at a given (increasing) reference pressure the transducer indicated relatively low when compared with the calibration curve. This implies that the transducer is delayed compared to the reference manometer, and consequently to be blamed for the hysteresis.

- For pressure differences larger than 100 Pascal (28 A/D counts) the transducer has non-linear response: the residuals of samples on the right systematically increase.

The small gain in  $\chi^2_{\text{reduced}}$ , which is achieved by an increase of the number of model parameters to 5, is small when compared to the intrinsic inaccuracy of the transducer, which is introduced by hysteresis. We therefore have decided not to use non-linear models and accept the straight line as practical description of the transducer. The example makes clear the necessity of residual plots.

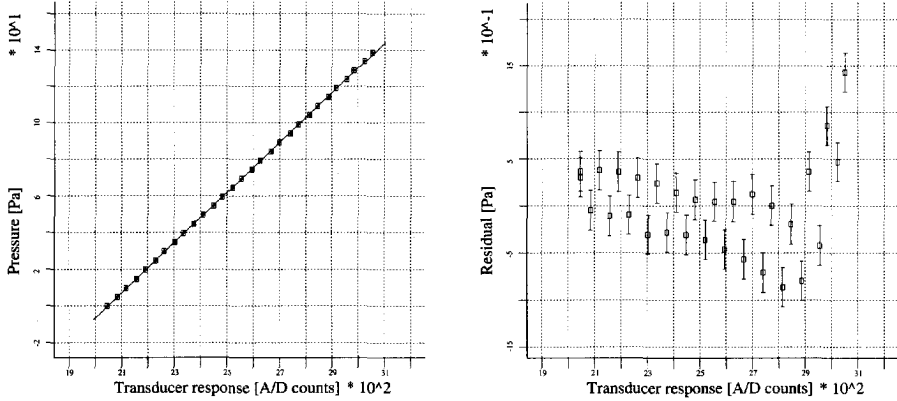


Figure A.7: Calibration curve of electronic pressure transducer.

When the range of the residuals takes several orders of magnitude (e.g. in the study of decay processes), it is common practice to plot the ratio of the residuals to the corresponding internal errors.

## A.6 Process of fitting

In literature (Press et al., 1992) many methods are provided for fitting relations to sampled data. In the current study two of these methods are used: fit by singular-value-decomposition for functions linear in the fit-parameters (SVD-fitting) and the Levenberg-Marquardt method for relations nonlinear in the fit-parameters. The former method, which is used in different forms in this research, will be outlined here. For an explanation of the latter method the reader is referred to e.g. Numerical Recipes (Press et al., 1992).

The assumption that the function to be found is a linear combination of base-functions  $p_j(x)$  (possibly nonlinear in their argument) means:

$$f(x) = \sum_{j=1}^J \alpha_j p_j(x) \quad (\text{A.32})$$

When  $\chi^2$  is optimal, then the derivative of  $\chi^2$  to the fit-parameters is zero. Differentiation of relation A.1 combined with relation A.32 yields:

$$\sum_{j=1}^J M_{ij} \alpha_j = \beta_i \quad (\text{A.33})$$

$$M_{ij} \equiv \sum_{k=1}^N W_k p_i(x_k) p_j(x_k) \quad (\text{A.34})$$

$$\beta_i \equiv \sum_{k=1}^N W_k p_i(x_k) y_k \quad (\text{A.35})$$

This defines a linear matrix equation. Matrix  $M_{ij}$  is called the *design matrix*. We see from relation A.34 that the design matrix is symmetric and consequently has real eigenvalues and orthogonal eigenvectors. Inversion of the matrix relation will provide coefficients  $\alpha_j$ . In this study routines from Numerical Recipes (Press et al., 1992) are used to find the singular value decomposition of matrix  $M$ . This means that the matrix is written as a product of three matrices:

$$M_{ij} = M_{il}^{(1)} \circ M_{lr}^{(2)} \circ M_{rj}^{(3)T} \quad (\text{A.36})$$

in which  $M_{il}^{(1)}$  is a  $J \times J$  column-orthonormal matrix,  $M_{lr}^{(2)}$  is a  $J \times J$  non-negative diagonal matrix and  $M_{rj}^{(3)T}$  the transpose of a column-orthonormal  $J \times J$  matrix.

After this decomposition has been made, a careful look is taken at the eigenvalues of design matrix  $M$ , which can be found in diagonal matrix  $M^{(2)}$ . Small eigenvalues belong to eigenvectors which do not contribute substantially to the problem. Inversion of the matrix problem can lead to a situation in which these unimportant eigenvectors will get large coefficients. This effect will push the coefficients of the important eigenvectors to less significant numbers. To prevent this from happening, all eigenvalues in  $M^{(2)}$  which are less than  $10^{-5}$  of the largest eigenvalue, are set to infinity, such that after inversion they do not contribute.

The inverse of the matrix equation is (summation over repeated indices is assumed):

$$\alpha_i = M_{ij}^{-1} \beta_j = M_{il}^{(3)} \circ \frac{1}{M_{lr}^{(2)}} \circ M_{rj}^{(1)T} \beta_j \quad (\text{A.37})$$

Estimates for the accuracies  $\sigma(\alpha_i)$  of fitcoefficients  $\alpha_i$  are found with:

$$\sigma^2(\alpha_i) = \sum_{j=1}^J \left[ \frac{M_{ij}^{(3)}}{M_{jj}^{(2)}} \right]^2 \quad (\text{A.38})$$



## Appendix B

# Time-ordered exponential for non-commuting tensor fields

### Introduction

In section 1.5 we were confronted with a differential equation, in which the time rate of change of a vector  $\omega(t)$  was linearly proportional to the vector itself via contraction with a second order tensor  $\bar{\bar{S}}(t)$ , which from now on will be called the *evolver*:

$$\frac{d}{dt}\omega(t) = \bar{\bar{S}}(t) \cdot \omega(t) \quad (\text{B.1})$$

In section 1.5 we proposed to solve this equation for  $\omega(t)$  with an evolution tensor  $\bar{\bar{A}}(t)$  as follows:

$$\omega(t) = \bar{\bar{A}}(t) \cdot \omega(0) \quad \Rightarrow \quad \frac{d}{dt}\bar{\bar{A}}(t) = \bar{\bar{S}}(t) \cdot \bar{\bar{A}}(t) \quad (\text{B.2})$$

For tensor fields  $\bar{\bar{S}}(t)$  with constant eigenvector directions we found the following expression for the evolution tensor:

$$\bar{\bar{A}}(t) = e^{\int_0^t \bar{\bar{S}}(\tau) d\tau} \quad (\text{B.3})$$

where the exponential of a tensor is defined via series expansion:

$$e^{\bar{\bar{x}}} \equiv \sum_{n=0}^{\infty} \frac{1}{n!} (\bar{\bar{x}})^n \equiv \bar{\bar{\delta}} + \bar{\bar{x}} + \frac{1}{2} \bar{\bar{x}} \cdot \bar{\bar{x}} + \frac{1}{6} \bar{\bar{x}} \cdot \bar{\bar{x}} \cdot \bar{\bar{x}} + \dots \quad (\text{B.4})$$

Without the restriction on the directions of the eigenvectors, the solution of equation B.2 for tensor  $\bar{\bar{A}}(t)$  is called the *time-ordered exponential* (TOE). In the coming analysis we will see the origin of this name.

In this appendix we will construct time-ordered exponential  $\bar{\bar{A}}(t)$  for the case when evolvers on different times do not commute. We will start to make a series expansion for the TOE, starting from small evolution times. The necessity for a method, which takes into account the non-Abelian (= non-commutative) structure of tensor fields, will then become apparent. The

exponential function for tensors, which plays a central role in the analysis, will be studied. A model for the TOE will be constructed using a series expansion with higher order terms representing higher order commutators of instantaneous evolvers  $\bar{\bar{S}}(t)$  and  $\bar{\bar{S}}$ -tensors integrated over time.

The method, which will be developed in this appendix, will be tested in a practical case: The resulting expression for the time ordered exponential will be calculated for circular cylinder flow, where the mean strain field acts as evolver, distorting fluctuating vorticity. Convergence of the series expansion of the TOE to the exact solution will be checked.

## B.1 Commutation problems

We will now make an integral formulation of the TOE as function of the evolver. To get to such a formulation, we first observe the expressions for  $\omega$  and for the TOE when a small time step  $dt$  is taken:

$$\omega(dt) = \bar{\bar{A}}(dt) \cdot \omega(0) \quad (\text{B.5})$$

$$\bar{\bar{A}}(dt) = \bar{\bar{\delta}} + \bar{\bar{S}}(0)dt \quad (\text{B.6})$$

An expression for the TOE for a macroscopic step is found by recursive use of relations B.5 and B.6 as follows (definition of the symbols is given below):

$$\bar{\bar{A}}(t) = P_0' (\bar{\bar{\delta}} + \bar{\bar{S}}(\tau)d\tau) \quad (\text{B.7})$$

$$= \bar{\bar{\delta}} + \int_0^t \bar{\bar{S}}(\tau)d\tau + \underbrace{\int_0^t \int_\tau^t \bar{\bar{S}}(\tau') \cdot \bar{\bar{S}}(\tau)d\tau'd\tau + \dots}_{\text{Term 3}} \quad (\text{B.8})$$

Symbol  $P_0'$  is the (left) product analogue of integration symbol  $\int_0^t$ . Its definition resembles the transition of a discrete summation usually written as  $\sum$  to a continuous summation, written as  $\int$ :

$$P_0' (\bar{\bar{\delta}} + \bar{\bar{S}}(\tau)d\tau) \equiv \lim_{\Delta t \rightarrow 0} \prod_{j=0}^{t/\Delta t} (\bar{\bar{\delta}} + \bar{\bar{S}}(j\Delta t)\Delta t) \quad (\text{B.9})$$

Symbol  $\prod$  is the conventional (left-) product symbol. The  $P_0'$ -symbol is cast by the author to compactly represent product integrals. The strict time-order of the tensors  $\bar{\bar{S}}$  in relation B.8 for the evolution tensor has led to the name **time-ordered exponential** for  $\bar{\bar{A}}(t)$  as function of tensor field  $\bar{\bar{S}}(t)$ .

In the analysis of the TOE we will use the following notation for integrals of tensor  $\bar{\bar{S}}(t)$  over time (integrals involving higher order commutators are defined in section B.5):

$$\bar{\bar{B}}^{(0)}(t) \equiv \int_0^t \bar{\bar{S}}(\tau)d\tau \quad (\text{B.10})$$

$$\bar{\bar{B}}^{(1)}(t) \equiv \int_0^t [\bar{\bar{S}}(\tau), \bar{\bar{B}}^{(0)}(\tau)]d\tau \quad (\text{B.11})$$



The brackets in the last equations denote the commutator of its arguments, and is defined by the following expression:

$$[\bar{x}, \bar{y}] \equiv \bar{x} \cdot \bar{y} - \bar{y} \cdot \bar{x} \quad (\text{B.12})$$

Note that  $\bar{B}^{(0)}(0) = 0$ . Quantity  $\bar{B}^{(0)}(t)$ , which is defined in relation B.10 as the integral over time of evolver tensor  $\bar{S}(t)$ , will be called the *average evolver* (from a reference time 0 to time  $t$ ).

We will now work out the third term in relation B.8 for the TOE and show that commutation problems cause deviations of this term from the corresponding term in the commuting solution for the TOE, which was given in relation B.3. For the third term we can write:

$$\begin{aligned} \text{Term 3} &= \int_0^t \left( \bar{B}^{(0)}(t) \cdot \bar{S}(\tau) - \bar{B}^{(0)}(\tau) \cdot \bar{S}(\tau) \right) d\tau \\ &= \bar{B}^{(0)2}(t) - \int_0^t \bar{B}^{(0)}(\tau) \cdot \bar{S}(\tau) d\tau \\ &= \frac{1}{2} \bar{B}^{(0)2}(t) + \frac{1}{2} \bar{B}^{(1)}(t) \end{aligned} \quad (\text{B.13})$$

The last equality in relation B.13 for Term 3 is a consequence of the following integral relation for average evolver  $\bar{B}^{(0)}$ :

$$\begin{aligned} \bar{B}^{(0)2}(t) &= \int_0^t \partial_{\tau'} \left( \bar{B}^{(0)2}(\tau') \right) \Big|_{\tau} d\tau \\ &= \int_0^t \left( \bar{B}^{(0)}(\tau) \cdot \bar{S}(\tau) + \bar{S}(\tau) \cdot \bar{B}^{(0)}(\tau) \right) d\tau \\ &= \int_0^t \left( 2\bar{B}^{(0)}(\tau) \cdot \bar{S}(\tau) + [\bar{S}(\tau), \bar{B}^{(0)}(\tau)] \right) d\tau \end{aligned} \quad (\text{B.14})$$

If relation B.3, the solution for commuting  $\bar{S}$ -fields, would be the correct solution for the TOE in non-commuting  $\bar{S}$ -fields, then a series expansion of the exponential in this expression would yield only powers of tensor  $\bar{B}^{(0)}$  (defined in relation B.10). The first two terms in relation B.8 for the series expansion of the TOE equal the first two terms in the Taylor-expansion of the exponential of the average evolver  $B^{(0)}$ . However, expression B.13 for the third term in the expansion of the TOE for con-commuting evolvers contains two terms: the first term being the second order term of the exponential of the average evolver, the second term in relation B.13 shows the *non-commuting deviation with which we are concerned in this appendix*.

We have now shown that relation B.3 does not correctly give the TOE for non-commuting evolvers. The deviation in the second order term of the series expansion of the exponential vanishes if the average  $\bar{S}$  from a reference time to a certain time  $t$  commutes with the instantaneous  $\bar{S}$ . Then the exponential of the average  $\bar{S}$  gives a correct solution of differential equation B.1 up to first order. Relation B.14 shows that when solving a tensor-differential-equation one has to take care handling the order of factors, i.e. take care of commutation.

For a general solution for the TOE more work needs to be done. Before we will continue constructing a solution for tensor  $\bar{A}(t)$  in non-commuting  $\bar{S}$ -fields, we will see in the following subsection that the determinant of this tensor can already be easily found.

## B.1.1 The determinant of the time-ordered exponential

Though the problem of finding the time-ordered exponential is an *essentially nonscalar* matter, one particular *scalar* property of it can already be calculated: its determinant. The analysis goes as follows:

The determinant of a product of matrices equals the product of the determinants of those matrices:

$$\begin{aligned}\text{Det}(\bar{\bar{\mathcal{A}}})(t) &= \text{Det} \left( P_0' (\bar{\bar{\delta}} + \bar{\bar{S}}(\tau) d\tau) \right) \\ &= P_0' \text{Det}(\bar{\bar{\delta}} + \bar{\bar{S}}(\tau) d\tau)\end{aligned}$$

Expansion of the determinant under the product integral into powers of  $d\tau$  and neglectation after first order contributions gives the following expression for the determinant of the TOE:

$$\begin{aligned}\text{Det}(\bar{\bar{\mathcal{A}}})(t) &= P_0' (1 + \text{Tr}(\bar{\bar{S}}(\tau)) d\tau) \\ &= e^{\int_0^t \text{Tr}(\bar{\bar{S}})(\tau) d\tau}\end{aligned}\tag{B.16}$$

where  $\text{Tr}(\bar{\bar{S}})(\tau)$  is the trace of tensor  $\bar{\bar{S}}$  at time  $\tau$ .

For traceless evolver fields the TOE has determinant 1.

## B.2 Analysis of the exponential function

Before we can write down the solution for the time-ordered exponential first some notations and lemmas have to be explained. (For further reading on exponential functions, one is referred to e.g. the lecture notes by Veldkamp (1985).) We will also demonstrate the error in the commuting solution, when one adopts this solution for non-commuting evolvers. The subtlety of this error will provide clues for a solution of the commutation problem.

### B.2.1 Mathematical lemmas

We introduce symbol  $\mathcal{L}_{\bar{\bar{B}}}$  for the operator, which does left-multiplication with tensor  $\bar{\bar{B}}^{(0)}$ . Correspondingly, we use notation  $\mathcal{R}_{\bar{\bar{B}}}$  for right-multiplication with  $\bar{\bar{B}}^{(0)}$ . We define adjugation operator  $\text{Ad}_{\bar{\bar{B}}}$  as their difference:

$$\text{Ad}_{\bar{\bar{B}}} \cdot \bar{\bar{x}} \equiv [\bar{\bar{x}}, \bar{\bar{B}}^{(0)}] = \bar{\bar{x}} \cdot \bar{\bar{B}}^{(0)} - \bar{\bar{B}}^{(0)} \cdot \bar{\bar{x}} = (\mathcal{R}_{\bar{\bar{B}}} - \mathcal{L}_{\bar{\bar{B}}}) \cdot \bar{\bar{x}}\tag{B.17}$$

Since operator  $\mathcal{R}_{\bar{\bar{B}}}$  commutes both with itself and with operator  $\mathcal{L}_{\bar{\bar{B}}}$ , it also commutes with operator  $\text{Ad}_{\bar{\bar{B}}}$ .

We now calculate the  $n$ -th power of left-multiplication with  $\bar{\bar{B}}^{(0)}$  using Newton's binomial:

$$\begin{aligned} (\mathcal{L}_{\bar{\bar{B}}})^n \cdot \bar{\bar{x}} &= \bar{\bar{B}}^{(0)n} \cdot \bar{\bar{x}} = (\mathcal{R}_{\bar{\bar{B}}} - \text{Ad}_{\bar{\bar{B}}})^n \cdot \bar{\bar{x}} \\ &= \sum_{j=0}^n (-1)^j \binom{n}{j} (\text{Ad}_{\bar{\bar{B}}})^j \bar{\bar{x}} \cdot \bar{\bar{B}}^{(0)n-j} \end{aligned} \quad (\text{B.18})$$

where the binomial coefficients are defined by the following relation:

$$\binom{n}{j} \equiv \frac{n!}{j!(n-j)!}. \quad (\text{B.19})$$

We know from relation B.18 how to change the order of a tensor and a power of another tensor. This relation will be very useful later in this subsection.

Another relation that will be useful is:

$$\sum_{r=l}^{l+m} \binom{r}{l} = \binom{l+m+1}{l+1} \quad (\text{B.20})$$

This relation can be proved by induction.

## B.2.2 Differentiating the commuting solution

We return to the exponential function. We have seen that the exponential of the average evolver is not the solution for the time-ordered exponential. In order to see the error arising when we use it as a solution we substitute the exponential of the average evolver into the left side of relation B.2 for the time-ordered exponential tensor:

$$\frac{d}{dt} e^{\bar{\bar{B}}^{(0)}(t)} = \sum_{j=1}^{\infty} \frac{1}{j!} \left( \bar{\bar{S}}(t) \cdot \bar{\bar{B}}^{(0)j-1}(t) + \bar{\bar{B}}^{(0)}(t) \cdot \bar{\bar{S}}(t) \cdot \bar{\bar{B}}^{(0)j-2}(t) + \dots + \bar{\bar{B}}^{(0)j-1}(t) \cdot \bar{\bar{S}}(t) \right) \quad (\text{B.21})$$

We use relation B.18 to shift all factors  $\bar{\bar{S}}(t)$  to the left. This leads us to the following expression for the time derivative of the commuting solution for the evolution tensor in a non-commuting situation:

$$\begin{aligned} \frac{d}{dt} e^{\bar{\bar{B}}^{(0)}(t)} &= \sum_{j=1}^{\infty} \frac{1}{j!} \left\{ \sum_{l=0}^{j-1} (-1)^l \binom{j-1}{l} (\text{Ad}_{\bar{\bar{B}}(t)})^l \cdot \bar{\bar{S}}(t) \cdot \bar{\bar{B}}^{(0)j-1-l}(t) \right. \\ &\quad + \sum_{l=0}^{j-2} (-1)^l \binom{j-2}{l} (\text{Ad}_{\bar{\bar{B}}(t)})^l \bar{\bar{S}}(t) \cdot \bar{\bar{B}}^{(0)j-1-l}(t) + \dots \\ &\quad \left. + \bar{\bar{S}}(t) \cdot \bar{\bar{B}}^{(0)j-1}(t) \right\} \end{aligned} \quad (\text{B.22})$$

We now substitute  $m \equiv j - l - 1$  into the last relation. This gives us:

$$\frac{d}{dt} e^{\bar{\bar{B}}^{(0)}(t)} = \sum_{j=1}^{\infty} \sum_{l+m=j-1} \left[ \frac{1}{j!} \sum_{r=l}^{l+m} \binom{r}{l} \right] (-1)^l (\text{Ad}_{\bar{\bar{B}}(t)})^l \bar{\bar{S}}(t) \cdot \bar{\bar{B}}^{(0)m}(t) \quad (\text{B.23})$$

With help of relation B.20 for binomial coefficients, we can find the following relation for the time derivative of the commuting solution for the evolution tensor:

$$\begin{aligned}
 \frac{d}{dt} e^{\bar{\bar{B}}^{(0)}(t)} &= \sum_{j=1}^{\infty} \sum_{l+m=j-1} \frac{1}{(l+1)!m!} (-1)^l (\text{Ad}_{\bar{\bar{B}}(t)})^l \bar{\bar{S}}(t) \cdot \bar{\bar{B}}^{(0)m}(t) \\
 &= \left( \sum_{l=0}^{\infty} \frac{(-1)^l}{(l+1)!} (\text{Ad}_{\bar{\bar{B}}(t)})^l \bar{\bar{S}}(t) \right) \left( \sum_{m=0}^{\infty} \frac{1}{m!} \bar{\bar{B}}^{(0)m}(t) \right) \\
 &= \left( \sum_{l=0}^{\infty} \frac{(-1)^l}{(l+1)!} (\text{Ad}_{\bar{\bar{B}}(t)})^l \bar{\bar{S}}(t) \right) e^{\bar{\bar{B}}^{(0)}(t)}
 \end{aligned} \tag{B.24}$$

Note that if at a time the instantaneous evolver commutes with the average evolver up to that time, then relation (B.24) shows that the exponential of the average evolver provides the correct solution for  $\bar{\bar{A}}(t)$  since then the operator in the braces reduces to the unity operator. Relation B.24 will be the basis of the solution for  $\bar{\bar{A}}(t)$ , which will be constructed in the following section.

### B.3 Solving the time-ordered exponential

Expression (B.24) gives a series of terms for the time-derivative of the commuting solution for the evolution tensor. Higher order terms contain higher order commutators. We see from this relation that the integrand in the exponent returns in the series as the first coefficient. It is natural to ask whether it could be possible to construct a slightly more intricate function in the exponent, such that the second term in the series, the one with the first order commutator, cancels out.

We try the following expression for the time-ordered exponential:

$$\bar{\bar{A}}(t) = e^{\bar{\bar{B}}^{(0)}(t) + c_1 \bar{\bar{B}}^{(1)}(t) + \dots} \tag{B.25}$$

and determine coefficient  $c_1$  by substitution of the proposed evolution tensor into relation B.2:

$$\begin{aligned}
 \left( \frac{d}{dt} \bar{\bar{A}}(t) \right) \cdot (\bar{\bar{A}}^{-1}(t)) &= \bar{\bar{S}} + c_1 [\bar{\bar{S}}, \bar{\bar{B}}^{(0)}] + \dots \\
 &\quad - \frac{1}{2} [\bar{\bar{S}} + c_1 [\bar{\bar{S}}, \bar{\bar{B}}^{(0)}] + \dots, \bar{\bar{B}}^{(0)} + c_1 \bar{\bar{B}}^{(1)} + \dots] + \dots \\
 &= \bar{\bar{S}} + c_1 [\bar{\bar{S}}, \bar{\bar{B}}^{(0)}] - \frac{1}{2} [\bar{\bar{S}}, \bar{\bar{B}}^{(0)}] + \text{higher order commutators.}
 \end{aligned} \tag{B.26}$$

It is clear that the choice  $c_1 = \frac{1}{2}$  gives a solution for  $\bar{\bar{A}}$  that satisfies relation B.2 for the TOE up to first order commutation of the instantaneous evolver with the average evolver. In exactly the same manner we can try to gain one more order of commutators. We propose the following functional form for the evolution tensor (see section B.5 for definitions of the integrals):

$$\bar{\bar{A}}(t) = e^{(\bar{\bar{B}}^{(0)} + \frac{1}{2} \bar{\bar{B}}^{(1)} + c_2 \bar{\bar{B}}_1^{(2)} + c_3 \bar{\bar{B}}_2^{(2)} + \dots)(t)} \tag{B.27}$$

and determine  $c_2, c_3$ :

$$\begin{aligned} \left(\frac{d}{dt}\bar{\bar{\mathcal{A}}}(t)\right) \cdot (\bar{\bar{\mathcal{A}}}^{-1}(t)) = & \bar{\bar{S}} + \frac{1}{2}[\bar{\bar{S}}, \bar{\bar{B}}^{(0)}] + c_2[\bar{\bar{S}}, \bar{\bar{B}}^{(1)}] + c_3[[\bar{\bar{S}}, \bar{\bar{B}}^{(0)}], \bar{\bar{B}}^{(0)}] + \dots \\ & - \frac{1}{2}[\bar{\bar{S}}, \bar{\bar{B}}^{(0)}] - \frac{1}{4}[\bar{\bar{S}}, \bar{\bar{B}}^{(1)}] - \frac{1}{4}[[\bar{\bar{S}}, \bar{\bar{B}}^{(0)}], \bar{\bar{B}}^{(0)}] + \dots \\ & + \frac{1}{6}[[\bar{\bar{S}}, \bar{\bar{B}}^{(0)}], \bar{\bar{B}}^{(0)}] + \dots + \text{higher order commutators} \end{aligned} \quad (\text{B.28})$$

Now choose  $c_2 = \frac{1}{4}$  and  $c_3 = \frac{1}{12}$  and we have:

$$\bar{\bar{\mathcal{A}}}(t) = e^{(\bar{\bar{B}}^{(0)} + \frac{1}{2}\bar{\bar{B}}^{(1)} + \frac{1}{4}\bar{\bar{B}}_1^{(2)} + \frac{1}{12}\bar{\bar{B}}_2^{(2)} + \dots)(t)} \quad (\text{B.29})$$

which is up to second order commutators the solution to relation B.2. The third order solution for the time-ordered exponential is:

$$\begin{aligned} \bar{\bar{\mathcal{A}}}(t) = & \exp(\bar{\bar{B}}^{(0)} + \frac{1}{2}\bar{\bar{B}}^{(1)} + \frac{1}{4}\bar{\bar{B}}_1^{(2)} + \frac{1}{12}\bar{\bar{B}}_2^{(2)} + \frac{1}{8}\bar{\bar{B}}_1^{(3)} \\ & + \frac{1}{24}\bar{\bar{B}}_2^{(3)} + \frac{1}{24}\bar{\bar{B}}_3^{(3)} + \frac{1}{24}\bar{\bar{B}}_4^{(3)} + 0\bar{\bar{B}}_5^{(3)} + \dots)(t) \end{aligned} \quad (\text{B.30})$$

Though it is a matter of algebra we have not found a general formula to determine the coefficients for arbitrary order commutators.

## B.4 An application of the commutator method: circular cylinder flow

In section 1.4 we saw that, under rapid distortion assumptions, the mean strain acts as evolver on the fluctuating vorticity. To see if the commutator expansion for the time-ordered exponential gives a useful tool in the study of vorticity distortion, we apply the method to vortical cylinder flow.

The closer one gets to a cylinder, the more strain will change from place to place, and therefore instantaneous strain will have more chance not to commute with its average. Therefore the use of the commutator method to estimate integrated strain tensors over trajectories will be clear in situations where the background strain does not change much or abruptly over the region to be examined. It is expected that for flow in the neighbourhood of bluff bodies the first few terms in the exponent of the expression for the evolution tensor are sufficient for a fair estimate in a reasonably large region.

We assume the flow to be incompressible. Consequently, the strain tensor is traceless, and, as we have seen, the time-ordered exponential has trace 1. This characteristic, that the determinant of the evolution tensor equals 1, could also have been seen from a comparison of the behaviour of vorticity  $\Omega$  and material line elements  $d\mathbf{l}$  (see e.g. Batchelor (1967, formula 5.3.4)):

$$\frac{\Omega(t)}{|\Omega(0)|} = \frac{d\mathbf{l}(t)}{|d\mathbf{l}(0)|} \quad (\text{B.31})$$

For incompressible flow material elements do not change their volume and thus the distortion tensor of material elements has determinant equal to 1. From relation B.31 for the equivalence of line-elements and vorticity we see that the same reasoning must apply to vorticity.

To compare the estimates generated with the different models, a matrix-norm is introduced:

$$||A||^2 \equiv \sum_{i,j} A_{ij}^2 \quad (\text{B.32})$$

This norm is used to define truncation error  $R(n)$  in the  $n$ -th order commutator approximation of the distortion matrix  $\bar{\mathcal{A}}^{(n)}$ :

$$R(n) \equiv \frac{||\bar{\mathcal{A}} - \bar{\mathcal{A}}^{(n)}||}{||\bar{\mathcal{A}}||} \quad (\text{B.33})$$

Relation B.30 is now used to estimate the vorticity evolution matrix for flow around a circular cylinder (radius  $a$ ). For the mean flow a potential flow has been taken (going to  $U_\infty$  far from the cylinder).

The distortion matrix is estimated using commutator approximation B.30 from zeroth order up to third order commutators. A set of trajectories is followed from starting points, which lie one cylinder diameter upstream the cylinder centre and at a distance  $y_0$  away from the stagnation line. "Impact parameter"  $y_0/a$  is taken in the range from 0 to 2.5. Trajectories are followed during a time  $3a/U_\infty$ . Along every trajectory the largest value of  $R(n)$  is recorded and plotted in figure (B.1). We see from figure B.1 that for trajectories with an impact parameter larger

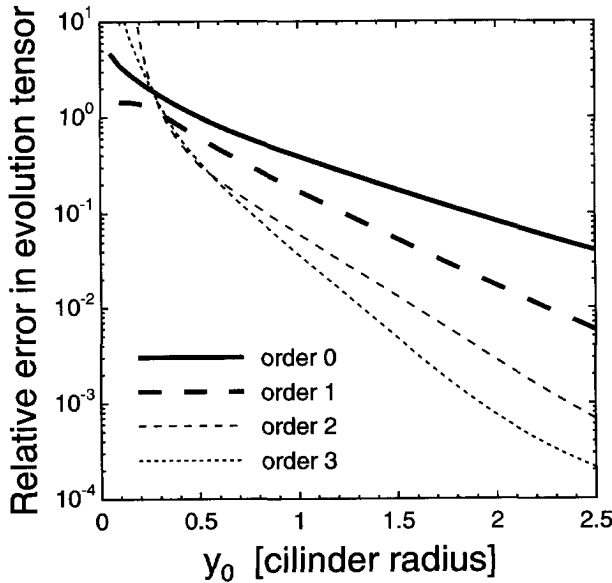


Figure B.1: Estimation error in different orders of commutator expansions for the vorticity evolution tensor in circular cylinder flow as function of the impact parameter

than 0.5, a higher order commutator approximation ensures better approximation of the vorticity distortion matrix along all of the trajectory. Close to the stagnation line the lower order approximations give a very poor result. It is not surprising that the largest errors are found close to the body: strain varies strongest from position to position along trajectories close to the body. An error of ten percent is made by the zeroth order expansion at impact  $y_0/a \sim 2$  whereas a third order expansion reaches the same level of confidence at  $y_0/a \sim 0.7$ . Therefore, for a fixed confidence level we can divide the flow domain into subdomains that need an increasing order expansion the closer they are to the stagnation line. Close to both the stagnation line and to the rear side of the cylinder it becomes more difficult for the commutator expansion to converge to the exact calculation. For all expansions the error decreases exponentially with the impact parameter. Exponents increase with the order of the expansions.

For a complete view of what happens near a cylinder (or any other obstacle) one more problem must be considered: the region close to the stagnation line cannot be examined using the theory set out in this text since in this slow region the Rapid Distortion assumption, formulated in relation 1.33, is violated and consequently cannot be assumed.

## Conclusions

We have found a way to estimate the time-ordered exponential for non-commuting evolvers. It is based on the exponential of a series of tensors; higher order terms in the series are higher order commutators of instantaneous evolvers and average evolvers. No general expression has been found yet for the coefficients in this series, though the algorithm allows to find coefficients for any order of approximation.

Application of a third order expansion of this series to weak vortical flow past a circular cylinder showed that the truncation error of the commutator expansion decreases exponentially with the impact parameter (distance of starting point of trajectories to the stagnation line measured in cylinder radius). Furthermore, it has been shown that, for impact parameters larger than 0.3, higher order commutator models converge faster to the exact solution for the evolution tensor than lower order commutator models. (The region close to both the body and the stagnation line does not satisfy RDT-conditions. Therefore this regime needs attention in the future.)

Future analytic work will have to provide a convergence criterion enabling one to calculate when the "small terms" in the expansion of the time-ordered exponential are really small.

A three dimensional application is worth examining since in three dimensions the consequences of the non-Abelian nature of tensor multiplication can give rise to a different convergence of the commutator expansion than in two dimensional cases.

## B.5 Definitions of commutator integrals

The commutator integrals used in this appendix are defined as follows:

$$\bar{\bar{B}}^{(0)}(t) \equiv \int_0^t \bar{\bar{S}}(\tau) d\tau \quad (\text{B.34})$$

$$\bar{\bar{B}}^{(1)}(t) \equiv \int_0^t [\bar{\bar{S}}(\tau), \bar{\bar{B}}^{(0)}(\tau)] d\tau \quad (\text{B.35})$$

$$\bar{\bar{B}}_1^{(2)}(t) \equiv \int_0^t [\bar{\bar{S}}(\tau), \bar{\bar{B}}^{(1)}(\tau)] d\tau \quad (\text{B.36})$$

$$\bar{\bar{B}}_2^{(2)}(t) \equiv \int_0^t [[\bar{\bar{S}}(\tau), \bar{\bar{B}}^{(0)}(\tau)], \bar{\bar{B}}^{(0)}(\tau)] d\tau \quad (\text{B.37})$$

$$\bar{\bar{B}}_1^{(3)}(t) \equiv \int_0^t [\bar{\bar{S}}(\tau), \bar{\bar{B}}_1^{(2)}(\tau)] d\tau \quad (\text{B.38})$$

$$\bar{\bar{B}}_2^{(3)}(t) \equiv \int_0^t [\bar{\bar{S}}(\tau), \bar{\bar{B}}_2^{(2)}(\tau)] d\tau \quad (\text{B.39})$$

$$\bar{\bar{B}}_3^{(3)}(t) \equiv \int_0^t [[\bar{\bar{S}}(\tau), \bar{\bar{B}}^{(0)}(\tau)], \bar{\bar{B}}^{(1)}(\tau)] d\tau \quad (\text{B.40})$$

$$\bar{\bar{B}}_4^{(3)}(t) \equiv \int_0^t [[\bar{\bar{S}}(\tau), \bar{\bar{B}}^{(1)}(\tau)], \bar{\bar{B}}^{(0)}(\tau)] d\tau \quad (\text{B.41})$$

$$\bar{\bar{B}}_5^{(3)}(t) \equiv \int_0^t [[[ \bar{\bar{S}}(\tau), \bar{\bar{B}}^{(0)}(\tau) ], \bar{\bar{B}}^{(0)}(\tau) ], \bar{\bar{B}}^{(0)}(\tau)] d\tau \quad (\text{B.42})$$



# Appendix C

## Characterisation of anisotropy

### Introduction

Reynoldsstress-tensor  $R_{ij} \equiv \overline{u'_i u'_j}$  is symmetric. Hence it has orthogonal eigenvectors with real eigenvalues. The three eigenvalues are the turbulent energies associated with turbulent motions in the direction of the respective (orthogonal) eigenvectors.

The aim of this section is to develop a mathematical means to characterise the anisotropy of  $R_{ij}$ . The Lumley-triangle (Lumley, 1978) will be introduced and modified such that departures from an isotropic energy distribution, which are taken to be linear in the energy space (squared velocity space), are associated with linear displacements in the modified Lumley-triangle. Furthermore we will introduce the "character plot", in which the elongation of the fluctuations in the flow are shown, together with the deviation of the character from axisymmetry.

### C.1 Invariants

A tensor is called invariant when its components are unaltered under orthonormal transformations of coordinates. Scalars are zeroth order tensors and by definition invariant. Eigenvalues are invariants. When the solutions of the secular equation for the eigenvalues are invariants, then the coefficients in this secular equation must be invariants either. According to the Cayley-Hamilton theorem (Lumley, 1978) every  $3 \otimes 3$ -tensor  $T$  (with eigenvalues  $(\lambda_1, \lambda_2, \lambda_3)$ ) satisfies its own secular equation and the coefficients in this equation are linearly independent invariants:

$$T_{ik}T_{kl}T_{lj} - IT_{ik}T_{kj} + IIT_{ij} - IIIT_{ij}^0 = 0 \quad (\text{C.1})$$

where  $T_{ij}^0 = \delta_{ij}$  is the Kronecker delta, and where  $I$ ,  $II$  and  $III$  are the invariants of  $T$ . They are related to  $T$  by:

$$I = T_{ii} \equiv \text{Trace}(T) \quad (\text{C.2})$$

$$II = -\frac{1}{2}T_{ij}T_{ji} \quad (\text{C.3})$$

$$III = \frac{1}{3}T_{ij}T_{jk}T_{ki} \quad (\text{C.4})$$

## C.2 Invariants of the Reynoldsstress-tensor

According to relation C.1 Reynoldsstress-tensor  $R$  has three independent invariants. We will use these invariants to construct three mutually independent invariants which can be used to characterise anisotropy.

The first invariant, the trace of the Reynoldsstress-tensor, gives twice the total turbulent energy  $q^2$ :

$$I = 2q^2 \equiv \lambda_1 + \lambda_2 + \lambda_3 \quad (\text{C.5})$$

Normalisation of  $R_{ij}$  with  $2q^2$  allows for comparison of different experiments. We define the normalised Reynoldsstress-tensor  $r_{ij}$  (with trace 1):

$$r_{ij} \equiv \frac{R_{ij}}{2q^2} \quad (\text{C.6})$$

We now split normalised Reynoldsstress-tensor  $r_{ij}$  into an isotropic energy distribution and a normalised anisotropy-tensor  $b_{ij}$ . The latter term redistributes the energy introduced by the isotropic part over the eigenvectors of  $R$ . The constraint we impose on this splitting is that it must conserve the tensor's trace, which represents total energy. We therefore reject multiplicative decomposition, known from linear mapping theory, and adopt additive decomposition:

$$r_{ij} = \frac{1}{3}\delta_{ij} + b_{ij} \quad (\text{C.7})$$

$$b_{ij} \equiv r_{ij} - \frac{1}{3}\delta_{ij} \quad (\text{C.8})$$

Tensor  $b$  has zero trace and is symmetric.

The invariants of  $R$  are now mapped on a dependent set of invariants as follows:

$$(I(R), II(R), III(R)) \rightarrow (I(R), II(b), III(b)) \quad (\text{C.9})$$

These three invariants characterise the distribution of turbulent energy over three axes.  $I(R)$  gives the total energy,  $II(b)$  and  $III(b)$  are different measures for departure from isotropy. The meaning of  $II(b)$  and  $III(b)$  will be clarified in the following section.

### C.3 The original Lumley-triangle

Invariants  $II(b)$  and  $III(b)$  determine how turbulent energy is distributed over three orthogonal directions (regardless of these directions!). Since 2D-plots are easy to make and give immediate visual insight, Lumley (1978) proposed to plot these invariants as follows:  $III(b)$  is put horizontally and  $-II(b)$  is put vertically.

Not every point in this plot can be associated with a realizable Reynoldsstress-tensor. Cauchy-Schwarz-inequalities hold for the off-diagonal elements in  $R$ . These realisability-inequalities exclude all points in the  $(III(b), -II(b))$ -diagram outside three bounding curves from possible association with a Reynoldsstress-tensor. Without derivation we give these bounding curves:

$$F \equiv \frac{1}{9} + 3III + II = 0 \tag{C.10}$$

$$-II = G(III) \equiv \sqrt{3} \left( \frac{|III|}{2} \right)^{2/3} \tag{C.11}$$

The resulting diagram is shown in figure C.1a. The origin in the Lumley-triangle represents

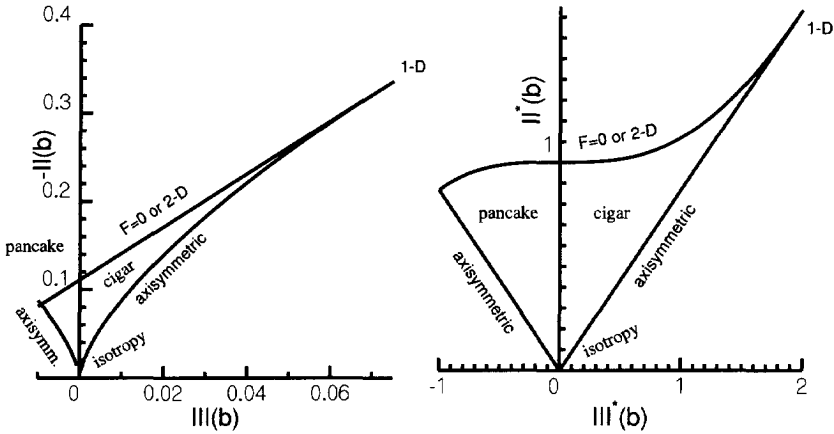


Figure C.1: a: Original Lumley diagram

b: modified Lumley-diagram

isotropy. The two curves leaving the origin mark axisymmetric turbulence. The curve  $F = 0$  marks two-dimensional turbulence. The quantity  $III(b)$  can now be interpreted as the elongation of the energy distribution: from left to right in the diagram the energy distribution goes from "pancake-turbulence" to "cigar-turbulence". Vertical quantity  $-II(b)$  can be seen as the "mutual disagreement" among the three energies: the vertical line through the origin goes from isotropic turbulence (with energy distribution 1 : 1 : 1) to a turbulent state with energy distribution 0 : 1 : 2.

### C.4 Modified Lumley-triangle and character plot

Consider an experiment in which initially isotropic turbulence is either linearly squeezed or linearly stretched along an axis. The normalised Reynoldsstresstensor associated with this tur-

bulent flow, given in eigenvector coordinates, is:

$$r_{ij}(\epsilon) = \begin{pmatrix} \frac{1}{3}(1+\epsilon) & & \\ & \frac{1}{3}(1-\frac{1}{2}\epsilon) & \\ & & \frac{1}{3}(1-\frac{1}{2}\epsilon) \end{pmatrix} \quad (\text{C.12})$$

Linear stretch parameter  $\epsilon$  can range from -1 to 2, given the fact that all diagonal components  $r_{\alpha\alpha}$  must be nonnegative.

The place in the Lumley-diagram of this flow is ( $III = \frac{1}{108}\epsilon^3$ ,  $-II = \frac{1}{12}\epsilon^2$ ). We see that though the turbulent flow is stretched linearly, departure from isotropy in the Lumley-triangle is a second-order effect! As a consequence the diagram will classify many highly anisotropic flows as fairly isotropic ones. This is an unwanted feature of the Lumley-triangle. To make the Lumley triangle into a diagram from which we can read the character of the anisotropy (e.g. the linear stretch parameter of the suggested experiment), we have to linearise it. To linearise the Lumley-diagram we propose the following modification:

$$(III, -II) \rightarrow (6\sqrt{\frac{III}{2}}, 3\sqrt{-II}) \equiv (III^*, II^*) \quad (\text{C.13})$$

The modified Lumley-triangle is shown in figure C.1b. The invariants in the rescaled Lumley-diagram give a linear measure for the anisotropy of a turbulent flow. The boundaries of the rescaled Lumley-diagram are found by substitution of relation C.13 for the rescaled invariants into relations C.10 and C.11 for the boundaries of the original Lumley-diagram:

$$II^* = F^*(III^*) \equiv \sqrt{1 + \frac{1}{4}III^{*3}} \quad \text{2D} \quad (\text{C.14})$$

$$II^* = G^*(III^*) \equiv \frac{1}{2}\sqrt{3}|III^*| \quad \text{axisymmetry} \quad (\text{C.15})$$

To be able to discriminate between flow characters, which have "more" or "less" resemblance with axisymmetric turbulence, we define the "fourth invariant" (indicated with symbol  $IV^*$ ), which is dependent on the second and third invariants via the following relation:

$$IV^* \equiv \frac{II^* - G^*(II^*)}{F^*(III^*) - G^*(II^*)} \quad (\text{C.16})$$

The fourth invariant can take values between 0 and 1, where  $IV^* = 0$  corresponds with axisymmetry, and where  $IV^* = 1$  characterises 2D-flow.

When elongation and deviation from axisymmetry are important measures, then one can use a rescaled Lumley-diagram defined by the relation:

$$(III, -II) \rightarrow (III^*, IV^*) \quad (\text{C.17})$$

This diagram (see figure C.2), which we will call a "**character plot**" to distinguish it from the rescaled Lumley diagram, has rectangular bounding curves. For extreme values of the rescaled third invariant ( $III^*$  close to either -1 or to 2) the fourth invariant is degenerate. This will in practice give a large error-bar for estimates of  $IV^*$  in the far left and far right ends of the character plot. The degeneracy makes clear that, apart from the rescaled third invariant, the anisotropy of the flow has no interesting other independent invariant: the subtle difference

between a round shoestring (axisymmetric, nearly 1D turbulence) and a flat shoestring (2D turbulence with major preference for fluctuations in one of the two directions) is both hard to tell and of little interest.

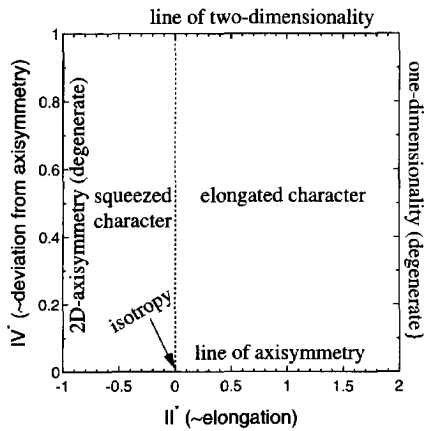


Figure C.2: Boundaries of a character plot



# Appendix D

## Betz-manometer and air-density

### Introduction

In this appendix we give the relations that have been used to translate pressure differences measured using a Betz-manometer in millimetres watercolumn, into Pascals. Furthermore we give the relation which has been used to establish the density of air, which is necessary in the application of Bernoulli's law to find air-flow velocity from a pressure difference.

### D.1 Calibration of a Betz-manometer

The density of water  $\rho_{H_2O}$  in  $\text{kg/m}^3$  as function of temperature  $T$  is given by Smith and Ness (1984):

$$\rho_{H_2O}(T[^\circ\text{C}]) = 999.931 + 5.010 \cdot 10^{-2} T - 7.441 \cdot 10^{-3} T^2 + 3.48 \cdot 10^{-5} T^3 \quad (\text{D.1})$$

In this relation the dissolved air in water is neglected.

Relation D.1 can be used to translate pressure in millimetres water column into Pascals:

$$p[\text{Pa}] = p[\text{mm water}] g \rho_{H_2O}(T) \quad (\text{D.2})$$

where  $g = 9.81\text{m/s}$  is gravity acceleration (Jansen, 1977).

### D.2 Density of wet air

Bernoulli's law 1.20 can be used to interpret pressure difference  $\Delta p$  between a points in the flow and a stagnation point in terms of air velocity  $u$ . Pressure  $\Delta p$  can be the difference  $p_t - p_s$  between total pressure  $p_t$  observed at the head of a pitot/static-tube (stagnation point) and the static pressure  $p_s$  observed at holes in the side of the tube, see figure D.1). In a different situation  $\Delta p$  can be the difference in pressure between a wind tunnel's settling chamber (where

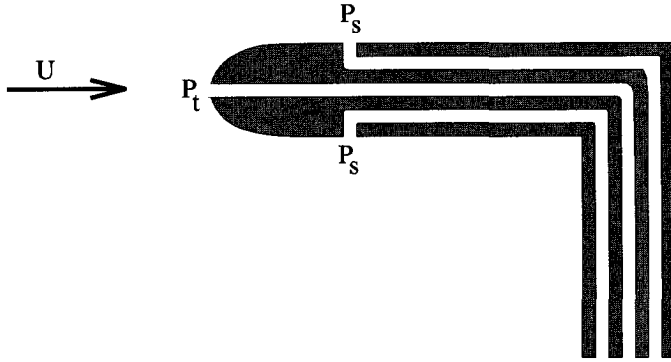


Figure D.1: Definition of pressures at pitot/static-tube

the velocity is negligible) and its contraction. Let us take

$$\Delta p = \frac{1}{2} \rho_{\text{wet air}} u^2 \quad (\text{D.3})$$

To compute  $u$  from this relation we need to know  $\rho_{\text{wet air}}$ . We calculate the density of wet air  $\rho_{\text{wet air}}$  [ $\text{kg/m}^3$ ] as function of temperature  $T$ , atmospheric pressure  $p_{\text{atm}}$  and relative humidity RH.

First we transform  $p_{\text{atm}}$  [mm Hg] to  $p_{\text{atm}}$  [Pa] by application of (Jansen, 1977):

$$760 \text{ mm Hg} = 1.01325 \cdot 10^5 \text{ Pa} \quad (\text{D.4})$$

Next we use the relation for an ideal gas:

$$p = \frac{\rho R T}{m} \quad (\text{D.5})$$

where  $R = 8.3144 \cdot 10^3 \text{ J kmol}^{-1} \text{ K}^{-1}$  is Boltzman's universal gas constant (Jansen, 1977) and where  $m$  is the molecular weight of the gas.  $T$  is absolute temperature. According to Dalton's rule moisture-free air plus water vapour coexist independently and total pressure  $p_{\text{atm}}$  is the sum of both fractional pressures  $p_{\text{dry components}}$  and  $p_{\text{water}}$ :

$$p_{\text{atm}} = p_{\text{dry components}} + p_{\text{water}} \quad (\text{D.6})$$

Application of relation D.5 to the two gasses gives:

$$\rho_{\text{wet air}}(T) = \rho_{\text{dry air}}(T) + \rho_{\text{water vapour}}(T) \quad (\text{D.7})$$

$$= \frac{p_{\text{dry components}} m_{\text{dry components}}}{RT} + \frac{p_{\text{water}} m_{\text{water}}}{RT} \quad (\text{D.8})$$

In this relation  $m$  indicates respective molecular weights ( $m_{\text{dry components}} = 28.964 \text{ kg/kmol}$  and  $m_{\text{water}} = 18.02 \text{ kg/kmol}$ ).  $T$  is measured in  $K$ .



Relative humidity is defined as the ratio of the fractional water vapour pressure relative to its saturation pressure at that temperature, measured in percent:

$$\text{RH} \equiv \frac{p_{\text{water}}}{p_{\text{water,sat}}} \cdot 100 \Rightarrow p_{\text{water}} = \frac{\text{RH}}{100} \cdot p_{\text{water,sat}} \quad (\text{D.9})$$

saturation pressure  $p_{\text{water,sat}}$  [Pa] of water in air can be determined via (Janssen and Warmoeskerken, 1987):

$$p_{\text{water,sat}}(T[^\circ\text{C}]) = 611.4 + 43.74 T + 1.554 T^2 + 1.79 \cdot 10^{-2} T^3 + 5.39 \cdot 10^{-4} T^4 \quad (\text{D.10})$$

Combination of relations D.8, D.9 and D.6 gives:

$$\rho_{\text{wet air}}(T) = \frac{p_{\text{atm}} m_{\text{dry components}}}{RT} - \frac{\text{RH}}{100} p_{\text{water,sat}} \frac{m_{\text{dry components}} - m_{\text{water}}}{RT} \quad (\text{D.11})$$

Define  $\rho_{\text{dry}}$  as the density which the air would have had at the same pressure and temperature provided that it were dry. Keep in mind that  $\rho_{\text{dry}}$  is a purely imaginative quantity, not related to any real density.

$$\rho_{\text{dry}}(T) \equiv \frac{p_{\text{atm}} m_{\text{dry components}}}{RT} \quad (\text{D.12})$$

With this definition we can rewrite relation D.11 to:

$$\begin{aligned} \rho_{\text{wet air}}(T) &= \rho_{\text{dry}}(T) \left( 1 - \frac{\text{RH}}{100} \frac{p_{\text{sat}}}{p_{\text{atm}}} \left( 1 - \frac{m_{\text{water}}}{m_{\text{dry components}}} \right) \right) \\ &= \rho_{\text{dry}}(T) \left( 1 - 0.378 \frac{\text{RH}}{100} \frac{p_{\text{sat}}}{p_{\text{atm}}} \right) \end{aligned} \quad (\text{D.13})$$

This relation gives the density of wet air.



# Appendix E

## Correction of hot-wire data for ambient temperature drift

### Introduction

In section 6.3 we have derived two relations (6.14) and (6.15) that enable us to reduce measured hot-wire signals to the situation in which the fluid has a reference temperature  $T_{\text{ref}}$ :

$$E_{\text{out}}(T_{\text{ref}}) = E_{\text{out}}(T) \sqrt{\frac{T_{\text{hot}} - T_{\text{ref}}}{T_{\text{hot}} - T}} \quad (\text{E.1})$$

$$= E_{\text{out}}(T) \sqrt{\frac{R(T_{\text{hot}}) - R(T_{\text{ref}})}{R(T_{\text{hot}}) - R(T)}} \quad (\text{E.2})$$

In this appendix we will examine the applicability of both methods, which we will call the temperature-method and the resistance-method respectively. In the first section some problems concerning the temperature method are pointed out. Then the temperature method is tested in an experiment. After this will have been done, relations are calculated for practical application of the resistance method. These relations are also tested in an experiment. Finally in a general discussion on ambient temperature correction of hot-wire response a recommendation will be made of which correction method is to be preferred in practice.

### E.1 Application of the temperature method

In this section we will discuss how we can use relation E.1 in practice to correct hot-wire signals for a drift in temperature of the cooling fluid. The problem of finding the operation temperature of a hot-wire is reduced to finding the temperature coefficient of resistance of the wire's material. The latter problem turns out to be difficult. A direct method to find the operation temperature of the wire is presented.

### E.1.1 Determination of hot-wire temperature

It is common practice to calibrate hot-wires at a temperature which is called  $T_{\text{ref}}$ , and then to apply relation E.1 to correct the samples of the experiment for a deviation from these calibration conditions. This method allows one to apply relations found during calibration to the samples taken at a temperature different from the reference temperature.

There is one quantity in relation E.1 that needs to be determined:  $T_{\text{hot}}$ . This is a crucial step in the application of relation E.1, and it is here that many researchers take wrong assumptions. The difficulties will be outlined below.

A CTA-bridge (see figure 6.1 for definitions of the components) keeps constant the resistance of the hot-wire and the value of the bridge component containing this hot resistance ( $R_2 + R_{\text{hw}}$ ) is manually set on the bridge as follows:

1. Choose an overheat ratio  $a$  (here we use to take  $a = 0.6$ ).
2. Measure the hot-wire probe's resistance including cables. Call this  $(R_2 + R(T_{\text{ref}}))$ . Read temperature  $T_{\text{ref}}$ ! A special Ohmmeter is needed since normal Ohmmeters' sensing current heats up the hot-wire.
3. Measure or estimate parasite resistance  $R_2$  of contacts, cables etcetera. This is often done by measuring the resistance of a probe from which the wire has been taken off, and of which the prong tips are immersed in mercury.
4. Calculate the cold resistance of the wire  $R(T_{\text{ref}})$ .
5. Calculate the desired hot resistance of the wire  $R(T_{\text{hot}})$  by multiplication of the resistance at reference temperature by  $(1 + a)$ .
6. Add estimated parasite resistance  $R_2$  to the hot resistance of the wire, giving the resistance that is to be set on the bridge.

Relation 6.1 gives the temperature dependence of a hot-wire's resistance:

$$\frac{R_w(T)}{R_w(T_0)} = 1 + \alpha_{T_0}(T - T_0) \quad (\text{E.3})$$

or in a form which gives coefficient  $\alpha$ :

$$\alpha_{T_0} = \frac{1}{R_w(T_0)} \frac{R_w(T) - R_w(T_0)}{(T - T_0)} \quad (\text{E.4})$$

$$= \frac{1}{R_w(T_0)} \frac{dR_w(T)}{dT} \quad \text{for linear functions } R_w(T) \quad (\text{E.5})$$

Since we are reducing signals to reference temperature, we take  $T_0 = T_{\text{ref}}$ , the temperature at which we have determined the cold wire's resistance. The hot-wire's temperature is now found to be:

$$T_{\text{hot}} = \frac{1}{\alpha_{T_{\text{ref}}}} \frac{R(T_{\text{hot}}) - R(T_{\text{ref}})}{R(T_{\text{ref}})} + T_{\text{ref}} = \frac{a}{\alpha_{T_{\text{ref}}}} + T_{\text{ref}} \quad (\text{E.6})$$

This simple relation, which contains known variables  $a$  and  $T_{\text{ref}}$  plus material constant  $\alpha_{T_{\text{ref}}}$  is still not readily applicable, because we do not know temperature coefficient of resistance  $\alpha_{T_{\text{ref}}}$  of the hot-wire material.

### E.1.2 Temperature coefficient of resistance

There are many ways to determine temperature coefficient of resistance  $\alpha_{T_{\text{ref}}}$  and they will be given and analysed here.

- The first method is to take estimates for  $\alpha(T_{\text{book}})$  from literature. To translate these values to reference temperature we apply relation E.5:

$$\alpha(T_{\text{ref}}) = \alpha(T_{\text{book}}) \frac{R(T_{\text{book}})}{R(T_{\text{ref}})} = \alpha(T_{\text{book}}) \frac{1}{1 + \alpha(T_{\text{book}})(T_{\text{ref}} - T_{\text{book}})} \quad (\text{E.7})$$

BINAS (Jansen, 1977) gives  $\alpha = 0.0049\text{K}^{-1}$  for tungsten without reference temperature. Handbook of Chemistry and Physics (Weast and Selby, 1984) does not provide  $\alpha$ , but from a table of resistances at different temperatures we find  $\alpha(0^\circ\text{C}) = 0.00482\text{K}^{-1}$ . From a similar table in the American Institute of Physics Handbook (Gray, 1963) we find  $\alpha(0^\circ\text{C}) = 0.0047\text{K}^{-1}$ . We see that different references give estimates which already differ in value by 4 percent.

Call the value for the temperature coefficient of resistance which is found following the above "procedure":  $\alpha(\text{bulk})$ . This method will give a proper value in situations involving macroscopic amounts of hot-wire material (e.g. if a metallurgic factory melts a litre of tungsten and pours it into a mould).

In the process of making a spool of thin wire out of a raw tungsten lump, the tungsten will go through tormenting processes such as stretching, etching etcetera. Therefore the crystal-structure of hotwire material on a spool will be less ordered than of the raw metal. This breaking of the crystal ordering leads to an increased resistance for phonons (thermal and acoustic waves) to travel through the material. This will give rise to a lower value of the thermal coefficient of electrical resistance  $\alpha(\text{spool})$ :

$$\alpha(\text{spool}) < \alpha(\text{bulk}) \quad (\text{E.8})$$

For Dantec 5  $\mu\text{m}$  thick tungsten wire (Bruun, 1995, table 2.1) reports  $\alpha(20^\circ\text{C}) = 0.0036\text{K}^{-1}$ . This value corresponds with  $\alpha(0^\circ\text{C}) = 0.0039\text{K}^{-1}$ . Apparently the disordering of the crystal-structure, which is a consequence of the making process of this particular trade of wire, reduces  $\alpha$  by 20 percent.

After it has been produced the wire material will be mounted on the prongs of a probe. This involves another tormenting of the structure of the material. After welding or soldering the mounted wire material will even have a worse resistance coefficient ( $\alpha(\text{mounted})$ ) than before mounting:

$$\alpha(\text{mounted}) < \alpha(\text{spool}) < \alpha(\text{bulk}) \quad (\text{E.9})$$

Without reference to his source Lemonis (1995, p.46), who uses relation E.1 to correct for ambient temperature drift, adopts  $\alpha = 4.82 \cdot 10^{-3} K^{-1}$  for tungsten (no reference temperature given). On page 45 Lemonis points out that the problem of ambient temperature drift is that "Flow temperature variations cause changes of the electrical wire resistance". This is incorrect, since the very principle of CTA is to maintain the wire's resistance. It is the heat exchange to the fluid that is affected by the ambient temperature drift, not the wire's resistance.

Fingerson and Freymuth (1983) adopt  $\alpha = 4.5 \cdot 10^{-3} K^{-1}$  for tungsten (no reference to a source; no reference temperature given).

- A second method to determine the temperature coefficient of the hot-wire is the following: One estimates  $\alpha(\text{mounted})$  by measuring the resistance of a probe in an oven at several temperatures (Stainback and Nagabushana, 1993). This gives  $\alpha(\text{oven})$ . In the oven the whole probe is heated. During operation of the CTA only the sensitive part of the probe is heated. Usually one assumes that resistances of prongs, supports, leads, contacts etcetera are temperature indifferent, but a small deviation from this assumption will lead to serious misestimation of the hot-wire's temperature. When we will use relation E.6 to find operation temperature  $T_{\text{hot}}$  of the wire, we have to extrapolate the curve of the probe resistance found at various temperatures in the oven. When the whole probe has been heated we will find a coefficient  $\alpha(\text{oven})$  which is too high:

$$\alpha(\text{mounted}) < \alpha(\text{oven}) \quad (\text{E.10})$$

- One can try to reduce the influence of parasite resistances by doing the oven-experiment of the former method on a long piece of wire material (e.g. 5 cm instead of 1 mm). This will give  $\alpha(\text{long-oven})$ . A first disadvantage is that thus  $\alpha$  of the specific piece of material on the hot-wire probe that is used for measuring wind velocities is not determined. One has to assume that  $\alpha$  is constant for all the wire material on the spool. Furthermore: This method may have reduced the influence of parasite resistances, but now the portion of the mounted wire that may have suffered from the mounting procedure (welding or soldering) is essentially smaller than for a real probe. Once more this will lead to a value for  $\alpha$  which is too high:

$$\alpha(\text{mounted}) < \alpha(\text{long-oven}) \quad (\text{E.11})$$

- Saastrup Kristensen (1973) derives  $\alpha$  from the difference in hot-wire signals between a situation with velocity  $u$  and fluid temperature  $T$ , and a situation with zero velocity and fluid temperature  $T_{\text{ref}}$ , applying the following relation:

$$E^2(U, T) - E^2(U = 0, T_{\text{ref}}) = BU^n \left( 1 - \frac{\alpha}{a}(T - T_{\text{ref}}) \right) \Rightarrow \quad (\text{E.12})$$

$$\alpha = \left( 1 - \frac{E^2(U, T) - E^2(U = 0, T_{\text{ref}})}{BU^n} \right) \frac{a}{T - T_{\text{ref}}} \quad (\text{E.13})$$

In the derivation of this relation one extrapolates Collis and Williams' relation 6.8 to zero velocity. This is incorrect since at  $u = 0$  free thermal convection is involved, leading to

higher heat exchange from the wire than what is expected to be induced by forced convection solely (see e.g. the original text by Collis and Williams (1959)). Moreover, zero velocity can never be achieved: even the slightest draft will cause the wire to loose heat. Wubben (1991, p.25) suggests to apply relation E.12 directly to compensate for ambient temperature drift: he suggests to record  $E^2(U = 0, T_{\text{amb}})$  at regular intervals during the experiment. A glass cover is used to shield the probe from wind during the determination of  $E^2(U = 0, T_{\text{amb}})$ .

We see from relation E.12 that non-zero heat exchange during determination of  $E^2(U = 0, T_{\text{ref}})$  will lead (once more) to an estimate for  $\alpha$  which is too high.

From the preceeding we can see that most estimates for  $\alpha$  will be too high. Taking a too high value for  $\alpha$  leads to an underestimation of the operation temperature of the wire. The influence of temperature drift on Nusselt's number at a given Reynolds' number will therefore be overestimated, and correction methods will overcompensate the ambient temperature drift.

Vasanta Ram (1992), who does not explain which value he uses for  $\alpha$ , nor how he came to that value, observes that, even after application of relation E.1, his calibration data do not collapse on one curve. In figure 1 (Vasanta Ram, 1992, p.158) it is shown that the Nusselt's number for high temperatures is lower than for low temperatures. If Vasanta Ram would have introduced this effect by taking a too high value for  $\alpha$ , then the order of the curves from low  $T$  to high  $T$  would have been the reverse of what is shown. This means that Vasanta Ram possibly adopted a too low value for  $\alpha$ , which cannot be explained by the sources of error given in this subsection. The rest of his analysis strongly depends on his assumption that his value for  $\alpha$  is correct. The absence of justification for the value for  $\alpha$  which is adopted by Vasanta Ram makes the value of his further analysis uncertain.

### E.1.3 Direct determination of $T_{\text{hot}}$

In the previous subsection we have seen that it is very difficult to calculate the hot-wire temperature via temperature coefficient of resistance  $\alpha$ . There is however a simple way to determine  $T_{\text{hot}}$  directly :

1. Record the anemometer output at a collection of velocities within the interval that is needed for the experiment to be carried out with the probe, and repeat this at different ambient fluid temperatures. As long as temperature is recorded, it is not necessary that temperature remains constant within one velocity-sweep.
2. Choose a first estimate for  $T_{\text{hot}}$  which is probably too high, e.g. 300°C.
3. Reduce all samples to reference temperature by application of relation E.1, using the respective ambient temperatures recorded for each sample.
4. Fit a simple relation (e.g. a fourth order polynomial) to the complete "corrected" data-set, and note  $\chi^2$ .
5. Lower the estimate for  $T_{\text{hot}}$  by one degree.

6. Repeat steps 3 to 5 until  $\chi^2$  starts to increase.

This process iterates to the true hot temperature  $T_{\text{hot}}$  of the wire. Even if certain effects have been incorrectly accounted for and the true hot temperature is different from the value found in this way, then at least the method provides a means to pragmatically correct hot-wire measurements for ambient fluid temperature drift such that the accuracy of the method is known.

Some researchers have come up with the same method just described:

- Wubben (1991, p.13) points out that:

“...can be improved by considering  $(T_{\text{hot}} - T_{\text{ref}})$  as a free parameter to match calibration curves measured at different temperatures. It will be clear that  $(T_{\text{hot}} - T_{\text{ref}})$ , used in this way, no longer represents true initial overheat temperature.”

It is a misfortune that Wubben did not see the merit of the method.

- Maciel (1994, chapter on hot-wires, section 2.8) observes that:

“..., il est impossible de connaître directement avec précision le coefficient de surchauffe des fils. Donc, à chaque fois que les coefficients de surchauffe pour les 4 fils ont été réglés, les valeurs correspondantes des coefficients  $(T_{\text{hot}} - T_{\text{ref}})/T_{\text{ref}}$  pour chaque fil ont été ensuite déterminées expérimentalement.”

This observation is followed by a description similar to the method described in this subsection.

## E.2 Practical test of the temperature method

Relation E.1 has been derived from theory. In this section its practical use will be tested in a simple experiment. Many scientists have the impression that such an experiment will be time consuming (“...does not require a lengthy temperature calibration”, Bruun (1995)). The experiment described in this section yields the value of  $T_{\text{hot}}$  in fifteen minutes. First the set-up will be described, then the experiment, followed by the results.

### E.2.1 The set-up

The apparatus and set-up used in this experiment is schematically drawn in figure E.1. A blow-drier (type Carmen Mirage 1800, price: US\$ 30) is placed 3 meters in front of the inlet of a mini windtunnel's ventilator. The blow-drier has three operating positions: 0 (off), 1 (900 Watt) and 2 (1800 Watt). In the warm operating positions the blow-drier creates a bubble of warm air around the inlet of the mini windtunnel. Inhomogeneities in temperature are levelled out in the windtunnel. An advantage of the blow-drier above closed windtunnels with climate control is the response time. The blow-drier reacts instantly, whereas closed windtunnels with climate control take a long time to reach equilibrium. The distance between blow-drier and windtunnel



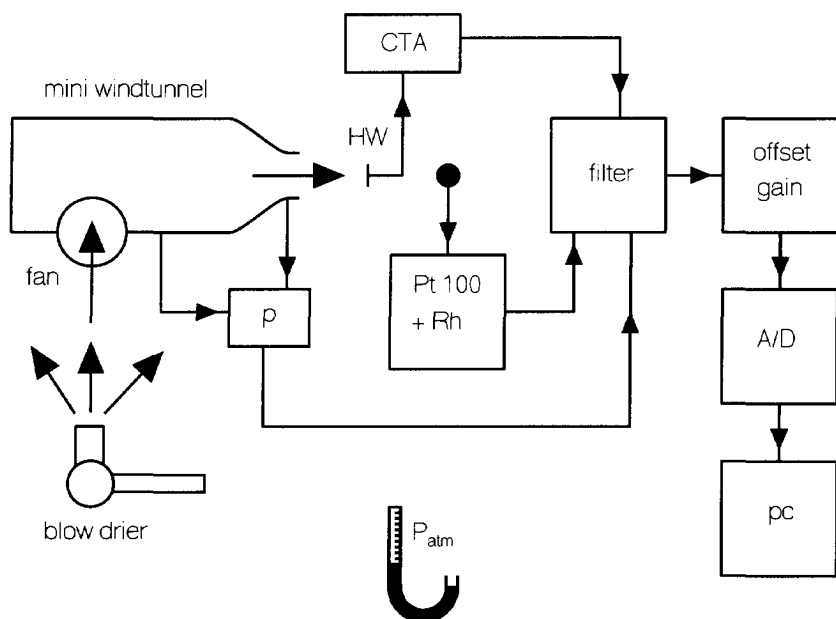


Figure E.1: Set-up for temperature calibration

has been chosen such that air temperature at the windtunnel's inlet increases by 6 Kelvin when operating position 2 is used. This temperature difference reflects ambient temperature drift as expected in real experiments.

Design and calibration of the mini windtunnel are described in detail in section 5.3.

A single hot-wire probe (home-made type, connected to DISA CTA-bridge type 56C01) is placed in the centreline of the flow coming out of the mini windtunnel, 0.8 outlet-diameter downstream of the outlet.

A Vaisala combined temperature/relative-humidity sensor (type HMI-33) is placed in the centreline of the flow 0.5 meter downstream of the hot-wire probe (the air temperature was constant over this range). The protective head has been removed from the Vaisala sensor to enhance its response time by a factor five. The probe's Pt100 element was calibrated against a Philips PM-2535 system multimeter, the relative humidity element was calibrated following a procedure outlined in the sensor's manual.

A mercury barometer is used to measure atmospheric pressure.

A Setra type 239 (range: 14 mm H<sub>2</sub>O) electric pressure transducer is connected to both the pressure chamber and the contraction of the mini windtunnel. The pressure transducer was calibrated against a Betz manometer.

Signals from pressure transducer, CTA and Vaisala sensor are fed to DIFA programmable elliptic filters (type SICOS) to eliminate aliasing. Filtered signals are conditioned by a home-made offset/gain amplifier. Conditioned signals are digitised by a Keithley Instruments DAS40

a/d-board. Experimentation software written in Borland PASCAL 7.0 allows for sampling under DMA. Samples are recorded a specified number of times at a specified frequency. Calibration relations established in previous experiments are applied to the voltages offered by pressure transducer, CTA and Vaisala sensor. Related quantities (dynamic pressure and wind velocity at hot-wire position) are calculated and both mean values and variances of all quantities are stored.

## E.2.2 The experiment

The hot-wire's response has been recorded in three different runs, which were performed sequentially in one series. Every data point is the mean of 100 samples recorded at 50 Hz. In all three runs the response was recorded at regular velocity intervals (1 m/s) in the range from 2 m/s up to 16 m/s at one constant direction relative to the wire. In the first run the blow-drier was off. In the second and third run the blow-drier was operated in positions 1 and 2 respectively. To eliminate systematic errors in the measurements, we subdivided every run (with constant setting of the blow-drier) into a first sub-run in which the velocity of the calibration unit was increased from 2 m/s up to 16 m/s with steps of 2 m/s, and a sub-run in which velocity was decreased with steps of 2 m/s from 15 m/s down to 3 m/s.

Temperature/velocity conditions of the calibration jet during this experiment are presented in figure E.2. The hot-wire's response is shown in figure E.3. The curve shown was obtained by

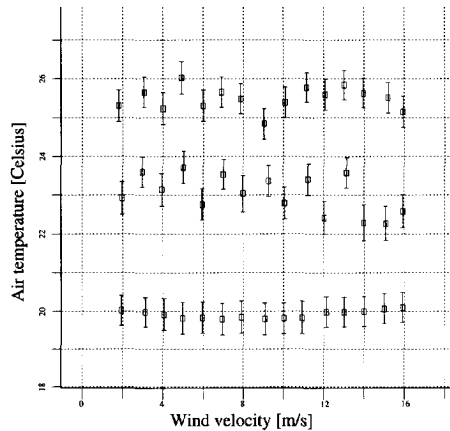


Figure E.2: Flow conditions offered in temperature calibration

$\chi^2$ -optimisation. It is a third order Chebychev polynomial taken orthogonal on the interval of the (uncorrected) hot-wire response. An RMS-deviation of 1.1 m/s (7 percent full scale) was found at an optimum  $\chi^2 = 2400$  which is clearly beyond acceptable. The operation temperature of the hot-wire has been established according to the method described on page 255. A value of  $T_{\text{hot}} = 113^\circ\text{C}$  was found. This corresponds with an overheat ratio of 1.3. This value is relatively low when compared with the ranges of values  $T_{\text{hot}} \in [200^\circ\text{C}, 250^\circ\text{C}]$  which is commonly used (Bruun, 1995). This deviation is caused by the CTA, which had a prefixed bridge setting for

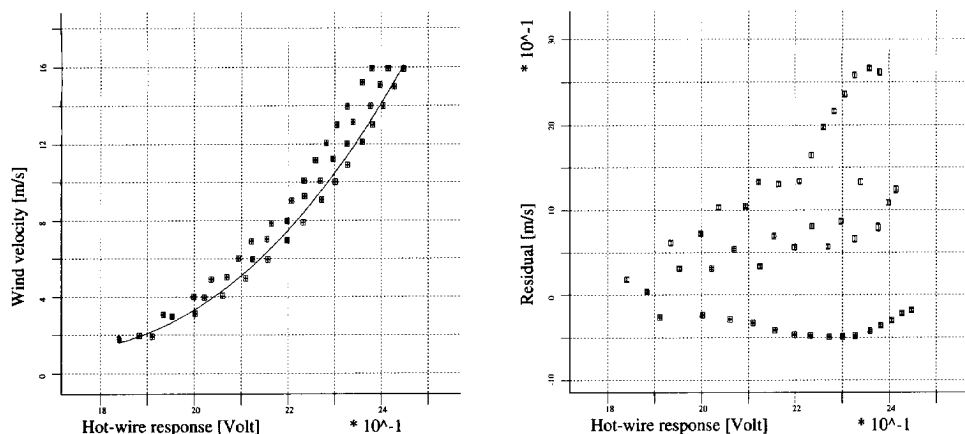


Figure E.3: Hot-wire response in temperature calibration. In the figure on the left temperature of the samples increases from right to left. In the figure on the right, temperature increases from bottom to top.

wires with lower cold resistance than the wire that was used. This difference in hotwire operating temperature between the test and the experiments that will be carried out later in this study, do not render the method just outlined inadequate.

The wire's response after correction for ambient temperature drift is presented in figure E.4. The fitcurve now has RMS-deviation of 5.6 cm/s (3.5 promille full scale) at  $\chi^2 = 4.5$ .

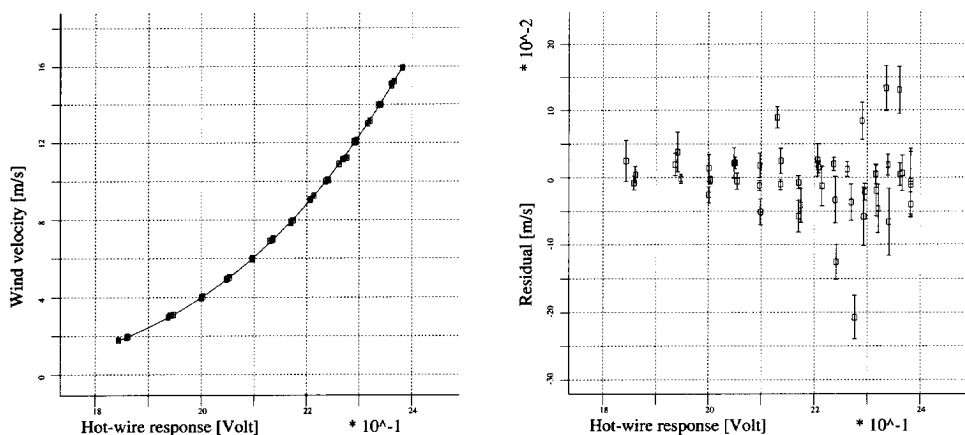


Figure E.4: Hot-wire response after temperature correction

### E.2.3 Discussion

From figure E.2 we see that the bubble of warm air produced by the blow-drier is so large that the temperature of the jet leaving the windtunnel is independent of the jet's velocity. This is a

favourable condition since the absence of major temperature change with wind velocity in the experiment reduces emphasis on reaction time of the thermometer.

The value of  $\chi^2 = 4.5$  after temperature correction is reasonable for such a simple experiment. The internal errors of the samples are underestimated by a factor of only 2. Careful temperature control and temperature recording combined with sufficient waiting between the samples for temperature to reach equilibrium could have reduced  $\chi^2$  even more. The random character of the residuals suggests that with application of these improvements a similar value for  $T_{\text{hot}}$  would be found.

The experiment shows that the method presented on page 255 provides a cheap and fast way to directly calibrate a wire's temperature sensitivity.

### E.3 Application of the resistance method

Instead of applying relation E.1 we can use relation E.2. This relation can be applied without knowledge of hot-wire temperature  $T_{\text{hot}}$ . The application of this relation in practice is examined in this section.

The parameters that have to be known to apply relation E.2 look simple to determine: Both the cold resistance  $R(T_{\text{ref}})$  and the hot resistance  $R(T_{\text{hot}})$  can be determined according to the method described in subsection E.1.1. The cold resistance of the wire at different room-temperatures can be measured in an oven. This time, in contrast with what was pointed out in the previous subsection, it is correct to put the *whole* probe in the oven, since if ambient temperature will rise, then the whole probe will heat up either.

The correction is applied to measured voltages as follows: For each sample the temperature  $T$  has been recorded. This temperature is used to find the cold resistance of the wire at this ambient temperature  $T$  from the relation determined from the temperature calibration described in the former paragraph. Then relation E.2 is applied to the sample.

The problem with this method is that the way to determine both hot and cold resistances of the wire, as described in subsection E.1.1, is inaccurate. Resistance  $R_2$  represents all parasite resistances present in the CTA-bridge when the anemometer is operated. When we disconnect a probe from the anemometer to measure its cold resistance, then we replace contact resistances between probe and anemometer plus resistance present inside the anemometer by the (different) resistance of contact to the Ohmmeter plus internal resistance inside the Ohmmeter.

The dependence of temperature correction on parasite resistances is analysed in the following steps (we assume all parasite resistances to be temperature indifferent; for temperature dependent parasite resistances a similar reasoning can be done):

1. Define the following quantities:

- In a non-operational CTA the actual parasite resistance is  $R_2$  (see figure 6.1). Furthermore the wire has resistance  $R(T_{\text{ref}})$  and  $R(T)$  at temperatures  $T_{\text{ref}}$  and  $T$  respectively.

- The difference in contact and internal resistances between CTA and Ohmmeter is called  $\Delta_1$ . This means that the total cold resistances  $R_{\text{total,cal}}(T_{\text{ref}})$  and  $R_{\text{total,cal}}(T)$ , which are recorded in temperature calibration differ from the real total cold resistances  $R_{\text{total}}(T_{\text{ref}})$  and  $R_{\text{total}}(T)$  at these temperatures by  $\Delta_1$  and are defined by:

$$R_{\text{total,cal}}(T_{\text{ref}}) = R_{\text{total}}(T_{\text{ref}}) + \Delta_1 = R(T_{\text{ref}}) + R_2 + \Delta_1 \quad (\text{E.14})$$

$$R_{\text{total,cal}}(T) = R_{\text{total}}(T) + \Delta_1 = R(T) + R_2 + \Delta_1 \quad (\text{E.15})$$

- The difference between the correct (true) value for parasite resistance  $R_2$  and the estimate for  $R_2$  found in step 3 in subsection E.1.1 is called  $\Delta_2$ .

2. When we want to set the CTA to overheat  $a$ , we set total bridge resistance  $R_{\text{total}}(T_{\text{hot}})$  to:

$$R_{\text{total}}(T_{\text{hot}}) = R_2 + (1 + a)(R(T_{\text{ref}}) + \Delta_1) - a\Delta_2 = R_2 + R(T_{\text{hot}}) \quad (\text{E.16})$$

3. The fraction in the square root in expression E.2 can be converted into total actual resistances:

$$\frac{R(T_{\text{hot}}) - R(T_{\text{ref}})}{R(T_{\text{hot}}) - R(T)} = \frac{\left( R_{\text{total}}(T_{\text{hot}}) - R_2 \right) - \left( R_{\text{total}}(T_{\text{ref}}) - R_2 \right)}{\left( R_{\text{total}}(T_{\text{hot}}) - R_2 \right) - \left( R_{\text{total}}(T) - R_2 \right)} \quad (\text{E.17})$$

$$= \frac{R_{\text{total}}(T_{\text{hot}}) - R_{\text{total}}(T_{\text{ref}})}{R_{\text{total}}(T_{\text{hot}}) - R_{\text{total}}(T)} \quad (\text{E.18})$$

4. The total hot resistance in the bridge is known in principle. One simply *selects* its value and sets the anemometer bridge accordingly. Nevertheless one has to assume that the switches on the anemometer's front panel are accurately set to the total resistance in the bridge and that no parasite resistance is present in this part of the anemometer setup. Any such parasite resistance will contribute to  $\Delta_1$ . When we replace the actual total cold resistances in the bridge by values obtained from temperature calibration we get (use relation E.15):

$$E_{\text{out}}(T_{\text{ref}}) = E_{\text{out}}(T) \sqrt{\frac{R_{\text{total}}(T_{\text{hot}}) - R_{\text{total,cal}}(T_{\text{ref}}) + \Delta_1}{R_{\text{total}}(T_{\text{hot}}) - R_{\text{total,cal}}(T) + \Delta_1}} \quad (\text{E.19})$$

There are two important remarks to be made on relation E.19. The first is that the difference in contact and internal resistance  $\Delta_1$  does enter the relation for temperature correction of hot-wire signals, and therefore has to be accounted for. The second remark is that it appears that both parasite resistance  $R_2$  and its mis-estimate  $\Delta_2$  do not appear. This is surprising.

When relation E.2 is used instead of relation E.1, then resistance difference  $\Delta_1$  is neglected. It has not yet been shown whether this omission will introduce serious misinterpretation of hot-wire signals. In order to check this, the influence of omitting  $\Delta_1$  has been measured. This experiment is described in the following section.

## E.4 Practical test of resistance method

In order to find the importance of  $\Delta_1$  in the resistance method for correction for ambient temperature drift (and hence the applicability of the method) a detailed experiment is conducted. First the set-up will be outlined, then the experiment will be reported and finally the results will be discussed.

### E.4.1 Set-up

The set-up used to test the resistance method for ambient temperature drift correction is shown in figure E.5. The test of the resistance method for ambient temperature drift correction was

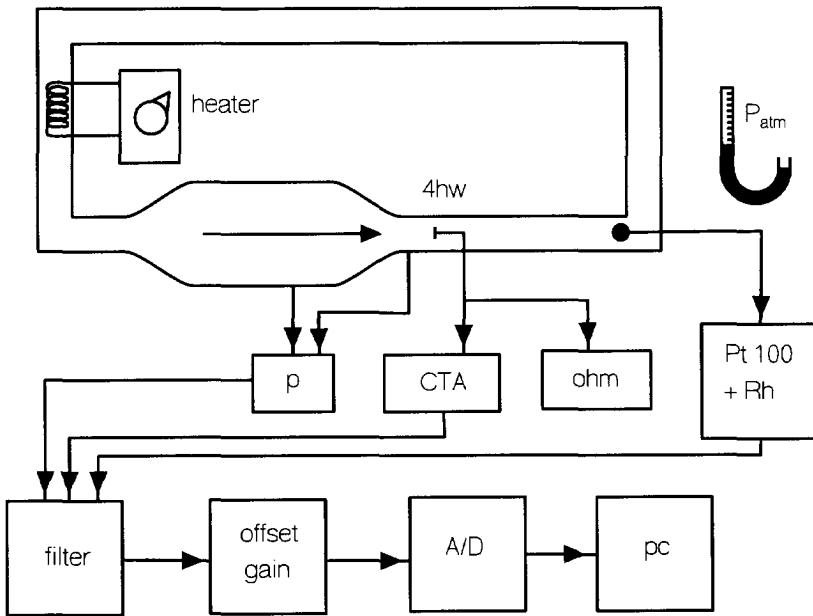


Figure E.5: Set-up for testing resistance method

conducted in a closed loop windtunnel equipped with a heating element. The test section had circular crosssection (diameter 29 cm). The heating element's power was tunable and at maximum power there was a difference in temperature between air in- and outside of the tunnel of 15 Kelvin.

For this test a home-made four-wire probe was used. Four slanted wires ( $45^\circ$  between wires and probe axis) are places like the sides of a pyramid.

A low-sensing-current devise (Philips PM-2535 system multimeter) was used for the measurement of cold resistances of the wires in the four-wire probe.

The pressure difference over the tunnel's contraction was calibrated against the differential pressure of a pitot-tube which was connected to a second electronic pressure transducer (Setra type 239, range: 14 mm H<sub>2</sub>O). The pitot-tube was placed at the position at which in a later phase of the experiment the four-wire probe was placed.

The four wires of the probe were connected to four equal CTA bridges (type 56C17, Dantec Electronics).

Pressure transducer, Pt100 element, relative humidity sensor, barometer, filters, signal conditioner, a/d-board, PC and software are described in subsection E.2.1.

### E.4.2 The experiment

First, the cold resistance of the four wires in the probe was recorded at 11 different temperatures in the range 18°C to 32°C. The tunnel was set to a moderate velocity of 5 m/s. Before each sample was taken, both tunnel and thermometer were given 15 minutes to reach temperature equilibrium. Linear relations were fit to the cold resistances as function of ambient temperature, resulting in RMS-deviations of 0.002Ω, at  $\chi^2 = 0.5$ .

The response of the four hot-wires was measured as function of both wind velocity and temperature. Velocity calibrations (ranging from 1 to 8 m/s) were carried out at five different temperatures (18°C to 32°C). The raw response of one of the wires is shown in figure E.6. Data of all four wires showed an RMS-deviation of about 1 m/s from a third order Chebychev polynomial ( $\chi^2 \sim 4 \cdot 10^5$ ). The response of the wire, corrected for ambient temperature drift

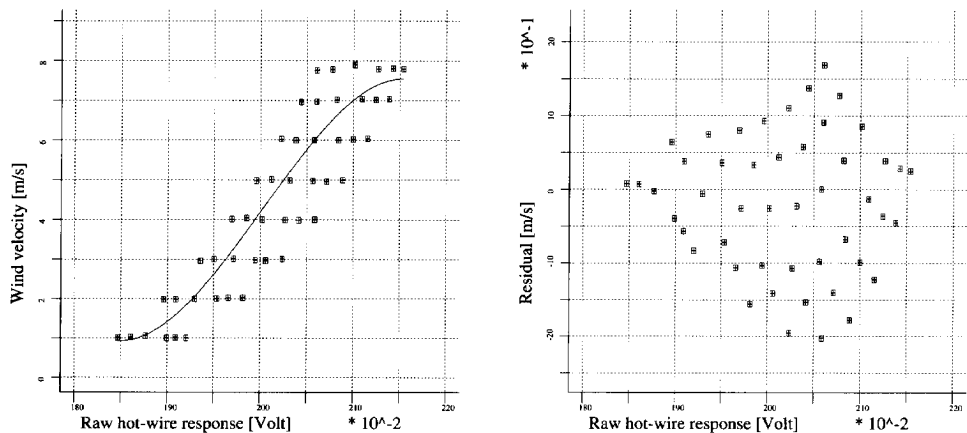


Figure E.6: Raw hot-wire response. In the figure on the left temperature increases from right to left.

according to relation E.2 to the response, is presented in figure E.7. The RMS-deviations of the wires' responses to third order Chebychev polynomials improved by factors of 3 or 4 to (37, 39, 24, 28) cm/s respectively ( $\chi^2 \sim 3 \cdot 10^4 - 7 \cdot 10^4$ ).

We have used contact resistance differences  $\Delta_1$  as a free parameter. The values of  $\Delta_1$  have been optimised such that the hot-wire responses corrected with relation E.19 had minimum values

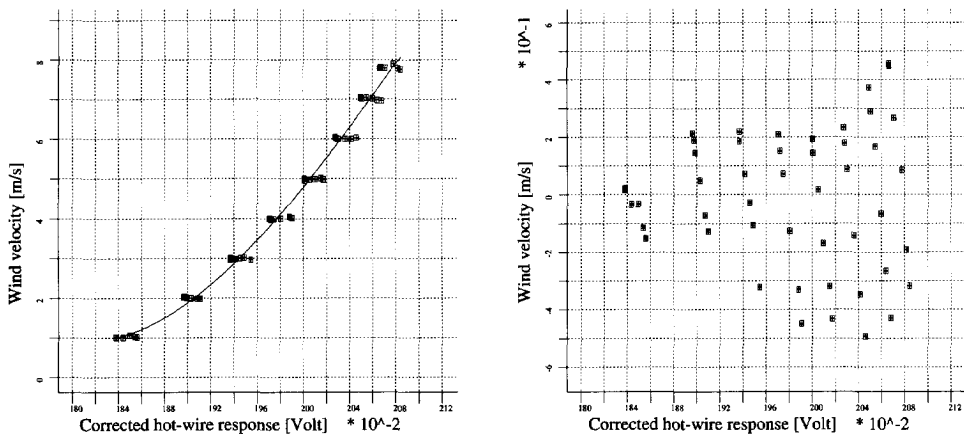


Figure E.7: Corrected response ( $\Delta_1 = 0$ ). In the figure on the left temperature increases from left to right.

for  $\chi^2$ . The respective values found for  $\Delta_1$  are: (0.34, 0.38, 0.25, 0.26)  $\Omega$ . RMS-deviations to fit-curves reduced to (4.4, 4.8, 2.9, 4.1) cm/s respectively ( $\chi^2 \sim 300 - 460$ ). Response of wire three corrected in this manner for temperature drift is given in figure E.8.

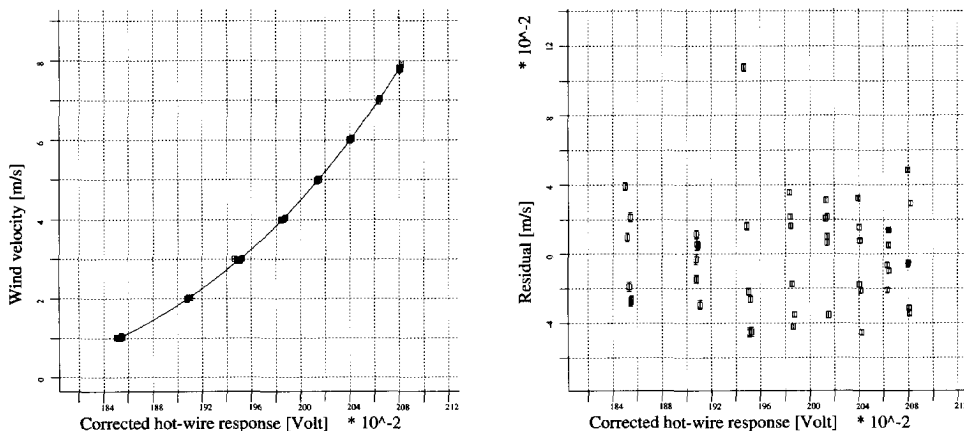


Figure E.8: Corrected response ( $\Delta_1$  optimised). There is no correlation between the place of the samples in the figure with temperature.

### E.4.3 Discussion

We observe from the results presented in the former subsection that application of the resistance method with  $\Delta_1 = 0$  provides a reduction in RMS-deviation by a factor 3 or 4. The residual plot in figure E.7 still shows large systematic errors. Correction with  $\Delta_1 = 0$  overcorrects the samples for temperature drift: before correction the warmer samples were found on the left side of the



fit-curve, after correction this order has reversed. Optimisation of  $\Delta_1$  improves the resistance method by nearly an additional order of magnitude! The deviations in the residual plot of figure E.8 are random. The high value of  $\chi^2$  (300-460) is probably caused by overestimation of the accuracy of the samples, which is introduced by slow response of the thermometer.

It appears that, even though the value of  $\Delta_1$  is as low as  $0.25 - 0.38 \Omega$ , the presence of  $\Delta_1$  can spoil the resistance method.  $\Delta_1$  has to be found by optimisation, which is analogue to the determination of  $T_{\text{hot}}$  in the temperature method. This makes application of both methods for ambient temperature correction equally difficult.

## E.5 Discussion on temperature correction

In this section we will first give some additional ideas which one has to keep in mind when temperature corrections of hotwire measurements are to be carried out. Then some concluding remarks will be made.

### E.5.1 Additional ideas

- The random character of the residuals in both figure E.4 and in figure E.8 shows that it is not necessary to devise a velocity dependent interpolation scheme for the temperature dependent calibration curves, which was suggested by Lomas (1986) and by Vasanta Ram (1992, p.277).
- When the reference temperature  $T_{\text{ref}}$  is chosen in the middle of the expected temperature range, then the samples need the weakest correction for temperature drift. This would be appropriate since the influence of correction methods has to be kept as small as possible.
- It may happen that temperature remains constant during the experiment, but that the calibration facility introduces severe temperature drift during calibration. Therefore it is important to record temperature during *both* calibration *and* experiment, and to apply temperature drift corrections to both data-sets involved.

### E.5.2 Conclusion

It has been shown in this appendix that the temperature method (relation E.1) can adequately correct hot-wire response if  $T_{\text{hot}}$  is determined directly from a calibration. The resistance method (relation E.19) is equally accurate provided that the difference in contact and internal resistance  $\Delta_1$  between Ohmmeter and CTA is determined via optimisation. Application of either correction method reduces the standard deviation of an uncorrected wire response versus velocity calibration curve by a factor 30.

For practical applications we advise (and adopt) the temperature method to the resistance method (though both methods lead to equally accurate estimates for the temperature corrected hotwire

response). The reason is the following: In both methods one has to record the ambient temperature dependence of the anemometer output. The resistance method requires additional calibration of the ambient temperature dependence of the wire's cold resistance. The temperature method can be applied without this extra calibration. As a consequence the temperature method is quicker in use than the resistance method.

## Appendix F

### The effects of hot-wire separation

In this appendix we will consider the effect of wire separation in a 4-sensor hot-wire probe on the estimate for wavenumber spectral tensor  $\bar{\Psi}(k)$  (see section 2.7 for it's definition). An idealised probe model is used: the probe's angular sensitivity is velocity independent, and is described by the cosine-response (relation 6.11). First the response of the probe to a single wave is calculated. Then all (incompressible) waves with the same wavelength are integrated to get the response of the probe to an isotropic distribution of waves. The effects of wire separation on velocity correlations are studied.

In this appendix we assume that the angular response of the wires can be described with the cosine-law (see relation 6.11). We use a Reynolds-decomposition of all quantities (velocities and wire-responses) into their mean and fluctuating parts. Consider a wire pointing in the  $(1, -1, 0)$ -direction (hotwire 4 in figure F.1), placed in a weakly turbulent flow with mean velocity in the  $x$ -direction. Linearisation of the cosine law shows that the fluctuating part of the cooling velocity consists of two terms: the sum of the velocity-fluctuations in the  $x$ -direction plus velocity-fluctuations in the  $y$ -direction:

$$u'_{\text{eff}} \left( \text{wire in } (1, -1, 0) \text{ direction} \right) = (u'_1 + u'_2)/\sqrt{2} \quad (\text{F.1})$$

Let four wires be located at positions  $(0, d, 0)$ ,  $(0, 0, d)$ ,  $(0, -d, 0)$  and  $(0, 0, -d)$  respectively (see figure F.1). All four wires make an angle of 45 degrees with the  $(1, 0, 0)$ -axis, thus forming a pyramid. The sensing zones of the wires are assumed to be infinitely small and all wire-responses  $E_i$  are electronically transformed into their corresponding effective cooling velocities  $u_{\text{eff},i}$ .

Let the wires be placed in a mean flow  $U$  in  $(1, 0, 0)$ -direction on which is superposed a fluctuating velocity  $\mathbf{u}'$ . With use of relation F.1 we find that the linearised fluctuating response  $u'_{\text{eff},i}$  of the wires is given by the following relation:

$$\begin{pmatrix} u'_{\text{eff},1} \\ u'_{\text{eff},2} \\ u'_{\text{eff},3} \\ u'_{\text{eff},4} \end{pmatrix} = \begin{pmatrix} u'_1(0, d, 0) - u'_2(0, d, 0) \\ u'_1(0, 0, d) - u'_3(0, 0, d) \\ u'_1(0, -d, 0) + u'_2(0, -d, 0) \\ u'_1(0, 0, -d) + u'_3(0, 0, -d) \end{pmatrix} / \sqrt{2} \quad (\text{F.2})$$

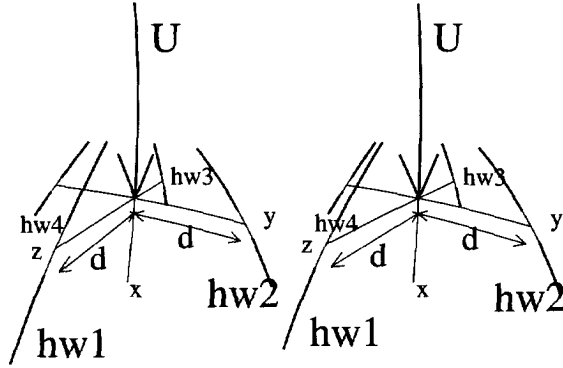


Figure F.1: Orientation of four hot-wires and of mean flow

Using these responses we construct first estimates  $u'_e$  for the fluctuating velocity vector, assuming that all wires measure in the same point (which they obviously do not). These estimates are constructed to see the difference with proper estimates, which do take into account the separation of the wires:

$$\begin{pmatrix} u'_{e,1} \\ u'_{e,2} \\ u'_{e,3} \end{pmatrix} = \sqrt{2} \begin{pmatrix} (u'_{\text{eff},1} + u'_{\text{eff},2} + u'_{\text{eff},3} + u'_{\text{eff},4})/4 \\ (u'_{\text{eff},3} - u'_{\text{eff},1})/2 \\ (u'_{\text{eff},4} - u'_{\text{eff},3})/2 \end{pmatrix} \quad (\text{F.3})$$

We will now consider the response of the probe to a plane wave (single Fourier component) with wavevector  $\mathbf{k}$  and (complex valued) polarisation (amplitude)  $\hat{\mathbf{u}}$ :

$$\mathbf{u}' = \hat{\mathbf{u}} e^{i\mathbf{k} \cdot \mathbf{x}} \quad (\text{F.4})$$

With use of relations F.2 and F.3 for the response of the probe, we find that the estimate for the fluctuating velocity is given by the following relation:

$$\begin{pmatrix} u'_{e,1} \\ u'_{e,2} \\ u'_{e,3} \end{pmatrix} = \begin{pmatrix} v_1 \left[ \cos(k_2 d) + \cos(k_3 d) \right] / 2 - i \left[ v_2 \sin(k_2 d) - v_3 \sin(k_3 d) \right] / 2 \\ v_2 \cos(k_2 d) - i v_1 \sin(k_2 d) \\ v_3 \cos(k_3 d) - i v_1 \sin(k_3 d) \end{pmatrix} e^{i\mathbf{k} \cdot \mathbf{x}} \quad (\text{F.5})$$

The correlation function of a harmonic function drops to zero in a quarter of its wavelength. We now assume that when the separation between the wires becomes larger than this distance, then the signals of the wires in practice remain uncorrelated. In this case no meaningful estimate for the velocity vectors of waves with this (or smaller) wavelength can be given. For larger separations signals from individual wires cannot be combined, because they have responded to velocity vectors that are too much out of phase with one another. The sines and cosines in relation F.5 represent de-correlation factors. For relatively large waves (when compared with the wire-separation) we can approximate these goniometric expressions with their Taylor-expansion ( $i=2,3$ ):

$$\sin(k_i d) = k_i d + O(k_i d)^3 \quad (\text{F.6})$$

$$\cos(k_i d) = 1 - (k_i d)^2 / 2 + O(k_i d)^4 \quad (\text{F.7})$$

We adopt expression 2.45 for  $\mathbf{k}$  and expression 2.52 for unitvector  $\mathbf{b}$  in the direction of vector  $\hat{\mathbf{u}}$ . We select relation 2.72 for the isotropic solenoidal spectral structure-pdf. Integration of the weighted spectral diadics  $C(\mathbf{k}, \mathbf{b}) \left( \mathbf{b} \otimes \mathbf{b}^* \right)$  for all waves with the same wavelength via relation 2.55 gives the following relation between the estimated wavenumber spectral tensor  $\bar{\bar{\Psi}}_e(k)$  and the actual wavenumber spectral tensor  $\bar{\bar{\Psi}}(k)$ :

$$\Psi_{e,11}(k) = \Psi_{11}(k) \left( 1 - \frac{7}{20}(k^2 d^2) + O(k^4 d^4) \right) \quad (\text{F.8})$$

$$\Psi_{e,22}(k) = \Psi_{22}(k) \left( 1 + \frac{1}{5}(k^2 d^2) + O(k^4 d^4) \right) \quad (\text{F.9})$$

$$\Psi_{e,33}(k) = \Psi_{33}(k) \left( 1 + \frac{1}{5}(k^2 d^2) + O(k^4 d^4) \right) \quad (\text{F.10})$$

$$\Psi_{e,ij}(k) = \Psi_{ij}(k) = 0 \quad i \neq j \quad (\text{F.11})$$

We see that the longitudinal wavenumber-spectra are underestimated and that the lateral spectra are overestimated. The effect is quadratic in wavelength, and the longitudinal effect is roughly twice as strong as the lateral effect. Wire separation makes that isotropic turbulence is misinterpreted to be axisymmetric turbulence with a smartie-like anisotropy character. This can be seen as follows: in one direction velocity fluctuations are attenuated (relation F.8), whereas in the other two direction the fluctuations are amplified (relations F.9 and F.10).

According to relation F.8 an error of ten percent in estimates for the longitudinal wavenumber-spectrum is found for waves with:

$$\frac{7}{20}k^2 d^2 = 0.1 \quad \Rightarrow \quad \lambda = \frac{2\pi}{k} = 11.7d \quad (\text{F.12})$$

This is about six times the distance between two wires' sensing zones (which is  $2d$ ). For waves with a quarter-wavelength equal to the wire-separation ( $2d$ ) the attenuation factor for  $\Psi_{11}$  becomes 0.8.

We can conclude from the analysis in this appendix that the influence of wire separation on the wavenumber spectral tensor can only be neglected for waves larger than six times the distance between the wires. For the estimation of  $\bar{\bar{\Psi}}(k)$  for smaller waves, corrections have to be applied to the estimated components. For isotropic turbulence we have found expressions for these corrections.



# Appendix G

## Fitting laws of King and Jørgensen

### Introduction

In chapter 6 we have introduced King's law and Jørgensen's law for hotwire response:

$$E_{hw}^2 = A + BU_{eff}^n \quad \text{King's law} \quad (G.1)$$

$$U_{eff}^2 = U_n^2 + k^2 U_t^2 + h^2 U_b^2 \quad \text{Jørgensen's law} \quad (G.2)$$

In this appendix we will show how constants  $A, B, n, k$  and  $h$  in these laws plus the orientation angles  $\theta$  and  $\phi$  of a wire can be found from calibration. Sometimes (Kreplin and Eckelmann, 1979) one can measure the geometric angles of the wires. In this section we assume that we cannot directly measure these angles. In this case laws of King and of Jørgensen have to be fitted stepwise, because the nonlinear character of the relations involved makes it difficult to find all coefficients concerned in one go. The following steps are taken:

### G.1 Conversion to reference temperature

First all calibration samples  $(T, u, E(T))$  are reduced to samples  $(u, E(T_{ref}))$  at reference temperature by application of relation 6.14.  $T_{ref}$  can be chosen at will and temperatures  $T$  and  $T_{hot}$  are supposed to be known (see section 6.4.2 on how to estimate  $T_{hot}$ ).

### G.2 Determination of $A$ and $n$

One either uses relation G.1 directly, or one linearises the hot-wire response to  $U_{eff} = A + B \cdot E$ , with appropriate constants  $A$  and  $B$ , applying analogue electronics (Sastrup Kristensen, 1973). In either method one has to estimate coefficients  $A$  and  $n$  from King's law G.1. In this step we will show how they are determined. To determine the coefficients in King's law 6.9 one has to establish a calibration dataset with the wires' responses as function of the offered wind-velocity with a known arbitrary constant direction. The effective cooling velocities cannot be estimated

from this calibration since the wire's orientation is unknown. Therefore coefficient  $B$  will be found up to a functional factor, in other words: it cannot be determined yet.

Combination of relation G.1 for the velocity dependence of the wire response and relation 6.10 for the functional form of the effective cooling velocity gives:

$$E^2 = A + C||\mathbf{u}||^n \quad (\text{G.3})$$

$$C \equiv \left( B f^n(\text{flow and wire orientations}) \right) \quad (\text{G.4})$$

To fit relation G.3 to the calibration samples (at reference temperature) we use the nonlinear Levenberg-Marquardt method from Numerical Recipes (Press et al., 1992). This gives calibration parameters  $A(T_{\text{ref}})$  and  $n$  and intermediate parameter  $C$ .

A different method often used to find the effective cooling velocity from the hot-wire response is by fitting a given function (e.g. a polynomial or a spline curve) to the relation between hot-wire response and wind velocity (Bruun et al., 1988; Marasli et al., 1993).

### G.3 Estimation of $\phi$

To complete the set of calibration constants we use samples from an angular calibration of the wire: the response of the wire to flow with constant velocity, but varying orientation angles with respect to the flow.

We start by peeling off King's law from the angular calibration samples according to:

$$E \rightarrow \frac{(E^2 - A)^{2/n}}{|\mathbf{u}|^2} \equiv \tilde{f}(B, \theta, \phi, k, h) \quad (\text{G.5})$$

Quantity  $\tilde{f}$  only contains the wire's orientation  $(\theta, \phi)$  and its angular sensitivity  $(k, h)$  (plus normalisation constant  $B$ ). An example of this angular function for a slanted wire ( $\theta = 45$  degrees) is shown in figures G.1 and G.2.

The minimum in figure G.1 indicates where flow is most parallel to the wire. To find the wire's orientation we transform the orientations of the velocities offered to the probe to coordinates  $(\theta', \phi')$  (see figures 6.5, 6.6 and 6.7 for their definition), where  $\theta'$  is the angle between the  $x_3$ -axis and the velocity vector and where  $\phi'$  is the rotation angle of the velocity vector around the  $x_3$ -axis counting from the  $x_1$ -axis. Information concerning this minimum in figure G.2 is most profoundly found in the annular section within  $\theta' \in [10^\circ, 30^\circ]$  shown in figure G.3. We model the hilly scenery in this annulus with a single valley by:

$$\tilde{f} = c_1 - c_2 \cos \phi' - c_3 \sin \phi' \quad (\text{G.6})$$

using the linear least squares fitting routine "svdfit.for" from Numerical Recipes (Press et al., 1992). It appeared from several tests on mathematical calibration sets generated using the laws of King and of Jørgensen that the wire orientation angle  $\phi$ , which is obtained by:

$$\phi = \arctan(c_3/c_2) \quad (\text{G.7})$$

is up to 6 digits accurate, provided  $\theta$  differs substantially from zero.



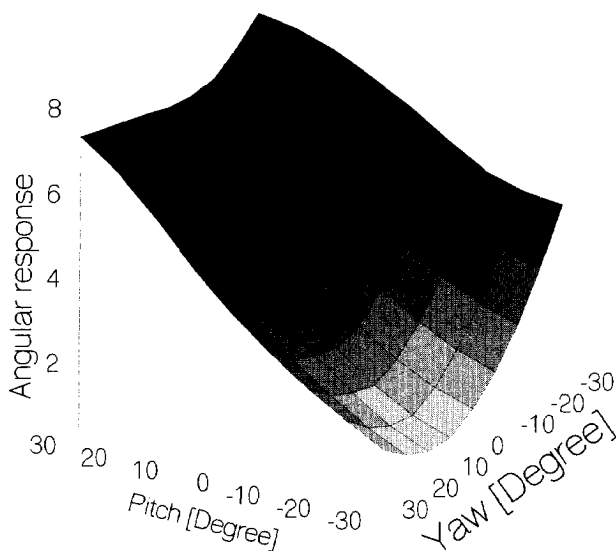


Figure G.1: Angular response of a slanted wire

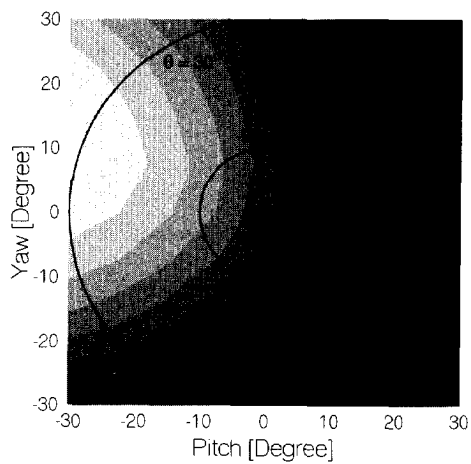


Figure G.2: Angular response of a slanted wire.

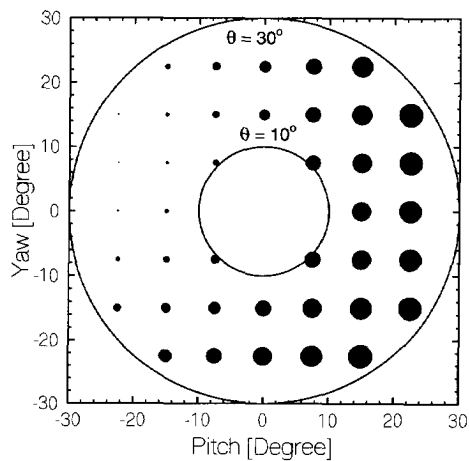


Figure G.3: Annular section of angular calibration samples. The size of the dots is proportional to the response of the wire.

## G.4 Estimation of $\theta$ , $k$ , $h$ and $B$

Parameters  $A$ ,  $n$  and  $\phi$  have been found in previous steps. Coefficients  $\theta$ ,  $k$  and  $h$  are determined iteratively from the angular calibration data:

- In the first stage of every iteration an estimate is constructed for the wire's second orientation angle  $\theta$ . The non-linear Levenberg-Marquardt method is used to fit  $\theta$  (and coefficient  $c_4$ ). In the first iteration we set  $k = 0$  and  $h = 1$ . The following relation (based on Jørgensen's law) is used:

$$\tilde{f} = c_4^2 \left( G_1 + k^2 G_2 + (h^2 - 1) G_3 \right) \quad (\text{G.8})$$

$$\begin{aligned} G_1 &\equiv \frac{(\mathbf{u} \cdot \mathbf{n})^2}{|\mathbf{u}|^2} \\ &= u_x^2 + u_y^2 + \sin^2 \theta \left[ u_z^2 - (u_x \cos \phi - u_y \sin \phi)^2 \right] + 2u_z \sin \theta \cos \theta [u_x \cos \phi - u_y \sin \phi] \end{aligned} \quad (\text{G.9})$$

$$G_2 \equiv \frac{(\mathbf{u} \cdot \mathbf{t})^2}{|\mathbf{u}|^2} = -u_x \sin \theta \cos \phi + u_y \sin \theta \sin \phi + u_z \cos \theta \quad (\text{G.10})$$

$$G_3 \equiv \frac{(\mathbf{u} \cdot \mathbf{b})^2}{|\mathbf{u}|^2} = u_x \sin \phi + u_y \cos \phi \quad (\text{G.11})$$

where vectors  $\mathbf{n}$ ,  $\mathbf{t}$  and  $\mathbf{b}$  are normal, tangential and binormal unit vectors as defined in figure 6.2. The direction of the stem of the probe (necessary to find vector  $\mathbf{b}$ ) is supposed to be known.

- In the second stage of every iteration we use the provisional orientation of the wire from the former stage to find coefficients  $k$  and  $h$  in Jørgensen's law and  $B$  from King's law. We fit the following relation (with "svdfit.for" from Numerical Recipes):

$$\tilde{f} = c_5 u_n^2 + c_6 u_t^2 + c_7 u_b^2 \quad (\text{G.12})$$

Coefficients  $k$ ,  $h$  and  $B$  are found from fit-coefficients  $c_5$ ,  $c_6$  and  $c_7$  via relations:

$$k = \sqrt{\frac{c_6}{c_5}} \quad h = \sqrt{\frac{c_7}{c_5}} \quad B = c_5^{n/2} \quad (\text{G.13})$$

Tests have shown that this process will converge within 100 iterations.

# Literature

- Acrivlellis, M. (1977). Hot-wire measurements in flows of low and high turbulence intensity. *DISA Info*, 22:15–20.
- Apollonius of Perga (250 BC - 175 BC). Proof of the equivalence of the epi-cycle motion and an excentre motion in astronomy.
- Atassi, H. and Grzedzinski, J. (1989). *J.Fluid Mech.*, 209:385–403.
- Batchelor, G. (1953). *The theory of homogeneous turbulence*. Cambridge University Press, Cambridge.
- Batchelor, G. (1967). *An introduction to fluid dynamics*. Cambridge University Press.
- Batchelor, G. and Proudman, I. (1954). *Quart.J.Mech.Appl.Math.*, 7:83–103.
- Batchelor, G. and Proudman, I. (1956). *Phil.Trans.Roy.Soc.*, 248A:369.
- Bearman, P. (1972). Some measurements of the distortion of turbulence approaching a two dimensional body. *J. Fluid Mech.*, 53:451–460.
- Bordoni, U. (1912). Un procedimento per la misura della velocita dei gas. *Nuovo Cimento*, 3:241–283.
- Boussinesq, J. (1901). Sur le pouvoir refroidissant d'une courant liquide ou gazeuse. *Compt.Rend.*, 132,133:1382,257–262.
- Bradshaw, P. (1971). *An introduction to turbulence and its measurement*. Pergamon Press, Oxford.
- Bradshaw, P. and Pankhurst, R. (1964). The design of low speed wind tunnels. *Prog.Aeronaut.Sci.*, 5:1–69.
- Broersen, P. (1996). Best order of long autoregressive models for moving average estimation. *Eusipco, Triest*.
- Broersen, P. (1998). Facts and fiction in spectral analysis. *Proc. IEEE*, pages 1325–1330.
- Browne, L., Antonia, R., and Chua, L. (1989). Calibration of x-probes for turbulent flow measurements. *Exp.in Fluids*, 7:201–208.
- Bruun, H. (1995). *Hot-wire anemometry*. Oxford University Press, New York.
- Bruun, H., Khan, M., Al-Kayiem, H., and A.A.Fardad (1988). Velocity calibration relationships for hot-wire anemometry. *J.Phys.E: Sci.Instrum.*, 21:225–232.
- Chauvenet, W. (1863). *Vol 2: Theory and use of astronomical instruments; method of least squares*, pages 558–566. J.B. Lippincott & Co, Philadelphia, 1871, revised and corrected fourth edition.
- Citriniti, J. and George, W. (1996). The reduction of spatial aliasing by long hot-wire anemometer probes. *submitted to Exp.in Fluids*.
- Collis, D. and Williams, M. (1959). Two-dimensional convection from heated wires at low reynolds numbers. *J.Fluid Mech.*, 6:357–389.
- Comte-Bellot, G. and Corrsin, S. (1966). The use of a contraction to improve the isotropy of grid-generated turbulence. *J.Fluid Mech.*, 25(4):657–682.
- Corrsin, S. (1963). *Encyclopedia of Physics*, 8(2):568.
- Dryden, H. and Kuethe, A. (1929). The measurement of fluctuations of air speed by the hot-wire anemometer. *NACA TR*, 320.
- Durbin, J. (1959). Efficient estimation of parameters in moving average models. *Biometrika*, 46:306–316.
- Farge, M. (1992). Wavelet transforms and their applications to turbulence. *Ann.Rev.Fluid Mech.*, 24:395–457.

- Favre, A., Gaviglio, J., and Dumas, R. (1953). *Recherche aéronaut.*, 32:21.
- Fingerson, L. and Freymuth, P. (1983). *Thermal anemometers*, chapter 4, pages 99–154. Hemisphere, Washington.
- Forbes, G. (1884). On the relation which ought to subsist between the strengths of electric current and the diameter of conductors to prevent overheating. *J.Inst.of Electric Engrs*, 13:232–262, 312–313.
- Gieseke, T. and Guezennec, Y. (1993). An experimental approach to the calibration and use of triple hotwire probes. *Exp.in Fluids*, 14:305–315.
- Goldstein, M. (1978). *J.Fluid Mech.*, 89(3):433–468.
- Gooden, J. (1995). Error analysis of x hotwire measurements on the garteur 3d boundary layer experiment. *NLR Report*.
- Gray, D. (1963). *American Institute of Physics Handbook*. McGraw-Hill Book Company, New York, second edition.
- Griffel, D. (1981). *Applied functional analysis*. Ellis Horwood Limited, Chichester, England.
- Groth, J. and Johansson, A. (1988). Turbulence reduction by screens. *J.Fluid Mech.*, 197:139–156.
- Harper, D. (1912). Thermometric lag. *NBS Scientific Paper*, 185.
- Hinze, J. (1975). *Turbulence*. McGraw-Hill, New York, second edition.
- Hipparchos of Rhodos (First quarter of second century BC - 127 BC). Introduction of the epicycle motion in the astronomy.
- Hirota, M., Fujita, H., and Yokosawa, H. (1988). Influences of velocity gradient on hot-wire anemometry with an x-wire probe. *J.Phys.E, Sci.Instr*, 21:1077–1084.
- Hoskin, M. (1997). *The Cambridge illustrated history of astronomy*. Cambridge University Press, Cambridge.
- Hunt, J. (1973). A theory of turbulent flow round two-dimensional bluff bodies. *J.Fluid Mech.*, 61:625–706.
- Hunt, J. and Hussain, F. (1991). *J.Fluid Mech.*, 229:569–587.
- Jansen, A. (1977). *BINAS*. Wolters-Noordhoff, Groningen.
- Janssen, L. and Warmoeskerken, M. (1987). *Transport phenomena data companion*. Delftse Uitgevers Maatschappij, Delft.
- Johnson, F. and Eckelmann, H. (1984). A variable angle method of calibration for x-probes applied to wall-bounded turbulent shear flow. *Exp.Fluids*, 2:121–130.
- Jørgensen, F. (1971). Directional sensitivity of wire and fibre-film probes. *DISA Info*, 11:31–37.
- Kampé de Fériet, J. (1948). Le tenseur spectral de la turbulence homogène non isotrope dans un fluide incompressible. In *Proceedings of the seventh international congress for applied mechanics*, London.
- Kanevce, G. and Oka, S. (1973). Correcting hot-wire readings for influence of fluid temperature variations. *DISA Info*, 14:15–18.
- Kármán, T. V. (1948). *Proc.Natl.Acad.Sci.U.S.*, 34:530.
- Kastrinakis, E. and Eckelmann, H. (1983). Measurement of streamwise vorticity fluctuations in a turbulent channel flow. *J.Fluid Mech.*, 137:165–186.
- Katsaros, K., Smith, S., and Oost, W. (1987). Hexos-humidity exchange over the sea. a program for research on water-vapor and droplet fluxes from sea to air at moderate to high wind speeds. *Bul.Am.Met.Soc.*, 68 No 5:466–476.
- Kay, S. and Marple, S. (1981). Spectrum analysis, a modern perspective. *Proc. IEEE*, 69:1380–1419.
- Kennelly, A., Wright, C., and Van Bylevelt, J. (1909). The convection of heat from small copper wires. *Trans.A.I.E.E.*, 28:363–397.
- Kevlahan, N.-R. and Hunt, J. (1997). Nonlinear interactions in strained turbulence. *J.Fluid Mech.*, 337:333–364.
- Kida, S. and Hunt, J. (1989). Interaction between different scales of turbulence over short times. *J.Fluid Mech.*, 201:411–445.
- King, L. (1914). On the convection of heat from small cylinders in a stream of fluid: Determination of the convection constants of small platinum wires with applications to hot-wire anemometry. *Phil.Trans.Roy.Soc. A*, 214:373–432.
- Kovasnay, L. (1959). Turbulence measurements. *Appl.Mech.Rev.*, 12:375–379.

- Kramers, H. (1946). Heat transfer from spheres to flowing media. *Physics*, 12:61–80.
- Kreplin, H. and Eckelmann, H. (1979). Behaviour of the three fluctuating velocity components in the wall region of a turbulent channel flow. *Phys. Fluids*, 22:1233–1239.
- Lamb, H. (1879). *Hydrodynamics*. Dover Publications, New York, 1945, first american edition.
- Laws, E. and Livesey, J. (1978). Flow through screens. *Ann.Rev.Fluid Mech.*, 10:247–266.
- Lemonis, G. (1995). *An experimental study of the vector fields of velocity and vorticity in turbulent flows*. PhD thesis, ETH Zürich. Diss.ETH Nr.11033.
- Lemonis, G. and Dracos, T. (1994). A new calibration and data reduction method for turbulence measurement by multihotwire probes. *Submitted to Exp.in Fluids*.
- Lighthill, M. (1956). Drift. *J.Fluid Mech.*, 1:31–53.
- Lindborg, E. (1995). Kinematics of homogeneous axisymmetric turbulence. *J.Fluid Mech.*, 302:179–201.
- Lomas, C. (1986). *Fundamentals of hot-wire anemometry*. Cambridge University Press, Cambridge.
- Lowell, H. (1950). Design and application of hot-wire anemometers for steady state measurements at transonic and supersonic air speeds. *NACA TN*, 2117.
- Lueptow, R., Breuer, K., and Haritonidis, J. (1988). Computer aided calibration of x-probes using a look-up table. *Exp.Fluids*, 6:115–118.
- Lumley, J. (1978). Computational modeling of turbulent flows. *Adv.Appl.Mech.*, 26:183–309.
- Maciel, Y. (1994). *Anémometrie à fils chaud*. PhD thesis, ONECERT, France. Draft version of Ph.D.-Thesis.
- Marasli, B., Nguyen, P., and Wallace, J. (1993). A calibration technique for multiple-sensor hot-wire probes and its application to vorticity measurements in the wake of a circular cylinder. *Exp.in Fluids*, 15:209–218.
- Meneveau, C. (1991). Analysis of turbulence in the orthonormal wavelet representation. *J.Fluid Mech.*, 232:469–520.
- Michard, M., Mathieu, J., Morel, R., Alcaraz, E., and Bertoglio, J. (1987). *Grid generated turbulence exhibiting a peak in the spectrum*, volume 1, pages 163–169. Springer Verlag.
- Milne-Thomson, L. (1938). *Theoretical Hydrodynamics*. The Macmillan Press, London, 1968, fifth edition.
- Morris, J. (1912). The electrical measurement of wind velocity. *Engineering*, 44:892–894. see also *Electrician* 69, pp. 1056–1059.
- Nieuwstadt, F. (1992). *Turbulentie*. Epsilon Uitgaven, Utrecht. (in dutch).
- Oberbeck, A. (1895). Über die abkühlende Wirkung von Luftströmen. *Annalen d.Phys.u.Chem.*, 56:397–411.
- Park, S. and Wallace, J. (1993). The influence of instantaneous velocity gradients on turbulence properties measured with multi-sensor hot-wire probes. *Exp.Fluids*, 16:17–26.
- Parthasarathy, S. and Tritton, D. (1963). Impossibility of linearizing a hot-wire anemometer for measurements in turbulent flows. *AIAA Journal*.
- Perry, A. (1982). *How-wire anemometry*. Clarendon Press, Oxford.
- Piercy, N. and Richardson, E. (1930). *Phil. Mag.*, 9(1038–1040).
- Pourquié, M., Boersma, B., and Nieuwstadt, F. (1997). About some performance issues that occur when porting les/dns codes from vector machines to parallel platforms. In *Preprints of: Parallel CFD 97, Recent developments and advances using parallel computers*. Computational Engineering Group, CLRC Daresbury Laboratory.
- Press, W., Teukolsky, S., Vetterling, W., and Flannery, B. (1992). *Numerical recipes in FORTRAN*. Cambridge University Press, Cambridge, second edition.
- Priestley, M. (1981). *Spectral analysis and time series*. Academic Press Limited, London, 1992, seventh edition.
- Ptolemaeus (about 100–170). *Almagest*. Best known ancient reference to epicycle motion.
- Reynolds, A. and Tucker, H. (1975). The distortion of turbulence by general uniform irrotational strain. *J.Fluid Mech.*, 68:673.
- Rodi, W. (1975). A new method of analysing hot-wire signals in highly turbulent flow, and its evaluation in a round jet. *DISA Info*, 17:9–18.
- Roshko, A. (1954). *N.A.C.A. Tech. Note*, 3168.
- Sausttrup Kristensen, H. (1973). Hot-wire measurements in turbulent flows. *Disa Info*.

- Saxena, V., Hunt, J., and Savill, M. (1998). An rdt based model for large scale turbulent flows around bluff bodies. *submitted to Flow, Turbulence and Combustion*.
- Serrin, J. (1959). Mathematical principles of classical fluid mechanics. In S. Flugge and C. Truesdell, editors, *Handbuch der Physik* 8, pages 125–263.
- Smith, J. and Ness, H. V. (1984). *Introduction to chemical thermodynamics*. McGraw-Hill Book Company, New York, 4-th edition.
- Squires, G. (1993). *Practical Physics*. Cambridge University Press, third revised edition.
- Sreenivasan, K. and Narasimha, R. (1978). Rapid distortion of axisymmetric turbulence. *J. Fluid Mech.*, 84:497–516.
- Stainback, P. and Nagabushana, K. (1993). Review of hot-wire anemometry techniques and the range of their applicability. In *Thermal anemometry*, volume FED-Vol.167, pages 93–133. ASME.
- Tennekes, H. (1976). Fourier-transform ambiguity in turbulence dynamics. *J. Atm. Sci.*, 33:1660–1663.
- Tennekes, H. and Lumley, J. (1972). *A first course in turbulence*. The MIT Press.
- Thurston, H. (1994). *Early Astronomy*. Springer verlag, New York.
- Tsinober, A., Kit, E., and Dracos, T. (1992). Experimental investigation of the field of velocity gradients in turbulent flows. *J. Fluid Mech.*, 242:169–192.
- Uittenbogaard, R. (1995). *The importance of internal waves for mixing in a stratified estuarine tidal flow*. PhD thesis, Delft University of Technology.
- van Haarlem, B., Boersma, B., and Nieuwstadt, F. (1998). Direct numerical simulation of particle deposition onto a free-slip and no-slip surface. *submitted to Phys. Fluids*.
- Vasanta Ram, V. (1992). On the effects of fluid temperature on hot-wire characteristics. *Exp. in Fluids*, 13:155–162, 267–278.
- Veldkamp, F. (1985). Elementaire lie-theorie. Technical report, RUU, Utrecht. Lecture notes.
- Weast, R. and Selby, S. (1984). *Handbook of Chemistry and Physics*. The Chemical Rubber Company, 64-th edition.
- Weber, H. (1868). *J. reine angew. Math.*, 68:286–292.
- Weinberg, S. (1985). *Applied linear regression*. John Wiley and Sons, Chichester.
- White, F. (1986). *Fluid mechanics*. McGraw-Hill Book Company, New York.
- Willmarth, W. and Bogar, T. (1977). Survey and new measurements of turbulent structure near the wall. *Phys. Fluids*, 20:S9–S21.
- Wubben, F. (1991). Single and cross hot-wire anemometry in incompressible flow. Report LR 663, Delft University of Technology, Faculty of Aerospace Engineering, The Netherlands.
- Wyngaard, J. (1968). Measurement of small-scale turbulence structure with hot wires. *J. Phys. E, Sci. Instr.*, 1:1105–1108.
- Wyngaard, J. (1969). Spatial resolution of the vorticity meter and other hot-wire arrays. *J. Phys. E, Sci. Instr.*, 2:983–987.
- Zhu, Y. and Antonia, R. (1995). Effect of wire separation on x-probe measurements in a turbulent flow. *J. Fluid Mech.*, 287:199–223.
- Zhu, Y. and Antonia, R. (1996). Spatial resolution of a 4-x-wire vorticity probe. *Meas. Sci. Technol.*, 7:1492–1497.
- Ziegler, M. (1934). The construction of a hot-wire anemometer with linear scale and negligible lag. *Proc. K. Ned. Akad. Wet.*, 15(1).







vermelden of te suggereren, want die modellen zijn 'waar', hoewel een afschatting van de consequenties van de in het model gemaakte aannamen best een significantieaanduiding had kunnen opleveren.

- c Zolang het een goed gebruik is in het vakgebied stromingsleer bij het presenteren van berekende en gemeten grootheden en parameters geen significantie of meetnauwkeurigheid te vermelden, is elke discussie over verschillen tussen gevonden waarden zinloos, hetgeen betekent dat iedereen het *à priori* met elkaar eens is.

## Wis- en natuurkunde

- 7 Negentig procent van de studenten natuurkunde die zich in de afstudeerfase bevinden heeft geen beeld bij de op de middelbare school geleerde begrippen massa, impuls, traagheidsmoment en impulsmoment.
- 8 Als Ruud Zweistra, door uit te gaan van de Lorentz-invariantie van de uitkomst van natuurkundige proeven, een geheel van Bohrse vaagheden ontdane afleiding van de Dirac-vergelijking denkt te kunnen geven, waarmee Einsteins uitspraak dat God niet dobbelt bekrachtigd zou zijn, dan verdient hij óf een serieuze weerlegging óf het doctoraat.
- 9 De verhouding tussen wis- en natuurkunde is gelijk aan de verhouding tussen solfège en muziek.
- 10 Het verschil tussen een HTS-er en een TU-er is dat de HTS-er iets kan toepassen wat hij niet wil begrijpen terwijl de TU-er iets kan begrijpen wat hij niet wil toepassen.
- 11 In tegenstelling tot wat veel mensen aannemen, is het een voordeel dat steeds meer onderzoeksresultaten - van memo tot artikel - door verregaande automatisering met een uniforme opmaak worden gepresenteerd. Het verwijt namelijk, dat het gebeuzel van laag opgeleide mensen zich nu als wetenschappelijke publicatie zou voordoen, veronderstelt abusievelijk dat de status "is gepubliceerd" van een wetenschappelijke publicatie de lezer zou ontslaan van de plicht op te letten of de inhoud van het stuk wel zinvol is.
- 12 Ook een vector kan complex-waardige componenten hebben.
- 13 a De aanname in autoregressieve modellen, dat een signaal het best gemodelleerd wordt als de voorspellingsfout in het *eerstvolgende* sample geminimaliseerd wordt, is zelden interessant, omdat ze voorbij gaat aan het continue karakter van de meeste signalen (dat herbemonstering met een hogere frequentie toestaat), en omdat men vaak liever de fout in een combinatie van locale en globale uitspraken over het signaal wil optimaliseren. Een voorbeeld hiervan uit de economie: De lange termijn belegger, die zijn oudedagsvoorziening veilig hoopt te stellen door een mandje met aandelen samen te stellen, is niet geïnteresseerd in de fout in de voorspelling van de waarde van zijn portefeuille op de dag nadat de beursorderlijn zijn aankooporder heeft uitgevoerd, maar in de verwachtingswaarde van zijn vermogen als hij zijn reserves wil gaan aanspreken, en eventueel één maal per jaar in de tussentijdse waarde

# Stellingen

## Stromingsleer

- 1 Op basis van de in de literatuur opgegeven bedrijfstemperaturen van hete draden in hete draad anemometers, is een goede maat te geven voor de temperatuur waarbij lucht gebakken wordt.
- 2 Het begrip "Taylor's microschaal" wordt in de opleiding Stromingsleer als een wiskundige grootte geïntroduceerd, en niet als een natuurkundige. Hierom dient óf dit begrip te worden afgeschaft óf er moet meer reclame worden gemaakt voor het boek van Hinze. (J.O. Hinze, "Turbulence", second edition, 1975, McGraw-Hill, New York)
- 3 Er wordt een hoop aan duidelijkheid gewonnen als iedereen die zich geconfronteerd ziet met het begrip impulsverliesdikte vooraleer er mee aan de slag te gaan eerst of het dictaat Grenslagen A van Prof. van Ingen (TU Delft) of het dictaat Fysische Stromingsleer van Dr. A. Jacobs (LU Wageningen) na zou slaan op het idee achter deze grootte.
- 4 In hun analyse hebben Kida en Hunt in relatie 2.18a verzuimd de commutatie van de lokale en de gemiddelde rektensor te onderzoeken, waardoor hun relatie niet geldig is. Hun verdere analyses zijn echter beperkt tot stromingen met een constante rek, die triviale op elk tijdstip commuteert met zijn gemiddelde. Hierom zijn toevalligerwijs hun resultaten niet door commutatie-perikelen beïnvloed.  
(S. Kida and J.C.R. Hunt, 1989, "Interaction between different scales of turbulence over short times", J.Fluid Mech. 201, pp.411-445)
- 5 Met de in dit proefschrift ontwikkelde relaties voor het corrigeren van vertekening in éénpuntsmetingen is misschien een stuk gereedschap beschikbaar gekomen om in atmosferische turbulentie het *spectral gap* te identificeren tussen turbulente bewegingen en bewegingen die zich afspelen op een synoptische meteorologische tijdschaal.
- 6
  - a Binnen het vakgebied stromingsleer is het een goed gebruik om, bij het grafisch presenteren van (numerieke en experimentele) bevindingen en modellen, symbolen te gebruiken ter grootte van de externe fout tussen model en bevinding, om daarmee een interne fout te suggereren die hoort bij een  $\chi^2$  van 1 en het publiek in slaap te sussen omdat hun bevindingen dus *ok* zijn.
  - b Binnen het vakgebied stromingsleer is het een goed gebruik om, bij het grafisch presenteren van theoretische bevindingen en bestaande modellen, nooit een fout te

als hij in één punt ging meten, "de meeste wind ernaast waaide", zodat het meeste dat in zijn tunnel gebeurde hem ontglipte. De signalen die hij registreerde bleken voor meer dan één uitleg vatbaar. Hier bleek een onopgelost probleem achter te schuilen, dat hij is gaan temmen. Dat is gelukt. De windtunnel ging weer aan en er werd verder gemeten. Het resulterend verslag heeft u nu vast.

Naast zijn AIO-schap heeft Arjan, gedreven door zijn drang de wereldlast op zijn schouders te nemen, als vrijwilliger gewerkt aan de telefonische hulplijn van de NVSH, waarvoor hij ook het opleidingsmateriaal heeft verzorgd. Door dit werk heeft hij veel over mensen geleerd.

Sinds enige tijd vindt hij de Nederlandse literatuur ook weer te pruimen. Dit komt goed uit, want het vak Nederlands vond hij al leuk. Hoewel er nog niet veel op papier staat, heeft hij aspiraties om, na dit boek, iets verhalends uit te geven. We zijn benieuwd.

Sinds 1 mei 1998 is hij terug bij het weer: hij heeft een tweejarig contract als postdoc bij de vakgroep Meteorologie en Luchtkwaliteit van de Landbouw Universiteit Wageningen. Daar bekijkt hij hoeveel water, warmte en andere zaken er uit de bodem komen.

Op 25 juni 1999 zal Arjan doctor worden. Die dag zullen veel mensen, om verschillende redenen, opgelucht ademen.

Karin

# Curriculum vitae

Tijdens het gezang van de zusters ter gelegenheid van Pinksterzondag 17 mei 1964 is Arjan geboren aan de Overtoom te Amsterdam. Hij had toen al een damesmaat hoofdomtrek, hetgeen duidde op een filosofische aanleg. Later dat jaar is hij dieper Noord Holland ingetrokken, waar hij van 1976 tot 1982 het Marmellius Gymnasium te Alkmaar doorliep. In de tweede klas van die school bleek dat een aantal zaken die hij altijd al leuk had gevonden gedoceerd werden onder de verzamelnaam "natuurkunde". Er werd begonnen met de bouw van een sterrenkijker, bas-klarinet gespeeld in de schoolband en winkelwagentjes verzameld en flessenhok gedraaid voor een grote supermarkt. In deze cruciale fase van ontwikkeling heeft Arjan zich Noordhollandse karaktertrekken aangemeten die, naar het zich nu laat aanzien, nooit meer zullen verdwijnen. Ook de invloeden van Edgar Allan Poe, de apologie van Socrates, de Donald Duck, Pink Floyd en Jon Lord moeten niet onderschat worden.

In 1982 begon hij aan zijn studie theoretische natuurkunde in Utrecht. Destijds leek voor derden Amsterdam een logische keuze. Achteraf is het tegendeel gebleken: nergens zou Arjan beter gepast hebben dan in het Utrechtse natuurkundeonderwijs. In 1989 rondde hij, begeleid door Henk van Beijeren, zijn scriptie over het achtvertexmodel af en behaalde z'n diploma. Sindsdien mag hij zich "theoretisch fysicus uit Utrecht" noemen, een, naar later bleek, vreeswekkende term. Tijdens zijn studie heeft hij veel bijles en werkcollege gegeven. Verder ontdekte hij in deze periode dat de levenloze wereld alleen niet zaligmakend is. Hij gaf diverse verzamelingen terug aan zijn ouders "omdat ze zo weinig terug zeiden" en begon aan zijn huidige relatie.

De vervangende dienst werd van 1989 tot 1991 vervuld bij de afdeling Oceanografie van het KNMI, waar het leren kennen van diverse computerspelletjes en een heel goede vriend van onschatbare waarde bleek te zijn. Verder heeft de altijd enthousiaste Wiebe Oost hem daar voor de stromingsleer warm gemaakt, door te vragen: "Wat moeten we met al die magneetbanden vol gegevens die er tijdens onze reises zijn verzameld?"

In een vroeg stadium is Frans Nieuwstadt van het Laboratorium voor Aëro- en Hydrodynamica van de TU Delft bij het project betrokken. Deze stelde als voorwaarde voor zijn medewerking "dat er meer tijd in gestoken moest worden dan die anderhalf jaar". Zo kan het gebeuren dat Arjan, geheel in stijl met zijn studie, ruim de tijd heeft genomen voor het promotieonderzoek. Nadat hij jarenlang gezworen had nooit te zullen gaan promoveren, begon de wetenschappelijke queeste serieus in 1991 te Delft: het KNMI-onderzoek werd voortgezet in universitair verband aan de TU. Na vijf jaar bouwen was de opstelling klaar om in een windtunnel metingen te verrichten. Zinnen waarin combinaties gemaakt worden van de woorden *renderen*, *lijmklem*, *postscript* en *netwerk* zullen hierdoor nog tijden niet straffeloos gebezigd mogen worden. Hij heeft zijn zwaarbevochten opstelling aanvankelijk maar een week gebruikt. Arjan ontdekte dat,

Als ik er goed over nadenk, beseft ik dat ik mijn kennis en ervaring om ingewikkelde ruimtelijke problemen op te lossen niet in Utrecht heb geleerd, maar in Alkmaar. Conrector Dompeling, die ons in de vijfde als proefwerk gewoon de schoolonderzoeken van de zesde gaf, heeft al zijn wiskundige hobbies op me gebotvierd. En met succes. Daarnaast heb ik op die school van Dompeling en Wolfswinkel mogen zien wat relativiseringsvermogen is. Sowieso kan ik (op basis van een vergelijkend warenonderzoek onder vrienden) stellen dat er op het Murmellius bijna alleen bovengemiddeld goede leraren rondlopen.

Dat de aandelen Hoogovens zo hard zijn gestegen is de persoonlijke verdienste van Ruud, die, uit het volle staal, een opstelling voor me heeft opgetrokken die zijn meerdere in deze wereld niet kent.

In Utrecht had ik mathematische fysica geleerd. Of een poging gedaan dat te leren. Van René heb ik natuurkunde geleerd. Een hele openbaring. Ook ben ik blij dat ik, als echte kameraden, veel met René heb gezongen.

Jennifer, Bennie, René, Dineke, Mathieu, Jacobiene, Lourens, Bendiks Jan, Aswin, Christian en Bas stonden garant voor gezelligheid op de vakgroep.

Tussen een 100 uren werkweek door heeft Bennie binnen een dag zorg gedragen voor het zinvol redigeren van de laatste stukken van dit boekje. Hiervoor, en voor de gezangen en de filosofische discussies, wil ik hem bedanken.

Sander Mertens heeft de karikatuur getekend die ik heb gebruikt voor de tweede voorkant van dit boek. Bij het ontwerpen van de kaft was Sander niet te bereiken, waardoor ik het plaatje nu zonder zijn toestemming heb geplaatst. Als hij toch bezwaren heeft tegen mijn gebruik van zijn plaatje moeten we maar eens praten over passende sancties. Met Arkady Tsinober heb ik op hoog niveau (165 m) discussies gehad over het vakgebied. Van hem weet ik hoe je een tandenborstel moet vasthouden.

Frans heeft een keer zijn Kerst opgeofferd om relaties (2.123) en (2.124) te kraken, hetgeen resulteerde in de gegeven oplossing. Zijn toewijding aan het vak kent geen grenzen, en ik heb er mede vrucht van mogen plukken.

Met mijn studenten Floris, Martijn en Hein heb ik een goede samenwerking gehad en zij hebben bijgedragen aan de totstandkoming van de inhoud van dit boek. Verder was het met zijn tweeën en met zijn drieën vaak veel gezelliger dan alleen.

Piet Broersen dank ik voor de niet-lineaire wisselwerking.

Wanneer ik na 25 juni weer eens ontspannen zal zijn, schieten me ongetwijfeld nog horden mensen te binnen die ik ook had willen noemen. Bij voorbaat mijn excuses.

Arjan van Dijk  
Utrecht, 1999

# Ten geleide

Boekjes schrijven is mensenwerk. Ook een context van "opleiding tot *zelfstandig* onderzoeker" houdt niet in dat je zoiets in je eentje doet. Impliciet besloten in de opleiding tot onderzoeker wachten synchroon lopende cursussen "groepsdynamica" en "relatie-onderhoud".

Waar het de eerste cursus betreft: ook nadat het boekje klaar is, zullen groepsprocessen (hopelijk) tot de dagelijkse zaken behoren. Er bestaat een kleine kans dat iemand zijn voordeel nog kan doen met mijn bevindingen. Hiertoe verwijs ik naar de stellingen die ik heb gegroepeerd onder het kopje "Communicatie".

Het tweede onderwerp is specifiek: als AIO offer je grote plukken tijd en aandacht op voor jezelf. Onder andere omstandigheden zou je deze tijd wellicht aan een ander (partner, vrienden) hebben toebedeeld en je belooft beterschap voor in de toekomst. De illusie echter dat je na je promotie heel anders zult gaan leven veronderstelt dat je gemakkelijk uit je ritme zult stappen. Dat is niet het geval. Je bent namelijk opgeleid om te zijn wie je door die opleiding bent geworden: iemand die zijn tijd offert aan de wetenschap. Helaas hebben ze je tijdens je opleiding doorgaans alleen maar studieboeken op je vakgebied laten lezen. Om de risico's van een monomane ontwikkeling te beteugelen heb ik gedurende mijn onderzoek een tijd vrijwilligerswerk verricht. Hierbij ben ik een paar boeken tegengekomen die op een actuele en heldere wijze inzicht geven in het menselijk functioneren. Een informele introductie van één van deze werken op de vakgroep Stromingsleer heeft geresulteerd in een ongekende populariteit. Het betrof de 23-ste druk van "Liefde is een werkwoord: Spelregels voor een relatie" van de hand van Alfons Vansteenwegen, dat in 1997 verscheen bij Uitgeverij Lanno nv uit Tiel. Naar schatting 15 integrale kopieën zijn gemaakt door collega's uit alle gelederen.

Dit proefschrift is het verslag van een inspanning, waaraan bijdragen zijn verleend door een grote groep mensen. Bij deze dank ik iedereen voor zijn of haar bijdrage aan deze studie en aan mijn vorming op wetenschappelijk of enig ander ander terrein. Zonder de niet door hen verrichte inspanningen te geringschatten, wil ik mijn uitdrukkelijke dank uitspreken aan een paar mensen.

Mijn ouders dank ik voor het door hen gestelde vertrouwen in mijn capaciteiten.

Uitwisseling gaat het hardst als de verschillen het grootst zijn. Dit is zeker van toepassing op mijn leven met Karin. In ons proberen onze verschillen te overbruggen kom ik dimensies van mezelf tegen, waarvan ik het bestaan nooit had vermoed, maar waar ik me met graagte in stort. Ik wil haar graag bedanken dat ze er is. Wat ze tijdens de totstandkoming van dit boek voor me heeft betekend is hier niet te beschrijven. Bij deze nodig ik haar uit voor een aantal lange vakanties.

Do was onmisbaar als mentale coach. Kom gauw terug!

**Vertekening in eenpuntsmetingen aan turbulentie**  
Theorie, DNS en hittedraadproeven

**Aliasing in one-point turbulence measurements**  
Theory, DNS and hotwire experiments

**Stellingen**

ter verkrijging van de graad van doctor  
aan de Technische Universiteit Delft,  
op gezag van de Rector Magnificus prof.ir. K.F. Wakker,  
in het openbaar te verdedigen ten overstaan van een commissie,  
door het College voor Promoties aangewezen,  
op vrijdag 25 juni 1999 te 10.30 uur

door

**Arjan VAN DIJK**  
doctorandus in de natuurkunde,  
geboren te Amsterdam

Deze stellingen zijn goedgekeurd door de promotor:  
Prof.dr.ir. F.T.M. Nieuwstadt

Samenstelling promotiecommissie:

Rector Magnificus,	voorzitter
Prof.dr.ir. F.T.M. Nieuwstadt,	Technische Universiteit Delft, promotor
Prof.dr.ir. P.G. Bakker,	Technische Universiteit Delft
Dr.ir. P.M.T. Broersen,	Technische Universiteit Delft
Prof.dr.ir. H. Hoeijmakers,	Universiteit Twente
Prof.dr. J.C.R. Hunt, FRS,	University of Cambridge, Engeland
Dr.ir. A.F.G. Jacobs,	Landbouwniversiteit Wageningen
Prof.dr. D. Lohse,	Universiteit Twente

Copyright ©1999 by  
A. van Dijk  
Frederik Hendrikstraat 125  
NL - 3583 VJ Utrecht  
All rights reserved

ISBN 90-9012799-2  
NUGI 812, 811 en 815



# **Vertekening in eenpuntsmetingen aan turbulentie**

Theorie, DNS en hittedraadproeven

